ION-SPECIFICITY: FROM AIR-WATER INTERFACE TO THE FREE ENERGETICS OF HYDROPHOBIC ASSOCIATION

by

Shu-Ching Ou

A dissertation submitted to the Faculty of the University of Delaware in partial fulfillment of the requirements for the degree of Doctor of Philosophy in Chemistry and Biochemistry

Spring 2014

© 2014 Shu-Ching Ou
All Rights Reserved

UMI Number: 3631200

All rights reserved

INFORMATION TO ALL USERS
The quality of this reproduction is dependent upon the quality of the copy submitted.

In the unlikely event that the author did not send a complete manuscript
and there are missing pages, these will be noted. Also, if material had to be removed,
a note will indicate the deletion.

UMI 3631200

Published by ProQuest LLC (2014). Copyright in the Dissertation held by the Author.

Microform Edition © ProQuest LLC.
All rights reserved. This work is protected against
unauthorized copying under Title 17, United States Code

ProQuest LLC.
789 East Eisenhower Parkway
P.O. Box 1346
Ann Arbor, MI 48106 - 1346

ION-SPECIFICITY: FROM AIR-WATER INTERFACE TO THE FREE ENERGETICS OF HYDROPHOBIC ASSOCIATION

by

Shu-Ching Ou

Approved: _____

Murray V. Johnston, Ph.D.
Chair of the Department of Chemistry and Biochemistry

Approved: _____

George H. Watson, Ph.D.
Dean of the College of Arts and Sciences

Approved: _____

James G. Richards, Ph.D.
Vice Provost for Graduate and Professional Education

I certify that I have read this dissertation and that in my opinion it meets the academic and professional standard required by the University as a dissertation for the degree of Doctor of Philosophy.

Signed: _____

Sandeep Patel, Ph.D.
Professor in charge of dissertation

I certify that I have read this dissertation and that in my opinion it meets the academic and professional standard required by the University as a dissertation for the degree of Doctor of Philosophy.

Signed: _____

Steven Brown, Ph.D.
Member of dissertation committee

I certify that I have read this dissertation and that in my opinion it meets the academic and professional standard required by the University as a dissertation for the degree of Doctor of Philosophy.

Signed: _____

Douglas Doren, Ph.D.
Member of dissertation committee

I certify that I have read this dissertation and that in my opinion it meets the academic and professional standard required by the University as a dissertation for the degree of Doctor of Philosophy.

Signed: _____

Edward R. Lyman, Ph.D.
Member of dissertation committee

ACKNOWLEDGEMENTS

First and foremost, I would like to express my sincere gratitude to my advisor and mentor, Dr. Sandeep Patel for his generous support throughout the past five years. I have learned a lot from him in deep thinking, and tackling challenges with intelligence and perseverance. He is a dedicated professor, whose patience and encouragement has been instrumental in my growth as a researcher. He constantly makes him available to the group members and is always ready to help. Besides research, his wisdom and knowledge from society to life is exemplary. His unique sense of humor brings a heartfelt smile to those he encounters. I feel honored and I am blessed to have him as my advisor.

I am grateful to all current and past members in Patel Group: Dr. Brad A. Bauer, Dr. Yang Zhong, Timothy R. Lucas, Yuan Hu, Di Cui, Xiaorong Liu, and Dr. Sudipta Kumar Sinha. I have learned a lot from the insightful and stimulating discussions with them, and I really cherish the sleepless nights working on the clusters. I also thank our collaborators Dr. Michela Taufer and Dr. Narayan Ganesan for their expertise on the FEN-ZI project.

Besides my advisor, I would like to thank faculty, staff, and students in the Department of Chemistry & Biochemistry at the University of Delaware. Particularly, I would like to thank Dr. Steven Brown, Dr. Douglas Doren, and Dr. Edward R. Lyman for dedicating their time for service on my dissertation committee, for their encouragement and insightful comments.

I would like to thank my family: Hsi-Liang Ou, Chen-Huei Lin, Tzu-Chen Ou for their love and support. Last but not the least, I thank Ruizhi Xie whose love, encouragement and companionship help me persist through the completion of my degree.

TABLE OF CONTENTS

LIST OF TABLES . . . . . **x**
LIST OF FIGURES . . . . . **xii**
LIST OF ABBREVIATIONS AND CONSTANTS . . . . . **xix**
ABSTRACT . . . . . **xxii**

Chapter

1 INTRODUCTION **1**

1.1 Ion Specificity at the Interface 2

1.1.1 Kosmotrope and Chaotrope 4
1.1.2 Modeling Single Ions/Molecules at Interfaces Using MD Simulations 7

1.2 Outline 10

2 FORCE FIELDS AND COMPUTATIONAL METHODS **14**

2.1 Force Fields 14

2.1.1 Charge Equilibration Force Fields (CHEQ) 15
2.1.2 Drude Polarizable Force Field 17

2.2 Common Calculation Methods 18

2.2.1 Density Profile 18
2.2.2 Radial Distribution Function 19
2.2.3 Orientational Profile 20
2.2.4 Hydrogen Bond Profile and Tetrahedral Parameter 21
2.2.5 Time Dependent Properties 22

2.2.5.1 Residence Time 22

2.2.5.2 Velocity Autocorrelation Function 23
2.2.5.3 Self-Diffusion Coefficient 24

2.2.6 Free Energe Calculation: Potential of Mean Force 25

2.2.6.1 Relation between Potential of Mean Force and Free Energy Profile 27
2.2.6.2 Umbrella Sampling 29
2.2.6.3 Adaptive Biasing Force (ABF) 30

2.2.7 Surface Tension 31

2.2.7.1 Kirkwood-Buff Method 31
2.2.7.2 Capillary Wave Method 31

2.2.8 Surface Height Fluctuation and Covariance Entropy 33

3 SINGLE MONOVALENT ION AT THE LIQUID-VAPOR INTERFACE 35

3.1 Introduction: Adsorption of Ions 35
3.2 Methods 38

3.2.1 Common Simulation Protocol 38
3.2.2 Detail of Each Model 39

3.2.2.1 SPC/E, TIP4P-FQ and TIP4P-QDP 39
3.2.2.2 SWM4-NDP 41

3.2.3 Potential of Mean Force Calculation 42

3.3 Correlation between Potential of Mean Force and Surface Fluctuation 44
3.4 Solvation Structure 48
3.5 Dynamical Properties 49
3.6 Temperature Dependence: the case of TIP4P-FQ 51

3.6.1 Thermodynamic Free Energetics and Solvation Structures . . 52
3.6.2 Temperature Effects of the Surface Height Fluctuations 56

3.7 Surface Entropy 57
3.8 Discussion and Conclusions 58

4 MOLECULAR ION AT THE LIQUID-VAPOR INTERFACE . . 83

4.1 Introduction: Protein Denaturant 83
4.2 Method 85

4.2.1 Simulation Protocol 86
4.2.2 Validation 88

4.3 Potential of Mean Force and Orientational Preference 91
4.4 Connection between Conditional Potential of Mean Force and Corresponding Fluctuation 95
4.5 Solvation Structure 97
4.6 Dynamical Properties 98
4.7 β-Conditional Fluctuation 99
4.8 Discussion and Conclusions 100

5 ION SPECIFIC INDUCED FLUCTUATIONS AND FREE ENERGETICS OF AQUEOUS PROTEIN HYDROPHOBIC INTERFACES 115

5.1 Introduction: Connecting Liquid-Vapor Interfaces to Protein Hydrophobic Interfaces 115
5.2 Method 119

5.2.1 Ion Translocation Across Aqueous Liquid-Vapor Interface . . . 119

5.2.1.1 Single Halide Anion 119
5.2.1.2 Single Guanidinium Cation 121

5.2.2 HFBII with Single Ion 122

5.2.2.1 Single Halide Anion 123
5.2.2.2 Single Guanidinium Cation 125

5.2.3 Calculating Surface Height Fluctuations 126

5.3 Single Halide Anion: PMF and Surface Fluctuations 128

5.3.1 Validation: Anions at Liquid-Vapor Interfaces 128
5.3.2 Free Energetics for Anions with Protein Surfaces 130
5.3.3 Surface Fluctuation 132

5.3.4 The Effect of Protein Flexibility . . . 135

5.4 Single Guanidinium Cation: PMF and Surface Fluctuations . . . 136
5.5 Discussion and Conclusions . . . 138

6 SPECIFIC ION EFFECTS ON NANOMETER-SCALE HYDROPHOBIC ASSEMBLY . . . 151

6.1 Introduction . . . 151
6.2 Method . . . 154

6.2.1 Effect from Different Anions . . . 154
6.2.2 Temperature Effects on Hydrophobic Association . . . 157
6.2.3 Hydrophobe-Solvent Surface Fluctuation . . . 158

6.3 Hydrophobes in Different Aqueous Solutions . . . 159

6.3.1 Density Profile . . . 159
6.3.2 Free Energetics of Nanotube Association and Decompositions 163
6.3.3 Force Map: Spatial Distribution of Ions . . . 170
6.3.4 Enthalpic and Entropic Contribution . . . 174

6.4 Temperature Effects of Carbon Nanotube Association . . . 177

6.4.1 Free Energetics of Nanotube Association and Decompositions 178
6.4.2 Solvent Structure: Tube Center to Solution Bulk . . . 181
6.4.3 Solvent Structure: Intertube Region . . . 186

6.5 Conclusions . . . 190

7 CONCLUSION . . . 223

7.1 Summary of Key Results . . . 223
7.2 Future Work . . . 228

BIBLIOGRAPHY . . . 233

Appendix

A FORCE FIELD VALIDATION FOR GUANIDINIUM CHLORIDE SOLUTION: KIRKWOOD-BUFF ANALYSIS . . . 265
B CORRELATION LENGTH FOR TUBE-ION SURFACE . . . 273
C INTERTUBE REGION: LARGER VOLUME . . . 275

D LONG-RANGE CORRECTION OF LENNARD-JONES POTENTIAL FOR PMF CALCULATION OF NANOTUBE ASSOCIATION 277
E PERMISSIONS 280

LIST OF TABLES

3.1 Parameters of water models used in this study. 60

3.2 Parameters of ions used in this study. Uncertainty in the last digit denoted in parentheses. 61

3.3 Fitting results of residence time of water molecules in the first solvation shell. 62

3.4 Decomposition of $\Delta H(z)$ into water-water and ion-water components at some significant z-positions. 63

3.5 Estimated $\Delta S(z_1)$ and $\Delta S(z_{\mathrm{GDS}})$ obtained by the covariance matrix of surface height functions. z_1 indicates the window with largest fluctuations. 64

4.1 Force Field Parameters for Gdm^+, M-Gdm^+ and Cl^-. 102

4.2 Properties of the solution systems studied in this manuscript, including the position of Gibbs dividing surface (GDS), mass density (ρ_{mass}) and surface tension (γ). Values in parentheses indicate the uncertainties, which are obtained via the standard deviation of 4 replicates. 103

4.3 Surface excess calculated from our simulation and experimental data. $\Gamma^{\pm}_{\mathrm{comp}}$ refers to the surface excess of the cation/anion from our simulation. 104

5.1 LJ parameters for ions applied in this work along with the verification. 141

6.1 Parameters used in the simulation for carbon nanotube assembly. . 193

6.2 Average number of water molecules, anions and cations within the tube. 194

6.3 Decomposition of potential of mean force into contributions from water, tubes, anions, and cations. 195

6.4 Summary of key features from PMFs in Figure 6.4 b. 196

6.5 Decomposition of potential of mean force into contributions from water, tubes, anions, and cations. 197

6.6 Average number of water molecules, anions and cations within the tube. Values in parentheses denote the uncertainty in the last reported digit as determined from the standard deviation. 198

6.7 Features of the intertube water densities in Figure 6.19. The units for $\rho_{\mathrm{o,max}}$ and $\rho_{\mathrm{o,min}}$ are $\mathrm{Å}^{-3}$. 199

A.1 Coefficient activities for various concentrations of GdmCl solution. . 268

D.1 Long-range correction of Lennard-Jones Potential. 279

LIST OF FIGURES

3.1 PMF computed with different amount of sampling time. 65

3.2 Potential of mean force for single ions transporting from bulk to vapor phase in different water force fields. 66

3.3 Average surface fluctuation $\langle \delta h^2 \rangle$ for I^- in TIP4P-FQ, when the restrained position is at (a) $z = 10$ Å (b) $z = 21$ Å (c) $z = 25$ Å. Panel d shows the $\langle \delta h^2(x = 0, y = 0) \rangle$ (right above/below the ion, as indicated with arrows) as a function of ion restrained position for I^- and Cl^- in TIP4P-FQ. 67

3.4 Mean surface of I^- restrained at 4 Å below GDS for (a) small (b) large simulation cell box. Normalized surface fluctuation at 4 Å below GDS for (c) small (d) large simulation cell box. 68

3.5 Normalized average surface fluctuation $\langle \delta h_{\mathrm{L}}^2 \rangle$ as a function of radius from the I^-/Na^+ in (a) SPC/E (b) TIP4P-FQ (c) SWM4-NDP (d) TIP4P-QDP force fields. 69

3.6 The largest normalized average surface fluctuation $\left\langle \delta h_{\mathrm{L,max}}^2 \right\rangle$ versus the corresponding free energy ΔG for ions in different force fields. 70

3.7 Ion-water radial distribution function (RDF) for anions in (a) SPC/E (b) TIP4P-FQ (c) SWM4-NDP (d) TIP4P-QDP force fields. . . . 71

3.8 Average water oxygen density relative to (a) I^- (b) Cl^- (c) Na^+ at the position of 21.0 Å. (d)-(f) show the cartoon of ion with the cutoff of first solvation shell (dashed lines), second solvation shell (dot-dashed lines) and the calculated mean surface (solid black lines). 72

3.9 Oxygen velocity autocorrelation of water (TIP4P-FQ) in the bulk, near L-V interface, solvation shell water above I^-/Cl^-. 73

3.10 Potential of mean force for single (a) iodide and (b) chloride ions across the TIP4P-FQ LV-interface, relative to the value at $z = 10.0$ Å, which we consider sufficiently far away from the interface so as to represent bulk-like water region. 74

3.11 Decomposition of (a)(c) enthalpic and (b)(d) entropic contributions to the potential of mean force of single iodide and chloride ion crossing the TIP4P-FQ LV-interface, relative to the value at $z = 10.0$ Å. . . 75

3.12 Decomposition of enthalpic contributions into (a)(c) water-water and (b)(d) ion-water interactions of single iodide and chloride ion crossing the TIP4P-FQ LV-interface, relative to the value at $z = 10.0$ Å. . . 76

3.13 Anion-oxygen radial distribution function (RDF) for (a) I^- (b) Cl^- at different temperature. Average number of coordinated water for (c) I^- (d) Cl^- at different temperature. 77

3.14 Density profile of water oxygen along z-dimension, when (a) I^- (b) Cl^- is in the bulk ($z_{ion} = 10$ Å). The lower panels show the density profile along when (c) I^- and (d) Cl^- is at GDS, which is pushed toward the vapor phase as the temperature increases. 78

3.15 (a) Interaction energy between water molecule (at position (r, z) which is relative to the position of I^-) and all the other molecules. x-axis refers to the perpendicular distance from the ion, while y-axis indicates the vertical distance. Both units are in Å. The unit for energies is kcal/mol. Panel (b) and (c) show the similar profiles with ion restraining at 23 Å and 35 Å at 300 K. Panel (d)-(f) correspond to the case of I^- at 360 K. The unit for energy is kcal/mol. 79

3.16 Time profile of the estimated entropy. 80

3.17 Normalized surface height fluctuations, as functions of lateral displacement, for ions at (a) 300 K (b) 320 K, (c) 340 K and (d) 360 K. 81

3.18 Potentials of mean force (PMF's) for I^- and Cl^- in TIP4P-FQ. Symbols are semi-quantitative estimates of surface entropy (relative to bulk, hence ΔS) arising from ion-induced interfacial fluctuations. 82

4.1 Normalized number density profile of water oxygen, solute central carbon atom of ring (Gdm^+ or M-Gdm^+) and Cl^- in 1.1 m and 5.3 m solution. 105

4.2 Surface tension as a function of concentration, along with the linear fitting results. 106

4.3 Overlap of sampling between restrained windows for single Gdm^+ PMF. 107

4.4 (a) Potential of mean force of single Gdm^+/M-Gdm^+ from bulk transporting through L-V interface. Conditional potential of mean force for single (b) Gdm^+ or (c) M-Gdm^+. A vertical offset of 2 kcal/mol is added for clarity. 108

4.5 Orientational distribution of single Gdm^+ and M-Gdm^+. 109

4.6 Conditional, normalized fluctuation (δh_{L}^2) as a function of r from the center carbon of Gdm^+ or M-Gdm^+. 110

4.7 The largest, probability weighted, normalized fluctuation ($r = 0$ Å) as a function of z-position of the (a) Gdm^+ (b) M-Gdm^+. Inset shows the largest conditional fluctuation for each conditional orientation; black solid line is for single M-Gdm^+, while red dashed line corresponds to single Gdm^+. 111

4.8 Conditional density profiles of single Gdm^+ at different z-position. . 112

4.9 Oxygen VACF of water near the Gdm^+ for parallel/perpendicular orientation at (a) bulk ($z = 0$ Å) and (b) the restrained window with largest fluctuation ($z = 15$ Å). 113

4.10 β-conditional fluctuation profiles of single M-Gdm^+ at different z-position. 114

5.1 Representative snapshots of the protein HFBII system. 142

5.2 Representative snapshots of the HFBII with single ion system. . . . 143

5.3 Inherent interface fluctuations of HFBII. 144

5.4 (a) PMF of single Cl^-/I^- approaching the liquid-vapor interface in TIP3P water. (b) Normalized liquid-vapor interface fluctuation at ($x = 0$, $y = 0$) as a function of anion restrained position for Cl^- and I^-. 145

5.5 PMF for single Cl^-/I^- approaching the protein-solvent interface of (a) the hydrophobic patch (b) the less hydrophobic region (c) the hydrophilic region. 146

5.6 Average aqueous protein surface fluctuation $\langle \delta h^2(\theta, \phi) \rangle$ for (a) Cl^- locates at $z = 18$ Å (b) I^- locates at $z = 18$ Å. Reproduced with permission from Di Cui, Shuching Ou, Eric R. Peters and Sandeep Patel. "Ion-Specific Induced Fluctuations and Free Energetics of Aqueous Protein Hydrophobic Interfaces: Towards Connecting to Specific-Ion Behaviors at Aqueous Liquid-Vapor Interfaces." *Journal of Physical Chemistry B.* **2014**, *ASAP*, DOI: 10.1021/jp4105294. Copyright 2014 American Chemical Society. 147

5.7 Hydrophobic interface fluctuation at ($x = 0$ Å, $y = 0$ Å) as a function of anion z-position for Cl^- and I^- with the protein flexibility. Reproduced with permission from Di Cui, Shuching Ou, Eric R. Peters and Sandeep Patel. "Ion-Specific Induced Fluctuations and Free Energetics of Aqueous Protein Hydrophobic Interfaces: Towards Connecting to Specific-Ion Behaviors at Aqueous Liquid-Vapor Interfaces." *Journal of Physical Chemistry B.* **2014**, *ASAP*, DOI: 10.1021/jp4105294. Copyright 2014 American Chemical Society. . 148

5.8 (a) PMF of single Gdm^+ approaching the liquid-vapor interface in TIP3P water. For clarity, a vertical offset of 1 kcal/mol is added. (b) Liquid-vapor interface fluctuation at ($x = 0$, $y = 0$) as a function of cation restrained position. 149

5.9 (a) PMF of single Gdm^+ approaching the HFBII hydrophobic patch. (b) Normalized interface fluctuation at ($x = 0$, $y = 0$) as a function of cation restrained position. 150

6.1 Representative snapshots of the 3 m NaCl system used in this study; separation (d) is 26.0 Å, which is defined by the distance between the center axes of the tubes. 200

6.2 Radial number density profiles of (a) water molecules and (b) ions at $d = 19.4$ Å. 201

6.3 Average number of (a) water molecules, (b) anions, and (c) cations of the confined region in pure water and 3 m NaX (X = Cl, I) solutions. 202

6.4 (a) Total potential of mean force for tube association in pure SPC/E, 3 m NaCl, and 3 m NaI solutions. The inset shows the minimum region of the profiles. For clarity, in the inset a vertical offset of 2 kcal/mol is imposed for the case of 3 m NaI. The additional panels correspond to the decomposition of (b) water (c) anion and (d) cation contributions. The error bars are obtained from standard deviations among three independent replicates. 203

6.5 Density distribution of water molecules at location (y, z) around the carbon nanotubes, with various intertube separations. 204

6.6 The z-component of total forces from anions applied on the carbon nanotubes at position (y, z). 205

6.7 Product of the z-component of total forces ($\langle F_z \rangle$) from anions applied on the carbon nanotubes and the anion density (ρ_{anion}) at position (y, z). 206

6.8 Scaling effect of bulk anions and non-bulk anions. 207

6.9 Solvent contribution, ΔW_{solv} to the PMF and its enthalpic contribution (ΔH_{solv}), and entropic contribution ($-T\Delta S_{\text{solv}}$) for (a) pure water (b) 3 m NaCl and (c) 3 m NaI systems. Panel d-f show the comparison of the different solvents for the same thermodynamic properties. 208

6.10 Solvent-induced contribution to enthalpy of tube association, ΔH_{solv} (from Figure 6.9 d) is split into (a) the change in tube-solvent interaction ($\Delta U_{\text{tube-solv}}$) and (b) the remaining contribution from the change in solvent-solvent interactions and other mechanic work (ΔH_{rem}). All the quantities are referenced to the values at the dissociated distance $d = 26.0$ Å. 209

6.11 Ionic enthalpic contribution (ΔH_i, $i = (\text{Cl}^-, \text{I}^-, \text{Na}^+)$), and entropic contribution ($-T\Delta S_i$) in 3 m NaCl and NaI systems. 210

6.12 (a) Total potential of mean force for tube association in 3 m NaI solutions under different temperatures. The inset shows the minimum region of the profiles. (b)(c) The values of solvent-induced ΔW, ΔH and ΔS for association as functions of the temperature. The unit for y-axis in panel (a) and (b) is kcal/mol; for panel (c) it is kcal/mol/K. 211

6.13 Decomposition of PMF into (a) water (b) anion (c) cation contributions. 212

6.14 The z-component of total forces from water molecules applied on the carbon nanotubes at position (y, z) in NaI solution, for the intertube separation d = (a) 16.4 (b) 19.4 Å. Panel (c) and (d) show the difference of density of water oxygen at location (y, z) around the carbon nanotubes between 300 K and 360 K, at the corresponding intertube separations. (e) and (f) illustrates the difference of density-weighted force at location (y, z) between 300 K and 360 K. 213

6.15 Radial number density profiles of (a) water molecules (b) anions (c) cations at d = 16.4 Å under different temperatures. 214

6.16 Surface fluctuations (side facing the bulk) for (a) tube-water (b) tube-ion surface in 3 m NaI solution at different temperature. . . . 215

6.17 (a) Hydrogen bonds (N_{HB}) (b) tetrahedral configuration parameter (q) of water molecules as functions of r. 216

6.18 Average number of (a) water molecules, (b) anions, and (c) cations of the confined region in pure water and 3 m NaI solutions. 217

6.19 Intertube water oxygen density profile along z at several tube separations. 218

6.20 Intertube tube-water surface fluctuations. 219

6.21 Tube-water surface fluctuation at the side facing the solvent bulk, for (a) NaCl and NaI solutions at different concentration. 220

6.22 Normalized hydrogen bond profiles for (a) 300 K and (b) 360 K along z-axis at intertube region. 221

6.23 Tetrahedral configuration parameter (q) for (a) 300 K and (b) 360 K along z-axis at intertube region. 222

A.1 Radial distribution functions of the solute/solvent with water oxygen in GdmCl and M-GdmCl solutions. 269

A.2 Radial distribution functions between water oxygen atoms and solute nitrogen atoms in GdmCl and M-GdmCl solutions. 270

A.3 Radial distribution functions for Kirkwood-Buff analysis. 271

A.4 Kirkwood-Buff integrals correspond to panels in Figure A.3. 272

B.1 (a) Mean surface of tube-ion using different correlation length (η). (b) Tube-ion radial number density. 274

C.1 Calculated average number of (a) water molecules, (b) anions, and (c) cations of the larger confined region in pure water and 3 M NaX (X = Cl, I) solutions. 276

LIST OF ABBREVIATIONS AND CONSTANTS

ABF	Adaptive Biasing Force
CHARMM	Chemistry at HARvard Molecular Mechanics
CHEQ	Charge Equilibration
CNT	Carbon Nanotube
DFT	Density Functional Theory
DLVO	Derjaguin and Landau, Verwey and Overbeek Theory
EFP	Effective Fragment Potential
FEP	Free Energy Perturbation
fft	Fast Fourier Transform
FQ	Fluctuating Charge
Gdm$^+$	Guanidinium Cation
GDS	Gibbs Dividing Surface
GPU	Graphics Processing Unit
HFBII	Hydrophobin II
$\boldsymbol{k}_\mathrm{B}$	Boltzmann Constant, $1.3806504 \times 10^{-23}$ J/K $= 0.00198721$ kcal/mol/K
K-B	Kirkwood-Buff
LB	Lorentz-Berthelot
LCW	Lum-Chandler-Weeks Theory
LJ	Lennard Jones
LRC	Long Range Correction
LV	Liquid-Vapor

MC	Monte Carlo
MD	Molecular Dynamics
M-Gdm$^+$	Methyl-Guandinium Cation
MSD	Mean Square Displacement
NAMD	Not (just) Another Molecular Dynamics Program
PBC	Periodic Boundary Conditions
PME	Particle Mesh Ewald
PMF	Potential of Mean Force
PPC	Presssure Perturbation Calorimetry
RDF	Radial Distribution Function
SASA	Solvent-Accessible Surface Area
SHG	Second Harmonic Generation
SPC/E	Simple Point Charge Extended
SWM4-DP	Simple Water Model with 4-Sites and Drude Polarizability
SWM4-NDP	Simple Water Model with 4-Sites and Negative Drude Polarizability
SWNT	Single-Walled Nanotubes
TBA	Tert-Butyl Alcohol
TI	Thermodynamic Integration
TIP3P	Three-Point Transferable Intermolecular Potential
TIP4P	Four-Point Transferable Intermolecular Potential
TIP4P-FQ	Four-Point Transferable Intermolecular Potential with Fluctuating Charges
TIP4P-QDP	Four-Point Transferable Intermolecular Potential with Charge-Dependent Polarizability
VACF	Velocity Autocorrelation Function
VDOS	Vibrational Density of States

vdW	van der Waals
VSFG	Vibrational Sum Frequency Generation
VUV	Vacuum Ultraviolet
WHAM	Weighted Histogram Analysis Method
XPS	X-Ray Photoelectron Spectroscopy

ABSTRACT

Chemistry occurring at or near the aqueous interfaces influences various fields of processes and applications. With the development of computational resources, molecular dynamics (MD) simulations are widely used to complement the experimental results with the microscopic scale. The heart of this work is to study the stabilities of ions at different types of surface using MD.

This work begins with examining the single-ion potential of mean force (PMF) at the air-water interface with various force fields. Surface stable ions, characterized as such by minima in PMF, induce larger interfacial fluctuations, conferring more covariance entropy approaching the interface. Smaller anions show no interfacial PMF minima, nor are the enhanced interfacial fluctuation. The difference is traced to hydration shell properties of the anions, and the coupling of these shells with distant solvent.

The behavior of molecular guanidinium cation at the air-water surface is investigated next. Resulting PMF indicates that parallel orientations of the guanidinium plane (relative to the Gibbs dividing surface) exhibit pronounced minima, with significantly greater interfacial fluctuations, while the perpendicular orientations exhibit no discernible surface affinity.

At the interface between a hydrophobic region of HFBII and the aqueous solvent, we find similar ion-specific signature at the liquid-vapor interfaces. Where strong local interactions are not dominant, as in the case of protein's hydrophobic surfaces that inherently hold higher fluctuations, the anions tend to differentiate themselves based on their charge density (or "hydrophobicity"). In the case of hydrophilic interfaces, the strong charge-dipole and charge-charge interactions dominate and equalize the stabilities and interface perturbing effects of both anions.

This work next explores hydrophobic interaction between nonpolar solutes with the addition of inorganic salts. Iodide anion directly stabilizes the contact state to a much greater extent than chloride anion. Water is driven further away from the tube surface because of iodide anions segregating to the surface, which results in destabilizing contribution to the hydrophobic association.

Results of this work highlight how impurities induce long-ranged solvent perturbations that propagate to different interfaces, along with the connections between induced surface fluctuations and the impurities' surface affinities/stabilities. Future extension of this work and additional applications is suggested.

Chapter 1

INTRODUCTION

Addition of solutes and co-solutes to aqueous systems is the central to numerous physical, chemical, and biological processes such as protein stability and denaturation in aqueous solution by ions and co-solutes [1, 2, 3, 4], protein crystallization [5], protein-protein interactions [6] and protein-DNA interactions [7] to their impact on the function of nucleic acids and enzyme activity, anion-specific interfacial stability [8, 9, 10, 11, 12, 13, 14, 15, 16, 17, 18, 19], Hofmeister effects related to modulation of surface tension and protein solubility [20, 21, 22, 23], and the distinct cationic effects on multi-walled carbon nanomaterial aggregation kinetics [24]. The molecular and atomic origins, the driving forces along with the (free) energetic underpinnings have garnered a considerable number of scientific attention, along with plentiful qualitative or quantitative models purposed. The main focus in these studies usually lay on the interfaces (e.g. air-water interfaces, protein-water interfaces, hydrophobe-water interfaces), that is, the response of the interfaces to the added solutes. How different solute species behave at interfaces has been extensively studied both theoretically and experimentally. These different interfacial phenomena, or say specific surface affinities, are the key issues to understanding the behavior of (hydrophobic) molecules in eletrolyte solutions [25]. Therefore, it is natural to ask for a unified explanation about how these solutes influence/perturbate the interfaces.

In this work, we focus on the addition of ions to the system with different types of (hydrophobic) surfaces/interfaces, acknowledging that this is just one specific context. We would like to note here that "surface" is usually loosely defined in the literature [26]. One might visualize a flat, two-dimensional expanse, but in reality the surface may well be anything but flat especially in the biological interfaces [27], hence

defining the surfaces/interfaces is very critical. We will start with relatively simple interfacial systems, i.e., air-water interfaces (or liquid-vapor interfaces), which have been extensively studied using MD simulations since late 1980s [28, 29, 30, 31, 32, 8, 9, 10, 11, 12, 13, 14, 15]. Sequentially, we will extend our systems with molecular species, as well as replacing the simple liquid-vapor interfaces with more complicated hydrophobe-water surfaces, and heterogeneous protein-water surfaces. Our goal is to address how distinct interfacial stabilities of different co-soules/additives change the effective hydrophobicity in the interfacial regions, and hence manipulate the effective hydrophobicity using solution additives.

1.1 Ion Specificity at the Interface

In the late 19_{th} century, Franz Hofmeister published the famous paper titled "Zur Lehre von der Wirkung der Salze" (A discussion of the effects of salts) [20], in which he discovered that inorganic salts have different effects on precipitation of purified egg white. According to the efficiency of the different ions, they can be ordered reproducibly and are known as the Hofmeister series or lyotropic series. This systematic analysis led to the result that anions have a larger effect than cations, and therefore the Hofmeister series are divided into anionic and cationic series:

$$\text{Anions: } {SO_4}^{2-} > {HPO_4}^{2-} > \text{acetate} > \text{citrate} > Cl^- > {NO_3}^- > {ClO_3}^- > I^- > {ClO_4}^- > SCN^-$$

$$\text{Cations: } {NH_4}^+ > K^+ > Na^+ > Li^+ > Mg^{2+} > Ca^{2+} > \text{guanidinium}$$

The ions on the left decrease the solubility of hydrophobic molecules, known as having a "salting-out" effect, while ions on the right have a lesser effect and can even increase the solubility ("salting-in"). One can intepret that the addition of salts perturbate the effect hydrophobicity of protein surfaces, consequently affect the hydrophobic interactions and associations. In practical applications, e.g., in the processing of biomolecules, salts or co-solutes are frequently added to the solution to manipulate either biomolecular stability and/or solubility, or the strength of their binding to ligands

or surfaces. How these additives influence the protein surfaces, especially hydrophobic surfaces, directly or indirectly, is then the central issue to understanding/explaining the Hofmeister effects. For instance, Jain and Ahluwalia studied the thermal denaturation of lysozyme, confirmed that destabilization of the protein in tetraalkylammonium salts was due to the preferred interaction between hydrophobic ions with the hydrophobic patches on the surface of the protein [33]. Nelson and Schwartz investigated the effects of ions taken from opposite ends of the Hofmeister series (F^- and SCN^-) on the dynamics of a hydrophobic probe molecule [1] at a hydrophobic self-assembled monolayer (SAM)/aqueous interface [25]. They found that the adsorption rate of the probe molecule to the SAM increased systematically in the presence of ions that are expected to increase hydrophobic interactions.

In a broader context, the hydrophobic assembly/aggregation/association is inherent in a wide variety of fundamental and industrial processes [34, 35, 36, 37, 38, 39, 40, 41, 42]. Although water (solvent) is the dominant component, controlling assembly (either preventing it or exploiting it to create extended structures) often requires the addition of solubilizing intermediates [43, 41, 44]. As an example, Frolov et al. [34] studied the nature of interactions between different ions and single-walled carbon nanotubes using molecular simulations in order to explore specific ion effects in the context of these industrially relevant systems. Indeed, the effects of different ions on the energetics and kinetics of hydrophobe assembly/association are necessarily mediated through the interfacial region between hydrophobe and solvent.

To sum up, understanding the solvent-hydrophobe interfacial structure and dynamics in pure solvent (water) and aqueous electrolyte solutions is of fundamental relevance to a broad spectrum of applications ranging from protein stability [45, 46, 47, 21, 48, 49, 50] to material preparation [51, 34, 52, 53, 54, 55] and even atmospheric

[1] 4,4-Diffuoro-5,7-dimethyl-4-bora-3a,4a-diaza-s-indacene-3-dodecanoic acid, abbreviated fl-C12. It was selected because both the fluorophore and the fatty acid tail are strongly hydrophobic and uncharged at neutral pH, hence it can beit can be considered as a hydrophobic probe in that study.

chemistry [12, 56, 8].

1.1.1 Kosmotrope and Chaotrope

In spite of the widespread applicability of Hofmeister series, ion specific effects continue to defy an unified theory. The classification of Kosmotropic and Chaotropic ions was one of the most well-known explanation to the ion specific effects, which started from measuring the viscosity of different salt solutions. Jones and Dole found that the specific viscosity (η) of a salt solution can be written as [57]

$$\frac{\eta}{\eta_0} = 1 + Ac^{0.5} + Bc \tag{1.1}$$

where c is the concentration, η_0 is the viscosity of pure water at same temperature. A is always positive and is associated with counter ion screening and only appreciably affects the viscosity at low concentrations (< 0.05 M). B, known as the Jones-Dole B viscosity coefficient, becomes important in more concentrated solutions and is ion specific. Some typical values of B viscosity coefficient (B_η) with different anions and cations can be found in Reference [57, 58].

The effect of the ions on the viscosity can be related to the changes of water structure induced by the presence of ions. Ions are divided into two classes depending on the sign of the B-coefficient: kosmotropes ($B_\eta > 0$) and chaotropes ($B_\eta < 0$). Kosmotropes cause water molecules to tightly bound, which also stabilize intermolecular interactions in macromolecules, while the chaotropes lose their hydration sheath [59]. The radii of singly charged chaotropic ions are greater than 1.06 Å for cations and greater than 1.78 Å for anions [60]. Thus the hydrogen bonding between water molecules is supposed to be reduced in the immediate vicinity of ionic kosmotropes than ionic chaotropes [61]. In this simplified picture the making and breaking of water structure is central to the Hofmeister series, the direct or indirect binding of ions to hydrophobic solutes or patches of proteins (and the associated disruption to structure of water solvating these species) has emerged as a possible explanation of the Hofmeister mechanism [5, 62, 49, 63]. Kosmotropic (an)ions were shown to polarize the water molecules

hydrating the macromolecule, whereas the chaotropic (an)ions directly interact with the macromolecule. The former of these mechanisms resulted in salting-out of the macromolecule, whereas the latter influenced salting-in [62, 49]. Similar results were also observed from other model systems. Zangi et al. have performed simulations of the effect of model salts on the strength of hydrophobic association for two large plates [63]. They observed that ions with a high charge density preferably resided away from the hydrophobe surface; these ions were shown to decrease the free energy associated with plate association (relative to pure water). Conversely, ions with low charge density show significant density enhancement at the water-hydrophobe interface and increase the free energy for plate association.

The description of kosmotropic and chaotropic ions in terms of hydration is further supported by the values of absolute enthalpies of hydration ($\Delta H^{\circ}_{\mathrm{hyd}}$). Kosmotropes have very negative values of $\Delta H^{\circ}_{\mathrm{hyd}}$, which indicates that the hydration process is thermodynamically more favorable than for chaotropic ions. The consequence is that kosmotropic ions in water are strongly hydrated while chaotropes are only weakly hydrated. Morris reported the solution enthalpies at infinite dilution ($\Delta H^{\circ}_{\mathrm{sol}}$) versus the difference between the absolute hydration enthalpies of the corresponding gaseous anion and cation ($\Delta H^{\circ}_{\mathrm{hyd,anion}} - \Delta H^{\circ}_{\mathrm{hyd,cation}}$) [64, 65]. By considering the enthalpies of hydration as a measure of the water affinity of the single ions, Collins concluded an empirical rule that inner sphere ion pairs are preferentially formed between oppositely charged ions with matching absolute enthalpies of hydration (i.e. Kosmo-Kosmo or Chao-Chao combinations) [65]. When the anion and cation are both kosmotropes (e.g. $Li^{+}F^{-}$, Kosmo-Kosmo) or both chaotropes (e.g. $Cs^{+}I^{-}$, Chao-Chao), the enthalpy of salt dissolution is positive ($\Delta H^{\circ}_{\mathrm{sol}} > 0$) and is a endothermic process. On the contrary, when the combination is one kosmotrope plus one chaotrope (e.g. $Cs^{+}F^{-}$, Chao-Kosmo, or $Li^{+}I^{-}$, Kosmo-Chao), the enthalpy of salt dissolution is negative ($\Delta H^{\circ}_{\mathrm{sol}} < 0$) and is a exothermic process.

The success of Collins' rule is due to its simplicity and connection with some experimental observations. However, a detailed analysis of the model arises some

relevant questions. The enthalpy of solution ($\Delta H_{\rm sol}$) is determind by the ions' hydration enthalpy ($\Delta H_{\rm hyd}$) and their lattice energy (U), which gives $\Delta H_{\rm sol} = U + \Delta H_{\rm hyd}$. Since Collins' rule was based on the assumption of infinite dilution, i.e. the ion will effectively never see its counterion, their interaction energy in water (and hence their propensity to form ion pairs) can not play a significant role in the heat of solution. Besides, the calculated Gibbs hydration enthalpy is the average electrostatic interaction of the ion with the bulk water, therefore it cannot really be a measure of the ion-water affinity [66].

Several recent experiments also casted doubt on the central role of structure makers/breakers. Bakker and coworkers used femtosecond mid-infared pump-probe spectroscopy to study actual hydrogen bonds between water molecules in salt solutions ($Mg(ClO_4)_2$, $NaClO_4$, and Na_2SO_4). [2] Their results showed no effect on the rotational motion of bulk water outside of the the first hydration shell, suggested that the hydrogen bonding network was not changed by the presence of chaotropic (ClO_4^-) and kosmotropic (SO_4^{2-}) ions [67]. Pielak and coworkers used presssure perturbation calorimetry (PPC) to measure the temperature dependence of a solute's partial compressibility. [3] Their results showed that the effects of different solute on bulk water

[2] The basic principle of this technique is, when the system is excited by a pulse (pump) shorter than the vibrational period, vibrational coherence is induced both in the ground and excited electronic states, hence providing information also on the excited state nuclear dynamics. In practice, they used linear-polarized infrared pulses (pump) to excite OH groups in solution. The pump pulse was followed by a probe pulse polarized 45 degrees compared to the pump pulse. Eventually, only the excited OH groups that had rotated in the time interval between the pump and probe pulses would be excited by the probe, which led to the reorientation of the OH groups and the "stiffness" of the hydrogen bonds. For example, since Mg^{2+} ions are considered strong kosmotropic ions [57, 58], as the ions greatly increase the viscosity of water, there are supposedly more hydrogen bonds among water molecules.

[3] In PPC, a N_2 pressurization device is fitted to a differential scanning calorimeter, and pressure pulses of $\sim$ 350 kPa are alternatively applied (ΔP) to the two different cells (one sample and the other as reference). The differential heat (ΔQ) provides information about the difference in compressibility between the sample and the reference and, hence, about $\bar{\alpha}$ of the sample. Data are collected as a function of temperature to provide the coefficient of thermal expansion, $\bar{\alpha} = 1/\bar{V}(\partial\bar{V}/\partial T)_{\rm P}$, as a function of temperature using different solutes.

structure was uncorrelated with the Hofmeister series [68]. Clearly, Collins' law is not able to explain all the variety of effects that can be ascribed to the ion-specific effects, but the idea of kosmotropes and chaotropes is still commonly applied to the understanding of Hofmeister's series.

1.1.2 Modeling Single Ions/Molecules at Interfaces Using MD Simulations

As we mentioned, a lot of physical properties usually lay on the interfaces. Generally speaking, there are three catagories of modern approaches to investigate the interfacial solute specific phenomena: (1) based on surface selective experiments such as second-harmonic generation (SHG) [69, 70, 71], vibrational sum frequency generation spectroscopy (VSFG) [72, 73, 74, 75], high-pressure VUV photoelectron spectroscopy [76, 77], ambient pressure X-ray photoelectron spectroscopy (XPS) [78, 79]; (2) theoretical continuum dielectric models [80, 66], and (3) molecular simulations [23], while the last one is the focus of this work.

Although researcheres have been aware for decades that the properties of a solute depend on its adjacent solvation shell as well, it has been recently suggested that long-ranged perturbations of water dynamics might be crucial to investigate the actual physical behaviors [81, 82, 83, 84, 85, 86, 87, 88]. Therefore, simply probing the partition of interest (solutes/species) near the interface might not be able to provide the interfacial physical information sufficiently. However, the experimental determination of the kinetics and mechanisms of interfacial chemical processes is extremely challenging for the inherent difficulty in evaluating the structure, dynamics, and chemistry at liquid interfaces at a molecular scale. Consequently, much recent progress regarding the heterogeneous interfacial physics/chemistry at the molcular scale has come from classical molecular dynamics (MD) simulation studies. MD has become a very powerful tool to study the many-body problems in statistical physics, physical chemistry and biophysics since its introduction in late 1950s for theoretical physics [89, 90]. By explicitly including properties of water, MD simulations are helpful to understand the molecular origin of the long-ranged effects brought by the the presence of solutes [23, 91,

92, 93]. Nowadays, with the development of hardware, optimization of force fields and computational resources, MD simulations are widely used to complement or explain the experimental results with the microscopic scale up to atomic resolution.

In the last decades, computer simulations have provided robust information to understand the molecular origin of ion specific effects [94, 95, 14, 56, 96, 97, 98, 99, 100, 91, 101, 102, 103, 12, 23, 10, 104, 15, 105, 106, 107, 108, 109], particularly differential stabilities of halides at aqueous liquid-vapor interfaces and generally at hydrophobic interfaces. The understanding of physical origins of differential stabilities of anions is of broad interest are implicated in processes ranging from protein denaturation, surface tension modulation, carbon nanomaterial self-association [24, 110, 111], and ion association with lipid bilayers and membranes [112]. Efforts to present unifying explanations of the molecular, thermodynamic, and structural underpinnings of these effects has garnered significant attention from theory and experiment, and continues to do so. We refer to a sampling of the vast literature [23, 103, 70, 113, 69, 114, 115, 116, 117, 118, 119, 120, 112, 121, 122, 123, 124, 125].

In the context of modeling differential stabilities of ions at the aqueous liquid-vapor interface, there are still some inconsistencies among studies. In general, alkali cations and fluoride anions are repelled from the interface, but the extent of the adsorption of larger halides (I^- and Br^-) is controversial. The problem usually arises with the choice of the so-called "force field", which is the required input for any molecular simulation. Major molecular/atomic properties implicated are ion size, ion polarizability, ion hydration properties (free energy and entropy), ion charge density, and solvent polarizability and dipole moment [126]. Particularly, it is still under debate whether the polarizability is the most crucial factor or not. In classical MD simulations, polarizability can be taken into account by adding parameterized atomistic polarizability which is close to the full quantum mechanical description of molecular systems to the force field. Jungwirth and Tobias predicted that, since the ion-water interaction and the geometry of the water molecules at the interface are strongly influenced by the polarizability, the adsorption of the large halide ions at the air-water interface can only be obtained with

polarizable force fields but not with standard non-polarizable ones [103, 12]. However, it was later shown by Pal and Müller-Plathe that even non-polarizable anions are attracted to hydrophobic interfaces as long as the anion's corresponding effective radius is chosen large enough [127]. Horinek and Netz reported that if non-polarizable force fields are properly optimized, the ionic surface affinity can be reproduced in very good agreement with experimental surface tension results [128]. They also argued that adsorption of iodide at the air-water interface is mainly dominated by its partially hydrophobic nature [11].

Nowadays, ion specific effects are generally explained as the result of a interplay between hydration, non-electrostatic potentials and ionic polarizability [66, 129, 128]. While there are numerous force fields modeling the ion specific effects, we will not comment on the accuracy of any of these force fields, as all water-ion force field combinations have been carefully parametrized and validated via extensive structural and thermodynamic analysis elsewhere. The selection and validation of force fields in this work will be discussed in each chapter.

We next address the select of systems. In this work, our study primarily emphasis on (modeling) the response of an interface with a single ion/molecule/solute approaching. Strictly speaking, single ions in (extended) aqueous systems do not exist [23]. In conventional ensemble experiments, large numbers of molecules are examined simultaneously, and primarily averaged-out properties are observed corresponding to a finite ion concentration [23, 130]. Usually it also requires counterions to ensure the systematic neutrality. However, from the theoretical perspective, it is still plausible to consider single ions in aqueous systems as the "infinite dilution limit", in which we can investigate the ion-water interactions/structures without the disturbance of counterion effects. Besides, it is also feasible to study single ions with water molecules experimentally (in the form of ion-water clusters) [131, 132, 133, 134].

How the treatment of long-ranged electrostatic forces influences structural, energetic, and dynamical properties of the system is also an important issue in simulations. Commonly, researcheres use cutoff procedure (switching functions [135], reaction field

method [136], or simple truncation) or the Ewald summation technique [137, 138, 139] to treat long-ranged forces. The advantages of cutoff schemes is that they reduce computational demands on the system, while in the Ewald summation method the periodical boundary conditions are fully utilized and the lattice sum is calculated. In this dissertation, we use Particle mesh Ewald (PME) method to compute the long-ranged forces. Due to the periodicity assumption implicit in Ewald summation, in MD simulations this is normally required to construct a charge-neutral unit cell that can be treated as infinite "bricks" to form images. However, a particularly noteworthy feature in our single-ion systems is the non-neutrality for the absence of the counterion. We refer to previous studies regarding different long-ranged forces treatments [140, 141]. Berkowitz et al. systematically compared the diffusion coefficients of single anions in aqueous solutions and found that the difference between using Ewald summation technique and reaction field method is negligible [141]. Spohr further showed that the properties such as hydration shell structures, atom density profiles, preference of ion adsorption, or pair correlation functions, do not depend strongly on the treatment of long-ranged interactions and can be calculated with less computationally demanding techniques [140]. Therefore, in the limiting condition, in our case single ions in the aqueous solutions, we consider the use of PME still capable of depicting the properties of interest.

1.2 Outline

This dissertation is comprised of work for ions at different aqueous interfaces [93, 92, 142, 143] and how addition of salts effects the hydrophobic association [110, 111] using MD simulations. More specifically, we will study the origin of the ion-induced surface height fluctuation and how it associates with the ion's surface stability.

Chapter 2 includes the general discussion of the force fields used in this dissertation, along with some common computational methods.

In Chapter 3 the adsorption/exclusion of various single spherical monovalent ions to the air-water interface are investigated. The emphasize of this chapter is to

correlate the positions of ions in the Hofmeister series, which is depicted by the free energetics of an ion transporting from bulk solution phase to the gas phase, with the long-ranged ion-induced interface height fluctuation. We start with the discussion for the choice of polarizable/non-polarizable force fields, acknowledging variations in force field ability to recapitulate essential underlying physics. The starting point for most analyses of driving forces for ion adsorption is the single-ion potential of mean force (PMF) [109], which can be either decomposed into enthalpic and entropic components that are further dissected [126, 144, 9, 19] or partitioned into free energy components [145, 146]. Surface stable ions, characterized as such by minima in PMF computed using umbrella sampling MD simulations, induce larger interfacial fluctuations compared to nonsurface active species, conferring more covariance entropy approaching the interface. Smaller anions and cations show no interfacial potential of mean force minima, nor is the enhanced interfacial fluctuation. The difference is traced to the malleability of the hydration shell of the ions, and the coupling of these shells with distant solvent. Two halide anions, Cl^-/I^-, are selected to further investigate the temperature-dependence of free energetics and the associated surface height fluctuation. The increase in temperature of the solvent enhances the inherent thermally excited fluctuations and consequently reduces the relative contribution from anion to surface height fluctuations, which is consistent with the decrease in surface affinity of I^-.

Chapter 4 mainly discusses the free energetics and induced surface height fluctuation of single guanidinium (Gdm^+) and methyl guanidinium (M-Gdm^+) with air-water interface. As one of the strongest denaturants used in biophysical studies of protein folding, guanidnium salts increase the solubility of nonpolar molecules ("salting-in") and decrease the ordering of water. We start with the validation of our charge equilibration (CHEQ) method for the polarizable force fields, by comparing the calculated surface properties of guandinium salt solution with the experimental reported values. The results for single molecular ions reveal that methyl guanidinium cation is less excluded from the air-water surface than guanidinium cation, but both cations show

orientational dependence of surface affinity. Parallel orientations of the guanidinium plane (relative to the Gibbs dividing surface, GDS) show pronounced free energy minima in the interfacial region, while ring orientations perpendicular to the GDS exhibit no discernible surface stability. Calculations of surface fluctuations demonstrate that, near the air-water surface, the parallel-oriented cations generate significantly greater interfacial fluctuations compared to other orientations, which induces more long-ranged perturbations and solvent density redistribution. These results have implications for interpreting molecular-level, mechanistic action of this osmolyte interaction with hydrophobic interfaces as they impact protein denaturation (solubilization).

Chapter 5 extends the interface fluctuations from the simple air-water interface to the more complicated and realistic protein-water interfaces to explore and bridge the underlying connection. Specifically, we focus on fluctuations of an interface between water and a hydrophobic region of hydrophobin-II (HFBII), a 71 amino acid residue protein expressed by filamentous fungi and known for its ability to form hydrophobically-mediated self-assemblies at interfaces. Again the halide anions I^- and Cl^- were chosen as to compare the difference between the surface stable and non-surface stable species. Consistent with the results at aqueous air-water interfaces, we find that I^- induces larger fluctuations of the protein-water interface compared to Cl^-.

Chapter 6 explains how the ion-specific nature and the corresponding spatial distribution effect the large-scale hydrophobic assembly, including two parallel hydrophobic, single-walled carbon nanotubes (SWNTs). Addition of NaCl/NaI salts enhances stability of the contact state between the hydrophobes on the order of 2-4 kcal/mol, changes the critical hydrophobe separation distance and characteristic wetting/dewetting transitions. The ion-specific spatial distribution of different halide anions gives rise to starkly different contributions to the free energy stability of hydrophobes in the contact state. Iodide anion directly stabilizes the contact state to a much greater extent than chloride anion. The enhanced stability arises from the locally repulsive forces imposed on hydrophobes by the surface-segregated iodide anion. We further incorporate the graphics processing unit (GPU) for the simulations of SWNTs

in NaI solutions to study how temperature effects the association of hydrophobes. By calculating the surface height fluctuation of coarse-grained tube-solvent interfaces, we found that the three components in the solution (water, I^- and Na^+) exhibit distinct characteristics, which can also be explained via the malleability of their corresponding tube-solvent solvation shells.

This work concludes in Chapter 7 with a summary of key findings and proposed future work.

Chapter 2

FORCE FIELDS AND COMPUTATIONAL METHODS

2.1 Force Fields

Most of the problems that we are dealing with molecular modelling are unfortunately too large and time-consuming to be considered by quantum mechanics, even if we ignore some of the electrons. Based on Born-Oppenheimer approximation, force field methods bypass the electronic motions and calculate the energy of a system as a function of the nuclear positions only. Within the Chemistry at HARvard Molecular Modeling (CHARMM) package [147, 148], the potential energy for a fixed-charge representation can be expressed as the sum of terms as:

$$E(\vec{r}) = E_{\text{bonds}}(\vec{r}) + E_{\text{angles}}(\vec{r}) + E_{\text{dihedrals}}(\vec{r}) + E_{\text{nonbond}}(\vec{r}) \tag{2.1}$$

or expressed explicitly,

$$\begin{aligned} E(\vec{r}) &= \sum_{\text{bonds}} K_{\text{b}}(b-b_0)^2 + \sum_{\text{angles}} K_\theta(\theta-\theta_0)^2 + \sum_{\text{dihedrals}} K_\phi(1+\cos(n\phi-\delta)) \\ &+ \sum_{\text{non-bonded}} \left[\frac{q_i q_j}{4\pi\epsilon_0 r_{ij}} + \varepsilon_{ij}\left(\frac{R^{12}_{\text{min},ij}}{r^{12}_{ij}} - 2\frac{R^{6}_{\text{min},ij}}{r^{6}_{ij}}\right) \right] \end{aligned} \tag{2.2}$$

K_{b}, K_θ and K_ϕ are the force constants with respect to each term. Parameters b_0 and θ_0 represent the equilibrium bond length and angle. In the dihedral term, n represents the multiplicity which gives the number of minimum points in the function as the bond is rotate through 360°; δ is the phase factor which determines where the torsion angle passes through its minimum value [149]. The non-bonded term is extracted into the electrostatic and the dispersion/repulsion interactions. The former is treated as the Coulomb potential term. The latter term is modelled via the Lennard-Jones (LJ) "12-6" potential with two adjustable parameters. $R_{\text{min},ij} = 2^{1/6}\sigma_{ij}$ is the separation where

the first derivative of the energy is zero. σ_{ij} is the separation which makes the energy to be zero. ε_{ij} is the potential well depth. Each atomic type has its individual pair of LJ parameters. Interactions between two different atom sites are treated with the Lorentz-Berthelot (LB) combining rules:

$$\varepsilon_{ij} = \sqrt{\varepsilon_i \varepsilon_j}, \quad R_{\min,ij} = \frac{R_{\min,i} + R_{\min,j}}{2} \tag{2.3}$$

We acknowledge that LB is not unique while there are other alternative combining rules such as Sikora [150], Fender-Halsey [151] and Kong [152] rules for Lennard-Jones potential. While some systematic studies revealed that LB combining rules may underestimate the collision diameter and overestimate the well depth between the non-bonded atoms [153, 154], LB rules are still one of the most widely used. Siginificant work towards novel rules to define a boarder range of interatomic potential is still required.

Futhermore, in order to reduce the cost of computational resources, Lennard-Jones interactions were gradually switched off using the switching function:

$$S(r_{ij}) = \begin{cases} 1 & r_{ij} \leq r_{\text{on}} \\ \frac{\left(r_{\text{off}}^2 - r_{ij}^2\right)^2 \left(r_{\text{off}}^2 + 2r_{ij}^2 - 3r_{\text{on}}^2\right)}{\left(r_{\text{off}}^2 - r_{\text{on}}^2\right)^3} & r_{\text{on}} < r_{ij} \leq r_{\text{off}} \\ 0 & r_{ij} > r_{\text{off}} \end{cases} \tag{2.4}$$

where interactions below r_{on} are treated via full LJ interactions, interactions between r_{on} and r_{off} are defined with the switching function, and interactions above r_{off} are zero.

Since atoms in this force field are depicted as fixed-charge LJ particles, this force field does not account for electronic polarization of the environment. This problem was addressed by developing "polarizable force fields" [155, 156, 157]. We will briefly introduce two polarizable force fields used in this dissertation.

2.1.1 Charge Equilibration Force Fields (CHEQ)

Although applied here as a classical potential [158], the CHEQ formalism derives rigorously from the density functional (DFT) theory of atoms in molecules[159] based

on Sanderson's idea of electronegativity equalization[160, 161], in which the chemical potential is equilibrated via the redistribution of charge density. Here, in a classical sense, charge density is reduced to partial charges, Q_i on each atomic site i. Polarization is affected via the transfer of partial charge among atoms with a given normalization unit (e.g. a water molecule or a function group).

The charge-dependent electrostatic energy for a system of M molecules containing N atoms per molecule can be expressed as:

$$\begin{aligned} E_{\text{electrostatic}} &= \sum_{k=1}^{M}\sum_{i=1}^{N}\chi_{ik}Q_{ik} + \frac{1}{2}\sum_{l=1}^{M}\sum_{\alpha=1}^{N}\sum_{\beta=1}^{N}\eta_{\alpha l,\beta l}Q_{\alpha l}Q_{\beta l} + \\ &\quad \frac{1}{2}\sum_{i=1}^{MN}{}'\sum_{j=1}^{MN}{}'\frac{Q_iQ_j}{r_{ij}} + \sum_{j=1}^{Groups}\lambda\left(\sum_{i=1}^{N}Q_{ji} - Q_j^{total}\right) \end{aligned} \tag{2.5}$$

where χ denotes the atomic electronegativities and η denotes the atomic hardnesses. χ describes the tendency of an atom to attract electrons (or electron density) towards itself, i.e., the directionality of electron flow [162]. η measures the resistance of an atom to a charge transfer; its inverse, can be interpreted as the capacity of an atom to receive electrons [159]. Both of them are treated as empirical parameters with respect to the individual atom type. Homogeneous hardness values (for each atom type) are parameterized as discussed in Patel and Brooks [163]. Heterogeneous elements (interaction elements between different atom types) are derived from the individual atom type values based on the combining rule [164]:

$$\eta_{ij} = \frac{\frac{1}{2}(\eta_i + \eta_j)}{\sqrt{1 + \frac{1}{4}(\eta_i + \eta_j)^2 R_{ij}^2}} \tag{2.6}$$

where R_{ij} is the separation between atoms i and j.

The second term in Equation 2.5 represents the local charge transfer interaction generally restricted to within an appropriate charge normalization unit, i.e. no intermolecular charge transfer. The third term in Equation 2.5 is a standard Coulomb interaction between atom sites not involved in dihedral, angle, and bonded interactions with each other (the primed notation indicates a summation only over such sites). Finally, charge is constrained via a Lagrange multiplier, λ, which is included for each charge normalization unit as indicated in the last term of Equation 2.5 [165].

The charge degrees of freedom are propagated via an extended Lagrangian formulation imposing a molecular charge neutrality constraint, hence forcing electronegativity upon equalization at each dynamics step. The system Lagrangian is

$$L = \sum_{i=1}^{M}\sum_{\alpha=1}^{N_i}\frac{1}{2}m_{i\alpha}\dot{r}_{i\alpha}^2 + \sum_{i=1}^{M}\sum_{\alpha=1}^{N_i}\frac{1}{2}m_{Q,i\alpha}\dot{Q}_{i\alpha}^2 - E(Q,r) - \sum_{i=1}^{M}\lambda_i\sum_{\alpha=1}^{N_i}Q_{i\alpha} \tag{2.7}$$

where the first two terms represent the nuclear and charge kinetic energies, respectively. The third term is the total potential energy. The fourth term is the molecular charge neutrality constraint with the Lagrange multiplier λ_i with respect to each molecule, i. The fictitious charge dynamics, analogous to the fictitious wavefunction dynamics in Car-Parrinello (CP) type methods [166], are determined with a fictitious charge "mass" with the unit energy·time^2/charge^2. The charges are propagated based on forces arising from the difference between the average electronegativity of the molecule and the instantaneous electronegativity at an atomic site.

The molecular polarizability, α, can be calculated as:

$$\alpha_{\gamma\beta} = \bar{R}_\beta^T \bar{\bar{\eta}}^{-1} \bar{R}_\gamma \tag{2.8}$$

where $\bar{\bar{\eta}}$ denotes the molecular hardness matrix augmented with the appropriate rows and columns to treat the charge conservation constraints. $\bar{R}_\beta^T$ and $\bar{R}_\gamma$ are the β and γ Cartesian components of the atomic position vectors. A more detailed derivation can be found in Reference [165].

2.1.2 Drude Polarizable Force Field

Drude oscillator is an alternative model to include the induced polarization from the environment [167, 168, 169, 170]. For a given atom with partial charge q, a model Drude particle carrying a charge q_D is introduced and results in an atom-Drude pair. The charge of the atom is then reduced to $q - q_D$. This Drude particle is harmonically bound to the atomic particle with a force constant k_D, therefore in the absence of a field, the Drude particle oscillates around the position of the atom ($\vec{r}$) and the atom appears on average as a point charge q. In a uniform electric field $\vec{E}$, the the Drude

particle oscillates around a position $\vec{r}+\vec{d}$ with $\vec{d}=q_D\vec{E}/k_D$, with the induced dipole $\vec{\mu}=q_D^2\vec{E}/k_D$. Its associated polarizability is then expressed as:

$$\alpha=\frac{\vec{\mu}}{\vec{E}}=\frac{q_D^2}{k_D} \tag{2.9}$$

The resulting potential energy with auxiliary Drude particles is then written as:

$$\begin{aligned} E(\vec{r},\vec{d}) &= E_{\text{bonds}}(\vec{r})+E_{\text{angles}}(\vec{r})+E_{\text{dihedrals}}(\vec{r}) \\ &+ E_{\text{self}}(\vec{d})+E_{\text{elec}}(\vec{r},\vec{d})+E_{\text{LJ}}(\vec{r}) \end{aligned} \tag{2.10}$$

The first three terms are the same with Equation 2.1. $E_{\text{self}}(\vec{d})$ represents the atom-Drude harmonic bonds ($\frac{1}{2}kd^2$ terms), $E_{\text{elec}}(\vec{r},\vec{d})$ includes all Coulombic interactions (atom-atom, atom-Drude, and Drude-Drude), $E_{\text{LJ}}(\vec{r})$ is the L-J "12-6" nonpolar contribution.

2.2 Common Calculation Methods

In this work, several common calculations are frequently used to evaluate the structural, dynamic properties and free energetics. In our cases of single solute with the liquid-vapor interface, interfacial systems are set up in a rectangular simulation cell, where x and y-dimensions are parallel to the interface and z is in the direction normal to the interface. In the following sections, we will assume this geometry to illustrate the calculations with z-dependent profiles. Under some circumstances, the profile may depend on other variables due to the geometry or symmetry of the system.

2.2.1 Density Profile

Density profiles are calculated as the number of a given species within a sampling volume. The total volume of the system can be divided into slabs perpendicular to the interface normal, with Δz as the thickness of each slab. Δz is chosen to be small enough so that the density does not vary much when they are transversed, but big enough that a smooth analytical function can be obtained. The z-dependent density profile can be written as:

$$\rho_i(z)=\frac{\langle N_i\rangle}{L_x\times L_y\times\Delta z} \tag{2.11}$$

where L_x and L_y are the box lengths in the x and y directions. $\langle N_i \rangle$ is the average number of a given species i within the sampling volume over the simulation trajectory. Unless otherwise stated, density profiles are reported in units of particles/Å^3.

Results for the density profile are sometimes summarized by fitting to a mathematical form which is derived from some simple models [171]. For example, the van der Waals mean field theory gives rise to the expression for a liquid-vapor interface [172]:

$$\rho(z) = \frac{1}{2}(\rho_{\mathrm{L}} + \rho_{\mathrm{V}}) - \frac{1}{2}(\rho_{\mathrm{L}} - \rho_{\mathrm{V}}) \tanh\left(\frac{z - z_{\mathrm{G}}}{2\delta}\right) \tag{2.12}$$

where ρ_{L} and ρ_{V} are the bulk densities of liquid and vapor phases, respectively. δ refers to the interface width. z_{G} is a unique position, so-called Gibbs dividing surface (GDS), which can be defined as the position where water density is approximately one-half its bulk value, or equivalently defined by the condition that makes the surface excess zero:

$$\int_{z_\beta}^{z_{\mathrm{G}}} (\rho - \rho_\beta) dz + \int_{z_{\mathrm{G}}}^{z_\alpha} (\rho - \rho_\alpha) dz = 0 \tag{2.13}$$

where z_μ, $\mu = \alpha, \beta$ is a position in the bulk phase μ.

At the liquid-liquid interface, one can similarly define GDS using Equation 2.13 without an unique GDS. However, in practice the positions with the two liquids are quite close to each other and to the point where the density of each liquid is near half its bulk value. The GDS is useful in developing the thermodynamics of the interfacial systems, but its location does not affect any of the thermodynamic relations [173].

2.2.2 Radial Distribution Function

Radial distribution function (RDF) describes how (atomic/molecular) densities change as a function of distance from a reference particle [149, 174, 175]. Consider a spherical shell with thickness Δr at a distance r from a given particle, the corresponding volume of the shell is then given by:

$$V = \frac{4}{3}\pi[(r + \Delta r)^3 - r^3] \approx 4\pi r^2 \Delta r \tag{2.14}$$

If the mean number density is ρ, we have the RDF as:

$$\mathrm{g}(r) = \frac{n(r)}{\rho 4\pi r^2 \Delta r} \tag{2.15}$$

where $n(r)$ is the mean number of atoms/molecules in this shell. When g(r) is equal to one, the particles in the shell are uniformly distributed. Values greater than or less than one represent an enhanced or reduced probability relative to a uniform distribution. RDFs can be experimentally measured using neutron scattering or X-ray diffraction data [176, 177, 178].

2.2.3 Orientational Profile

The orientation of a molecule as it approaches an interface is commonly assessed as the angle between a characteristic vector of the molecule and the normal vector of the interface, i.e. the z-axis. For a water molecule, we use its dipole moment of a water as the characteristic vector, which is defined as

$$\vec{\mu} = \sum_{i=1}^{N} q_i \vec{r_i} \tag{2.16}$$

where N is the total atoms in the molecule, q_i and $\vec{r_i}$ are the charge and position of atom i. For z-axis, $\hat{z} = (0, 0, 1)$, the angle θ between $\vec{\mu}$ and $\hat{z}$ is then determined by their dot product and lengths.

We usually consider the average cosine of theta ($\langle \cos\theta \rangle$) to evaluate the orientational distribution of the molecules relative to the interfaces. In the case of perfect alignment of water dipoles in the z-direction (or negative z-direction) we have $\langle \cos\theta \rangle = 1$; $\langle \cos\theta \rangle = 0$ indicates the net alignment is parallel to the $\hat{z}$ (i.e. perpendicular to the interface). $\langle \cos\theta \rangle > 0$ indicates a net alignment of dipoles in the z-direction; $\langle \cos\theta \rangle < 0$ indicates a net alignment of dipoles in the negative z-direction.

We can further calculate the second order Legendre polynomial using

$$\langle P_2(\cos\theta) \rangle = \frac{1}{2} \left\langle (3\cos^2\theta - 1) \right\rangle \tag{2.17}$$

to measure the degree of orientation of the molecule relative to the interface normal. When the orientational configurations are completely random and isotropic, P_2 is zero, whereas for the perfectly aligned case $\langle P_2(\cos\theta) \rangle = 1$. $\langle P_2(\cos\theta) \rangle = -0.5$ when the orientations are entirely perpendicular. This parameter is then a measure of the uniaxial behavior of the species.

2.2.4 Hydrogen Bond Profile and Tetrahedral Parameter

Hydrogen bonding is especially relevant to understanding water properties for its sensitivity to the surface environment. In general there are two methods to define the hydrogen bonds in simulations. The first is defined by an interaction energy between two water molecules more negative than a certain value, e.g. -10 kJ/mol [179]. The second definition, which is used in this work, is based on the relative geometry between a pair of water molecules. Two water molecules are considered hydrogen bonded if the oxygen-oxygen distance is less than 3.5 Å and the HO$\cdots$O angle is less than 30° [180, 181, 110]. The choice of geometric criteria is generally preferred for providing more reliable results than energetic criteria in simulation studies [180, 182]. Hydrogen bond profiles are then the average number of hydrogen bonds formed at a given z-position.

Order parameters specific for tetrahedral configurations are of special interest for studying liquid water. We apply the conditional tetrahedral parameter (q) introduced by Godec et al. [183] to describe the configurations of water in different environment. For a tetrahedral configuration there are five points: the four vertices of the tetrahedron and the center. In a perfectly tetrahedral arrangement, all the angles between bonds hold the same value, and the cosine of this angle is $-1/3$. However, in the vicinity of a surface, water molecules may not have four nearest hydrogen-boned neighbors. Physically, at least two neighboring water molecules are necessary for a meaningful evaluation of tetrahedral order. Therefore, the generalized form of tetrahedral parameter can be written as:

$$q_i = 1 - \frac{1}{N(N-1)} \frac{9}{8} \sum_{j=1}^{N-1} \sum_{k=j+1}^{N} (\cos \psi_{j,k} + \frac{1}{3})^2 \tag{2.18}$$

where $\psi_{j,k}$ is the angle subtended at the central water between the j_{th} and k_{th} bonds. N is the number of neighboring water molecules with $2 \leq N \leq 4$. The squaring ensures the contribution from each inter-bond angle is always greater than or equal to zero. The normalization factor is chosen so that $q_i = 1$ when the configuration is perfectly tetrahedral (all the cosine values are $-1/3$); $q_i = 0$ indicates the extreme non tetrahedral arrangement.

2.2.5 Time Dependent Properties

In MD simulations, we gather data values at specific times, which enables us to correlate some property at some instant with another property at a later time t. Therefore, MD simulations can be used to calculate time-dependent properties. In this section, we will introduce some common dynamical properties such as water residence time, autocorrelation function and diffusion coefficient.

2.2.5.1 Residence Time

Water residence time is considered a time-dependent survival probability function $P(t)$ of a molecule uninterruptedly remaining in a region at time $t = t_0 + \Delta t$ having started in the region at time $t = 0$ [184, 185]. The region criteria can be within a solvation shell of an ion or a biomolecule, or any type of a pre-defined region. We consider molecules that are within the pre-defined region at time $t_0 = 0$ and remain within the corresponding region at t with no instances of leaving the region. The probability is:

$$P(t) = \frac{1}{N(0)} \sum_{t_0} N(t_0, t) \tag{2.19}$$

where t_0 indicates multiple time origins and $t = t_0 + \Delta t$ is the persistence time of a water molecule in a region after it was initially observed at time origin t_0. The number of molecules confined at each time t is normalized by the number of molecules observed at $t = 0$, such that $P(0) = 1$. $P(t)$ is fit to a stretched exponential (or Kohlrausch) function [186, 187, 188],

$$P(t) = P_0 \exp[-(t/\tau)^\gamma] \tag{2.20}$$

where P_0, τ, and γ are adjustable fitting parameters. P_0 is the probability that a water molecule initially is within the region at time $t = 0$; usually for the final functional fits, P_0 is approximately 1. γ is the stretched exponential constant, suggesting deviation from first order decay. τ is characteristic residence lifetime, which is the time required for the autocorrelation function to decay from 1 to $1/e$.

2.2.5.2 Velocity Autocorrelation Function

Suppose we have two sets of data values, x and y, and we try to determine what kind of correlation (if any) exists between them. A correlation function provides a numerical value that determines the degree to which two sets of data are associated. The most commonly used correlation function is obtained by dividing the covariance of x and y by the product of their standard deviations. The correlation value is between -1 and +1. The closer the coefficient is to either -1 or 1, the stronger the correlation between the variables; as the value approaches zero there is less of a relationship (closer to uncorrelated).

If the quantities x and y are different, then the correlation function is sometimes referred to as a cross-correlation function; when x and y are identical, the function is called an autocorrelation function. An autocorrelation function implies how long it takes the system to "lose" its memory of its previous values [149, 174].

Usually, if we choose the appropriate time correlation functions from the data collected in the MD simulations, dynamic properties from MD can be related to experimental results. For instance, the vibrational spectrum or vibrational density of states (VDOS) simulated in MD can be related to experimental results of incoherent inelastic neutron scattering [189] and spectroscopic methods such as Raman [190, 191, 192, 193] and infrared (IR) spectra [192, 194, 195, 196].

In this work, we use velocity of each atom as the autocorrelation variable, i.e., the velocity autocorrelation function (VACF) whose value indicates how closely the velocity at a time t is correlated with the velocity at time 0. The normalized, ensemble-averaged VACF can be calculated by averaging over the N atoms in the simulation [197, 198, 199]:

$$C_v(t) = \frac{1}{N}\sum_{i=1}^{N}\frac{\langle \overrightarrow{v_i}(t)\cdot\overrightarrow{v_0}(0)\rangle}{\langle \overrightarrow{v_i}(0)\cdot\overrightarrow{v_i}(0)\rangle} \tag{2.21}$$

where $\overrightarrow{v_i}(t)$ is the velocity vector of the i_{th} atom in the simulation system at time t. The brackets denote the ensemble average. In general, VACF has an initial value of 1.

As time progresses, it eventually has the value 0. The time taken to lose the correlation is often called the correlation time, or the relaxation time.

The vibrational density of states (VDOS) is a measure of the relative local motions of molecules in the context of a supermolecular entity undergoing intermolecular vibrational dynamics, and is computed by the Fourier transform of the VACF [200, 192, 195, 201]:

$$F(\omega) = \frac{1}{\sqrt{2\pi}} \int_{-\infty}^{\infty} dt e^{i\omega t} C_v(t) \tag{2.22}$$

The VDOS is then $\Phi(\omega) = F^2(\omega)$. When analyzing the vibrational data in such a way, one often requires only the frequencies of the peaks of the VDOS and not the actual power spectrum. If this is the case, it is useful to calculate only the real (cosine) part of the Fourier transform since the peaks will be more well defined by these data.

It is worth noting that VACF is an example of a single-particle correlation function. In other words, the average is calculated over time origins and over all atoms in the simulations. Some properties, such as the net dipole of the system, is the vector sum of all the individual dipoles of the molecules in the entire system [149, 202]. Its corresponding dipolar correlation function is given by

$$C_{\text{dipole}}(t) = \frac{\langle \overrightarrow{\mu_{\text{tot}}}(t) \cdot \overrightarrow{\mu_{\text{tot}}}(0) \rangle}{\langle \overrightarrow{\mu_{\text{tot}}}(0) \cdot \overrightarrow{\mu_{\text{tot}}}(0) \rangle}, \quad \text{where} \quad \overrightarrow{\mu_{\text{tot}}}(t) = \sum_{i=1}^{N} \overrightarrow{\mu_i}(t) \tag{2.23}$$

By calculating its Fourier transform along with quantum corrections applied, it is able to reproduce the infrared spectra for liquid water obtained from experiments [196].

2.2.5.3 Self-Diffusion Coefficient

In kinetic theory, the Einstein relation can be used to calculate the self-diffusion coefficient (D) from an equilibrium simulation by plotting the mean square displacement (MSD) as a function of time, and then obtain the limiting behavior as $t \to \infty$ [149]:

$$D = \lim_{t \to \infty} \frac{1}{6t} \left\langle |\vec{r}(t) - \vec{r}(0)|^2 \right\rangle \tag{2.24}$$

Alternatively, one can use Green-Kubo relation to calculate the diffusion coefficient via VACF [149, 203]. At a time t the displacement for an object is given by:

$$|\vec{r}(t) - \vec{r}(0)| = \int_0^t \vec{v}(t')dt' \tag{2.25}$$

The mean square displacement is then,

$$\langle|\vec{r}(t) - \vec{r}(0)|\rangle^2 = \int_0^t dt' \int_0^t dt'' \, \langle\vec{v}(t') \cdot \vec{v}(t'')\rangle \tag{2.26}$$

Since the correlation term is an ensemble average, changing the time origin does not affect the correlation function, which gives $\langle\vec{v}(t') \cdot \vec{v}(t'')\rangle = \langle\vec{v}(t'' - t') \cdot \vec{v}(0)\rangle$. By doing double integral, the Equation 2.26 eventually becomes

$$\left\langle|\vec{r}(t) - \vec{r}(0)|^2\right\rangle = 2t \int_0^t d\tau \, \langle\vec{v}(\tau) \cdot \vec{v}(0)\rangle \, (1 - \frac{\tau}{t}) \tag{2.27}$$

In the limit $t \to \infty$ we have

$$D = \frac{1}{3} \int_0^\infty d\tau \, \langle\vec{v}(\tau) \cdot \vec{v}(0)\rangle \tag{2.28}$$

2.2.6 Free Energe Calculation: Potential of Mean Force

The free energy is often considered as the most significant quantity in thermodynamics. However, it is difficult to obtain the free energy for systems such as liquids or flexible macromolecules, since there are numerous minimum energy configurations separated by low-energy barriers. It is also very difficult to calculate the associated quantities, e.g. the entropy and the chemical potential. For the sampling in MD simulations, it always pursues the lower-energy regions of the phase space, which leads to the lack of sampling in high-energy regions and poor convergence to the free energy profiles.

In molecular systems, the free energy problem can frequently be cast in terms of a free energy difference between two well-defined states [149, 204, 174, 175]. Methods such as free energy perturbation (FEP) [205, 206, 207, 204, 208, 149, 209], thermodynamic integration (TI) [205, 210, 211, 212, 149, 213, 214, 215, 216], have been

proposed to address the sampling issue. These methods calculate the free energy difference/change of two states with "chemical mutations", which means the change of states is along non-physical pathways. Be that as it may, our focus of free energy changes in this work do not involve this kind of "chemical mutations"; instead, we are more interested to know how the free energy changes as a function of some collectible variables, such as the distance between the solute and the interface, the center-of-mass distance between two model hydrophobes. The free energy surface along this type of chosen collectible variable (or reaction pathway, order parameter) is known as potential of mean force (PMF) [149], which is calculated for a physically achievable (and reversible) process. The calculation of PMF provides the point of highest free energy profile, which corresponds to the transition state for the process [149, 217] and is a practical general approach to estimating rate constants [149, 218, 219, 220].

We take a simple case to illustrate the calculation of PMF. Consider the system consisted of two particles only, PMF can be treated as the reversible work of moving one particle relative to the other. The distance between these two particles, ξ, is the collective variable in the previous discussion. PMF can then be calculated directly from the forces exerted on a particle as it moves along ξ:

$$\Delta W(\xi) = W(\xi) - W(\xi_0) = -\int_{\xi_0}^{\xi} \langle F(\xi) \rangle \, d\xi \tag{2.29}$$

ξ_0 represents a reference state, which can be inifinite separation between the two particles. $\langle F \rangle$ is the force on the given particle averaged over the simulation trajectory. By setting up a series of simulations/windows along the path ξ, we can eventually obtain the free energy profile. We can also calculate the PMF based on the probability of each state:

$$\Delta W(\xi) = -RT \ln \left(\frac{P(\xi)}{P_0} \right) \tag{2.30}$$

where P_0 indicates the reference probability and $P(\xi)$ is the probability of the event with state/separation ξ. Usually this can be recast with the RDF as

$$\Delta W(\xi) = -RT \ln \mathrm{g}(\xi) \tag{2.31}$$

This logarithmic relationship implies that a relatively small change in free energy may correspond to an order of magnitude in g(ξ) [149, 174]. Unfortunately, in most complicated systems, depending on the system's energy landscape, sometimes it is very difficult to gather the sampling in the regions where the RDF differs drastically from the most likely value, resulting in inaccurate values of PMF.

In the following sections, we will discuss more detail about the actual relations between PMF and free energy profiles, then we introduce the umbrella sampling and adaptive biasing force (ABF) techniques to address the sampling issue.

2.2.6.1 Relation between Potential of Mean Force and Free Energy Profile

In statistical mechanics, the free energy along ξ is defined as $A(\xi) = -(1/\beta)\ln Q(\xi)$, with Q as the partition function. As a generalized form, we can rewrite the free energy as:

$$A(\xi) = -\frac{1}{\beta}\ln\int\int e^{-\beta H(p,x)}\delta(\xi(x)-\xi)dxdp \tag{2.32}$$

where x and p denote the Cartesian coordinates and momenta of all the particles, respectively. H is the Hamilitonian function of the system. If ξ is a function of x only (not p), the above equation can be further simplified as

$$A(\xi) = -\frac{1}{\beta}\ln\int e^{-\beta U(x)}\delta(\xi(x)-\xi)dx \tag{2.33}$$

If we write this with generalized coordinates $\{q\}^{N-1}$ [217],

$$A(\xi) = -\frac{1}{\beta}\ln\int e^{-\beta U(\xi,\{q\}^{N-1})}|J(\xi,\{q\}^{N-1})|dq_1\cdots dq_{\mathrm{N}-1} \tag{2.34}$$

where N is the number of degrees of freedom, J is the Jacobian for changing from Cartesian to generalized coordinates and $|J|$ is the associated determinant. It measures the change of volume element (in phase space) between $dxdp$ and $d\xi dqdp^{\xi}dp^{q}$. For instance $|J| = r$ in polar coordinate and therefore $dxdy = rdrd\theta$ [217].

We can differentiate A with respect to ξ:

$$\frac{dA(\xi)}{d\xi} = \frac{\int\frac{\partial}{\partial\xi}(-k_{\mathrm{B}}Te^{-\beta U}|J|)dq_1\cdots dq_{\mathrm{N}-1}}{\int e^{-\beta U}|J|dq_1\cdots dq_{\mathrm{N}-1}}$$

$$
\begin{aligned}
&= \frac{\int \left(\frac{\partial U}{\partial \xi}|J| - k_{\mathrm{B}}T\frac{\partial |J|}{\partial \xi}\right) e^{-\beta U} dq_1 \cdots dq_{\mathrm{N}-1}}{\int e^{-\beta U}\delta(\xi(x)-\xi)dx} \\
&= \frac{\int \left(\frac{\partial U}{\partial \xi} - k_{\mathrm{B}}T\frac{1}{|J|}\frac{\partial |J|}{\partial \xi}\right) e^{-\beta U}\delta(\xi(x)-\xi)dx}{\int e^{-\beta U}\delta(\xi(x)-\xi)dx} \\
&= \frac{\int \left(\frac{\partial U}{\partial \xi} - k_{\mathrm{B}}T\frac{\partial \ln |J|}{\partial \xi}\right) e^{-\beta U}\delta(\xi(x)-\xi)dx}{\int e^{-\beta U}\delta(\xi(x)-\xi)dx} \\
&= \left\langle \frac{\partial U}{\partial \xi} - k_{\mathrm{B}}T\frac{\partial \ln |J|}{\partial \xi} \right\rangle_{\xi}
\end{aligned}
\tag{2.35}
$$

where $\langle \cdots \rangle_{\xi}$ denotes the ensemble average over all configurations. The derivative of A is therefore the sum of two contributions: the first term as the mechanical forces acting along ξ and the second term effectively as an entropic contribution. Integrating the first term over ξ provides us with the PMF. Since ξ can be any function of atomic position, $dA/d\xi$ is not necessarily a force, but a mean value of "generalized force" exerted on the "generalized particle" ξ [217, 221].

In a recent work by Wong and York [221], a third term from Leibniz's rule should be added into Equation 2.35:

$$
\frac{dA(\xi)}{d\xi} = \left\langle \frac{\partial U}{\partial \xi} - k_{\mathrm{B}}T\frac{\partial \ln |J|}{\partial \xi} \right\rangle_{\xi} - k_{\mathrm{B}}T \left\langle \sum_{i=1}^{N-1} \left[\delta(q_i - l_{\mathrm{U_i}})\frac{dl_{\mathrm{U_i}}(\xi)}{d\xi} - \delta(q_i - l_{\mathrm{L_i}})\frac{dl_{\mathrm{L_i}}(\xi)}{d\xi} \right] \right\rangle_{\xi} \tag{2.36}
$$

$l_{\mathrm{U_i}}$ and $l_{\mathrm{L_i}}$ are the upper and lower integration limits for q_i. The last term arises from interchange of the order of the differential and integral operators according to Leibniz rule [222, 221]. An example of a three-atom system to demonstrate the importance of the Leibnizian contribution is provided in the supporting information of Reference [221]. In this dissertation, as we retain the Cartesian z-component of the separation between centers of mass (the force is projected along this reaction pathway), and the domain of this order parameter is decoupled from those of the remaining coordinates (the derivatives in the Leibniz term are zero), the Jacobian and Leibniz terms vanish. Thus we discuss the PMF in terms of the free energy or reversible work for the remainder of this work.

2.2.6.2 Umbrella Sampling

To pump a system over an energy barrier, there are basically two ways: the first is to modify the energy expression in order to reduce the barrier; the second way is to restrict the sampling space to all degrees of freedom, but the reaction coordinate describing the transition over the barrier. The former is known as biased MD or umbrella sampling, which was developed by Torrie and Valleau [223, 224, 205]. The basic idea is to apply an additional energy term to the system to ensure efficient sampling throughout all windows of the simulations, which can be written as:

$$E_{\text{biased}}(\vec{r}) = E_{\text{unbiased}}(\vec{r}) + w_i(\xi) \tag{2.37}$$

w_i is the bias potential of window i depending only on the collectible varible of the free energy profile. Usually we use a harmonic form ($w_i(\xi) = K(\xi - \xi_{i,\text{ref}})^2$, $\xi_{i,\text{ref}}$ is a reference point) as this additional bias potential to connect energetically separated regions in phase space. The resulting distribution, of course, is non-Boltzmann [149], we therefore have to extract/recover the corresponding Boltzmann averages to obtain the unbiased free energy profile [205, 149, 224]. The recovered free energy correponds to window i can be written as:

$$A_i(\xi) = -\frac{1}{\beta} \ln P_{i,\text{biased}}(\xi) - w_i(\xi) + F_i \tag{2.38}$$

where $\beta = 1/(k_{\text{B}}T)$, k_{B} is the Boltzmann constant and T is the temperature. $P_{i,\text{biased}}$ is the biased distribution of window i. $F_i = -(1/\beta)\ln(\exp[-\beta w_i(\xi)])$ is independent of ξ. The detailed derivation can be found in Reference [224, 205]. After the simulations, the free energy profile along ξ is combined with weighted histogram analysis method (WHAM) technique [225].

The choice of the force constant K is very critical. Overall, K has to be large enough to derive the system over the energy barrier; however, if K is too large, the biased distribution will be very narrow. Consequently, the distributions of neighboring windows should have sufficient overlap with each other in order to obtain a converged free energy profile.

2.2.6.3 Adaptive Biasing Force (ABF)

Adaptive Biasing Force (ABF) algorithm is an alternative method to overcome the insufficient sampling issue with significant free energy barriers, by applying a properly chosen, position-dependent biasing force into the system [226, 227, 228, 229]. Assume that we bin the interval if interest in ξ. After N_{step} steps in the simulation, with $\lambda(N_{\text{step}}, i)$ samples in each bin i, the running average of the force acting along ξ in bin i is

$$\begin{aligned} F_\xi(N_{\text{step}}, i) &= \frac{1}{\lambda}\sum_{j=1}^{\lambda} F_j(t_j^i) \\ F_j(t_j^i) &= \frac{d}{dt}\left(M_\xi \frac{d\xi}{dt}\right)\Big|_{t_j^i} \end{aligned} \tag{2.39}$$

where $F_j(t_j^i)$ is the j_{th} force sample when ξ is in bin i and t_j^i is the time at which sample j was collected. M denotes the mass matrix.

In ABF, a force $-(\nabla\xi)F_\xi(N_{\text{step}}, i)$ is applied to bias the dynamics of the system. As sampling of the phase space proceeds, $F_\xi(N_{\text{step}}, i)$ progressively approximates the average thermodynamic force acting along ξ, i.e., the total biased average force acting on the system is close to zero. In practice, a good estimate of the average force is usually achieved rather rapidly [226, 227, 228]. Under this circumstance, the system experiences only a diffusive force along ξ. Since an external bias is applied in ABF, it needs to be removed when estimating F_ξ, which can be simply done by subtracting $F_j(t_j^i)$ in Equation 2.39.

In the case of a single parameter ξ, the free energy difference between two states α and β is obtained by integrating the biasing force F_ξ,

$$\Delta A_{\alpha\to\beta} = -\int_{\xi_\alpha}^{\xi_\beta} F_\xi d\xi \approx -\frac{\xi_\beta - \xi_\alpha}{i_{\max}}\sum_{i=1}^{i_{\max}} F_\xi(N_{\text{step}}, i) \tag{2.40}$$

Usually it is recommended to split long reaction pathways into consecutive ranges of ξ to obtain an adequate sampling in reasonable simulation times. In contrast to probability-based methods such as WHAM [225], ABF does not require that these windows overlap along ξ [226, 227, 229].

2.2.7 Surface Tension

2.2.7.1 Kirkwood-Buff Method

The surface tension of a liquid arises from the imbalance of intermolecular forces at the surface of a liquid-vapor interface. We calculate the surface tension for the liquid-vapor interface from the average difference in the normal and tangential elements of the internal pressure tensor [230], which is

$$\gamma_{\mathrm{p}} = \frac{L_{\mathrm{z}}}{2}(P_{\mathrm{zz}} - \frac{P_{\mathrm{xx}} + P_{\mathrm{yy}}}{2}) \tag{2.41}$$

where P_{xx}, P_{yy}, and P_{zz} are the diagonal elements of the internal pressure tensor and L_{z} is the length of the simulation cell in the direction normal to the surface. The outer factor of 1/2 in Equation 2.41 accounts for the presence of two liquid-vapor interfaces [231].

In most MD simulations, we have cutoff (r_{c}) for calculating the interatomic and electrostatic interactions, which reduces the surface tension. Therefore the actual surface tension should include a long-range correction (LRC):

$$\gamma = \gamma_{\mathrm{p}} + \gamma_{\mathrm{LRC}} \tag{2.42}$$

and the long-range correction term can be determind as [232, 233, 234, 231]

$$\gamma_{\mathrm{LRC}} = \frac{\pi}{2}\int_{-\infty}^{\infty}\int_{-1}^{1}\int_{r_{\mathrm{c}}}^{\infty} r^3 U'(r)\mathrm{g}(r)(1-3s^2)\times[\rho(z)\rho(z-sr)-(\rho_{\mathrm{G}})^2]drdsdz \tag{2.43}$$

where $U(r)$ is the pairwise potential, $\mathrm{g}(r)$ is RDF, $\rho(z)$ is the interfacial density profile, and ρ_{G} is a GDS.

2.2.7.2 Capillary Wave Method

For simple fluids, thermodynamic considerations would predict that the interfacial width Δ, depends only on temperature and on the interaction energies within each phase and across the interface [235]. However, the presence of the interface breaks the translational invariance of the system, inducing "capillary waves" at an interface [236, 237, 238, 231, 239, 240], therefore the interface is rough with certain fluctuations. These "capillary waves" have been found experimentally from X-ray scattering on L-V interfaces [241, 239, 242, 243, 244, 245].

An alternative method for computing the surface tension is based on the assumption that the observed magnitude of the fluctuations is derived from two sources: an intrinsic contribution plus a logarithmic term that represents the broadening of the interface as a result of the capillary waves [236, 237, 235]. The relationship between the observed interfacial width Δ and the intrinsic interfacial width Δ_0 is given by [231]

$$\begin{aligned} \Delta^2 &= \Delta_0^2 + \Delta_c^2 \\ &= \Delta_0^2 + \frac{k_B T}{2\pi\gamma} \ln\left(\frac{L_\parallel}{\xi_b}\right) \end{aligned} \tag{2.44}$$

where $L_\parallel = L_x = L_y$ is the length of x/y-dimension of the interface. ξ_b is the bulk correlation length, which is of the order of molecular length [238]. γ is the surface tension. Usually, to get γ, it is required to do at least two simulations (i, j) with different sizes ($L_{\parallel,i}$ and $L_{\parallel,j}$). Then, according to Equation 2.44, the surface tension can be obtained as [238, 231]

$$\gamma_{ij} = \frac{k_B T}{2\pi[(\Delta_c^2)_i - (\Delta_c^2)_j]} \ln\left(\frac{L_{\parallel,i}}{L_{\parallel,j}}\right) \tag{2.45}$$

In this way we can calculate the surface tension without the exact value of ξ_b. We can always use this method to trace back the bulk correlation length using Equation 2.44.

The only remaining issue is the calculation of Δ_c^2. Assume that the liquid has a very sharp interface, we can write the density as

$$\rho_L(z) = \rho_L \theta[H(x,y) - z], \quad \rho_V(z) = \rho_V\{1 - \theta[H(x,y) - z]\} \tag{2.46}$$

where θ is the step function, ρ_L and ρ_V are the bulk density of each phase, respectively. We can differentiate $\rho_L(z)$ and $\rho_V(z)$ and get

$$\frac{d\rho_L(z)}{dz} = -\rho_L \delta[H(x,y) - z], \quad \frac{d\rho_V(z)}{dz} = \rho_V \delta[H(x,y) - z] \tag{2.47}$$

Now we change the intefacial scenerio with fluctuations, i.e., assume that the interface has a finite width and replace the δ functions with Gaussian distributions of the same width. Integrate the equations and we get

$$\rho_L(z) = \frac{1}{2}\rho_L - \frac{1}{2}\rho_L \mathrm{erf}\left(\frac{z - \langle H_L\rangle}{\sqrt{2}\Delta_c}\right), \quad \rho_V(z) = \frac{1}{2}\rho_V - \frac{1}{2}\rho_V \mathrm{erf}\left(\frac{z - \langle H_V\rangle}{\sqrt{2}\Delta_c}\right) \tag{2.48}$$

where H_{L} and H_{V} are the average positions of the interface of liquid and vapor phase, respectively. erf is the error function. Finally we have [238, 235, 231]

$$\rho(z) = \frac{1}{2}(\rho_{\mathrm{L}} + \rho_{\mathrm{V}}) - \frac{1}{2}(\rho_{\mathrm{L}} - \rho_{\mathrm{V}})\mathrm{erf}\left(\frac{1}{\sqrt{2}\Delta_{\mathrm{c}}}\right) \tag{2.49}$$

We can fit the density profiles obtained in our MD trajectory to get H_{L} and H_{V}, subsequently the intrinsic width $\Delta_0 = |H_{\mathrm{L}} - H_{\mathrm{V}}|$.

2.2.8 Surface Height Fluctuation and Covariance Entropy

In our MD trajectory, we have the spatial information of all the particles in the system. We can then construct the coarse-grained/rendered instantaneous surface for individual snapshot/configuration using the definition developed by Willard and Chandler [246], which is based on capillary wave theory. To determine the density distribution from each water molecule to a certain space point, Gaussian mass distributions are assigned to each water oxygen atom:

$$\Phi(\vec{r};\xi) = (2\pi\xi^2)^{-d/2} exp(-r^2/2\xi^2) \tag{2.50}$$

where r is the magnitude of $\vec{r}$, d stands for dimensionality. ξ is the correlation length in the calculation, for water it is usually taken as 3.0 Å, which is roughly the diameter of a water molecule. At space-time point $\vec{r}$, t, we have the coarse-grained density as

$$\bar{\rho}(\vec{r},t) = \sum_i \Phi(|\vec{r} - \vec{r}_i(t)|;\xi) \tag{2.51}$$

The interface is then determined as the $(d-1)$-dimensional manifold with a constant value c. In practice, for our L-V interfaces, we set up series of spacial grid points (x, y, z) and compute the corresponding coarse-grained densities $\rho(x, y, z)$ by Equation 2.51 [19, 93, 92, 247]. The surface is then obtained as the manifold by setting $\rho(x, y, z) = \rho_{bulk}/2$. This choice, though arbitrary, is based on the empirical density of GDS. With sufficient sampling, we can average these instantaneous surfaces ($h_{\mathrm{t}}(x, y)$, at time t) and get the mean surface $\langle h(x, y)\rangle$; furthermore, $\langle \delta h(x, y)\rangle = 0$. Subtracting the mean values from the $h_{\mathrm{t}}(x, y)$, we obtain $\delta h_{\mathrm{t}}(x, y)$ and the height fluctuations $\delta h_{\mathrm{t}}^2(x, y)$. Using

this framework to characterize interface fluctuations, we can probe the magnitudes of interface fluctuations when the solutes reside at various positions.

We use concepts from multivariate statistics as discussed by Otten et al. [19] to formulate entropy estimates. For a random variable x with continuous density $f(x)$, the entropy can be written as [248]

$$S(f) = -\int_{-\infty}^{\infty}\int_{-\infty}^{\infty}\cdots\int_{-\infty}^{\infty}\ln[f(x)]f(x)dx \tag{2.52}$$

where $x = (x_1, x_2, \cdots, x_N)'$. For a multivariate normal distribution, the density function is given by

$$f(x) = \frac{1}{|2\pi\Sigma|^{1/2}}exp\Big[-\frac{1}{2}(x-\mu)'\Sigma^{-1}(x-\mu)\Big] \tag{2.53}$$

Σ is the covariance matrix, $\Sigma_{ij} = cov(x_i, x_j) = E[(x_i - \mu_i)(x_j - \mu_j)]$, where $\mu_i = E(x_i)$ is the expected value of the i_{th} entry of x. We can therefore rewrite the entropy as

$$\begin{aligned} S &= \frac{1}{2}\Big[N + N\ln(2\pi) + \ln|\Sigma|\Big] \\ &= \frac{1}{2}\Big[\ln e^N + \ln(2\pi)^N + \ln|\Sigma|\Big] \\ &= \frac{1}{2}\ln\Big[(2\pi e)^N|\Sigma|\Big] \\ &= \frac{N}{2}\ln(2\pi e) + \frac{1}{2}\ln|\Sigma| \end{aligned} \tag{2.54}$$

where $|\Sigma|$ is the determinant of covariance matrix Σ. The surface entropy can therefore be estimated with surface height function $\delta h = h - \langle h\rangle$ as long as δh is normal distributed. The covariance matrix (χ) is then defined as $\chi_{ij} = \delta h_i \delta h_j$. The $\frac{N}{2}\ln(2\pi e)$ term is a constant for different states (i.e., simulation windows) with the same resolution of grid points (i.e., same N). Consequently, we get the entropy described by the fineness of the resolution of grid points:

$$S = constant + \frac{k_{\text{B}}}{2}\ln|\chi| \tag{2.55}$$

Chapter 3

SINGLE MONOVALENT ION AT THE LIQUID-VAPOR INTERFACE

3.1 Introduction: Adsorption of Ions

The studies of halide salts at aqueous interfaces have generated great interest ranging from the effects to the protein precipitation [249, 22, 112, 20, 1] to the understanding of the heterogeneous ozone chemistry [250, 98, 251]. In order to explain their results, e.g., the measured oxidation reaction rates in the marine boundary layer, researchers postulate that (an)ions must be present at the interface [252]. However, according to conventional picture, ions are repelled from surfaces, as reflected by surface tension measurements of numerous aqueous inorganic salt solutions, which show that the salts raise the surface tension of water. This implies, via the Gibbs adsorption equation, that there is a net surface deficit of ions.

In the traditional measurements of surface tension and electric potential, researchers could only sample the ionic/molecular distribution at a surface indirectly. Due to the development of advanced experimental techniques over the last decades, affinity of ions to hydrophobic interfaces at the molecular level has been extensively documented with experiments [253]. Techniques such as vibrational sum frequency generation spectroscopy (VSFG) [254, 255, 72, 73, 74, 75, 253], high-pressure VUV photoelectron spectroscopy [76, 77], ambient pressure X-ray photoelectron spectroscopy (XPS) [16, 78, 79] have been proved to help presenting the ionic distribution of interfacial region.

Rankin et al. addressed differences in interactions between halide anions F^- and I^- and t-butyl alcohol (TBA) in aqueous solution using Raman spectroscopy with multivariate curve resolution (Raman-MCR) [256]. They demonstrated that for 3 M

NaI solutions, roughly 64 percent of TBA molecules are affected by I^- based on a red-shift of the CH stretch Raman frequency of about 5 cm^{-1} relative to TBA in pure water. Furthermore, computational modeling using EFP/MD and quantum mechanical QM/EFP1 methods showed that the alcohol interacts with I^- in the region of the alcohol headgroup (OH^-) and near the aliphatic CH_3 groups. Interestingly, the authors observed no experimental indication of Na^+ or F^- perturbations to the alcohol's vibrational modes.

Saykally and co-workers did series of work probing the presence of different species at the air-water interface using second-harmonic generation (SHG) [1] technique with Langmuir adsorption equation [113, 115, 70, 257, 19, 69]. They reported an enhanced anion concentration at the air-water interface with a -6 kcal/mol free energy of adsorption for I^- [70]. More recently, Otten et al. probed the surface adsorption of SCN^- at air-water interface with the same technique and found that the inherent enthalpy and entropy of adsorption for SCN^- are both negative, in keeping with earlier simulations [9] and experiment. Their results were further supported with the free

[1] Consider an optical wave at frequency ω impinging on a medium, and this wave induces a dipole oscillation of each molecule in the medium. Because of the anharmonic nature of molecules, the overtone oscillations are excited at frequency $n\omega$ (n is integer). These oscillating dipoles emit electromagnetic radiation, consequently one would expect the output radiation of the medium at the frequency $n\omega$. In the SHG technique, one focuses attention on the frequency 2ω. For a driven anharmonic oscillator, the induced-dipole component ($p(2\omega)$, the source of the second-harmonic radiation) is proportional to the quantity $E(\omega)E(\omega)$, which is the self product of the incoming field of strength E, at frequency ω. The induced second-harmonic dipole per unit volume, $P^{(2)}(2\omega)$ can be written as

$$E(2\omega) \sim P^{(2)}(2\omega) = \chi^{(2)}E(\omega)E(\omega) \tag{3.1}$$

where $\chi^{(2)}$ is a characteristic coefficient of the medium and is known as the nonlinear susceptibility. In principle, if a medium has inversion symmetry, the incoming fields $E(\omega)$ and $-E(\omega)$ must result in $P(2\omega)$ and $-P(2\omega)$ respectively, which requires $\chi^{(2)} = 0$, indicating that SHG is forbidden. At an interface, such inversion symmetry must be broken, the radiation at frequency 2ω is therefore allowed [71]. By applying SHG and Langmuir adsorption equation, one is able to measure the propensity of ions to the interfaces.

energy calculation of single SCN^-/I^- transporting from bulk solution to air-water interface by employing MD simulations. The negative adsorption enthalpies, while being considered to challenge currently held theoretical views of the thermodynamic underpinnings of these ion behaviors, actually reflect a simple repartitioning of water density among air-water interface, bulk, and coordination (water within the ionic hydration shell) regions. Based on the capillary wave theory, which describes the waves' traveling along the phase boundary of a fluid, the loss of entropy was associated with the reduction/suppression of the surface height fluctuations induced by the presence of the ion at the interface. This fluctuation effect is rather long-ranged and can be extended to several molecular diameters away. Their results brought a different perspective that an ion's position in the Hofmeister series might be determined by a coupling effect between the pinning of capillary waves (entropic contribution) and the competition between ion hydration energy and the neat solvent's surface tension (enthalpic contribution).

Zhang et al. examined the influence of 11 sodium salts on the stability of poly(N-isopropylacrylamide) using dark field microscopy [62, 49]. [2] Strongly hydrated anions were shown to polarize the water molecules hydrating the macromolecule, whereas the weakly hydrated anions directly bind with the macromolecule. Similar results were observed from MD simulations of model systems. Heyda et al. [102] showed using extensive molecular dynamics simulations of N-methylacetamide (NMA) in the presence of monovalent cations and anions in water that the cations exhibit strong association with the carbonyl moiety of the peptide bond, while the anions do not

[2] Standard brightfield microscopy relies upon light from the lamp source being gathered by the substage condenser and shaped into a cone whose apex is focused at the plane of the sample of study. Samples are seen because of the path of the light passing through them, therefore highly depending on the refractive index and the opacity of the samples. Rather than illuminating the sample with a filled cone of light, the condenser is designed to form a hollow cone of light in dark field microscopy. That is, although the light travels around and past the objective lens, no rays enter it. The entire field appears dark when there is no sample on the microscope stage. But once the sample becomes on the stage, the image is made only by those rays scattered by the sample and captured in the objective lens, appears bright against the dark background.

interact with the amide group. Moreover, the larger anions, Br^- and I^-, demonstrated preferential spatial correlation with the hydrophobic methyl group. This interaction was more evident in the simulations with polarizable force fields.

Recent studies have illuminated the contributions of effects characteristic of hydrophobic hydration to halide interface propensity [145, 128, 11]; moreover, fluctuations of water-hydrophobe interfaces have been linked to differential interfacial stabilities. With the recent connection of surface stability of select inorganic anions (iodide, and partially charge iodide, for instance) to interfacial fluctuations and spatial correlations thereof [258, 19], there appears an intriguing mechanistic theme for ion-specific effects revolving around interfacial fluctuations induced by individual ions quite distant from the interface. This has broad implications in the context of discussing specific ion effects in a variety of circumstances. Thus, we also ask what differential influences single ions may have at distant interfaces.

Computational experiments measuring the reversible work (PMF) for transferring single ions from bulk aqueous environment to the aqueous liquid-vapor interface have been extensively used to explore the origins of surface stability [10, 107, 15, 128]. Netz and Horinek [128] proposed that the idea of negative adsorption entropy is independent of force field used to model the molecular components. In this chapter, we also consider the temperature dependence of the PMF for single iodide and chloride anions in TIP4P-FQ water. Few studies in the literature have addressed the temperature dependence of single ion free energetics at the liquid-vapor interface, and we hope to compare and contrast the properties we observe with those discussed in earlier studies. These analyses will also tie into recent work connecting local hydration properties and energetics of ions to surface stability.

3.2 Methods

3.2.1 Common Simulation Protocol

In this study we used one nonpolarizable force field as well as three different polarizable force fields. We will first introduce the common simulation protocol, then

describe them in detail. Molecular dynamics simulations were performed using the CHARMM package [148] (for SPC/E, TIP4P-FQ and TIP4P-QDP) and the parallel, scalable MD program NAMD 2.9b3 [259] (for SWM4-NDP). Simulations of liquid-vapor interfaces were performed in the NVT ensemble. Temperature was maintained at T = 300 K [3] using Nosé-Hoover thermostat [260] for SPC/E, TIP4P-FQ and TIP4P-QDP, while Langevin friction force scheme was used in NAMD with the damping coefficient = 5ps^{-1} for SWM4-NDP. The simulation cell was rectangular with dimensions 24 Å × 24 Å × 100 Å, in which z is the direction normal to the liquid-vapor interface. Periodic boundary conditions were applied in all three spatial directions. A bulk slab consisting of 988 water molecules (represented by the nonpolarizable SPC/E model [261] as well as the polarizable TIP4P-FQ model [262], TIP4P-QDP [263, 264], or SWM4-NDP [170]) and a single ion (F^-, Cl^-, Br^-, I^-, Na^+, K^+, Cs^+) was positioned in the center of the simulation cell, resulting in two liquid-vapor interfaces. A rigid water geometry is enforced using SHAKE [265] constraints. Before the production simulations, the system of each window was equilibrated for at least 0.5 ns. We summarize the parameters used in Table 3.1 and 3.2.

3.2.2 Detail of Each Model

3.2.2.1 SPC/E, TIP4P-FQ and TIP4P-QDP

The extened simple point charge model [261] (SPC/E) is a three-site, fixed-charge model for water, with the O-H bond distance of 1.0 Å and H-O-H bond angle of 109.47°. Point charges of oxygen and hydrogen atoms are q_O = -0.8476e and q_H = +0.4238e, respectively. Repulsion and dispersion interactions are modeled using a single Lennard-Jones site located on the oxygen center with parameters $R_{min,O}$ = 3.5532 Å and ε_O = 0.1554 kcal mol^{-1}. Ion parameters in SPC/E were parameterized by Fyta et al. [266, 267], which have been shown to reproduce experimental solvation free energies and the osmotic coefficients.

[3] In the temperature dependence study, T = 280, 300, 320, 340, 360 K.

We employ polarizable TIP4P-FQ [262] and TIP4P-QDP [264, 268] [4] water models and non-polarizable ions treated as charged Lennard-Jones spheres. Polarization of water is treated with a charge equilibration Hamiltonian [160, 158, 269, 161]:

$$E_{\text{elec}} = \sum_{i=1}^{N} \chi_i q_i + \frac{1}{2} \sum_{i=1}^{N} \eta_i q_i^2 + \frac{1}{2} \sum_{i \neq j}^{N} J_{ij} q_i q_j \tag{3.2}$$

where χ_i and η_i are associated with atomic electronegativities and hardnesses, respectively; the J_{ij} terms represent a parameterized molecular Coulomb integral between pairs of atoms.

Both TIP4P-FQ and TIP4P-QDP employ a rigid geometry having an O-H bond distance of 0.9572 Å, an H-O-H bond angle of 104.52° and a massless, off-atom M site located 0.15 Å along the H-O-H bisector which carries the oxygen partial charge. Repulsion and dispersion interactions also used a single Lennard-Jones (LJ) site located on the oxygen center with parameters $R_{\text{min,O}} = 3.5459$ Å and $\varepsilon_{\text{O}} = 0.2862$ kcal mol^{-1} for TIP4P-FQ, $R_{\text{min,O}} = 3.5520$ Å and $\varepsilon_{\text{O}} = 0.2902$ kcal mol^{-1} for TIP4P-QDP, respectively. Ions were treated as non-polarizable particles with interaction parameters based on those by Lamoureux and Roux [270] and validated for use with TIP4P-FQ [271, 272, 273, 143, 111]. For ions in TIP4P-QDP, the parameters were obtained from Reference [143].

We acknowledge that the use of a mixed polarizable water model with non-polarizable ion representation may appear unorthodox, but we consider that the combination of this empirical model is well-validated and reproduces many of the currently-accepted experimental observables upon which the quality of such force fields are based. Furthermore, the use of an alternative force field model allows us to speak to the universality (or at least the broad commonality) of molecular and atomic features underlying observed behaviors such as surface stability and negative surface adsorption entropy.

[4] The full name of TIP4P-QDP is 4-point transferable intermolecular potential with charge dependent-polarizability, as a modified model of TIP4P-FQ. TIP4P-QDP is capable of adjusting its atomic hardness parameters self-consistently via a scaling function dependent on the M-site charge.

The non-bond interactions were treated via the standard Lennard-Jones "12-6" potential

$$E_{LJ} = \sum_{ij} \varepsilon_{ij} \left(\frac{R_{\min,ij}^{12}}{r_{ij}^{12}} - 2\frac{R_{\min,ij}^{6}}{r_{ij}^{6}} \right) \tag{3.3}$$

For the systems with SPC/E, TIP4P-FQ, TIP4P-QDP, Lennard-Jones interactions were gradually switched off at interparticle distance of 11 Å, with a gradual switching between 10 Å (r_{on}) and 11 Å (r_{off}) using the switching function:

$$S(r_{ij}) = \begin{cases} 1 & r_{ij} \leq r_{\text{on}} \\ \frac{\left(r_{\text{off}}^2 - r_{ij}^2\right)^2 \left(r_{\text{off}}^2 + 2r_{ij}^2 - 3r_{\text{on}}^2\right)}{\left(r_{\text{off}}^2 - r_{\text{on}}^2\right)^3} & r_{\text{on}} < r_{ij} \leq r_{\text{off}} \\ 0 & r_{ij} > r_{\text{off}} \end{cases} \tag{3.4}$$

Charge degrees of freedom for the TIP4P-FQ and TIP4P-QDP water models were coupled to a thermostat at 1K with mass 0.000069 kcal mol^{-1} ps^2 e^{-2} using the Nosé-Hoover method and the charge degrees of freedom were propagated in an extended Lagrangian formalism; each water molecule was taken as a charge normalization unit (charge conserved with this unit), thus preventing any charge transfer between water molecules or between water and ion. We acknowledge recent developments of charge transfer models of water [274, 275], and anticipate that application of charge transfer models to the study of specific-ion effects will soon be realized and further elucidate underlying mechanisms and physics. Conditionally convergent long-range electrostatic interactions were treated using Particle Mesh Ewald (PME) [137] approach with a $30 \times 30 \times 128$ point grid, 6th order interpolation, and $\kappa = 0.33$. Dynamics were propagated using a Verlet leap-frog integrator with a 0.5 fs timestep for TIP4P-FQ and TIP4P-QDP, 1 fs timestep for SPC/E. Total sampling time for each window was 5-20 ns; properties were calculated from all but the initial 0.5 ns, which was treated as equilibration.

3.2.2.2 SWM4-NDP

SWM4-NDP model has a TIP4P-like structure [169, 170], as well as incorporating a Drude oscillator. It has an O-H bond distance of 0.9572 Å, an H-O-H bond angle

of 104.52°, with the M site 0.24 Å from the oxygen atom. The partial charge on each site is: q_{O} = -1.7164e, q_{H} = +0.5573e, $q_{\mathrm{Drude}} = -q_{\mathrm{O}}$ and $q_{\mathrm{M}} = -2q_{\mathrm{H}}$. The associated LJ parameters (of the oxygen atom) are $R_{\mathrm{min,O}} = 3.5698$ Å and $\varepsilon_{\mathrm{O}} = 0.2057$ kcal mol^{-1}.

Ions were also represented with a Drude oscillator model as discussed in Reference [276]. A timestep of 1.0 fs was used to integrate the equations of motion. Particle Mesh Ewald (PME) was implemented to treat conditionally convergent long-range electrostatic interactions using a grid of $32 \times 32 \times 128$ points. The cutoff for van der Waals (vdW) interactions was set to 15 Å without smoothing functions. An analytical correction of Lennard-Jones was applied to the reported vdW energy and virial that is equal to the amount lost due to cutoff of the LJ potential. The temperature was kept constant by applying the Langevin friction force scheme with a damping coefficient of 5ps^{-1}.

The long-ranged Coulombic forces were updated every two steps. The vdW interactions were modified using scale 1-3 parameters defined in the NAMD protocol and truncated smoothly at the cutoff distance. To ensure near-SCF [5] conditions, the thermostat for the relative motion of the Drude particles with respect to their parent atoms was set at a temperature of 1 K with a damping coefficient of 20 ps^{-1}. The rigid geometry of the SWM4-NDP water molecule was maintained using the SETTLE algorithm [277]. An additional quartic restraining potential of 4000 kcal/mol/Å^2, fitted from QM calculations, was applied to a Drude oscillator if its length exceeded 0.2 Å (fitted from QM calculations). These technical details are implemented in NAMD2.9 and were used without modification in the current work.

3.2.3 Potential of Mean Force Calculation

In this study, order paramter of the PMF, ξ_0, is the Cartesian z-component of the separation between the water slab center of mass and ion center of mass. We used umbrella sampling method for PMF calculations of SPC/E, TIP4P-FQ and TIP4P-QDP force fields. Ions were restrained to z-positions from 10 Å to 35 Å relative to the water

[5] Self-Consistent Field.

slab center of mass using a harmonic potential $U_{\text{restraint}}(z; z_{\text{relative,ref}}) = \frac{1}{2}k_{\text{restraint}}(z - z_{\text{relative,ref}})^2$ with the force constant of 4 (kcal/mol)/Å^2; this encompasses a range approximately 15 Å below the Gibbs Dividing Surface to approximately 10 Å above it at 300 K; though one could probe separations further into the bulk (towards the center of the system), this distance is sufficient to probe the differences of interest in this study, and also in keeping with previous studies to which we compare our results [143].

The PMFs in SWM4-NDP force field were performed by using NAMD software with the Adaptive Biasing Force (ABF) extensions integrated in the Collective Variables module and under the same conditions as described for MD simulations. Thirty-two "windows" along positive $z-$direction were explored, each with 1.5 Å width: [-1.5-00.5], [00-01.5], [01-02.5], [02-03.5], [03-04.5], [04-05.5], [05-06.5], [06-07.5], [07-08.5], [08-09.5], [09-10.5], [10-11.5], [11-12.5], [12-13.5], [13-14.5], [14-15.5], [15-16.5], [16-17.5], [17-18.5], [18-19.5], [19-20.5], [20-21.5], [21-22.5], [22-23.5], [23-24.5], [24-25.5], [25-26.5], [26-27.5], [27-28.5], [28-29.5], [29-30.5], [30-31.5]. Force samples were accumulated in the bin size of 0.02 Å.

The uncertainties in PMFs are determined using the approach of Zhu and Hummer [278]:

$$\text{var}[G(\xi_{\text{N}})] \approx \sum_{i=1}^{N} \text{var}[K\Delta\xi\bar{z}_{\text{i}}] \tag{3.5}$$

where $\bar{z}_{\text{i}}$ is the mean position of z in the i_{th} window, which can be obtained from block averages [279]. K is the force constant. The corresponding standard deviation $\sigma[G(\xi_{\text{N}})]$ is then the square root of $\text{var}[G(\xi_{\text{N}})]$. In our case, we chose the bulk state as the reference state, thus $\text{G}(z_{\text{bulk}}) = 0$, as a result the last window is expected to have the largest uncertainty. The largest uncertainties for the systems are approximately 0.1 kcal/mol. Alternative measures of estimating the mean and uncertainty of other properties will be discussed as needed.

The convergence of PMF is shown in Figure 3.1 by computing PMFs of I^- at 300 K with different amount of sampling. In this figure, 2.5 ns represents the PMF is computed using 2.5 ns of production data in each simulation window after the initial

equilibration. The inset shows the adsorption free energy (PMF minima) as a function of sampling time. In general, surface stable species (i.e. showing minimum near the interface) require more sampling time to get a well-converged PMF. In this study, all the surface stable species have at least 10 ns of sampling time for each simulation window, which ensures the convergence of PMF.

3.3 Correlation between Potential of Mean Force and Surface Fluctuation

We begin by looking at the free energetics of ions across the liquid-vapor interface. This will show which of the model ions (in their respective types of solvent) are predicted to be interface stable, and to what extent as indicated by the magnitude of the PMF well-depth at the interface. In all cases, the position of the Gibbs dividing surface (GDS) is around $z = 25.6$ Å (for 300 K); since the GDS is determined predominantly by the water density, the presence of a single ion of varying size does not influence the position of GDS among all systems. Figure 3.2 shows the PMF of single anion/cation in different force fields. For clarity, we added a vertical offset of 2 kcal/mol between each force field. The PMF is defined to be zero in the bulk (which is determined by window $z = 10$ Å). All the cations and F^- shows no PMF minimum regardless of force field. For Cl^-, the TIP4P-QDP force field shows modest surface stability; in SWM4-NDP there is a barrier observed around $z = 21$ Å, followed by a shallow minimum after the barrier. We observed PMF minima for Br^- in polarizable force fields but no surface stability in nonpolarizable force fields. Br^- has been considered marginally surface stable so the greatest effect of polarization may be expected to occur with this ion (i.e, surface stability systematically emerging with the introduction of ion polarizability). For I^-, PMF minima are observed in all force fields with the sequence $\Delta G_{\mathrm{SWM4-NDP}} < \Delta G_{\mathrm{TIP4P-QDP}} < \Delta G_{\mathrm{TIP4P-FQ}} \approx \Delta G_{\mathrm{SPC/E}}$. The results for Drude I^- are consistent with the surface stability discussed by Archontis et al. [280]. Incidentally, at 300 K, I^- shows a minimum of 0.5 kcal/mol in TIP4P-FQ, which is similar to the result for iodide at the L-V interface using non-polarizable ions in SPC/E water by Horinek et al. [11, 128]. This also corresponds with the DFT-D

value determined by Baer et al. [281, 146], though we do not discount that ours is a fortuitous result to some degree. Caleman et al. [9] observed a significantly deeper free energy minimum ($\approx$ 1.4 kcal/mol) for similar calculations but using water droplets and a polarizable force field based on classical Drude oscillators for water [282] and ions [270]; the force fields used in that study were parameterized to optimally recapitulate experimental hydration free energies of ions in bulk water and ion-water binding energies and geometries of gas-phase water-ion dimer complexes [270]. Later studies have concluded that the greater stability suggested by such classical models may arise from a representation of ion and water polarization response that is larger than the actual physical value. In our simulations of TIP4P-FQ and TIP4P-QDP, we do not include explicitly the polarization of the I^-, but we have taken care to faithfully capture the relative hydration free energetics of the individual ions to as great an extent as possible (refer to Table 3.2).

Recent studies have demonstrated a connection between L-V interfacial stability of chemical species (i.e. a free energy minimum state with the solute at the interface) and the extent to which the presence of these molecular species in the vicinity of the interface induces collective fluctuations of the interface in addition to the level inherent in pure water due to thermal motion [19]. In the next discussion, we explore the differences in interfacial fluctuations for the various ions discussed in this study. We aim to further demonstrate the general connection between interfacial stability and fluctuations with different force fields.

Figure 3.3 shows the absolute fluctuations $\langle \delta h^2(x,y) \rangle$ for I^- at different restrained z-position in TIP4P-FQ force field. When the anion is in the bulk (i.e. z = 10 Å), $\langle \delta h^2(x,y) \rangle$ is about 0.56, which corresponds to the value of pure TIP4P-FQ (refer to Ref [93]); at z = 18.0 Å, we observe onset of enhanced fluctuations relative to the pure water system. This enhancement reaches a maximum while I^- is restrained at z = 21 Å (as shown in Figure 3.3b). Finally when the anion moves across the GDS (z = 25 Å), the interfacial fluctuation is suppressed (as shown in Figure 3.3c). To illustrate this feature, we plot $\langle \delta h^2(x=0, y=0) \rangle$ as a function of the anion restrained

z-position, as presented in Figure 3.3d.

From Figure 3.3b and c we can see that the geometry of the $\langle \delta h^2(x,y) \rangle$ surface possesses radial symmetry and can thus be presented as a function of the lateral distance $r = \sqrt{x^2 + y^2}$. In the case of pure water (in the absence of ions), $\langle \delta h^2 \rangle$ for the current system size for the current force fields are 0.62 (SPC/E), 0.56 (TIP4P-FQ), 0.52 (SWM4-NDP) and 0.58 (TIP4P-QDP) Å^2. Therefore, in order to demonstrate and compare the fluctuations induced from the ions, we define $\langle \delta h_{\mathrm{L}}^2(r) \rangle$ as the fluctuations normalized by the value of pure water fluctuation in the corresponding force field. In this convention, when $\langle \delta h_{\mathrm{L}}^2 \rangle$ equals 1, the effect of ion is zero; when $\langle \delta h_{\mathrm{L}}^2 \rangle > 1$, the surface height fluctuation is enhanced relative to pure water with the presence of ion; when $\langle \delta h_{\mathrm{L}}^2 \rangle < 1$, the surface height fluctuation is suppressed. Here we would like to address that, although the surface fluctuation of pure water for the same force field does change according to the size of the simulation cell (basically, the larger the lateral dimensions, the larger the fluctuation value), the normalized $\langle \delta h_{\mathrm{L}}^2 \rangle$ remains the same for the same ion at the same relative position along the reaction path, which indicates that the ion-induced fluctuation is indeed a characteristic of the ion and is system size independent (as shown in Figure 3.4).

Figure 3.5 shows the $\langle \delta h_{\mathrm{L}}^2(r) \rangle$ from I^- (surface stable in all force fields) and Na^+ (non-surface stable), at the restrained window which induces the largest possible surface fluctuation and GDS. Here we chose these two species, I^- and Na^+, to describe the general properties and connection between surface stability and surface height fluctuation. First, either anion or cation suppresses the fluctuation when the ion is at the GDS, which is consistent with previous studies [19, 283, 93]. Na^+ does not generate any fluctuation enhancement. Only the surface stable species, I^-, induces interfacial fluctuation, in fact up to two times the inherent fluctuation from pure water. This fluctuation enhancement can influence the interface up to 8 Å from the ion center. Furthermore, at $r = 0$ Å (which indicates right above/below the ion), we have $\left\langle \delta h^2_{\mathrm{L,SWM4-NDP}} \right\rangle > \left\langle \delta h^2_{\mathrm{L,TIP4P-QDP}} \right\rangle > \left\langle \delta h^2_{\mathrm{L,TIP4P-FQ}} \right\rangle \approx \left\langle \delta h^2_{\mathrm{L,SPC/E}} \right\rangle$, which is the opposite sequence of the corresponding ΔG values. We also notice that from

Figure 3.3d, which plots values of $\langle \delta h_L^2(r=0) \rangle$ as a function of ion position along the interface normal from bulk to GDS, though Cl^- in TIP4P-FQ induces less enhancement of fluctuations (about half of I^--induced), yet we still find no surface stability for Cl^- in TIP4P-FQ water. This suggests a threshold level of induced fluctuations separating surface-stable and surface-unstable species; this would be ion-specific and the precise value for a particular ion-water force field would be determined by the complex interplay of water-water, ion-water interactions, and how these vary with proximity to the ion (i.e., nature of hydration shell of the ion in a particular solvent force field model as we will discuss further below).

To summarize up to this point, we have found that across a variety of force fields for ions and solvent, there is a group of ions that exhibit interfacial stability as seen in the potentials of mean force. In this work, we stress that we are not commenting on the accuracy of any of these force fields, as all water-ion force field combinations have been carefully parameterized and validated via extensive structural and thermodynamic analyses elsewhere. We have then seen that the species demonstrating an interfacial stability appear to enhance liquid-vapor interfacial fluctuations significantly, while those that show no interfacial stability induce no further fluctuation (or may even suppress levels of fluctuations). Our analysis further suggests the existence of inherent levels of fluctuation that correspond to interfacial stability that are force field specific, and arise from complex interactions of the models. Figure 3.6 shows results of the PMF minima (for surface stable ions) or the PMF value at the position of the GDS (for surface unstable ions) versus the maximum interfacial fluctuations induced. This is a plot that only distinguishes between ions; the different water force fields are not isolated. We see that the ions displaying interface stability lie in the upper left quadrant of the figure; those showing no stability (positive values of PMF) reside in the lower right quadrant. A best-fit straight line indicates a threshold value of about 1.5 dividing those ions that are interfacially stable and those that are not. The value of 1.5 is not an absolute threshold; this will depend on the force field (as noted above), and is sensitive to the parameters of the protocol (width of Gaussian for coarse-graining water

density) used to compute instantaneous interfaces and fluctuations. Nevertheless, the qualitative behavior and results should be robust.

We will next attempt to explain the current observations by considering the interaction of the local hydration environment of the ions with the solvent and solvent fluctuations at the L-V interface. We aim to show that the two types of ions (surface stable and unstable) present distinct hydration shell environments towards the interface upon approach; the surface stable ions presenting a solvent environment that is less rigid, more malleable, and thus more amenable to inducing fluctuations of the interface as a consequence of a greater disruption of solvent structure on approach to the interface. The surface-unstable ions present a more rigid hydration environment and decrease the efficacy of promoting interfacial fluctuations. These properties of the two orientations are discussed using radial distribution functions (RDF) of ion-water around the single ions and the dynamical properties of water in the hydration shells presented to the interface in the vicinity of the GDS.

3.4 Solvation Structure

We first consider general characteristics of ion hydration RDF's shown in Figure 3.7. In panels a,b,c and d we show results for anions and cations (in insets) in the various water models (no F^- ion model has been developed for the TIP4P-QDP water force field currently). Regardless of water force field or inclusion of polarizability, there is a general trend from F^- to I^- of decreasing water structuring around the anion (similarly for the cation series from Na^+ to Cs^+). The more severe ordering of water molecules around Cl^- is well-known [183, 270]. Smaller anions show dramatic first solvation peaks, and a sharply oscillatory probability function; in contrast, the larger anions show modest peaks, and significantly less oscillations. Figures 3.8a, b, and c show the 360° angle-averaged radial water density around I^-, Cl^-, and Na^+ as they reside at $z = 21.0$ Å, the position of maximum $< \delta h_L^2(x, y) >$ for the anions (the cation shows no maximum, but we use the same distance for all ions for consistency). This Figure demonstrates the different manners in which the hydration shells of the ions

couple with the solvent at the interface. I^-, while retaining its first, weakly-bound, less-ordered (malleable) hydration shell, sheds its outer hydration layers in the sense that these shells intermingle with the interfacial solvent. Cl^-, in contrast, retains the first and most of the second hydration shells (two bright rings); thus, the hydration shell environment is more rigid, well-ordered, tightly bound to the ion and does not support increased dynamical perturbation of local solvent. Moving to the cation, Na^+, panel c demonstrates the unambiguous, well-defined hydration shells, with a fully intact second shell clearly visible. We conjecture that the differences in water dynamics and structure in the first and second hydration shells of I^- and Cl^- lead to differences in induced interfacial fluctuations. To explore this, we will consider first water (oxygen) VACFs and residence times of water in the hydration shells of select ions. Since our contention is based on the nature of the hydration shell environment presented to the interface as the ion approaches, we will consider properties of hydrating water above the ion as depicted in panels d, e, and f of Figure 3.8. Shown in panels d,e, and f are the mean coarse-grained interfaces when the ions are positioned at $z = 21$ Å. These panels further demonstrate how the hydration shells of each ion (boundaries of which are delineated by the dashed circles around each ion) interact with the mean interface and the interfacial region in general. In the case of I^-, it is plausible to entertain the idea that less ordered, dynamic, weakly-bound water in these shells can help induced fluctuations about the mean interface. In the case of the other two ions, the mean interface is further away, and the rigidity of these ions' solvation shells prevents fluctuations that would penetrate into the local hydration shells.

3.5 Dynamical Properties

We now consider ensemble-averaged oxygen VACF [197, 198, 199] via

$$C_v(t) = \frac{1}{N}\sum_{i=1}^{N}\frac{\langle \overrightarrow{v_i}(t)\cdot\overrightarrow{v_0}(0)\rangle}{\langle \overrightarrow{v_i}(0)\cdot\overrightarrow{v_i}(0)\rangle} \tag{3.6}$$

where $\overrightarrow{v_i}(t)$ is the velocity vector of the i_{th} atom in the simulation system at time t. The brackets denote the ensemble average. Here we only look at the VACF of

water oxygen above the ion and within the first/second shell. We employ a 5 fs saving frequency for analyzing the dynamical properties.

Figure 3.9 shows oxygen VACF for I^- and Cl^- in TIP4P-FQ water for three ion positions corresponding to bulk solution ($z = 10$ Å), position of maximum fluctuation enhancement ($z = 21$ Å), and the GDS ($z = 25$ Å). Autocorrelation functions are shown for first hydration shell waters (solid line), second hydration shell waters (dashed line), pure bulk water (open circles), and pure water liquid-vapor interface (open squares). The solid and dashed lines represent correlation functions for water molecules in the regions depicted in Figure 3.8. We see that the location of the ions influences the dynamics of water in their hydration shells. At the bulk, for both anions, autocorrelation functions are bulk-like as expected. We notice the canonical caging effect of local solvent molecules manifest in oscillations around 100 fs. At ion position $z = 21$ Å, for the I^- system, we see little difference between autocorrelation decay in the first and second hydration shells unlike in the Cl^- system. The shortest time to approach zero is $185-190$ fs for I^-, 160 fs for Cl^- in the first shell, and 180 fs for Cl^- in the second shell. The shorter decorrelation times for Cl^- are consistent with a higher shell water density. Furthermore, the I^- curve takes a form closer to that of the pure L-V interface, while the Cl^- curve retains the oscillatory "hump" (though damped) of the bulk liquid curve, particularly the Cl^- first hydration shell. This indicates that the well-known caging effect persists for Cl^-. The local hydration environments for I^- and Cl^- are quite different approaching the interface.

Water residence time is considered a time-dependent probability function $P(t)$ of a molecule uninterruptedly remaining in a region at time $t = t_0 + \Delta t$ having started in the region at time $t = 0$ $P(t) = \frac{1}{N(0)} \sum_{t_0} N(t_0, t)$. We consider molecules that are within the first/second shell at time $t_0 = 0$ and remain within the corresponding shell at t with no instances of leaving the region. The probability is

$$P(t) = \frac{1}{N(0)} \sum_{t_0} N(t_0, t) \tag{3.7}$$

where t_0 indicates multiple time origins and $t = t_0 + \Delta t$ is the persistence time of a

water molecule in a region after it was initially observed at time origin t_0. The number of molecules confined at each time t is normalized by the number of molecules observed at $t = 0$, such that $P(0) = 1$. $P(t)$ is fit to a stretched exponential form,

$$P(t) = P_0 \exp[-(t/\tau)^\gamma] \tag{3.8}$$

where P_0, τ, and γ are adjustable fitting parameters. P_0 is the probability that a water molecule initially is within the shell at time t=0; for the final functional fits, P_0 is approximately 1. γ is the well-known stretched exponential constant and is generally around 0.85 in our systems, suggesting certain deviation from first order decay. τ is characteristic residence lifetime for the decay from 1 to $1/e$. Residence times of water molecules (again, only those above the ion) residing in the first solvation of I^- and Cl^- are shown in Table 3.3. Data for I^- and Cl^- using TIP4P-FQ and SWM4-NDP water models are shown as representative examples. For all positions, water residence times in the first hydration shell of Cl^- are higher than for I^-. At $z = 21$ Å, the ratio can reach a striking factor of 2. This suggests that the first hydration shell of Cl^- acts as a barrier to surface deformation, preventing deformation to the extent observed for I^-; moreover the mean surface for Cl^- resides in its second hydration shell. Observed differences in ion-induced interfacial fluctuations thus correlate with the lifetimes of hydration water molecules in a particular ion's local environment, the implication being that faster dynamics (smaller decorrelation time) allow more exchange of water in hydration shells, allowing for the ability to accommodate/mediate greater fluctuations.

3.6 Temperature Dependence: the case of TIP4P-FQ

To the best of our knowledge, to date, only one temperature dependence study on monovalent halides has been presented in the literature [128]. As mentioned in that work, the idea of negative adsorption entropy is independent of force field used to model the molecular components. This has also been demonstrated experimentally for NaSCN [19]. In this contribution, we start by considering the temperature dependence of the PMF for single I^- (surface stable) and Cl^- (surface unstable) anions in TIP4P-FQ water using the same computational convention discussed in the previous section,

then we analyze local self- and cross-interaction (i.e., water-water and water-ion) energies underlying the observed PMF and temperature dependencies. Followed by the spirit of our previous discussion, we then consider solvent properties in the hydration shells of the two halide anions to connect local hydration properties and energetics of halide anions to surface propensity.

3.6.1 Thermodynamic Free Energetics and Solvation Structures

The PMFs ($\Delta G(z)$) of I^- and Cl^- in TIP4P-FQ were calculated in the same manner with the previous section and is referenced to zero at $z = 10$ Å; results of I^- and Cl^- at different temperatures are shown in Figure 3.10 a and b, respectively. For clarity, a vertical offset of 2 kcal/mol is added to distinguish the PMF at different temperatures. While Cl^- shows no pronounced minimum independent of temperature, I^- shows minima below the GDS at all temperatures except 360 K. This, though being inconsistent with the study by Horinek [11, 128], in which they observe a minimum as the I^- moves across the L-V interface at 360 K, suggests that underlying temperature-dependent properties of water-water and water-ion interactions are not equivalent. Though not pursued presently, a comparison of the phase-equilibrium properties of the water-water interaction models used in the two studies would provide further insight as to the origins of this difference. We define ΔG^* as the adsorption free energy (PMF minimum) and plot it as a function of temperature, as shown in the inset of Figure 3.10a along with the uncertainty and the linear fitting result ($\Delta G^* = \Delta H^* - T\Delta S^*$). We observe a positive slope for ΔG^* versus T indicating $\Delta S^* < 0$.

We next decompose our PMF into total enthalpic and total entropic components, acknowledging that this analysis is not a definitive exploration of the inherent driving forces for surface adsorption as observed via molecular simulations using classical force fields. It does allow some connection to previous studies using droplet based simulations [9] so as to allow one to draw conclusions about general behaviors and trends related to observed behaviors in anion surface propensities. In our system the pressure-volume work is negligible and so we will estimate enthalpic contributions with

internal energy components. Furthermore, since we are interested in differences relative to specific positions in our simulation system, we will consider kinetic contributions to be equivalent at the endpoints, thus leaving us with interaction energy components as the determinants of the enthalpy changes. We consider the enthalpy change $\Delta H(z)$ as the difference of average interaction potential energy [9, 110, 284] when the anion resides at position z and in bulk ($z = 10$ Å), $\Delta H(z) = H(z_{\text{ion}}) - H(z_{\text{bulk}})$. The entropy change profile, $\Delta S(z)$, can therefore be estimated by subtracting enthalpy from free energy, $-T\Delta S(z) = \Delta G(z) - \Delta H(z)$. Figure 3.11 shows the enthalpic component $\Delta H(z)$ and entropic component $-T\Delta S(z)$ of the free energy for I^- and Cl^-. For clarity, we added 5 and -5 kcal/mol vertical offsets for $\Delta H(z)$ and $-T\Delta S(z)$, respectively. At 300K, relative to when the ion is located in a bulk-like z-position, the total system enthalpy for states where I^- is surface-adsorbed is lower, while the enthalpy for Cl^- (not surface-enhanced) effectively does not change at the GDS. Caleman et al. [9] observe a similar, though slightly deeper, minimum for I^-. Furthermore, the present relative enthalpies are not overly temperature sensitive. Entropy contributions are positive, suggesting inherent negative adsorption entropy as evidenced by the fitting slope of 0.01 kcal/mol/K obtained from a linear fit of the temperature versus PMF well-depth data.

We further decompose $\Delta H(z)$ into water-water (w-w) and ion-water (i-w) contributions [9], which are represented by the averaged potential energy at each window. These potential energies are plotted relative to the window where the anion is restrained at $z = 10$ Å, such that

$$\Delta H(z) = \Delta H_{\text{w-w}}(z) + \Delta H_{\text{i-w}}(z) \tag{3.9}$$

The results of $\Delta H_{\text{w-w}}(z)$ and $\Delta H_{\text{i-w}}(z)$ of I^- and Cl^- are shown in Figure 3.12. In the case of I^-, $\Delta H_{\text{w-w}}(z)$ shows a significant minimum at $z = 25$ Å, which is closer to the GDS than the minimum of $\Delta G(z)$ and $\Delta H(z)$ at $z = 23$ Å; at this z-position, the ion-water interaction is positive, thus restricting the minimum of the total enthalpy to below the GDS. The combination of water-water and water-ion enthalpies (interaction

energies) effectively cancel one another, leading to the flat profile of the Cl^- total enthalpy, though Figure 3.12 indicates that the water-water interaction in the Cl^- case does reach a minimum at the GDS location. We define $\Delta H^{\dagger}_{\mathrm{w-w}}$ as the minimum of $\Delta H_{\mathrm{w-w}}$, $\Delta H^{\dagger}_{\mathrm{i-w}} = \Delta H_{\mathrm{i-w}}(GDS) - \Delta H_{\mathrm{i-w}}(10\ \text{Å})$ and $\Delta H^{\ddagger}_{\mathrm{i-w}} = \Delta H_{\mathrm{i-w}}(35\ \text{Å}) - \Delta H_{\mathrm{i-w}}(10\ \text{Å})$ and list these values in Table 3.4. Although no significant minimum for $\Delta G(z)$ and $\Delta H(z)$ has been found for Cl^-, we still observe a minimum for $\Delta H_{\mathrm{w-w}}(z)$. These minima, while shallower compared with those in the I^- system, show the same temperature dependence. For both anions, $\Delta H_{\mathrm{i-w}}(z)$ terms monotonically increase as the ion approaches the vapor phase independent of temperature.

We address the difference of $\Delta H_{\mathrm{i-w}}(z)$ by considering the change in hydration of ions through the LV-interface. This is illustrated by calculating the number of coordination water molecules as a function of z-position ($\langle N_{\mathrm{coor}} \rangle$, as shown in Figure 3.13 c and d). We define the first solvation shell cutoff distance as the first minimum of the anion-oxygen radial distribution function, as shown in Figure 3.13 a and b. Moving through the GDS into the vapor, the coordination number decreases. All ions remain partially hydrated in the vapor; both anions maintain about four coordinating water molecules. Completely desolvated ions are not observed in our simulations. This is in agreement with calculations for transferring hydrated ion clusters from bulk water to 1,2-dichloroethane [285] and simulations of ions across air-water interface [10]. As the larger ion, I^- inherently has more water molecules in the first solvation shell, and thus experiences greater changes in its coordination environment upon transfer into the vapor phase. Since the ion-coordinated water interaction is negative, this reduction of $\langle N_{\mathrm{coor}} \rangle$ as the ion moves past the GDS result in the increase of $\Delta H_{\mathrm{i-w}}(z)$. The larger change in $\langle N_{\mathrm{coor}} \rangle$ for I^- necessarily leads to larger $\Delta H_{\mathrm{i-w}}(z)$ for I^- than Cl^- at the same temperature. As the temperature increases, both ions show less reduction of $\langle N_{\mathrm{coor}} \rangle$, and therefore leads to less $\Delta H_{\mathrm{i-w}}$.

Thus far, our analysis of the global enthalpy change indicates that the balance of water-water and water-ion interactions through the interface result in the enthalpy

minimum before the GDS in the I^- system. Since the water-water interaction component of the enthalpy yields the largest favorable contribution (Figure 3.12), we now adopt the analysis of Otten et al. [19] to consider the origin of this contribution, and its sign, based on consideration of the average interaction energy of a water molecule with other water molecules in the system; we consider this average interaction energy for the regions where the water molecule is in a bulk-like region, at the liquid-vapor interfacial region, and in the hydration shell of the anion. The total water-water energy is $\langle U_{\mathrm{w-w}}(z)\rangle = \bar{\varepsilon}_{\mathrm{coor}} N_{\mathrm{coor}}(z) + \bar{\varepsilon}_{\mathrm{L-V}} N_{\mathrm{L-V}}(z) + \bar{\varepsilon}_{\mathrm{bulk}} N_{\mathrm{bulk}}(z)$, where $\bar{\varepsilon}$ represents the average interaction energy of a water molecule with all the other water molecules in the corresponding environment. Here, N_{coor} indicates the number of water molecules within the first solvation shell of the ion, $N_{\mathrm{L-V}}$ refers to water molecules near the GDS but not within the first solvation shell of the ion, and finally, N_{bulk} refers to the water molecules that are in the bulk liquid (but not within the coordination criteria or near the L-V interface). $\Delta H_{\mathrm{w-w}}(z)$ is therefore

$$\Delta H_{\mathrm{w-w}}(z) = \bar{\varepsilon}_{\mathrm{coor}} \Delta N_{\mathrm{coor}}(z) + \bar{\varepsilon}_{\mathrm{L-V}} \Delta N_{\mathrm{L-V}}(z) + \bar{\varepsilon}_{\mathrm{bulk}} \Delta N_{\mathrm{bulk}}(z) \tag{3.10}$$

where ΔN is the difference in the number of water molecules in the region indicated by the subscript to ΔN; here, we adopt the definition of $\Delta N = N(z) - N(z = 10\mathring{A})$. Since the total number of water molecules is conserved, we have $\Delta N_{\mathrm{bulk}} = -(\Delta N_{\mathrm{coor}} + \Delta N_{\mathrm{L-V}})$, therefore Equation 3.10 can be written as:

$$\Delta H_{\mathrm{w-w}}(z) = (\bar{\varepsilon}_{\mathrm{coor}} - \bar{\varepsilon}_{\mathrm{bulk}}) \Delta N_{\mathrm{coor}}(z) + (\bar{\varepsilon}_{\mathrm{L-V}} - \bar{\varepsilon}_{\mathrm{bulk}}) \Delta N_{\mathrm{L-V}}(z) \tag{3.11}$$

In Figure 3.14 we present the density profile of water oxygen atoms along the z-dimension when an ion is restrained in bulk (z=10Å) or at the GDS. From Figure 3.14 c, d and previous discussion, we have $\Delta N_{\mathrm{L-V}}$ and $\Delta N_{\mathrm{coor}} < 0$. Since $\bar{\varepsilon}_{\mathrm{coor}}$ and $\bar{\varepsilon}_{\mathrm{L-V}}$ are both more positive than $\bar{\varepsilon}_{\mathrm{bulk}}$ (as shown in Figure 3.15), we obtain that $\Delta H_{\mathrm{w-w}}(GDS)$ is negative. This recapitulates the results of Otten et al. [19].

When the ion is in bulk, the number of bulk water molecules is reduced (the ions carve out a void that excludes water molecules); as the ion moves to GDS, water fills

in the void, leading to $\Delta N_{\text{bulk}} > 0$, which is a reflection of the change of ΔN_{coor} and $\Delta N_{\text{L-V}}$. From Figure 3.14 a and b we observe larger voids for I^- compared to those for Cl^-, which explains why $\Delta H_{\text{w-w}}(GDS)$ is more stabilizing for the larger anion. The size of these voids is not sensitive to the temperature. However, due to lower water-water interaction at high temperature (as shown in Figure 3.15 or evidenced by the shift of GDS to larger value as the water cohesive energy is reduced at elevated temperatures), we expect a less stabilizing $\Delta H_{\text{w-w}}(GDS)$ at elevated temperatures, shown in Figure 3.12 a and c.

3.6.2 Temperature Effects of the Surface Height Fluctuations

Figure 3.17 shows the normalized, mean-square amplitude of surface height fluctuations as a function of lateral distance from the ion. The normalization factors are: 0.56 (300 K), 0.66 (320 K), 0.78 (340 K) and 0.95 (360 K) $Å^2$, respectively.

As temperature increases, the maximum of $\langle \delta h_{\text{L}}^2 \rangle$ for I^- drops from 2 to 1.65; on the other hand, the maximum of $\langle \delta h_{\text{L}}^2 \rangle$ for Cl^- is rather insensitive to temperature change, remaining approximately 1.3. Since the fluctuations of surface height can be decomposed into the ion-induced and water-inherent contributions, this indicates the fact that the proportion of ion-induced fluctuations is weakened as the temperature increases. We rationalize this by considering the mechanism through which I^- effects its perturbation. Since the perturbation of solvent structure amplifies the inherent interface fluctuations at lower temperatures, the increase of inherent fluctuations at higher temperatures reduces the impact of any solvent structural perturbation induced by the ion. Again, the reduction in the magnitude of interface fluctuation induced by I^- correlates with reduction in surface stability (refer to Figure 3.10). Interestingly, we find that the absolute change in fluctuation magnitude from 12 Å to 0 Å is about 0.4 Å for I^-, independent of temperature (though the value we ascribe to the endpoints would change based on characteristics of the grid used to estimate the instantaneous interfaces, the argument would sill hold).

3.7 Surface Entropy

Finally, we provide some estimates of surface entropy related to enhanced interface fluctuations in the presence of anions. The general method is described in the previous section, here we just need to fill in some of the calculation detail. In this case, we obtain ΔS as $\Delta S(z) = S(z) - S(z = 10\text{Å})$. For every 50 picoseconds, we compute $\langle\chi\rangle$ and corresponding entropy. Eventually we use these to get the estimation of $\langle S(z)\rangle$. Shown in Figure 3.16 is a time profile of $\langle S(z)\rangle$ for I^- at $z = 10$, 21 and 25 Å, which is converged after 2 ns.

Figure 3.18 (symbols) shows estimates of the resulting interfacial entropy (relative to ion z-position 10.0 Å) at ion positions of 21.0 and 25.0 Å; we stress that these values are qualitative due to the grid-based approach used. In the barrier region, the entropy from surface fluctuations increases for both ions, with I^- contributing more due to larger fluctuations. We posit that in the case of I^-, this higher interfacial entropy acts in conjunction with other enthalpic (i.e., increase in water-water interactions leading to enthalpic stabilization of the system) contributions to greater stabilize I^- at these locations ($z = 20.0$, 21.0 and 22.0 Å) compared to Cl^-. This translates to higher probability of the I^- being in these positions; once at these locations, the I^- can then proceed to the interfacial region. At the GDS (vertical line, Figure 3.18), suppression of interface fluctuations by both anions leads to lower surface entropy relative to the bulk state. The surface adsorbed state for I^- shows a net decrease in entropy relative to the bulk state; this holds for Cl^- as well. For I^-, this is interpreted as one negative contribution to the standard entropy of adsorption. The estimated $\langle\Delta S(z)\rangle$ for I^- and Cl^- between the window of highest fluctuations and bulk for different temperature are listed in Table 3.5. As expected, the entropy at the position of highest interface fluctuations relative to the bulk ($z = 10$ Å) decreases with increasing temperature; values for Cl^- are smaller, also as anticipated based on differences in fluctuations. We reiterate that these are simply coarse estimates, with only qualitative descriptive value.

These results recapitulate the idea put forth by Noah-Vanhoucke et al. that surface stable anions, in part, derive their thermodynamic stability through collective

properties associated with the fluctuations of the interface and coupling of these with those fluctuations induced by the anions. Based on ion-induced interface fluctuations, the authors conclude, there is an entropic benefit for moving a volume-excluding solute from bulk to a position within the interface below the GDS; the free energy penalty for loss of electrostatic water-ion interactions becomes dominant after the passage of the anion through the GDS and into the vapor-like regions [258].

3.8 Discussion and Conclusions

In summary, negatively charged ionic impurities, induce long-ranged solvent perturbations that propagate to an interface when the ions are up to 8 Å away in accord with recent experiments and interpretations suggesting the long-ranged nature of ion-induced perturbations. Furthermore, we observe chemical specificity (ion-specificity); surface stable ions induce larger interfacial fluctuations than surface unstable species. The differences in induced fluctuations are traceable to the nature of the first few hydration shells of the ions. For I^-, the hydration shells consist of water molecules that are more dynamic, less persistent (lower residence times), while the opposite is true for surface unstable ions. Approaching the L-V interface, coupling of local solvent with solvent further away leads to differential contributions of surface entropy (arising from the different magnitudes of the interface fluctuations) to the stability of surface-adsorbed states. Long-ranged perturbations are not only relevant to the bulk, but also to the nature of fluctuations at water-biomacromolecule and water-nanomaterial interfaces. This will be further addressed in the following chapters.

Addressing implications of this work, we note the striking similarity of hydration properties of the less charge-densed I^- to that of hydrophobic hydration [43]. Analogous to enhanced solvent density fluctuations seen for molecular hydrophobic solutes in water [43], I^- perturbs solvent structure and dynamics (to a greater degree than Cl^-) leading to more fluid, dynamic, and fluctuating solvent structure. Furthermore, our observation regarding the connection between the extent of "rigidity" of the first hydration shell of the impurity and its surface stability is reminiscent of Figure S2 of the

Supplementary Information of Reference [19]. Overall, results indicate that ion-specific surface adsorption of inorganic monovalent anions may be discussed in the context of increasing ion hydrophobic character as recently suggested [128, 123].

Water model	$R_{\min}$ (Å)	ε (kcal/mol)
SPC/E	3.5532	0.1554
TIP4P-FQ	3.5459	0.2862
SWM4-NDP	3.5698	0.2057
TIP4P-QDP	3.5520	0.2902

Table 3.1: Parameters of water models used in this study. Reproduced with permission from Shuching Ou, Yuan Hu, Hongbin Wan and Sandeep Patel. "Spherical Monovalent Ions at Aqueous Liquid-Vapor Interfaces: Interfacial Stability and Induced Interface Fluctuations." *Journal of Physical Chemistry B.* **2013**, *117 (39)*, 11732-11742. Copyright 2013 American Chemical Society.

Force field	$R_{\min}$ (Å)	ε (kcal/mol)	ΔG_{hyd} (kcal/mol)
SPC/E			
F^-	4.6706	0.003585	-102.77
Cl^-	4.9388	0.1	-73.14
Br^-	5.1981	0.09847	-66.68
I^-	6.5451	0.003085	-57.60
Na^+	2.8993	0.1	-98.95
K^+	3.0194	0.5832	-82.22
Cs^+	3.9185	0.07768	-71.22
TIP4P-FQ			
F^-	4.52	0.01	-112.83(9)
Cl^-	4.92	0.07658	-78.93(8)
Br^-	5.14	0.10820	-71.87(14)
I^-	5.52	0.15910	-63.15(15)
Na^+	2.90	0.03151	-98.41(12)
K^+	3.29	0.18290	-82.05(10)
Cs^+	3.96	0.35279	-69.63(8)
SWM4-NDP			
F^-	4.9245	0.002618	-108.0
Cl^-	4.9622	0.07197	-78.4
Br^-	5.2526	0.0823	-71.6
I^-	5.5159	0.2084	-63.1
Na^+	2.9234	0.0315	-96.3
K^+	3.3733	0.1419	-78.6
TIP4P-QDP			
Cl^-	5.6419	0.01142	-74.4(2)
Br^-	5.6839	0.05740	-63.1(7)
I^-	5.8339	0.1569	-57.5(1)
Na^+	2.6939	0.031075	-103.2(1)

Table 3.2: Parameters of ions used in this study. Uncertainty in the last digit denoted in parentheses. Reproduced with permission from Shuching Ou, Yuan Hu, Hongbin Wan and Sandeep Patel. "Spherical Monovalent Ions at Aqueous Liquid-Vapor Interfaces: Interfacial Stability and Induced Interface Fluctuations." *Journal of Physical Chemistry B.* **2013**, *117 (39)*, 11732-11742. Copyright 2013 American Chemical Society.

System	τ (ps)	γ
I^-, TIP4P-FQ, 10.0 Å	1.62(0.28)	0.78(0.04)
I^-, TIP4P-FQ, 21.0 Å	1.12(0.25)	0.80(0.05)
I^-, TIP4P-FQ, 25.0 Å	1.47(0.13)	0.86(0.08)
Cl^-, TIP4P-FQ, 10.0 Å	2.57(0.22)	0.84(0.04)
Cl^-, TIP4P-FQ, 21.0 Å	2.74(0.08)	0.86(0.09)
Cl^-, TIP4P-FQ, 25.0 Å	2.46(0.08)	0.85(0.16)
I^-, SWM4-NDP, 10.0 Å	1.82(0.94)	0.76(0.14)
I^-, SWM4-NDP, 21.0 Å	1.27(0.86)	0.72(0.12)
I^-, SWM4-NDP, 25.0 Å	0.83(0.67)	1.04(0.25)
Cl^-, SWM4-NDP, 10.0 Å	3.38(1.91)	0.88(0.15)
Cl^-, SWM4-NDP, 21.0 Å	2.00(0.82)	0.91(0.10)
Cl^-, SWM4-NDP, 25.0 Å	2.41(2.33)	1.04(0.25)

Table 3.3: Fitting results of residence time of water molecules in the first solvation shell. Values in parentheses denote the uncertainty determined from the standard deviation. Reproduced with permission from Shuching Ou, Yuan Hu, Hongbin Wan and Sandeep Patel. "Spherical Monovalent Ions at Aqueous Liquid-Vapor Interfaces: Interfacial Stability and Induced Interface Fluctuations." *Journal of Physical Chemistry B.* **2013**, *117 (39)*, 11732-11742. Copyright 2013 American Chemical Society.

System	$\Delta H^{\dagger}_{\mathrm{w-w}}$	$\Delta H^{\dagger}_{\mathrm{i-w}}$	$\Delta H^{\ddagger}_{\mathrm{i-w}}$
I^-			
280 K	-13.97	11.35	37.17
300 K	-10.62	10.18	34.90
320 K	-10.31	8.83	32.50
340 K	-8.04	7.42	29.58
360 K	-7.38	7.84	27.11
Cl^-			
280 K	-8.85	11.22	31.92
300 K	-5.61	8.11	30.02
320 K	-4.78	6.97	27.53
340 K	-4.08	4.10	25.38
360 K	-3.06	3.20	23.16

Table 3.4: Decomposition of $\Delta H(z)$ into water-water and ion-water components at some significant z-positions. Refer to text for the detail definition. The units are in kcal/mol. Reproduced with permission from Shuching Ou and Sandeep Patel. "Temperature Dependence and Energetics of Single Ions at the Aqueous Liquid-Vapor Interface" *Journal of Physical Chemistry B.* **2013**, *117 (21)*, 6512-6523. Copyright 2013 American Chemical Society.

System	$\Delta S(z_1)$	$\Delta S(z_{\mathrm{GDS}})$
I^-		
300 K	31.80	-30.07
320 K	28.96	-28.98
340 K	23.35	-16.11
360 K	14.45	-14.13
Cl^-		
300 K	19.27	-11.61
320 K	15.21	-12.16
340 K	11.84	-9.59
360 K	14.13	-9.06

Table 3.5: Estimated $\Delta S(z_1)$ and $\Delta S(z_{\mathrm{GDS}})$ obtained by the covariance matrix of surface height functions. z_1 indicates the window with largest fluctuations. The units are k_{B}. Reproduced with permission from Shuching Ou and Sandeep Patel. "Temperature Dependence and Energetics of Single Ions at the Aqueous Liquid-Vapor Interface" *Journal of Physical Chemistry B.* **2013**, *117 (21)*, 6512-6523. Copyright 2013 American Chemical Society.

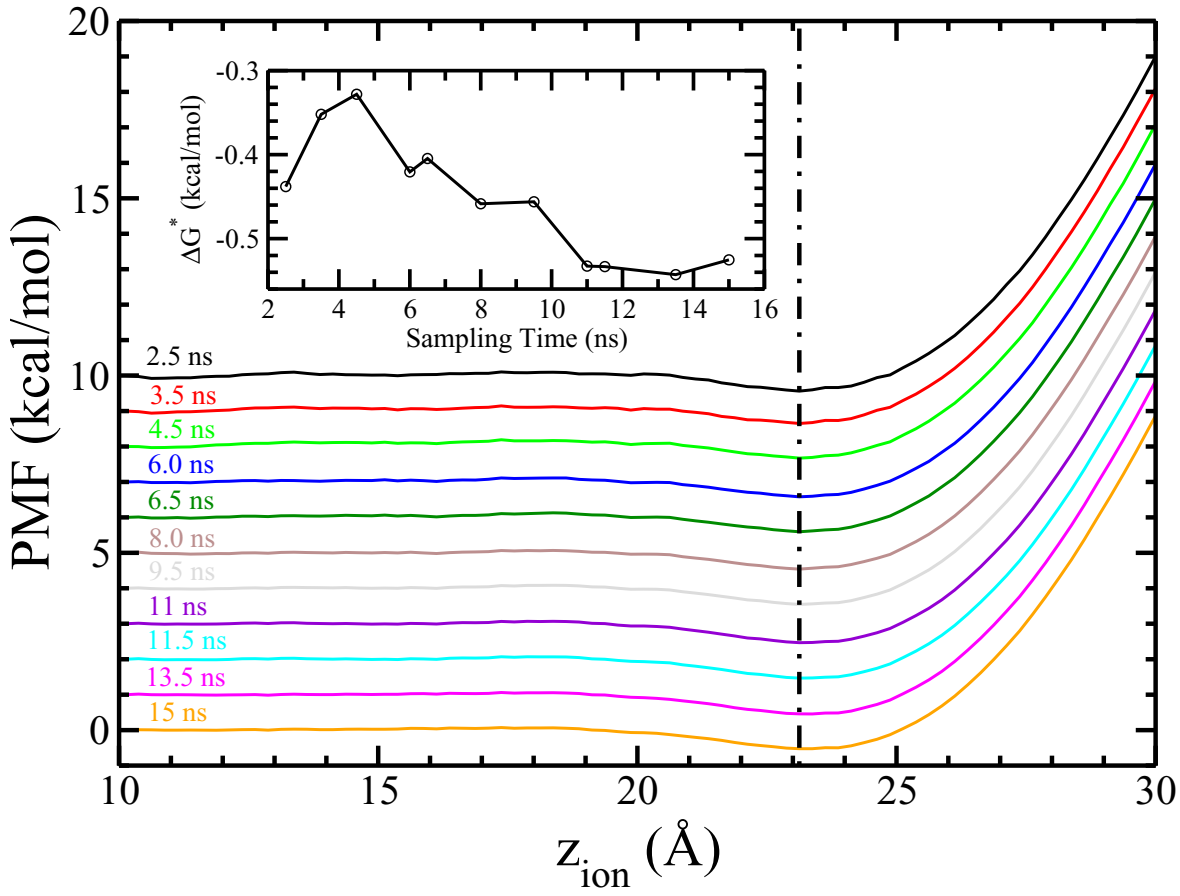

Figure 3.1: PMF computed with different amount of sampling time. The inset shows the PMF minima as a function of sampling time. Reproduced with permission from Shuching Ou, Yuan Hu, Hongbin Wan and Sandeep Patel. "Spherical Monovalent Ions at Aqueous Liquid-Vapor Interfaces: Interfacial Stability and Induced Interface Fluctuations." *Journal of Physical Chemistry B.* **2013**, *117 (39)*, 11732-11742. Copyright 2013 American Chemical Society.

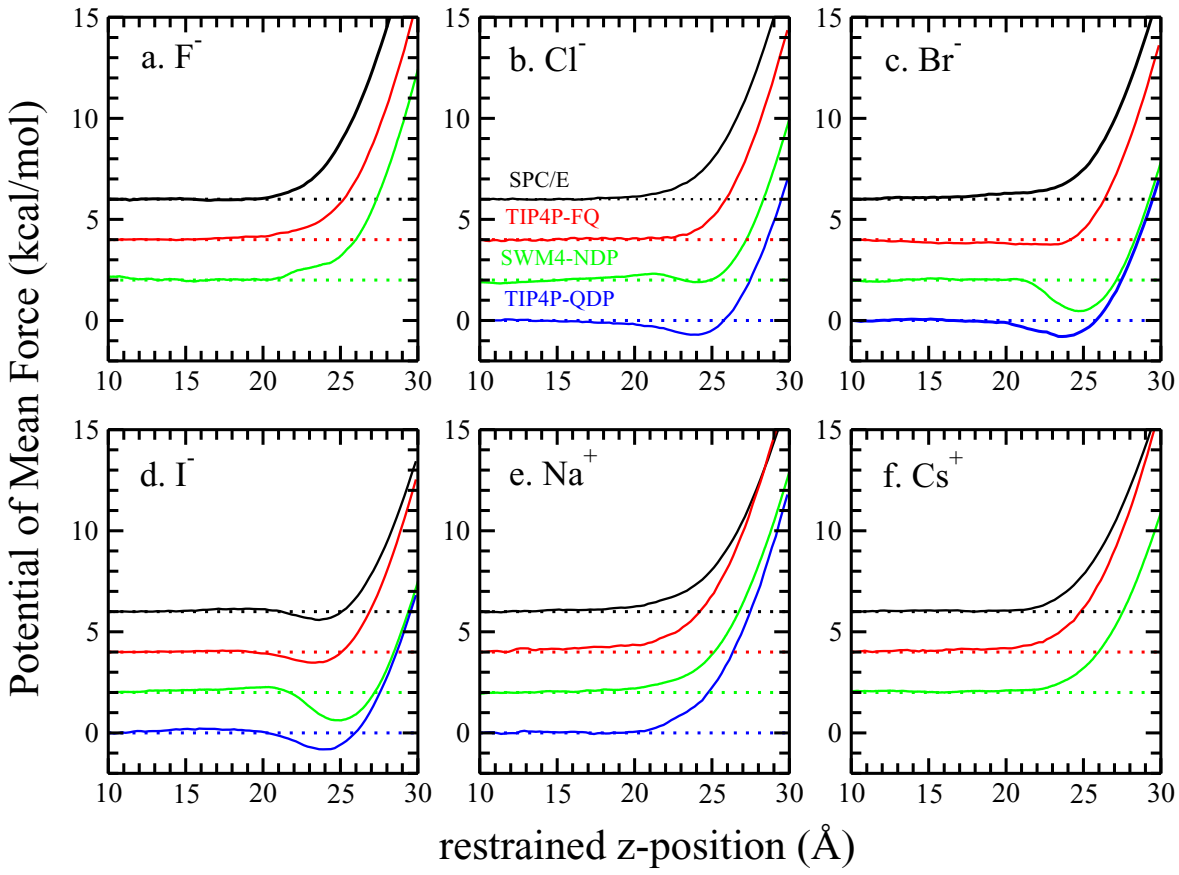

Figure 3.2: Potential of mean force for single ions transporting from bulk to vapor phase in different water force fields. A vertical offset of 2 kcal/mol is added for clarity. Reproduced with permission from Shuching Ou, Yuan Hu, Hongbin Wan and Sandeep Patel. "Spherical Monovalent Ions at Aqueous Liquid-Vapor Interfaces: Interfacial Stability and Induced Interface Fluctuations." *Journal of Physical Chemistry B.* **2013**, *117 (39)*, 11732-11742. Copyright 2013 American Chemical Society.

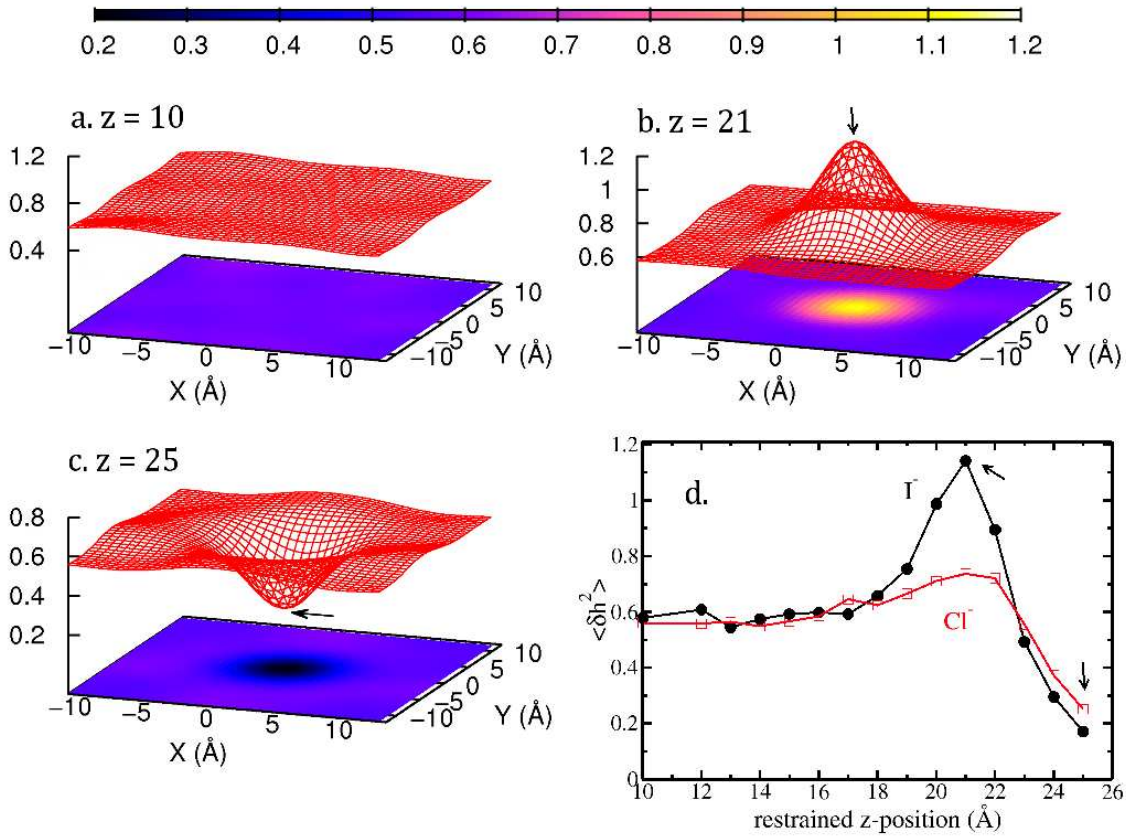

Figure 3.3: Average surface fluctuation $\langle \delta h^2 \rangle$ for I^- in TIP4P-FQ, when the restrained position is at (a) $z = 10$ Å (b) $z = 21$ Å (c) $z = 25$ Å. Panel d shows the $\langle \delta h^2(x = 0, y = 0) \rangle$ (right above/below the ion, as indicated with arrows) as a function of ion restrained position for I^- and Cl^- in TIP4P-FQ. The unit for fluctuations is $Å^2$. Reproduced with permission from Shuching Ou, Yuan Hu, Hongbin Wan and Sandeep Patel. "Spherical Monovalent Ions at Aqueous Liquid-Vapor Interfaces: Interfacial Stability and Induced Interface Fluctuations." *Journal of Physical Chemistry B.* **2013**, *117 (39)*, 11732-11742. Copyright 2013 American Chemical Society.

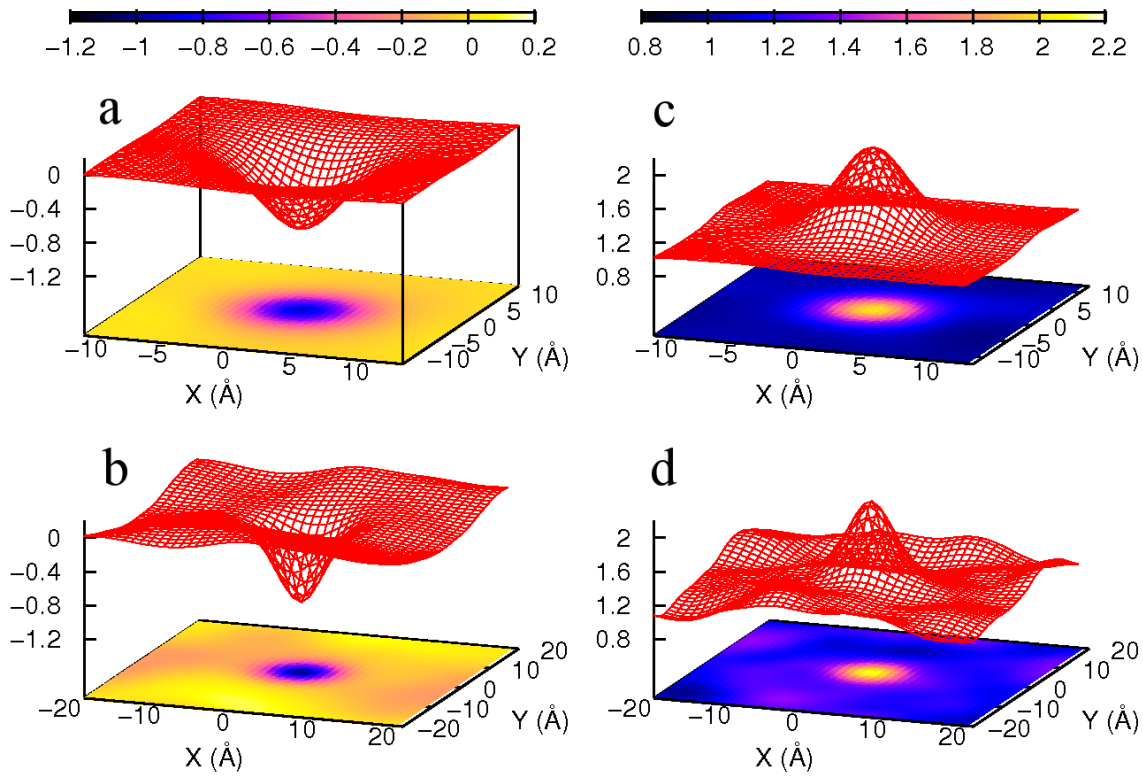

Figure 3.4: Mean surface of I^- restrained at 4 Å below GDS for (a) small (b) large simulation cell box. Normalized surface fluctuation at 4 Å below GDS for (c) small (d) large simulation cell box. For the small box, $L_x = L_y =$ 24 Å, yields inherent fluctuations of 0.56 $Å^2$; for the large box, $L_x = L_y$ = 40 Å, with the inherent fluctuation 0.96 $Å^2$. We stress that the analysis of relative enhancement of ion induced perturbations/fluctuations of the interface is not affected by the system size of the interface. Reproduced with permission from Shuching Ou, Yuan Hu, Hongbin Wan and Sandeep Patel. "Spherical Monovalent Ions at Aqueous Liquid-Vapor Interfaces: Interfacial Stability and Induced Interface Fluctuations." *Journal of Physical Chemistry B.* **2013**, *117 (39)*, 11732-11742. Copyright 2013 American Chemical Society.

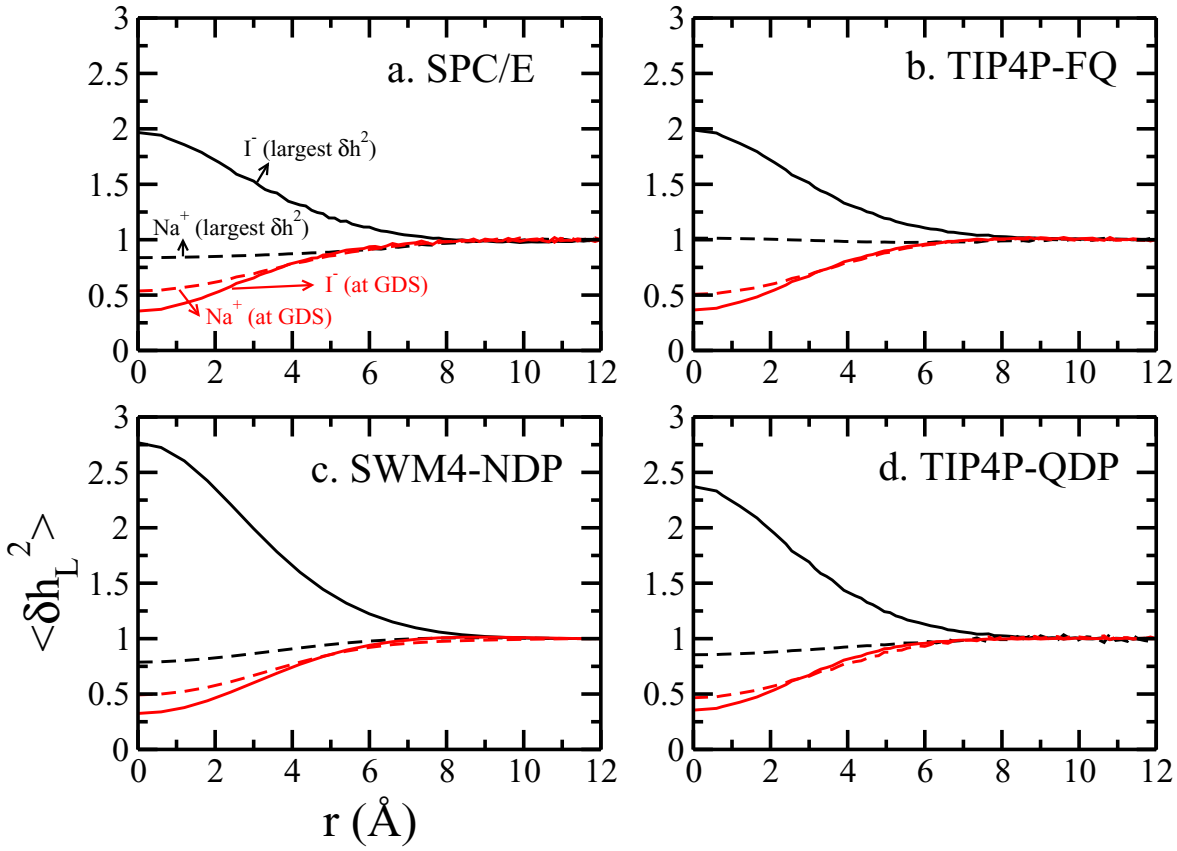

Figure 3.5: Normalized average surface fluctuation $\langle \delta h_{\mathrm{L}}^2 \rangle$ as a function of radius from the I^-/Na^+ in (a) SPC/E (b) TIP4P-FQ (c) SWM4-NDP (d) TIP4P-QDP force fields. Reproduced with permission from Shuching Ou, Yuan Hu, Hongbin Wan and Sandeep Patel. "Spherical Monovalent Ions at Aqueous Liquid-Vapor Interfaces: Interfacial Stability and Induced Interface Fluctuations." *Journal of Physical Chemistry B.* **2013**, *117 (39)*, 11732-11742. Copyright 2013 American Chemical Society.

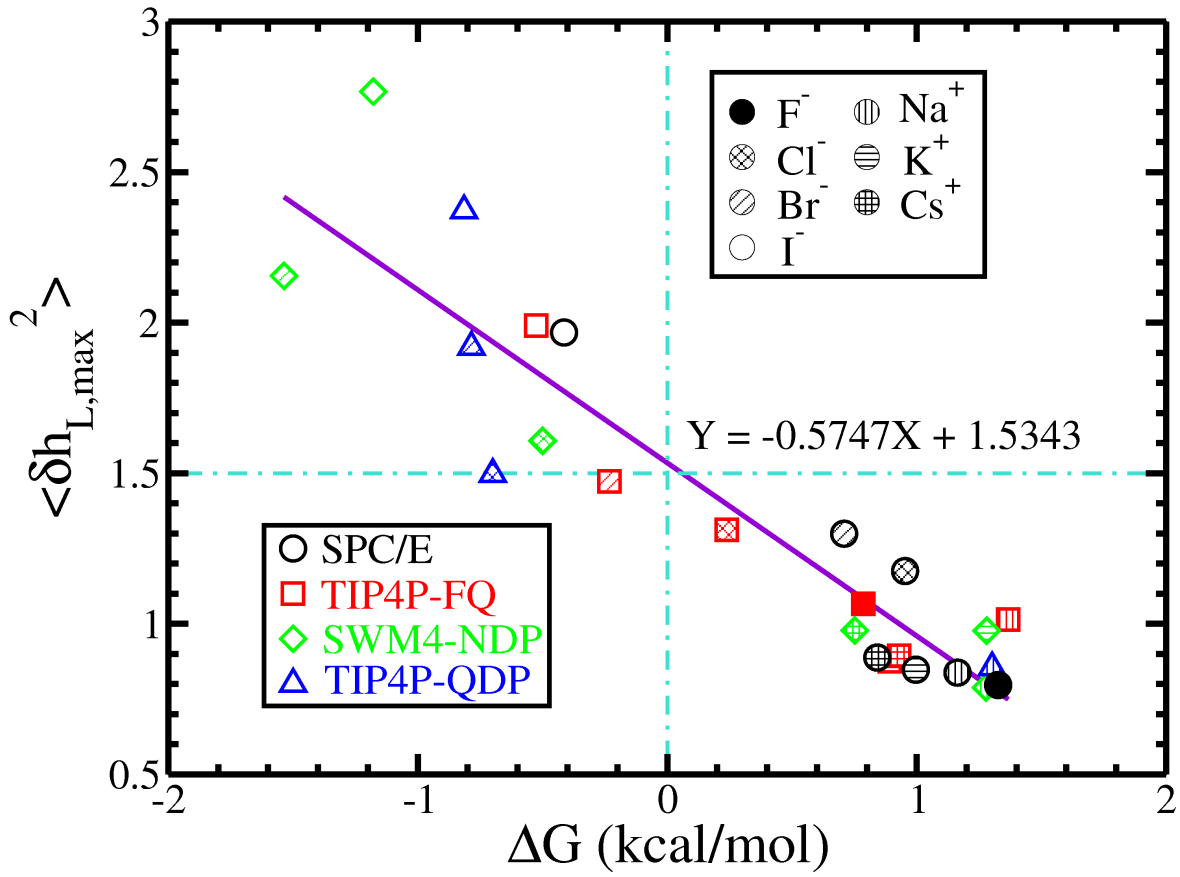

Figure 3.6: The largest normalized average surface fluctuation $\left\langle \delta h^2_{\mathrm{L,max}} \right\rangle$ versus the corresponding free energy ΔG for ions in different force fields. All cations, which are not found to be surface stable in our work, are located in the lower right quadrant of the graph. All surface stable species (anions described by certain force fields) are found in the upper left quadrant. Reproduced with permission from Shuching Ou, Yuan Hu, Hongbin Wan and Sandeep Patel. "Spherical Monovalent Ions at Aqueous Liquid-Vapor Interfaces: Interfacial Stability and Induced Interface Fluctuations." *Journal of Physical Chemistry B.* **2013**, *117 (39)*, 11732-11742. Copyright 2013 American Chemical Society.

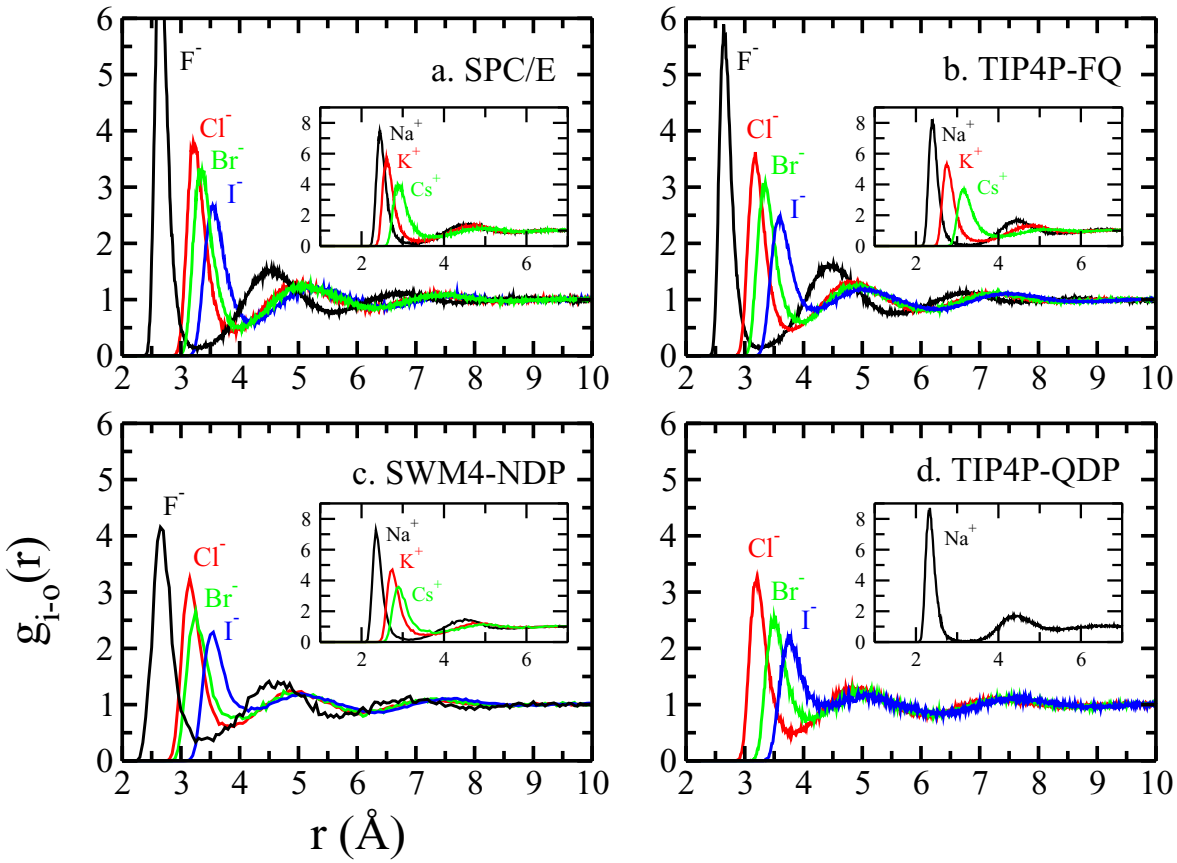

Figure 3.7: Ion-water radial distribution function (RDF) for anions in (a) SPC/E (b) TIP4P-FQ (c) SWM4-NDP (d) TIP4P-QDP force fields. The insets show the RDF of cations in the corresponding force field. Reproduced with permission from Shuching Ou, Yuan Hu, Hongbin Wan and Sandeep Patel. "Spherical Monovalent Ions at Aqueous Liquid-Vapor Interfaces: Interfacial Stability and Induced Interface Fluctuations." *Journal of Physical Chemistry B.* **2013**, *117 (39)*, 11732-11742. Copyright 2013 American Chemical Society.

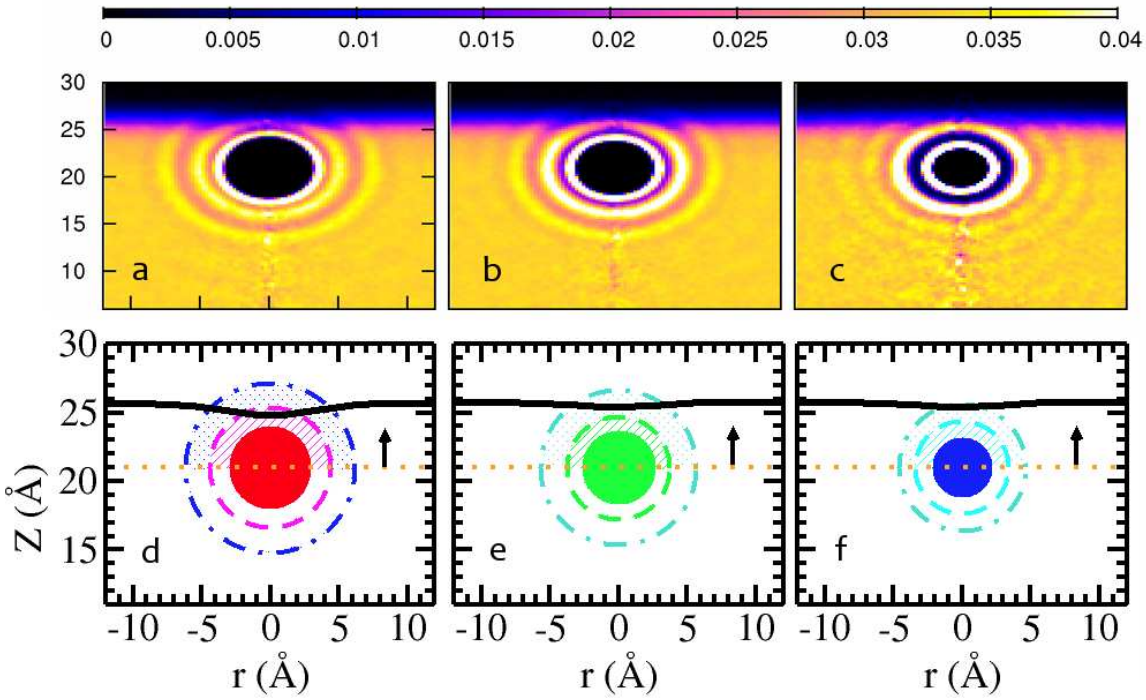

Figure 3.8: Average water oxygen density relative to (a) I^- (b) Cl^- (c) Na^+ at the position of 21.0 Å. (d)-(f) show the cartoon of ion with the cutoff of first solvation shell (dashed lines), second solvation shell (dot-dashed lines) and the calculated mean surface (solid black lines). For dynamical properties of water molecules in the shells of ions, we only study the water above the ion position (dotted lines). Reproduced with permission from Shuching Ou, Yuan Hu, Hongbin Wan and Sandeep Patel. "Spherical Monovalent Ions at Aqueous Liquid-Vapor Interfaces: Interfacial Stability and Induced Interface Fluctuations." *Journal of Physical Chemistry B.* **2013**, *117 (39)*, 11732-11742. Copyright 2013 American Chemical Society.

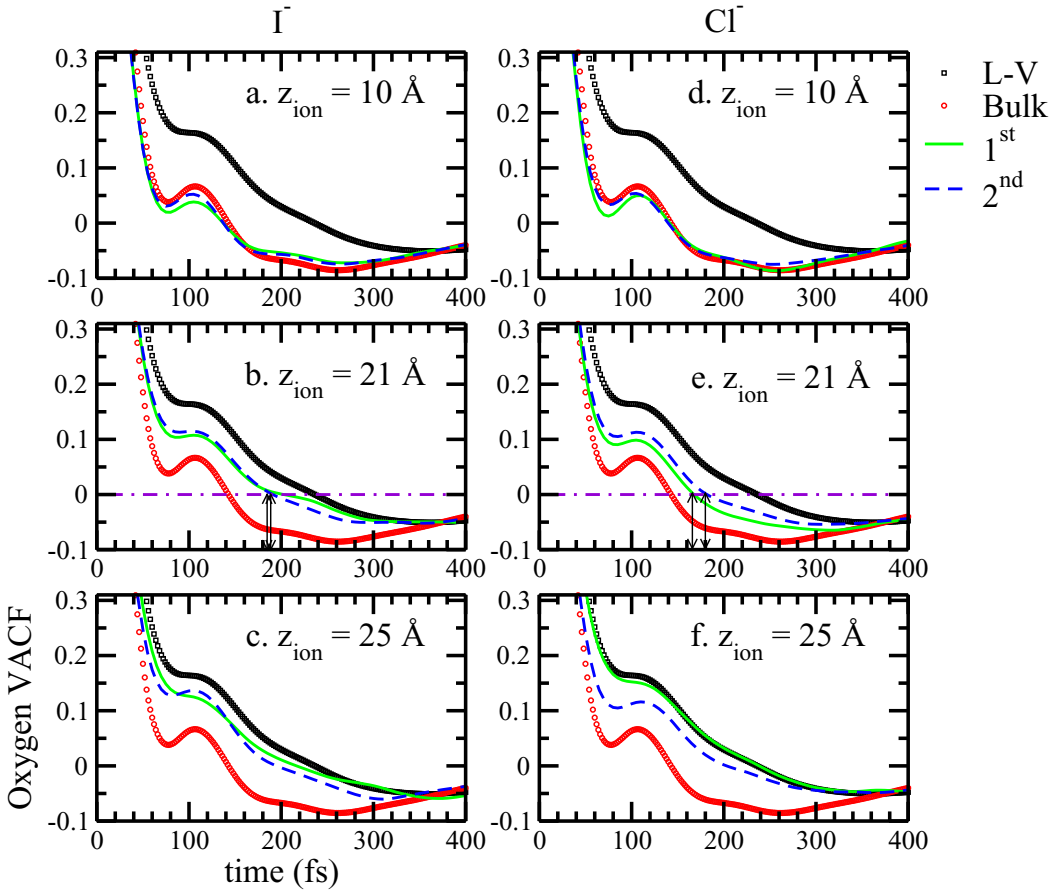

Figure 3.9: Oxygen velocity autocorrelation of water (TIP4P-FQ) in the bulk, near L-V interface, solvation shell water above I^-/Cl^-. Reproduced with permission from Shuching Ou, Yuan Hu, Hongbin Wan and Sandeep Patel. "Spherical Monovalent Ions at Aqueous Liquid-Vapor Interfaces: Interfacial Stability and Induced Interface Fluctuations." *Journal of Physical Chemistry B.* **2013**, *117 (39)*, 11732-11742. Copyright 2013 American Chemical Society.

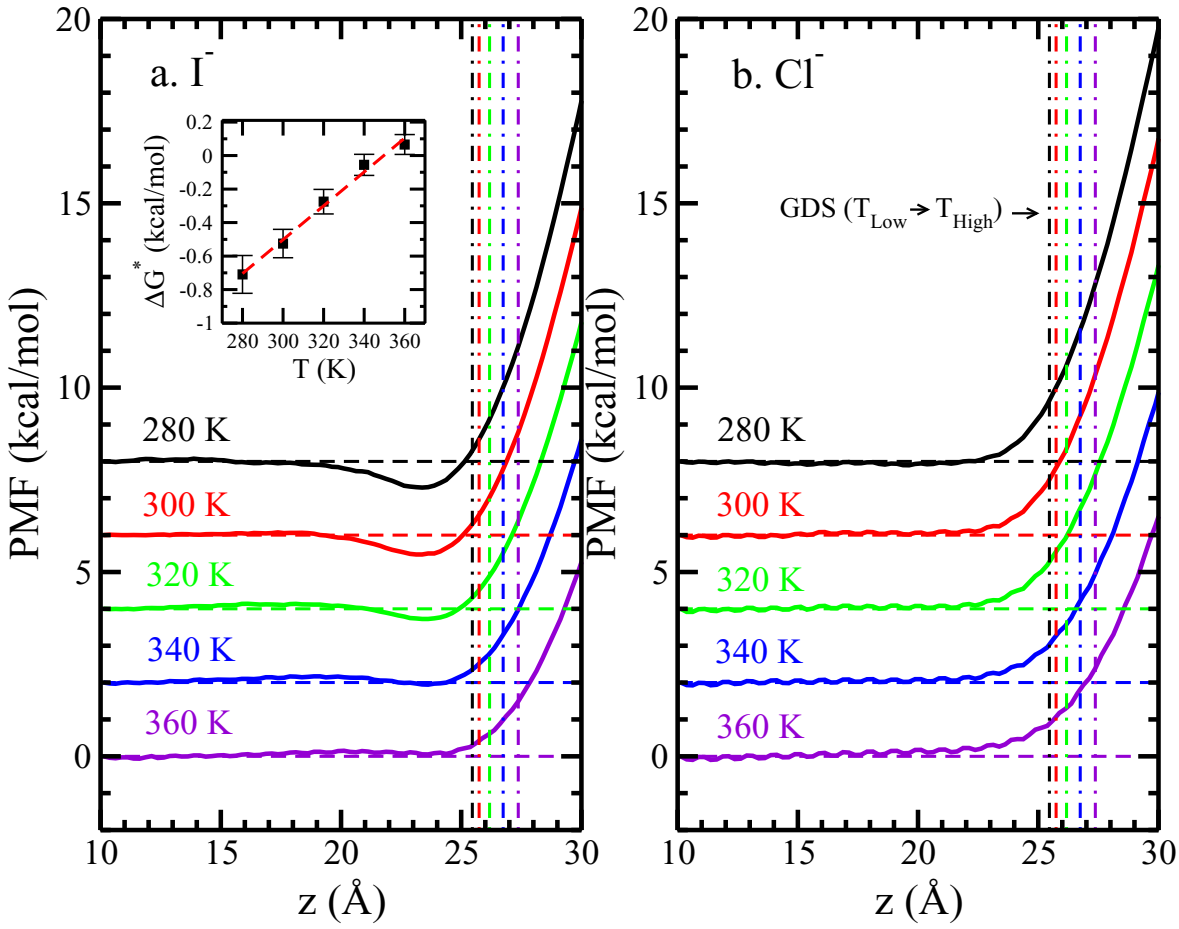

Figure 3.10: Potential of mean force for single (a) iodide and (b) chloride ions across the TIP4P-FQ LV-interface, relative to the value at $z = 10.0$ Å, which we consider sufficiently far away from the interface so as to represent bulk-like water region. Solid lines represent ions in TIP4P-FQ, a vertical offset of 2 kcal/mol is used to distinguish different temperature, each with a dashed horizontal line denoting zero. The inset shows the PMF minimum as the function of temperature for I^-. The dashed line indicates the linear fitting result, with slope = 0.01 and intercept = -3.53. Reproduced with permission from Shuching Ou and Sandeep Patel. "Temperature Dependence and Energetics of Single Ions at the Aqueous Liquid-Vapor Interface" *Journal of Physical Chemistry B.* **2013**, *117 (21)*, 6512-6523. Copyright 2013 American Chemical Society.

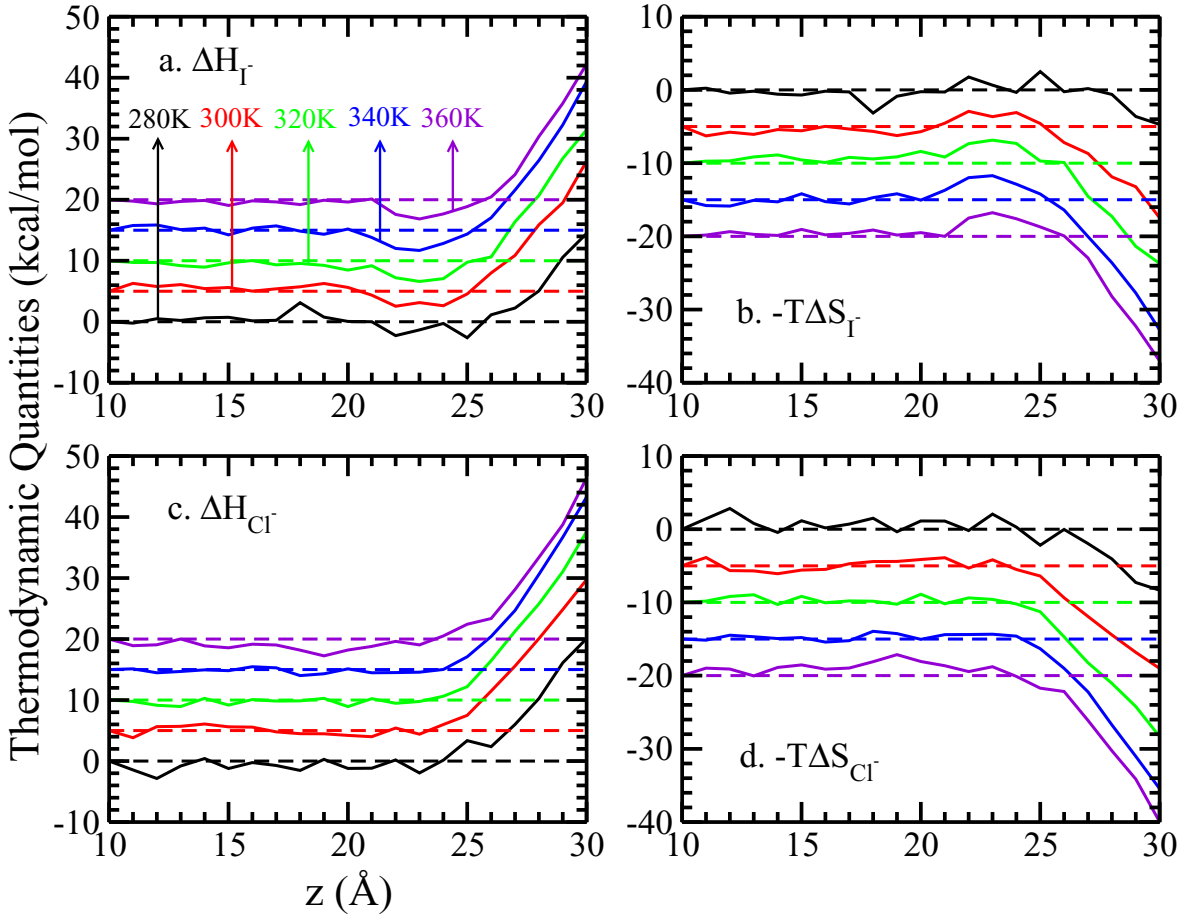

Figure 3.11: Decomposition of (a)(c) enthalpic and (b)(d) entropic contributions to the potential of mean force of single iodide and chloride ion crossing the TIP4P-FQ LV-interface, relative to the value at $z = 10.0$ Å. A vertical offset of 5 kcal/mol is used in panel (a) and (c), while in panel (b) and (d) the vertical offset is -5 kcal/mol, for clarity. Reproduced with permission from Shuching Ou and Sandeep Patel. "Temperature Dependence and Energetics of Single Ions at the Aqueous Liquid-Vapor Interface" *Journal of Physical Chemistry B.* **2013**, *117 (21)*, 6512-6523. Copyright 2013 American Chemical Society.

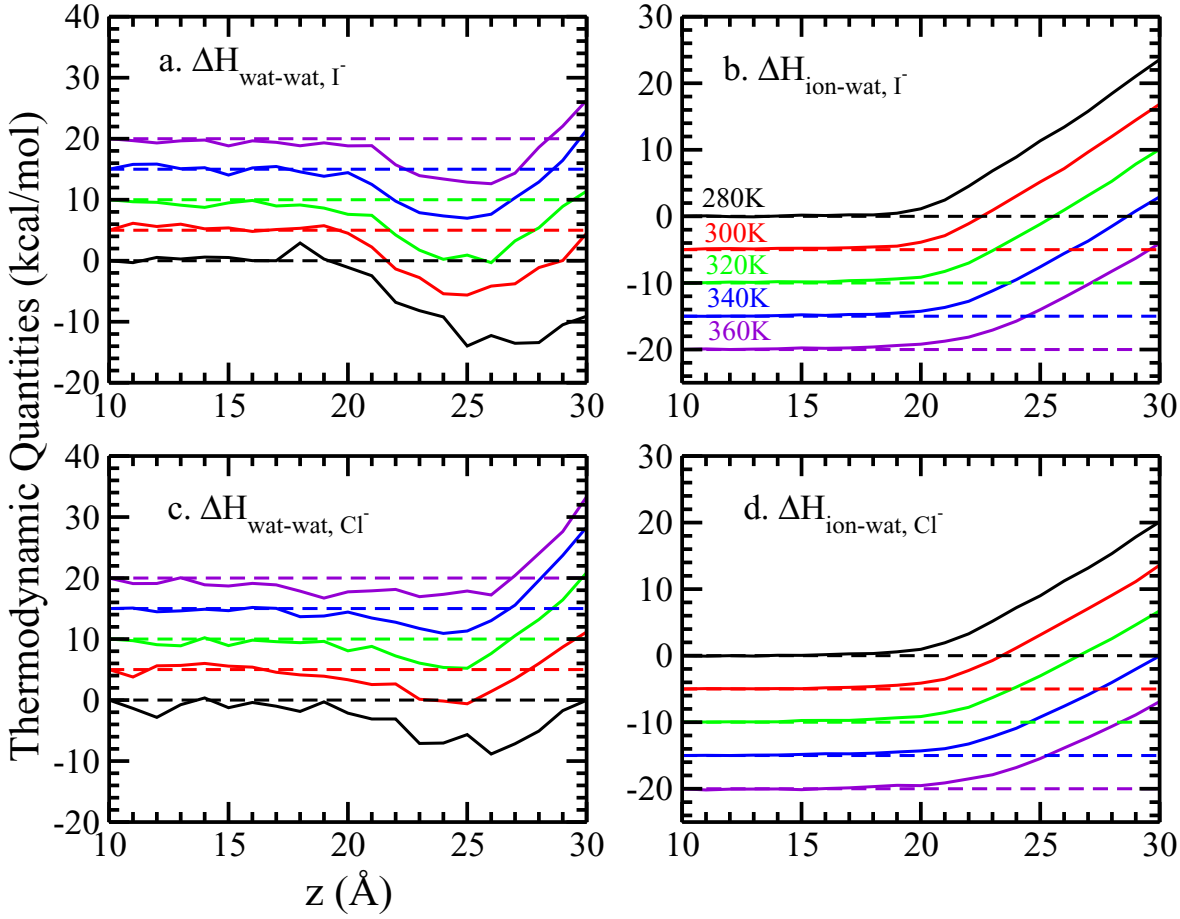

Figure 3.12: Decomposition of enthalpic contributions into (a)(c) water-water and (b)(d) ion-water interactions of single iodide and chloride ion crossing the TIP4P-FQ LV-interface, relative to the value at $z = 10.0$ Å. A vertical offset of 5 kcal/mol is used in panel (a) and (c), while in panel (b) and (d) the vertical offset is -5 kcal/mol, for clarity. Reproduced with permission from Shuching Ou and Sandeep Patel. "Temperature Dependence and Energetics of Single Ions at the Aqueous Liquid-Vapor Interface" *Journal of Physical Chemistry B.* **2013**, *117 (21)*, 6512-6523. Copyright 2013 American Chemical Society.

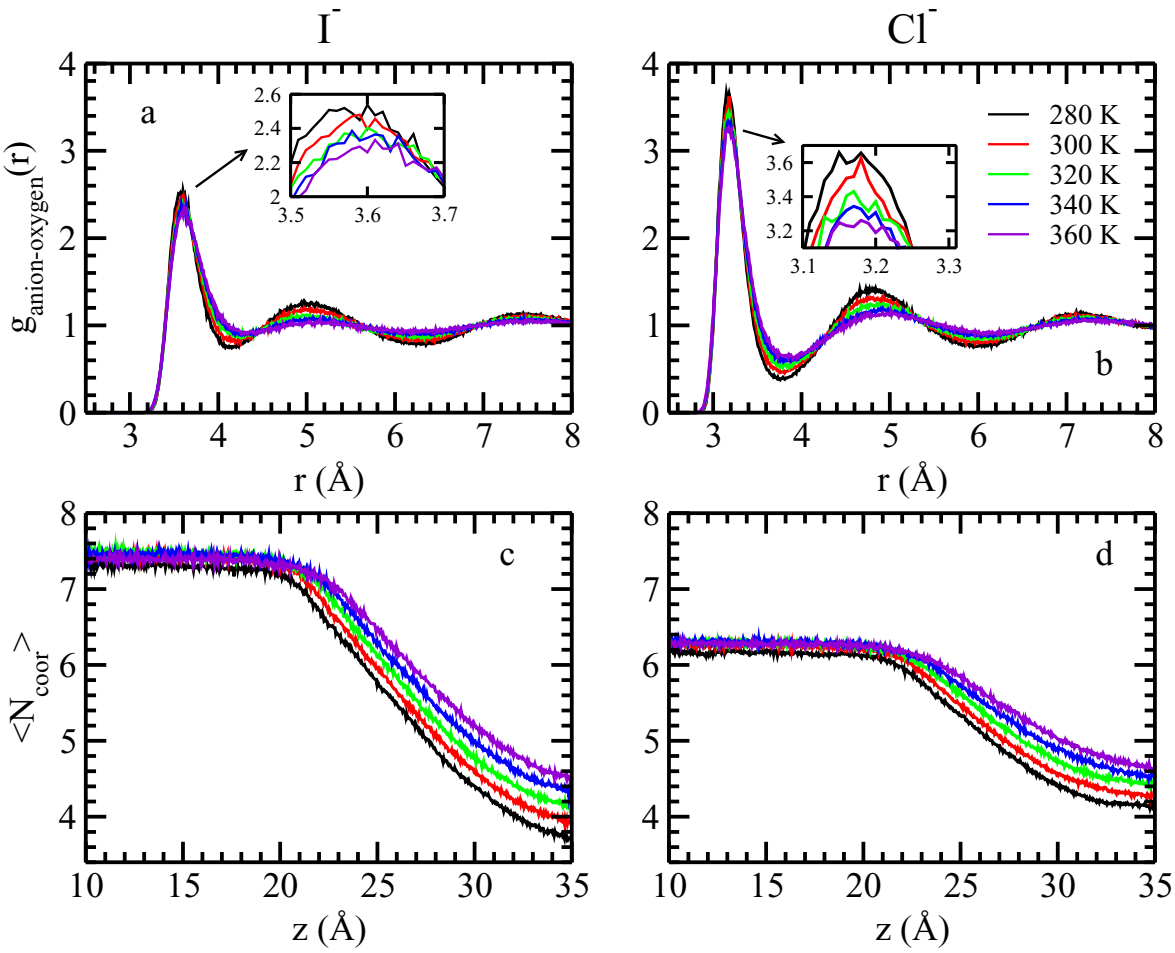

Figure 3.13: Anion-oxygen radial distribution function (RDF) for (a) I^- (b) Cl^- at different temperature. Average number of coordinated water for (c) I^- (d) Cl^- at different temperature. Reproduced with permission from Shuching Ou and Sandeep Patel. "Temperature Dependence and Energetics of Single Ions at the Aqueous Liquid-Vapor Interface" *Journal of Physical Chemistry B.* **2013**, *117 (21)*, 6512-6523. Copyright 2013 American Chemical Society.

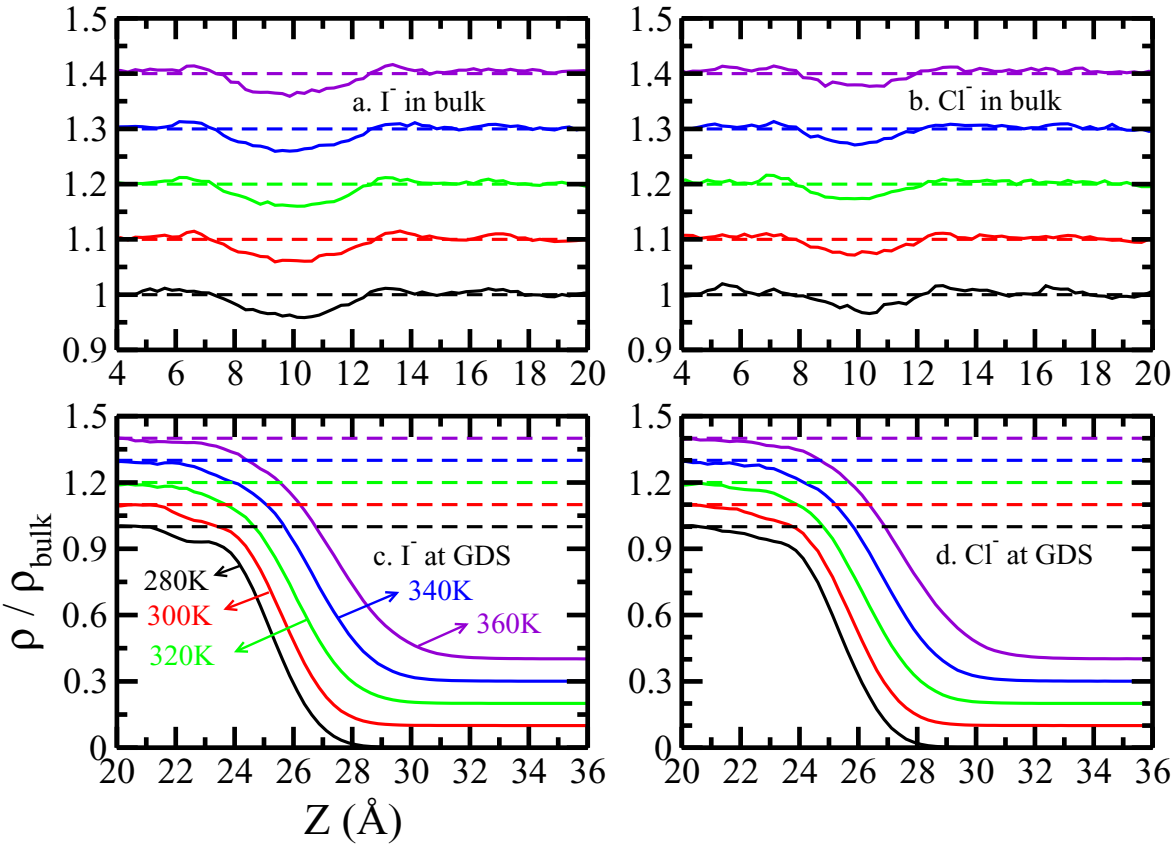

Figure 3.14: Density profile of water oxygen along z-dimension, when (a) I^- (b) Cl^- is in the bulk (z_{ion} = 10 Å). The lower panels show the density profile along when (c) I^- and (d) Cl^- is at GDS, which is pushed toward the vapor phase as the temperature increases. An offset of 0.1 is added for clarity. Reproduced with permission from Shuching Ou and Sandeep Patel. "Temperature Dependence and Energetics of Single Ions at the Aqueous Liquid-Vapor Interface" *Journal of Physical Chemistry B.* **2013**, *117 (21)*, 6512-6523. Copyright 2013 American Chemical Society.

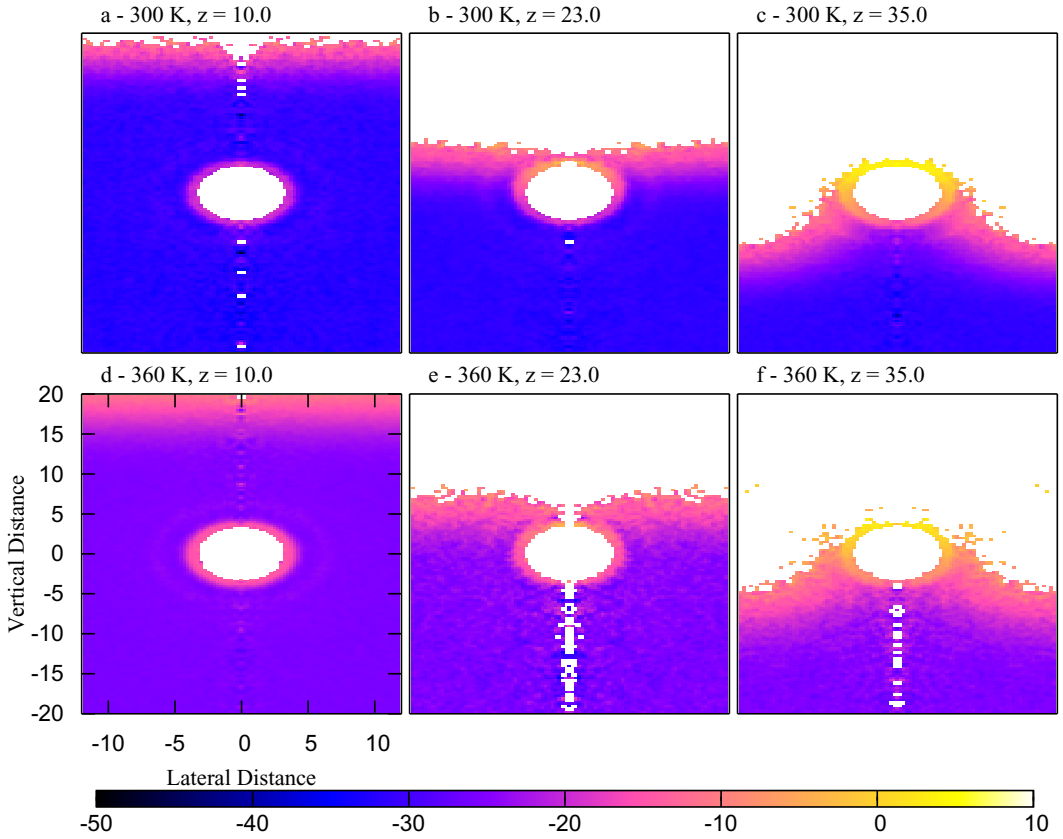

Figure 3.15: (a) Interaction energy between water molecule (at position (r, z) which is relative to the position of I^-) and all the other molecules. x-axis refers to the perpendicular distance from the ion, while y-axis indicates the vertical distance. Both units are in Å. The unit for energies is kcal/mol. Panel (b) and (c) show the similar profiles with ion restraining at 23 Å and 35 Å at 300 K. Panel (d)-(f) correspond to the case of I^- at 360 K. The unit for energy is kcal/mol. Reproduced with permission from Shuching Ou and Sandeep Patel. "Temperature Dependence and Energetics of Single Ions at the Aqueous Liquid-Vapor Interface" *Journal of Physical Chemistry B.* **2013**, *117 (21)*, 6512-6523. Copyright 2013 American Chemical Society.

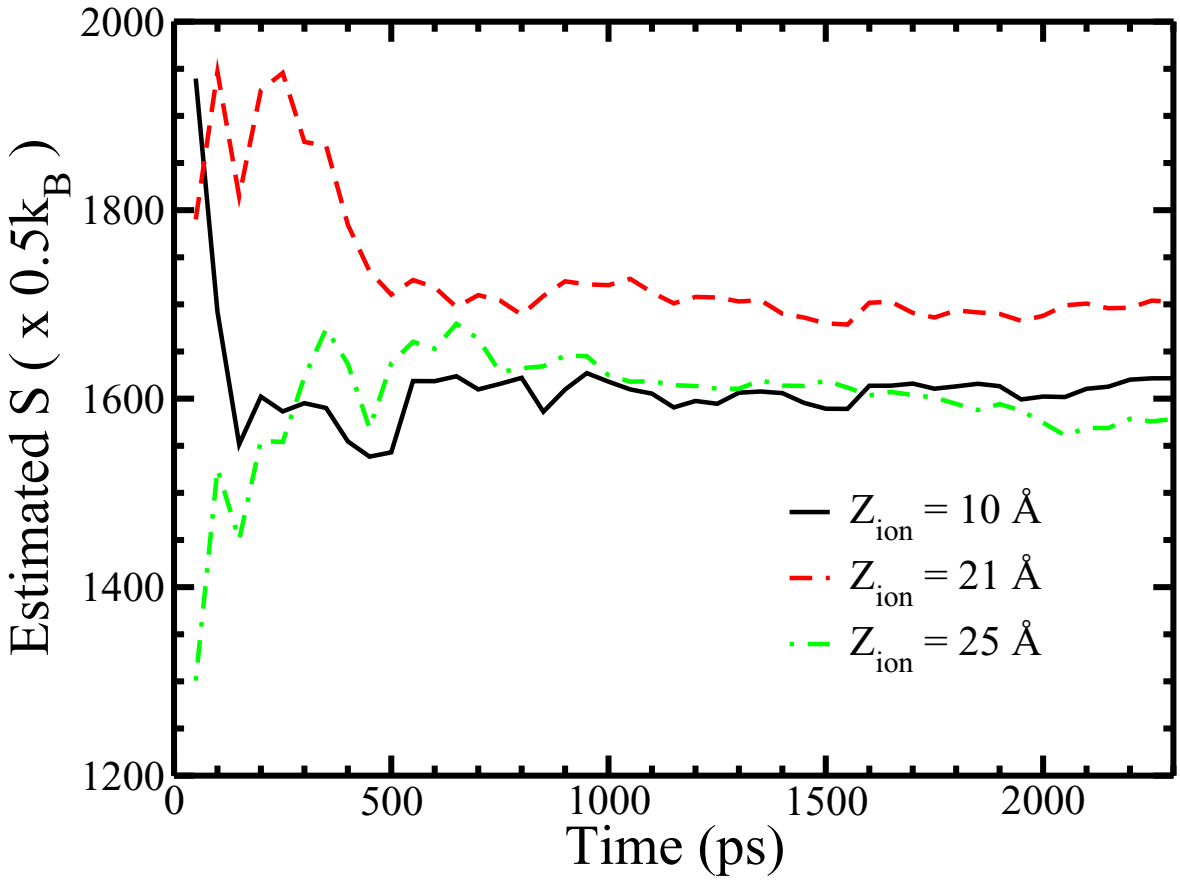

Figure 3.16: Time profile of the estimated entropy. Reproduced with permission from Shuching Ou and Sandeep Patel. "Temperature Dependence and Energetics of Single Ions at the Aqueous Liquid-Vapor Interface" *Journal of Physical Chemistry B.* **2013**, *117 (21)*, 6512-6523. Copyright 2013 American Chemical Society.

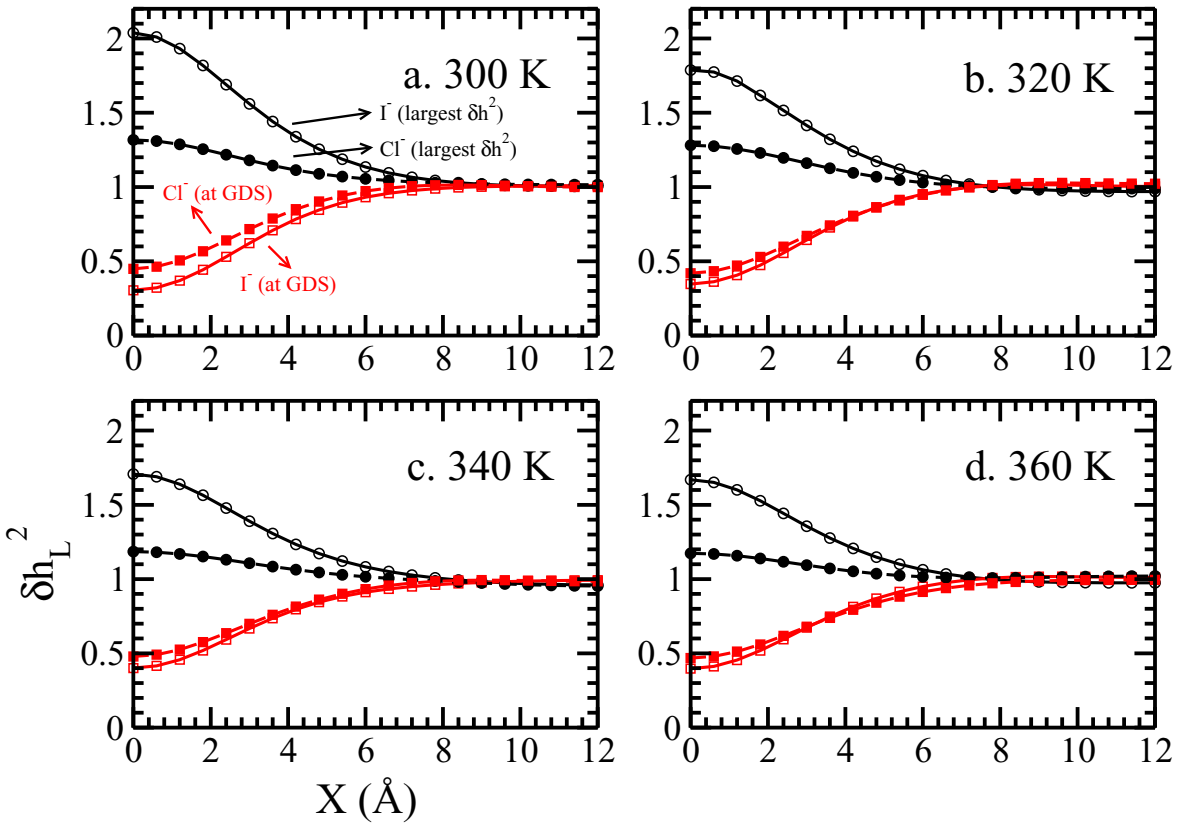

Figure 3.17: Normalized surface height fluctuations, as functions of lateral displacement, for ions at (a) 300 K (b) 320 K, (c) 340 K and (d) 360 K. Only the windows with largest δh_{L}^2 and the window of GDS are shown here. Reproduced with permission from Shuching Ou and Sandeep Patel. "Temperature Dependence and Energetics of Single Ions at the Aqueous Liquid-Vapor Interface" *Journal of Physical Chemistry B.* **2013**, *117 (21)*, 6512-6523. Copyright 2013 American Chemical Society.

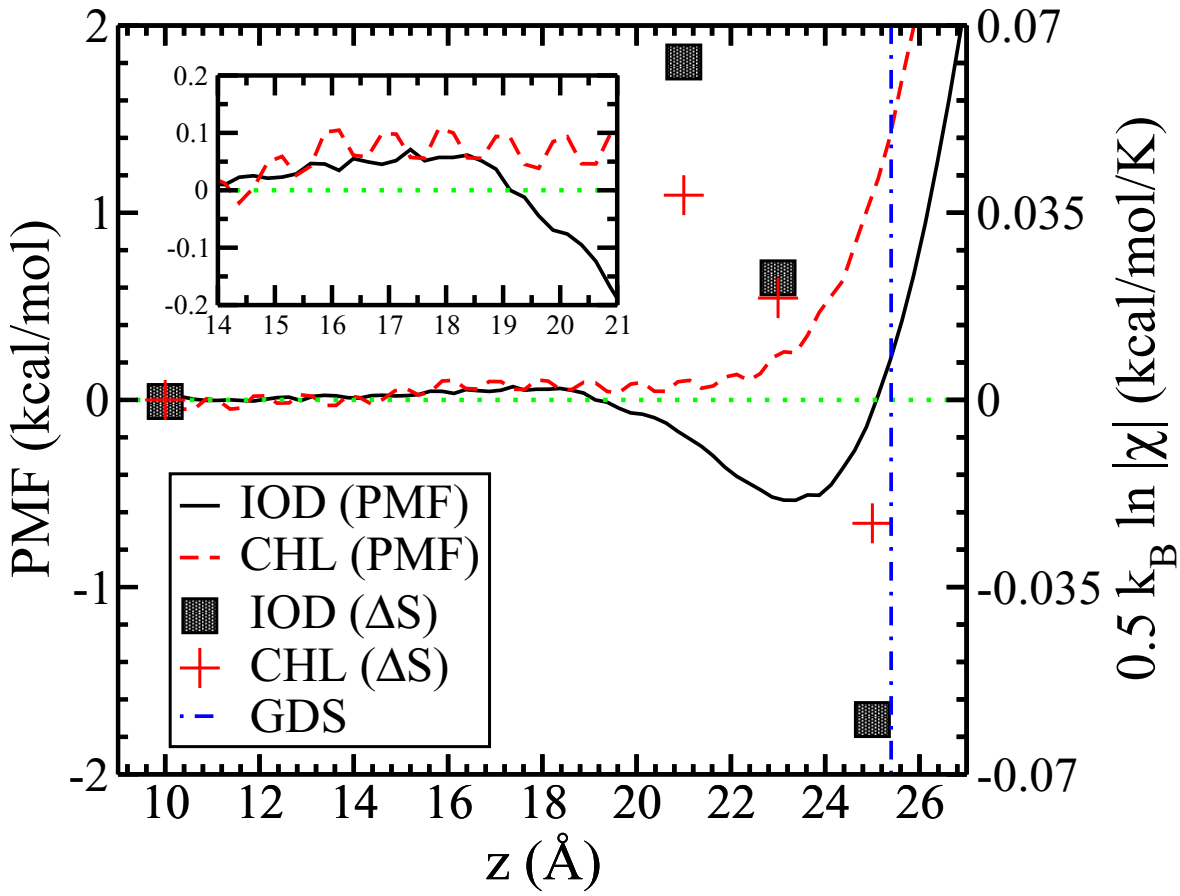

Figure 3.18: Potentials of mean force (PMF's) for I^- and Cl^- in TIP4P-FQ. Inset shows the region of ion positions from $z = 14.0$ to 21.0 Å. Symbols are semi-quantitative estimates of surface entropy (relative to bulk, hence ΔS) arising from ion-induced interfacial fluctuations using $S = constant + \frac{k_B}{2} \ln |\chi|$ where χ is the surface height function covariance matrix whose elements are $\chi(\mathbf{r}_i, \mathbf{r}_j) = \langle \delta h(\mathbf{r}_i) \delta h(\mathbf{r}_j) \rangle$. Finally, $\delta h(\mathbf{r}_i) = h(\mathbf{r}_i) - \langle h(\mathbf{r}_i) \rangle$. Reproduced with permission from Shuching Ou, Yuan Hu, Hongbin Wan and Sandeep Patel. "Spherical Monovalent Ions at Aqueous Liquid-Vapor Interfaces: Interfacial Stability and Induced Interface Fluctuations." *Journal of Physical Chemistry B.* **2013**, *117 (39)*, 11732-11742. Copyright 2013 American Chemical Society.

Chapter 4

MOLECULAR ION AT THE LIQUID-VAPOR INTERFACE

4.1 Introduction: Protein Denaturant

Specific-ion effects are relevant to a vast spectrum of biological and physical processes. The search for unifying and predictive theoretical foundations for describing a broad spectrum of specific-ion effects continues to garner significant scientific attention. These range from the differential stabilities of proteins in solution mediated by different ions, to interfacial propensities of inorganic halide ions to various interfaces, to modulation of aggregation kinetics of nanomaterials [112, 23, 103, 70, 113, 69, 114, 115, 116, 117, 118, 119, 120, 121, 122, 123, 124, 125, 286]. The effects are distributed across monovalent (simple) to molecular ions as well. As such, the need for a unifying picture is clear. One particular specific-ion effect involves the effects of osmolytes and co-solvents in modulating the stability of folded versus unfolded states of proteins [287, 288, 289]. In particular, guanidinium chloride (as well as urea) is a well-known protein chemical denaturant [287, 288, 289, 290, 291, 292, 68, 293]. Investigations into the mechanism of guanidinium's (Gdm^+) influence on protein stability have enjoyed a long history, though questions of mechanism still remain [294].

Focusing on a series of molecular simulations studies of interaction of guanidinium with hydrophobic systems, we draw attention to the very specific orientation adopted by the osmolyte when interacting with the model solutes in these studies [295, 286, 287, 296]; they demonstrate that guanidinium moieties orient in a parallel manner in the region next to hydrophobic surfaces. This has implications for the association of guanidinium with hydrophobic and planar, pi-electron rich sidechains of proteins. Intriguingly, the orientation of the guanidinium is parallel to the hydrophobic surface, vis-a-vis, the protein sidechain-solution interface. This orientation has

been rationalized as arising from its ability to optimize the overall hydration properties of the complex (i.e. peptide-guanidinium), i.e., the flat faces of guanidinium ions are locally water-depleted [287, 288], hence facilitate hydrophobic stacking of pairs of cations [286]. This is somehow different with another common denaturant, urea, which is found to be more likely to aggregate into nanosized clumps [297, 286]. Though controversies about the interaction of guanidinium with backbone moieties or sidechains, dispersion versus electrostatic interactions driving these associations, have abounded in the literature, the structural association with guanidinium (at least from a simulation perspective) appears quite general. Since the influence of co-solvents or osmolytes must occur through/at an interface, we consider investigations of interfacial properties involving these chemical components a relevant area of focus. Furthermore, since hydrophobic moieties are often implicated in discussions of the association of the guanidinium cation with peptide or peptide-like solutes, we here consider a much simpler interface, the aqueous air-water interface, as a proxy to a chemically defined hydrophobic interface. Consequently, a fundamental question we seek to address in this chapter concerns the relationship of the orientation of the guanidinium cation to its influence on interfacial properties in the context of how this effect mediates the observed nature of association of guanidinium with a molecular surface/interface.

In the previous chapter, we studied the relation between interfacial stability of spherical monovalent ions and induced interfacial fluctuations at model liquid-vapor interfaces. Species with interfacial stability tend on average to induce higher interfacial fluctuations. Moreover, the differing propensities of various ions to induce varying degrees of interfacial fluctuations is shown to be related to the local solvation environment of the ion and how this local environment couples to solvent further away from the ion. It is this coupling that is critical in the facilitating fluctuations. This leads to the question of whether this effect can be observed for the guanidinium species already mentioned, and further, if this effect depends on the orientation of the molecule relative to the interface. A novel aspect of this study is the analysis of induced interfacial fluctuations and their orientational dependence.

We consider several aspects related to aqueous solution liquid-vapor interfaces of guanidinium, Gdm^+, and methyl guanidinium, M-Gdm^+ (an amino acid analogue), interfaces of varying concentrations. We consider structural and thermodynamic aspects as considered in earlier studies using varying force fields, aiming to draw comparisons and contrasts in current modeling approaches to these systems. We further characterize the thermodynamics of the interface by computing potentials of mean force describing system free energetics as it depends on the location of a single Gdm^+/M-Gdm^+ (infinite dilution limit) from the liquid-vapor interface. Computational experiments measuring the reversible work (PMF) for transferring single ions/molecules from bulk aqueous environment to the aqueous solution liquid-vapor interface have enjoyed a long history as a means to explore the origins of surface stability [10, 107, 15]. To this end, we also anticipate insights into the details of interfacial stability (or lack of) based on PMF calculations. We further probe the influence of the molecular ions on interfacial fluctuations, again restricting our attention to the infinite dilution limit of a single ion in solution. It has been shown for the case of spherically symmetric ions that the magnitude of aqueous interfacial fluctuations is intimately related to the nature of the solute species [93, 92, 19], its interfacial stability, and hydration. In this study, we examine the interconnections between surface stability, hydration, and orientation of molecular ions as they impact on interfacial fluctuations and how these may be of relevance to a variety of osmolyte-mediated protein stability effects in biomacromolecular systems.

4.2 Method

In this chapter we use the charge equilibration (CHEQ) polarizable force field for guanidinium (Gdm^+), methyl guanidinium (M-Gdm^+) cations and TIP4P-FQ water model. We start with guanidinium chloride, methyl guanidinium chloride aqueous solution at different concentration as to verify the force field in modeling the molecular cations. This includes the comparison of the calculated surface excess, surface tension, and the Kirkwood-Buff analysis with the experiments. Then we use this force field to study the free energetics of transferring single Gdm^+/M-Gdm^+ from solvent bulk to

vapor phase.

4.2.1 Simulation Protocol

Molecular dynamics simulations were performed using the CHARMM package [148]. Simulations of liquid-vapor interfaces were performed in the NVT ensemble. Temperature was maintained at T=300 K using Nosé-Hoover thermostat [260] with a thermal piston mass of 50 kcal/mol $\cdot$ ps^2. The system contained 38, 71, 107, 142 or 190 pairs of guanidinium (or methyl guanidinium) and chloride ions, with 1977 water molecules (represented by the polarizable TIP4P-FQ model [262]) per unit cell, which resulted in molal concentration of 1.1, 2, 3, 4, 5.3 m, respectively. The simulation cell was rectangular with dimensions 40 Å $\times$ 40 Å $\times$ 150 Å, in which z is the direction normal to the liquid-vapor interface. Long-range electrostatics were accounted for by Particle mesh Ewald (PME) summation [137, 139] with a 40 $\times$ 40 $\times$ 150 Å^3 Fast Fourier transform (FFT) grid, sixth order B-spline interpolation, and screening parameter $\kappa = 0.33$. Dynamics were propagated using the Leapfrog Verlet integrator [298] with a 0.5 fs time step. The actual position of Gibbs Dividing Surface (GDS) at corresponding concentration, which is determined by half of bulk water oxygen density, is summarized in Table 4.2. Four different replicates were used and the first 1 ns of each replicate was considered as equilibration. At least 15 ns of production run for each replicate was used to compute properties such as density profiles and surface tensions.

Moreover, in order to illustrate the molecular detail and free energetics of Gdm$^+$/M-Gdm$^+$ with the presence of L-V interfaces, we simulated a system with 1977 TIP4P-FQ water molecules and single Gdm$^+$/M-Gdm$^+$, with the corresponding GDS around $\pm$ 18 Å from the center of water box. For potential of mean force calculations, our order parameter, ξ_0, is the Cartesian z-component of the separation between the water slab center of mass and Gdm$^+$/M-Gdm$^+$ center of mass; with this collective variable definition, no corrections for Jacobian or Leibniz transformations are required [221]. In all simulations used for computing potentials of mean force, Gdm$^+$/M-Gdm$^+$ were restrained to z-positions from 0 Å to 30 Å relative to the water slab center of mass using

a harmonic potential $U_{\text{restraint}}(z; z_{\text{relative,ref}}) = \frac{1}{2}k_{\text{restraint}}(z - z_{\text{relative,ref}})^2$ with the force constant of 4 (kcal/mol)/Å^2; this encompasses a range approximately 18 Å below the GDS to approximately 12 Å above it at 300 K. Again, the first 1 ns for each restraining window was considered as equilibration; the following 20 ns of data for each umbrella sampling window was used to compute the properties of single Gdm^+/M-Gdm^+. The PMF is computed using WHAM [225] and is defined to be zero in the bulk (which is determined by the window $z = 0$ Å), as presented in Figure 4.4a . The uncertainties in potentials of mean force are determined using the approach of Zhu and Hummer [278]:

$$\text{var}[G(\xi_{\text{N}})] \approx \sum_{i=1}^{N} \text{var}[K\Delta\xi\bar{z}_{\text{i}}] \tag{4.1}$$

where $\bar{z}_{\text{i}}$ is the mean position of z in the i_{th} window, which can be obtained from block averages [279]. The corresponding standard deviation $\sigma[G(\xi_{\text{N}})]$ is then the square root of var$[G(\xi_{\text{N}})]$. In our case, $G(z = 0 \text{ Å}) = 0$, therefore the window $z = 30$ Å is expected to have the largest uncertainty. The largest uncertainties for the systems are approximately 0.1 kcal/mol.

The charge equilibration (CHEQ) polarizable force field model for guanidinium and methyl guanidinium (M-Gdm^+) cations was constructed by adapting the CHARMM CHEQ force field for proteins [163, 299], extending the electrostatic parameters, hardnesses and electronegativities from the protein force field for an arginine side chain. In the present work, the methyl guanidinium was partitioned into two charge normalization units (charge conserved with this unit) to control polarizability scaling [247, 142]. The first unit encompasses the methyl (-CH_3) and secondary amine (-NH) groups while the second unit includes the central carbon and two primary amine groups (-$C(NH_2)_2$). For the force field of guanidinium cation (Gdm^+) we use the same analogue with M-Gdm^+ by replacing the methyl and secondary amine groups with another -NH_2 group, consider the whole cation as one unit. This partitioning allows for consistency with the existing CHARMM CHEQ protein force field and permits use of the existing non-bond (LJ and electrostatic) parameters for arginine from the polarizable force field [163, 299]. The force field parameters for guanidinium chloride and methyl guanidinium chloride

are summarized in Table 4.1. In Reference [247], validation of the present force field was presented in terms of interactions of the guanidinium group with water relative to predictions from ab initio calculations at the MP2 correlated level, as well as hydration free energies of methyl guanidinium compared with previous simulation and experimental estimate data.

The non-bond interactions between M-Gdm^+ and solvent species (water and chloride), were validated through the comparison of gas-phase small molecule geometries and interaction energies calculated using the CHEQ force field with those calculated using MP2/aug-cc-pVTZ level quantum mechanics [247]. In the absence of laborious reparameterization of the methyl guanidinium interactions with all system species, we consider it sufficient that for the purposes of the present work, the trend of relative interaction strengths based on QM and force field calculations are equivalent. Cl^- is treated as a non-polarizable Lennard-Jones sphere. The force field combination with water has been validated via calculation of single ion hydration free energies of both ions using accepted free energy methods in conjunction with appropriate corrections for condensed-phase simulation artifacts [271, 272, 273].

Charge degrees of freedom for the TIP4P-FQ water molecules and Gdm^+/M-Gdm^+ were coupled to a thermostat at 1K using the Nosé-Hoover method [300, 260]. Charge degrees of freedom were assigned fictitious masses of 0.000069 and 0.000099 kcal mol^{-1} ps^2 e^{-2}. The charge degrees of freedom were propagated in an extended Lagrangian formalism [262]. Each water molecule was taken as a charge normalization unit. No charge transfers between water molecules or between water and Gdm^+/M-Gdm^+.

4.2.2 Validation

In this section, we will compare some of the properties of the present force field with the experiments or previous studies. As will be apparent from the discussion of results below, the predictions of the present force field show rather strong consistency with previous force fields studying similar systems [296].

For the osmolyte solutions, we considered number density profiles of the center carbon of Gdm^+/M-Gdm^+, Cl^- and water oxygen along the z-dimension, normal to the L-V interface, as shown in Figure 4.1. The profiles are calculated by averaging over two equivalent halves of the slab, normalized by the density values at the center of the slab; the GDS is taken to be the zero and negative x-axis values indicate movement into the bulk solution and positive values movement towards the vacuum. The position of GDS is determined by the z-position where the water density is one-half of the bulk value for the corresponding system, as listed in Table 4.2. Solid curves represent data for the M-Gdm^+ system, dashed curves for the Gdm^+. Statistical uncertainties are less than 0.3% determined from the variance of 4 independent replicates. The water oxygen density profiles show little change as a function of cation concentration; in the case of Gdm^+, there is a slight shift of the GDS to larger value, correlating with the expansion of the Gdm^+ density at higher concentration (Figure 4.1a, b). Furthermore, a density fluctuation feature emerges in the 5.3 m Gdm^+ system; this is explained by the higher Gdm^+ density at higher concentrations. Figure 4.1 c and d show variation of M-Gdm^+ and Gdm^+ at 1.1 m and 5.3 m concentrations, respectively. At low concentrations, 1.1m, we observe no apparent interfacial enhancement of either cation. For the 1.1 m systems, due to its hydrophobic methyl group, the M-Gdm^+ solution populates configurations where the cation is closer to the GDS. The Gdm^+, relative to the M-Gdm^+ is substantially more depleted in the region of and just below the GDS, with an associated elevated density in the next layer towards the bulk. At the higher 5.3 m concentration, electrostatic interactions between charged cations lead to higher Gdm^+ density in the region of the GDS. The M-Gdm^+ density profile shows an oscillatory behavior, with enhancement relative to the bulk value below the GDS. Thus, in both systems, we observe increased population of the interfacial region by both cations, with the more hydrophobic M-Gdm^+ consistently showing greater propensity for the interface. The Cl^- anion in both solutions at both concentrations correlates with the density profiles of the cations. In contrast to the density profiles shown in Reference [296], we do not observe a shoulder (representing orientations of

the guanidinium ring that are parallel to the interface) in the Gdm^+ density profile below the GDS. This suggests that if multiple orientations are viable at the interface under the force fields we use, then there may be little difference in relative stabilities of the parallel and perpendicular orientations relative to the bulk. We will turn to free energetics of the two orientations in the following section. We stress that the lack of a shoulder in the present Gdm^+ density profiles (in contrast to those in Reference [296]) does not suggest the absence of a difference in stabilities (relative probabilities) of the two orientations, merely a difference in the degree of stability of one or both relative to the state where the cation is in the bulk.

The surface tension of a liquid arises from the imbalance of intermolecular forces at the surface of a liquid-vapor interface. We calculate the surface tension for the liquid-vapor interface at each concentration from the average difference in the normal and tangential elements of the internal pressure tensor [230], which is

$$\gamma = \frac{L_z}{2}(P_{zz} - \frac{P_{xx} + P_{yy}}{2}) \tag{4.2}$$

where P_{xx}, P_{yy}, and P_{zz} are the diagonal elements of the internal pressure tensor and L_z is the length of the simulation cell in the direction normal to the surface. Figure 4.2 shows surface tension variation with molal concentration for the two salt solutions. As measured experimentally, the Gdm^+ salt solution shows increasing surface tension [294]. However, the experimental surface tension versus concentration slope is not as large as estimated with the current force field combination. The current force field overestimates measured values given in Reference [294].

Nevertheless, both the current simulations and experiment consistently indicate a net surface depletion of the cation as often associated with surface tension increases of aqueous solutions of mono-valent inorganic ions [96]. The M-Gdm^+ surface tension is systematically lower as one would expect due to the slightly higher interfacial propensity of the methyl analogue as reflected in density profiles. In molecular simulations, the surface excess is easier to converge than the surface tension. The surface excess of

a solute is considered as [96]

$$\Gamma_{\mathrm{s}} = -\frac{1}{RT}\left(\frac{\partial\gamma}{\partial \ln a_{\mathrm{s}}}\right)_{\mathrm{T}} \tag{4.3}$$

where R is the gas constant, T is the temperature, γ is the surface tension, and a_{s} is the activity of the solute. In general, for the case of salt solution, a_{s} is expressed as $a_{\mathrm{s}} = (f^{\pm} \times m)^{v}$, where $f^{\pm}$ is the mean activity coefficient of the two dissociated ions, m is the molal concentration, and v is the sum of the stoichiometric coefficients ($v = 2$ in this case). We can therefore extract a_{s} and γ from experiments (refer to Ref [294]) and compute Γ_{s} at the corresponding concentration by polynomial fitting of γ as a function of $\ln a_{\mathrm{s}}$. The results of Γ_{s} are shown in Table 4.3.

For our simulation data, we compute the surface excess of a solute with respect of the solvent as [23, 96]

$$\Gamma_{\mathrm{s}} = \int_{-\infty}^{z_{\mathrm{Gibbs}}} [\rho_{\mathrm{s}}(z) - \rho_{\mathrm{sb}}]\, dz + \int_{z_{\mathrm{Gibbs}}}^{\infty} \rho_{\mathrm{s}}(z) dz \tag{4.4}$$

where $\rho_{\mathrm{s}}(z)$ is the density profile of the solute and ρ_{sb} is the bulk density of the corresponding solute. We summarize our results from simulations in Table 4.3 as well. The values of the individual ions as well as the total solute (which turns out to be the sum of the individual ion surface excesses) follow qualitatively the experimental trend as a function of guanidinium chloride concentration. As observed for other polarizable force fields used for monovalent inorganic ions [96], the present force field combination overestimates surface excesses.

We also show results of Kirkwood-Buff analysis for the 1.1 m systems in Appendix A. Though the current force field tends to overestimate activity derivatives, while capturing the concentration dependence, we feel that the current combination of water and cation force field is still sufficiently robust considering the range of validation metrics for use in addressing the questions posed.

4.3 Potential of Mean Force and Orientational Preference

Next we consider the potential of mean force of single Gdm^+/M-Gdm^+ through L-V interface, as shown in Figure 4.4a. No minimum is found for both cations with

M-Gdm$^+$ being slightly more stable than Gdm$^+$. The planar geometry of both cations lends itself to an analysis of the free energetics associated with its unique orientations relative to the interface normal. Here we use the same convention from Reference [296] to define the orientation of the cations (the planar ring of each cation) relative to the L-V interface: the angle θ between the normal vector of the Gdm$^+$/M-Gdm$^+$ plane and the z-axis. θ ranges from 0 to 90°, when $\theta = 0°$, the Gdm$^+$/M-Gdm$^+$ cation is parallel to the L-V interface. The Gdm$^+$/M-Gdm$^+$ normal is computed from the cross product of two of the three carbon-nitrogen vectors (in the case of M-Gdm$^+$, the nitrogens on -NH_2 groups are chosen). We can then select the configurations with the angular conditions for each PMF window to construct the conditional potential of mean force $w(z, \theta)$ by using WHAM. We categorize the orientations with the condition $\theta_0 - \frac{\Delta\theta}{2} \leq \theta \leq \theta_0 + \frac{\Delta\theta}{2}$, with $\theta_0 = 0, 30, 60, 90°$, $\Delta\theta = 10°$. To assess the reliability of the PMF's we show the overlap distributions between umbrella windows in Figure 4.3; to address convergence, we claim that since the PMF's computed in an unambiguously different way than the angular probability distributions discussed in the next section provide the same information (i.e. that the stability of unique orientations, or their probabilities, are higher at the interfacial region) the PMF's are converged at least for qualitative discussion.

The result of the conditional PMF for Gdm$^+$/M-Gdm$^+$ cation is shown in Figure 4.4 b and c, respectively. When $\theta = 0°$, both cations show minima of roughly 0.5 kcal/mol, indicating preferred parallel configurations in the vicinity of the interface; this is consistent with the probability distributions of orientations as will be discussed further below. As θ increases, the corresponding conditional PMF becomes more repulsive; interestingly, M-Gdm$^+$ still behaves less repulsive than Gdm$^+$ at the same conditional θ_0.

Following Wernersson et al. [296], to quantify the orientational profile of the Gdm$^+$/M-Gdm$^+$ in a statistical manner, we consider the (coarse-grained) probability

of the single solute at position z' with orientation θ as

$$P(z',\theta) = \frac{\int_{z'-\frac{\Delta z}{2}}^{z'+\frac{\Delta z}{2}} dz \int_{\cos(\theta_0-\frac{\Delta\theta}{2})}^{\cos(\theta_0+\frac{\Delta\theta}{2})} d\cos\theta\, n(r,z',\theta)}{\int_{z'-\frac{\Delta z}{2}}^{z'+\frac{\Delta z}{2}} dz \int_{-1}^{1} d\cos\theta\, n(r,z',\theta)} \tag{4.5}$$

where $r = \sqrt{x^2+y^2}$ is the radial distance from the center carbon atom of Gdm^+/M-Gdm^+ in the plane of the surface. $n(r,z',\theta)$ denotes the number count of Gdm^+/M-Gdm^+ with the properties at (z',θ). For each bin region $(z'-\frac{\Delta z}{2}, z'+\frac{\Delta z}{2})$, we have $\int_{-1}^{1} d\cos\theta\, P(z',\theta) = 1$. The results of $P(z',\theta)$ for single Gdm^+/M-Gdm^+ are given in Figure 4.5 a and b. Again as a reminder, when $|\cos(\theta)| = 1$, the ion is parallel to the L-V interface; the ion is perpendicular to the interface when $|\cos(\theta)| = 0$. We further calculate the second order Legendre polynomial using

$$\langle P_2(\cos\theta)\rangle = \frac{1}{2}\left\langle (3\cos^2\theta - 1)\right\rangle \tag{4.6}$$

to measure the degree of orientation of the cations relative to the interface normal. When the orientational configurations are completely random and isotropic, P_2 is zero, whereas for the perfectly aligned case $\langle P_2(\cos\theta)\rangle = 1$. $\langle P_2(\cos\theta)\rangle = -0.5$ when the orientations are entirely perpendicular. This parameter is then a measure of the uniaxial behavior of the species. The results for θ are shown in Figure 4.5 c, when the restrained position is above $z = 15$ Å, $\langle P_2(\cos\theta)\rangle$ for both cations start to increase, indicating enhanced alignment of the cations.

Both cations show no orientational preference when they are in the bulk ($z \leq 13$, which is 5 Å below the GDS); as the ion approaches the GDS, both Gdm^+ and M-Gdm^+ show enhanced probability of configurations parallel to the L-V interface. This orientational preference of Gdm^+ is consistent with the previous studies by Mason et al. [288], Koishi et al. [295] and Wernersson et al. [296] using nonpolarizable force fields. They explained this preference with the weak and anisotropic hydration of Gdm^+ cation. Unlike with spherical cations, the hydration of Gdm^+ is limited to very few water molecules capable of forming hydrogen bonds within the planar surface of Gdm^+. Therefore, in the parallel orientation, desolvation occurs more facilely as the

ion nears the L-V interface. This can be connected to the efficiency of guanidinium cation as a denaturant via interactions with the hydrophobic side chains of proteins. Recently, new insights of the surface fluctuations to explain the anionic surface stability have been proposed based on the capillary wave theory [93, 19, 283]. We will continue this discussion in the following section.

From Figure 4.5 a and b we also observe that Gdm^+ shows stronger parallel preference near the L-V interface (as displayed with higher probability). As the cations move toward the vapor phase, the distribution profile of Gdm^+ recovers to equal for all orientations and bulk-like; on the other hand, M-Gdm^+ shows depletion of parallel configurations and increases the probability of being perpendicular to the L-V interface. We explain this by examining the second order Legendre polynomial of the cations. Define the angle β between positive z-axis and the vector constructed from center carbon to the carbon of the methyl group (CH_3) ($\overrightarrow{CC_M}$) for M-Gdm^+, we then compute the coarse-grained probability of the M-Gdm^+ at position z' with angle β as

$$P(z',\beta) = \frac{\int_{z'-\frac{\Delta z}{2}}^{z'+\frac{\Delta z}{2}} dz \int_{\cos(\beta_0-\frac{\Delta\beta}{2})}^{\cos(\beta_0+\frac{\Delta\beta}{2})} d\cos\beta\, n(r,z',\beta)}{\int_{z'-\frac{\Delta z}{2}}^{z'+\frac{\Delta z}{2}} dz \int_{-1}^{1} d\cos\beta\, n(r,z',\beta)} \tag{4.7}$$

The results are shown in Figure 4.5 d. As the M-Gdm^+ crosses through the L-V interface, $\cos\beta$ becomes more positive, which implies larger probability of C-$NH(CH_3)$ vector pointing toward vapor phase (positive z-direction). This demonstrates that, due to the asymmetry on the molecular plane caused by the methyl group, M-Gdm^+ has a strongly hydrophobic partition that favors the vapor phase. These configurations correspond to the perpendicular configurations shown in Figure 4.5 b, consequently reducing the probability of parallel configurations. We also find that when M-Gdm^+ is near the position $z = 15$ Å there is a strong enhancement of large $\langle\cos\beta\rangle$ (as shown with the white arrow in Figure 4.5 d), which is also confirmed by calculating the $\langle P_2(\cos\beta)\rangle$ (shown in Figure 4.5 c). It implies that when the M-Gdm^+ is 3-4 Å below the GDS, the C-$NH(CH_3)$ vector has a strong tendency of pointing to the vapor phase; however, when the cation is right on the GDS, this tendency is somehow weakened.

More discussion of this behavior will be continued in the following section.

4.4 Connection between Conditional Potential of Mean Force and Corresponding Fluctuation

We use the same convention of θ as in previous section to discuss fluctuations of instantaneous surfaces as they depend on Gdm^+/M-Gdm^+ orientation relative to the interface. Furthermore, for a particular orientation, θ, we will consider the variation of interface fluctuation as a function of the distance, r, away from the center of the guanidinium ring moving in the $x-y$ plane of the average interface generated from instantaneous interfaces. This average fluctuation we call $\delta h^2_{\mathrm{L}}(r,\theta)$ (L for lateral). In the case of pure TIP4P-FQ (in the absence of ions), $\langle \delta h^2 \rangle$ for the current system size is 0.96±0.07 Å^2. In our study, we have confirmed that the fluctuation for lateral distance far away from the center of the cation (r = 20 Å) is consistent with the value of pure TIP4P-FQ. We therefore define $\delta h^2_{\mathrm{L}}(r,\theta)$ as the conditional fluctuations normalized by 0.96 Å^2. In this convention, when $\langle \delta h^2_{\mathrm{L}} \rangle$ equals 1, the effect of cation is zero; when $\langle \delta h^2_{\mathrm{L}} \rangle > 1$, the surface height fluctuation is enhanced relative to pure water with the presence of ion; when $\langle \delta h^2_{\mathrm{L}} \rangle < 1$, the surface height fluctuation is suppressed. Furthermore, when we consider all the orientations at the same value of the reaction coordinate, the overall $\delta h^2_{\mathrm{L}}(r)$ will be the weighted linear combination of different θ conditions

$$\left\langle \delta h^2_{\mathrm{L}}(r) \right\rangle = \sum_{\theta} P(\theta) \cdot \left\langle \delta h^2_{\mathrm{L}}(r,\theta) \right\rangle \tag{4.8}$$

while $P(\theta)$ is the probability of θ condition (i.e., the probability of observing a particular value of the angle θ).

The results of $\langle \delta h^2_{\mathrm{L}}(r,\theta) \rangle$ for single Gdm^+/M-Gdm^+ at various positions using parallel and perpendicular conditions are shown in Figure 4.6 a, b, d and e. The parallel orientation induces the largest interfacial fluctuation enhancement is evident for both cations; the peak fluctuation is roughly twice that of the inherent pure water thermal fluctuation. At positions of 18 and 20 Å, the fluctuations are suppressed relative to pure water, again for both cations. Panels b and e of Figure 4.6 show

reduction in interfacial enhancement for both ions; the Gdm^+ shows a more dramatic decrease. We attribute this to the fact that M-Gdm^+ is larger, and its hydrophobic methyl group, which is projected towards the GDS, maintains the perturbation of the interface. The behavior here is remarkably similar to that observed for simple monovalent anions that display differential interfacial stabilities at the aqueous liquid-vapor interface. In the case of larger, less charge-dense anions that exhibit non-trivial free energy minima in their PMF's, interfacial fluctuations are significantly enhanced over the pure water case. In the present situation, for the Gdm^+ cation, again, a fairly low charge-density molecular ion, we observe a correlation with surface stability and enhanced interfacial perturbation, but in this case with the conditional requirement that the molecular solute present a particular orientation relative to the interfacial plane. The importance of this orientation in terms of hydration will be addressed further below. The probability weighted $\delta h_{\mathrm{L}}^2(r)$ for single Gdm^+/M-Gdm^+ is shown in Figure 4.6c and f. As expected, combining the fluctuations from all the possible orientations gives rise to overall fluctuation profiles that are intermediate between the zero and 90 degree orientations. We next consider the variation of the $\delta h_{\mathrm{L}}^2(r = 0, \theta)$ with the position of the cation along the interface normal reaction coordinate (for a series of four orientation angles, the value of $\delta h_{\mathrm{L}}^2(r, \theta)$ when $r = 0$ is plotted for points along z). These are shown in Figure 4.7. For clarity, a vertical offset of 0.25 is added between the curves. In general, independent of species or orientation, $\langle \delta h_{\mathrm{L}}^2 \rangle$ is around 1 when the cation is in the bulk ($z = 0$ Å). $\langle \delta h_{\mathrm{L}}^2 \rangle$ starts to increase when the cation position is 8 Å below the GDS, reaches to maximum at the position 3.5 Å below the GDS, eventually falls back and shows suppression when the cation is right at the GDS. The maximum fluctuations are accommodated by the smaller angles, with the perpendicular orientations (showing no interface stability) essentially inducing little to no interfacial enhancement. That the parallel orientation induces larger fluctuations coincides with the observation that solvation on this face of the guanidinium ring is weaker than around the periphery of the ring where strong water-cation hydrogen bonding is sustained.

Moreover, this behavior is similar with our previous study of surface fluctuations induced by single, low charge density anions [93, 92], and we attempt to explain the current observations by considering the interaction of the local hydration environment of the cation with the solvent and solvent fluctuations at the L-V interface. We aim to show that the two orientations present distinct hydration shell environments towards the interface; the parallel orientation presenting a solvent environment that is less rigid, more malleable, and thus more amenable to inducing fluctuations of the interface as a consequence of a greater disruption of solvent structure on approach to the interface. The perpendicular orientation presents a more rigid hydration environment due to the more effective hydrogen bonding of water in the plane of the ring, thus decreasing the efficacy of this orientation for promoting interfacial fluctuations. These properties of the two orientations are discussed using radial density profiles of water around the single cations and water velocity autocorrelation functions in the hydration shells presented to the interface in the vicinity of the GDS.

4.5 Solvation Structure

We first consider water radial density functions. Previously [93], we demonstrated that spherical, mono-valent anions with PMF minima (i.e., surface stable) at the liquid-vapor interfacial region tend to have solvation shells that are in a way fluid (or "malleable"); these solvation shells couple with solvent at the liquid-vapor interface as the anion approaches the interface in a manner that leads to enhancement of the inherent fluctuations of the interface. In contrast to such anions, those species that showed no interfacial stability (i.e., surface unstable) possessed well-ordered, more "rigid" solvation shells that, through little to no coupling with distal solvent on approach to the interface, did not mediate enhanced fluctuations. Thus, ions with interfacial stability possessed complementary solvation shells, while those not stable at the interface did not. Here, we consider the solvation shell environment presented towards the interfacial region as cations of different orientations approach the GDS. In like manner,

Gdm^+/M-Gdm^+ induce distinct perturbations of the L-V interface depending on orientation relative to the interface. Figure 4.8 shows the conditional density of water oxygen ($\rho(r,z)$, $r = \sqrt{x^2+y^2}$) around Gdm^+ for parallel (panel a-c) and perpendicular (panel d-f) configurations at z-position = 0, 15, 18 Å, which correspond to the cation in the bulk, the position that induces the largest fluctuation relative to pure water, and a surface state. When Gdm^+ is in the bulk (Figure 4.8 a and d) both configurations shows a bright "ring", corresponding to the first peak of RDF, followed by an outer, darker region signifying the first minimum of RDF. The radius of this "ring" is roughly 3.5 Å. When Gdm^+ is restrained at $z = 15$ Å, which is roughly 3.5 Å below the GDS, the first hydration shell of the parallel configuration merges with the L-V interfacial layer (indicated by white arrows in Figure 4.8 b), while that of perpendicular configuration does not (Figure 4.8 e). For the parallel configuration, the more malleable hydration water above the Gdm^+ plane couples with interfacial water resulting in greater deformation, and resulting fluctuations, of the interface [93] than the perpendicular configuration.

4.6 Dynamical Properties

To answer whether hydration water above the plane of the guanidinium ring is less ordered (structured) and diffuse, we analyzed oxygen atom velocity decorrelation functions for water in the region above the guanidinium ring when the cations are in the parallel and perpendicular orientation (relative to the interface) at a z position of 15Å(Figure 4.9). Oxygen VACF's are computed using well-known expressions [197, 198, 199]

$$C_v(t) = \frac{1}{N}\sum_{i=1}^{N}\frac{\langle \overrightarrow{v_i}(t)\cdot\overrightarrow{v_0}(0)\rangle}{\langle \overrightarrow{v_i}(0)\cdot\overrightarrow{v_i}(0)\rangle} \tag{4.9}$$

where $\overrightarrow{v_i}(t)$ is the velocity vector of the i_{th} atom in the simulation system at time t. The brackets denote the ensemble average. Here we only look at the water above the cation and within 5 Å of any atom on the cation.

Our analysis shows the similarity of water dynamics above the planar (parallel) orientation to be much like that of the liquid-vapor interface, while that of the

perpendicular orientation remains more bulk-like. For the perpendicular orientation when the cation is at $z = 15$ Å, we observe the typical oscillatory behavior signifying a caging effect of local hydrating water molecules on a central solvent molecule. At the bulk position, $z = 0$ Å, hydration waters are bulk like for both orientations. This difference was also observed for monovalent halide anions exhibiting contrasting surface stabilities.

4.7 β-Conditional Fluctuation

We next address behavior of the angle β when M-Gdm$^+$ resides in the L-V interface region (as shown in Figure 4.5 d). Recall we define the angle β between the positive z-axis and the vector constructed from center carbon to the carbon of the methyl group (CH_3) ($\overrightarrow{CC_M}$) for M-Gdm$^+$. We use the idea of conditional surface fluctuation to explain this preference with M-Gdm$^+$'s structure. Again we can define

$$\left\langle \delta h_L^2(r) \right\rangle = \sum_{\beta} P(\beta) \cdot \left\langle \delta h_L^2(r, \beta) \right\rangle \tag{4.10}$$

and decompose the surface fluctuation contribution from each β angle at the specific cation restrained position marked in Figure 4.5 d. In practice, we set each angular bin between $\beta_i - \Delta\beta$ and $\beta_i + \Delta\beta$, with $\Delta\beta = 10°$, and $\beta_i = 10$, 30, 50, 70, 90, 110, 130, 150, 170°. For $\beta = 0°$, $\overrightarrow{CC_M}$ points toward vapor phase (methyl group directed to vapor); for $\beta = 90°$, $\overrightarrow{CC_M}$ is along the xy-plane; for $\beta = 180°$, $\overrightarrow{CC_M}$ points toward the water bulk (methyl group directed more towards bulk region). The results for β-conditional, normalized fluctuation $\langle \delta h_L^2 \rangle$ for $z = 14$, 15, 16 and 18 Å are presented in Figure 4.10. Since no sampling for angles larger than 100° was observed, only the angles less than 100° are considered. For clarity, a vertical offset of 0.1, -0.1 and -0.1 is added for z = 14, 15 and 18 Å (Figure 4.10 a, b and d), respectively. At the window of largest probability-weighted fluctuation ($z = 14$ Å, shown in Figure 4.6 f), we notice that $\langle \delta h_L^2 \rangle$ decreases as $\overrightarrow{CC_M}$ points from vapor phase to the xy-plane; however, at the following window ($z = 15$ Å) although all the orientations still show enhanced fluctuations, this

trend of β-dependence is reversed (also shown in the inset of panel b). At the next following window, $z = 16$ Å, we even found that as $\overrightarrow{CC_M}$ points more toward vapor phase, the M-Gdm$^+$ starts to suppress the interfacial fluctuations. As the M-Gdm$^+$ moves to the GDS ($z = 18$ Å), all β-orientations show similar magnitude of fluctuation suppression. Based on the previous discussion connecting θ-conditional surface stability and interfacial fluctuation, it is natural to consider this β-preference as another manifestation of the drive to maximize fluctuation; this also leads to maximizing interfacial entropy as the two are related through spatial correlations of fluctuations [19]. At $z =$ 14 Å, $\overrightarrow{CC_M}$ points towards the vapor, facilitating the largest fluctuations; thus, small β angles are preferred. As M-Gdm$^+$ approaches the GDS, $\overrightarrow{CC_M}$ residing in the xy-plane leads to larger fluctuations, consequently the preference of β shifts to larger angles (as demonstrated with the white arrow in Figure 4.5 d). As M-Gdm$^+$ approaches a critical position, $\overrightarrow{CC_M}$ pointing toward vapor phase causes the suppression of interfacial fluctuation, which forces the cation to show higher probability of large β, as evidenced in the $\langle P_2(\cos\beta)\rangle$ in Figure 4.5 c. Structurally, it indicates that the methyl group prefers to be partially desolvated rather than fully desolvated. We note that for the β-dependence analysis presented here, we are actually considering the average over all possible θ values. Although not pursued here, it would be interesting to study δh_L^2 as a function of both θ and β.

4.8 Discussion and Conclusions

Via all-atom molecular dynamics simulations, we have shown that though on average there is no liquid-vapor interfacial propensity for either the Gdm$^+$ or M-Gdm$^+$ cations, there is a stark orientation-based dispersion of stabilities. Orientations of the guanidinium ring parallel to the interfacial plane are unambiguously more stable (though we do not make any strong claims on the relative stability with the force field based analysis here). Our results recapitulate the differential stabilities observed for the parallel and perpendicular orientations observed in Reference [296]. Furthermore,

we find that the configurations that show a PMF minimum at the interface also induce strong perturbing interfacial fluctuations defined as the variance from a mean, coarse-grained interface. Orientations of the guanidinium ring parallel to our proxy for a hydrophobic interface are slightly favored over perpendicular ones. The hydration shell environment exposed to the interface on approach of the cation to the interface is intimately coupled to the different fluctuation behaviors observed for the parallel and perpendicular orientations. The parallel orientation presents a solvent environment that is less rigid, more malleable, and thus more amenable to inducing fluctuations of the interface as a consequence of a greater disruption of solvent structure on approach to the interface. The perpendicular orientation presents a more rigid hydration environment due to the more effective hydrogen bonding of water in the plane of the ring, thus decreasing the efficacy of this orientation for promoting interfacial fluctuations. These differential behaviors are consistent with the fact that in bulk solution, the contact ion pair of Gdm^+ shows a distinct preference for pairs that are stacked parallel to one another (rather than perpendicular to one another) [286]. For the force field used, this suggests the ease with which the hydration waters above the guanidinium ring plane are removed to accommodate a second hydrophobic partner. When considering the denaturant properties of guanidinium, and a direct contact mechanism, the results we present here seem to indicate that association with sidechains groups that are not robustly hydrated is a plausible mechanism of action of this osmolyte.

Distance[a]	r_0 (Å)	k_B (kcal/mol/Å^2)		
C-N	1.365	463.0		
N-H	1.000	455.0		
N-CT3[b]	1.490	261.0		
Angles[c]	θ_0 (°)	k_A ($\frac{kcal/mol}{rad^2}$)		
N-C-N	120.00	52.0		
C-N-H	120.00	49.0		
H-N-H	120.00	25.0		
C-N-CT3	120.00	62.3		
H-N-CT3	120.00	40.4		
N-CT3-HA[d]	107.50	51.5		
HA-CT3-HA	108.40	35.5		
NB[e]	σ (Å)	ε (kcal/mol)	$\frac{\eta}{2}$ ($\frac{kcal/mol}{e}$)	χ ($\frac{kcal/mol}{e^2}$)
C	4.450	-0.16000	326.16817	123.33139
N	3.700	-0.20000	350.96041	145.30623
H	1.249	-0.01600	276.49391	297.48634
Cl	4.920	-0.07658		
CT3	4.040	-0.07300	319.64684	120.17339
HA	2.640	-0.02200	315.55701	250.71405
Dihedrals[f]	k_D (kcal/mol)	n[g]	δ (°)	
N-C-N-H	2.25	2	180.0	
C-N-CT3-HA	0.00	6	180.0	
Imp. Dihedrals[h]	k_I ($\frac{kcal/mol}{rad^2}$)	ψ		
N-N-N-C	40.0000	0.0000		

Table 4.1: Force Field Parameters for Gdm^+, M-Gdm^+ and Cl^-. [a] $U_B = k_B(r - r_0)^2$. [b] CT3 is the carbon atom in methyl group. [c] $U_A = k_A(\theta - \theta_0)^2$. [d] HA is the hydrogen atom in methyl group. [e] Non-bonded parameters in Lennard-Jones form; geometric combination rules. [f] $U_D = k_D(1 + \cos(n(\chi) - \delta))$. [g] Multiplicity of the dihedral angles. [h] $U_I = k_I(\psi - \psi_0)^2$, as improper dihedrals. Reproduced with permission from Shuching Ou, Di Cui and Sandeep Patel. "Liquid-Vapor Interfacial Properties of Aqueous Solutions of Guanidinium and Methyl Guanidinium Chloride: Influence of Molecular Orientation on Interface Fluctuations." *Journal of Physical Chemistry B.* **2013**, *117 (39)*, 11719-11731. Copyright 2013 American Chemical Society.

System	Pairs of Ions	GDS (Å)	ρ_{mass} (g/cm^3) (calc.)	γ (dyn/cm) (calc.)
GdmCl				
1.1 m	38	20.16	1.015	74.14(0.02)
2 m	71	21.58	1.022	75.49(0.02)
3 m	107	23.13	1.027	76.92(0.02)
4 m	142	24.64	1.032	78.11(0.16)
5.3 m	190	26.68	1.036	79.75(0.21)
M-GdmCl				
1.1 m	38	20.51	1.014	73.69(0.04)
2 m	71	22.23	1.020	74.20(0.03)
3 m	107	24.07	1.025	75.29(0.11)
4 m	142	25.87	1.030	76.13(0.26)
5.3 m	190	28.29	1.035	77.08(0.03)

Table 4.2: Properties of the solution systems studied in this manuscript, including the position of Gibbs dividing surface (GDS), mass density (ρ_{mass}) and surface tension (γ). Values in parentheses indicate the uncertainties, which are obtained via the standard deviation of 4 replicates. Reproduced with permission from Shuching Ou, Di Cui and Sandeep Patel. "Liquid-Vapor Interfacial Properties of Aqueous Solutions of Guanidinium and Methyl Guanidinium Chloride: Influence of Molecular Orientation on Interface Fluctuations." *Journal of Physical Chemistry B.* **2013**, *117 (39)*, 11719-11731. Copyright 2013 American Chemical Society.

System	Γ^{+}_{comp}	Γ^{-}_{comp}	Γ_{comp}	Γ_{exp}
GdmCl				
1.1 m	-0.017	-0.017	-0.034	-0.022
2 m	-0.031	-0.021	-0.052	-0.031
3 m	-0.033	-0.031	-0.063	
4 m	-0.039	-0.037	-0.077	
5.3 m	-0.039	-0.036	-0.075	
M-GdmCl				
1.1 m	-0.012	-0.014	-0.026	
2 m	-0.017	-0.016	-0.033	
3 m	-0.014	-0.017	-0.031	
4 m	-0.023	-0.022	-0.044	
5.3 m	-0.018	-0.013	-0.031	

Table 4.3: Surface excess calculated from our simulation and experimental data. $\Gamma^{\pm}_{\text{comp}}$ refers to the surface excess of the cation/anion from our simulation. Reproduced with permission from Shuching Ou, Di Cui and Sandeep Patel. "Liquid-Vapor Interfacial Properties of Aqueous Solutions of Guanidinium and Methyl Guanidinium Chloride: Influence of Molecular Orientation on Interface Fluctuations." *Journal of Physical Chemistry B.* **2013**, *117 (39)*, 11719-11731. Copyright 2013 American Chemical Society.

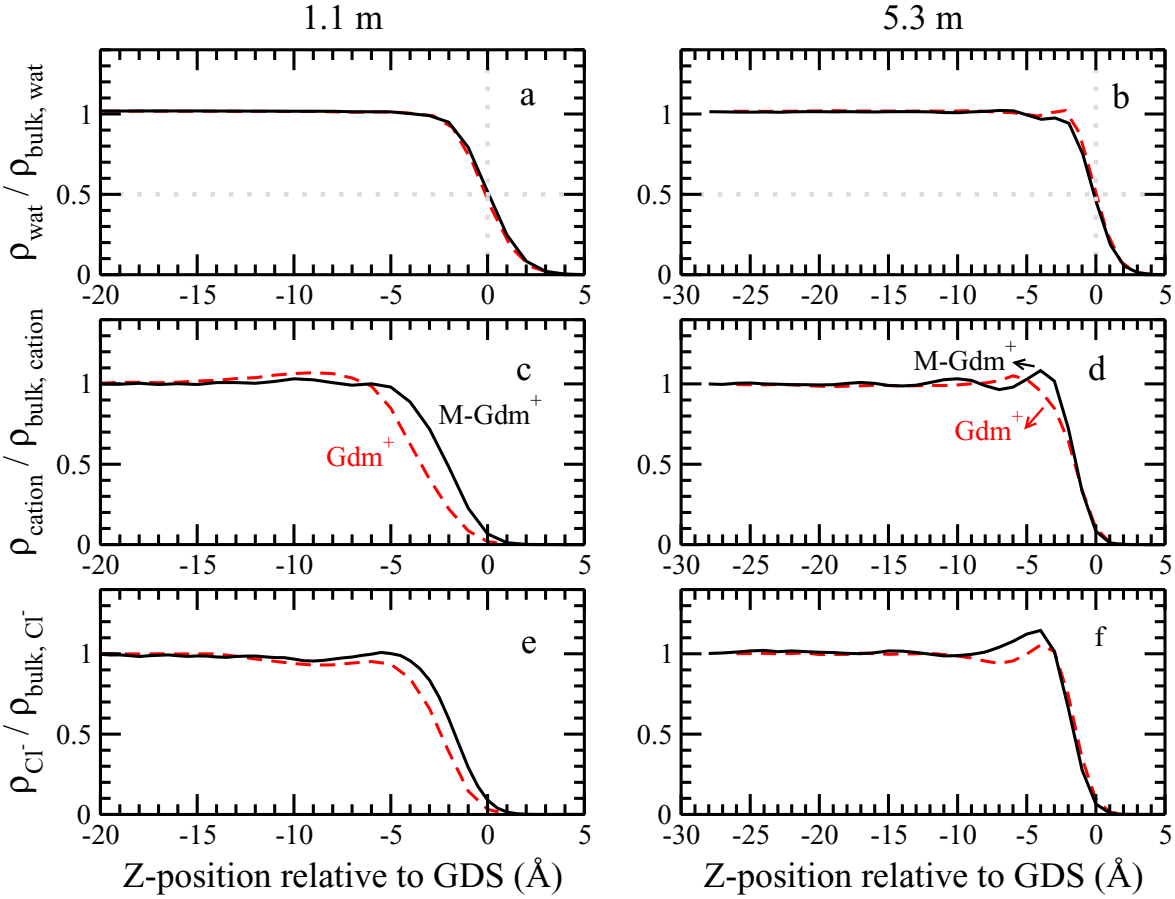

Figure 4.1: Normalized number density profile of water oxygen, solute central carbon atom of ring (Gdm^+ or M-Gdm^+) and Cl^- in 1.1 m and 5.3 m solution. Reproduced with permission from Shuching Ou, Di Cui and Sandeep Patel. "Liquid-Vapor Interfacial Properties of Aqueous Solutions of Guanidinium and Methyl Guanidinium Chloride: Influence of Molecular Orientation on Interface Fluctuations." *Journal of Physical Chemistry B.* **2013**, *117 (39)*, 11719-11731. Copyright 2013 American Chemical Society.

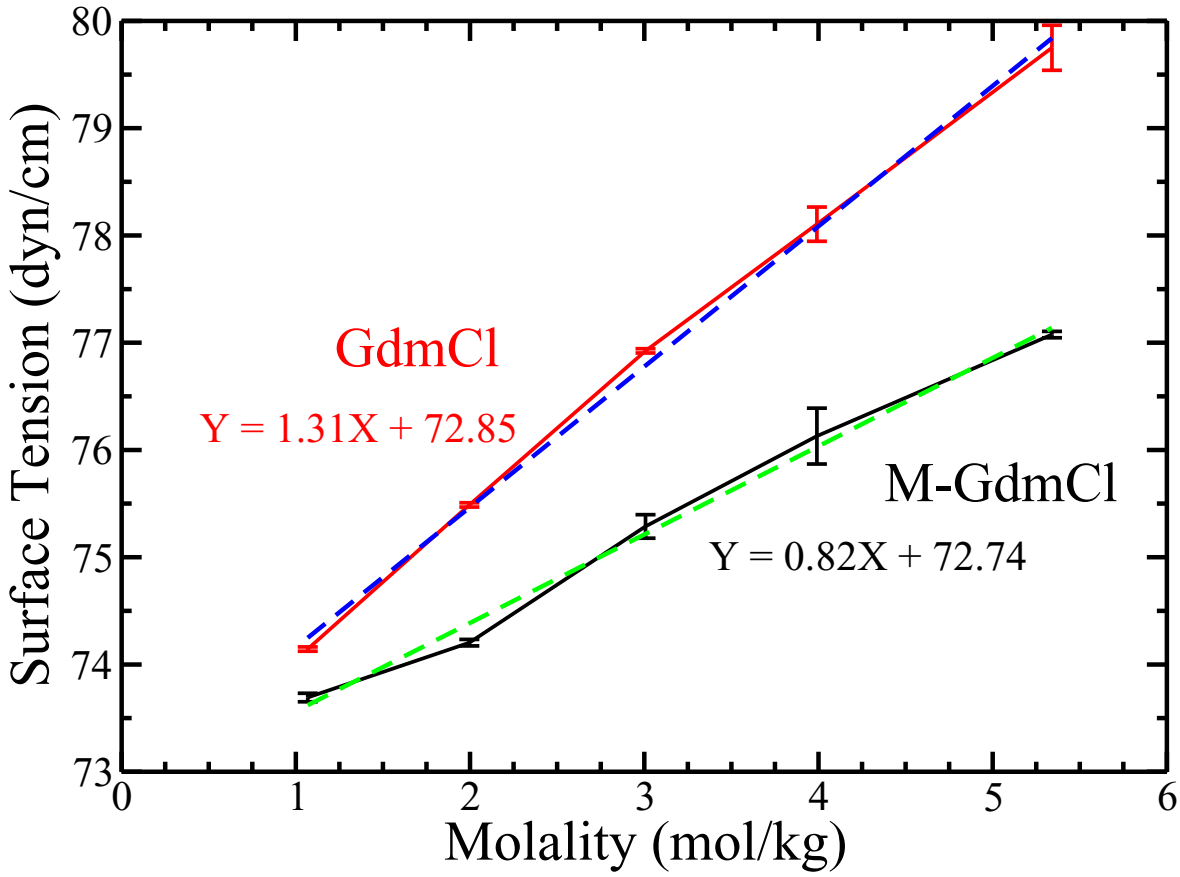

Figure 4.2: Surface tension as a function of concentration, along with the linear fitting results. Reproduced with permission from Shuching Ou, Di Cui and Sandeep Patel. "Liquid-Vapor Interfacial Properties of Aqueous Solutions of Guanidinium and Methyl Guanidinium Chloride: Influence of Molecular Orientation on Interface Fluctuations." *Journal of Physical Chemistry B.* **2013**, *117 (39)*, 11719-11731. Copyright 2013 American Chemical Society.

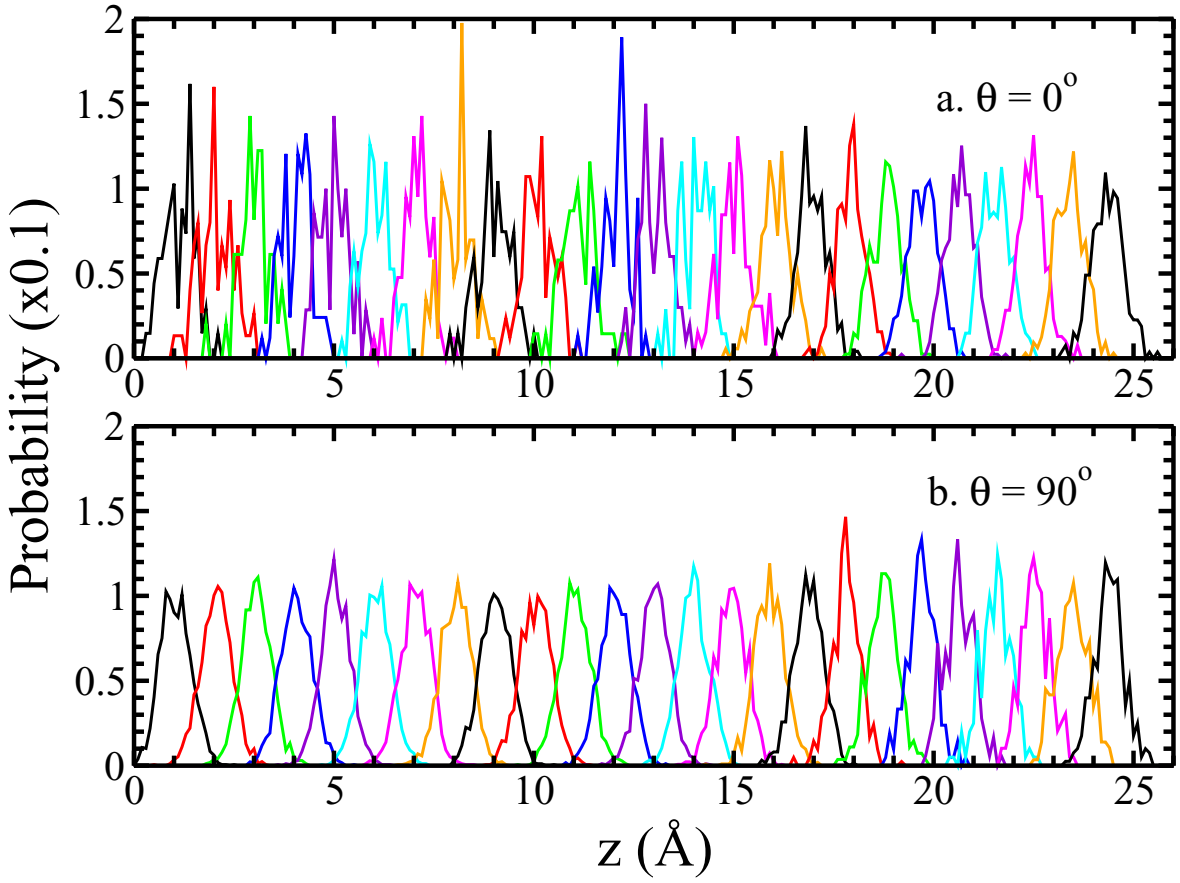

Figure 4.3: Overlap of sampling between restrained windows for single Gdm^+ PMF. Surface tension as a function of concentration, along with the linear fitting results. Reproduced with permission from Shuching Ou, Di Cui and Sandeep Patel. "Liquid-Vapor Interfacial Properties of Aqueous Solutions of Guanidinium and Methyl Guanidinium Chloride: Influence of Molecular Orientation on Interface Fluctuations." *Journal of Physical Chemistry B.* **2013**, *117 (39)*, 11719-11731. Copyright 2013 American Chemical Society.

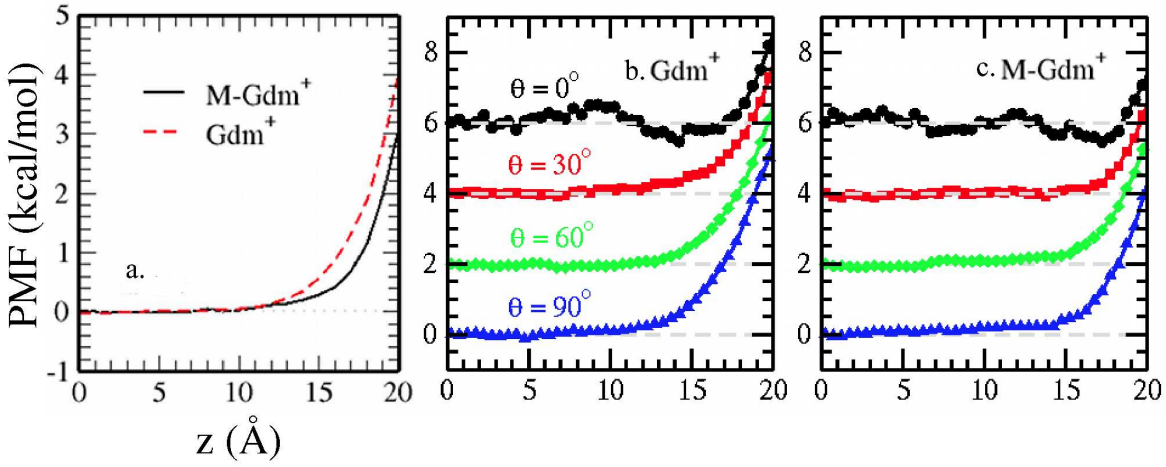

Figure 4.4: (a) Potential of mean force of single Gdm^+/M-Gdm^+ from bulk transporting through L-V interface. Conditional potential of mean force for single (b) Gdm^+ or (c) M-Gdm^+. A vertical offset of 2 kcal/mol is added for clarity. Reproduced with permission from Shuching Ou, Di Cui and Sandeep Patel. "Liquid-Vapor Interfacial Properties of Aqueous Solutions of Guanidinium and Methyl Guanidinium Chloride: Influence of Molecular Orientation on Interface Fluctuations." *Journal of Physical Chemistry B.* **2013**, *117 (39)*, 11719-11731. Copyright 2013 American Chemical Society.

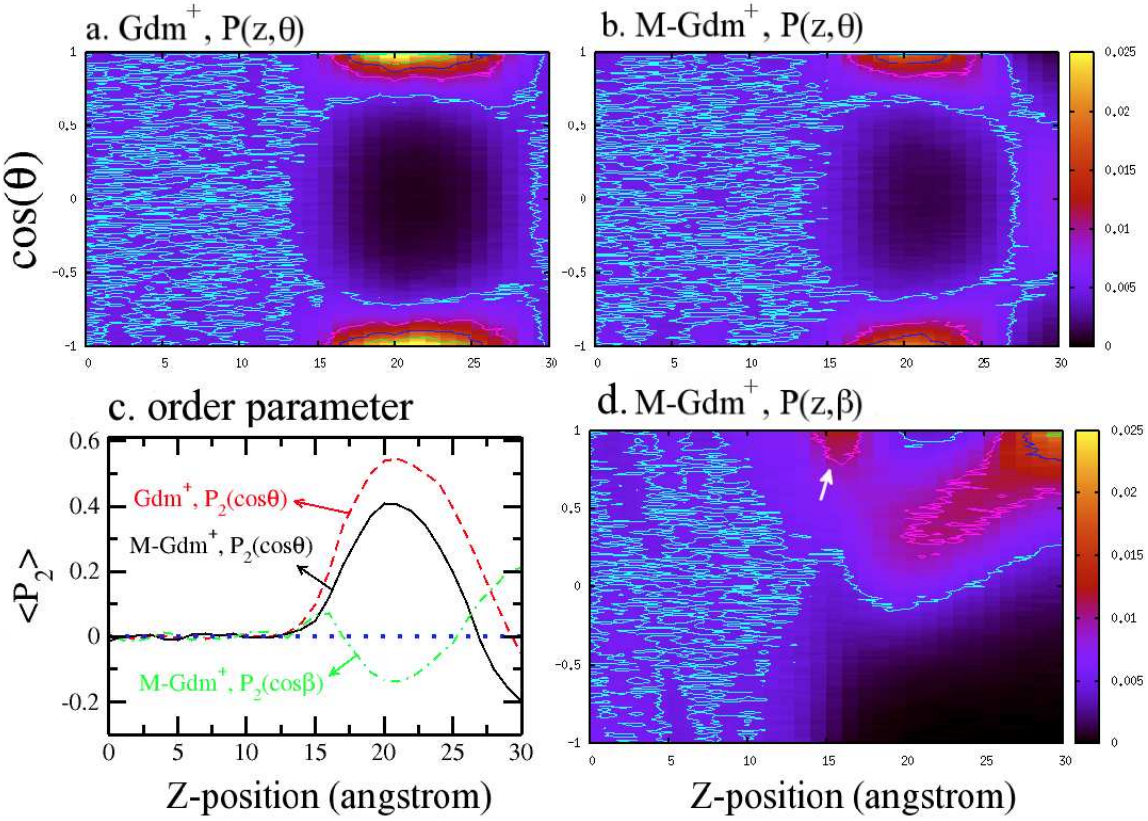

Figure 4.5: Orientational distribution of single Gdm^+ and M-Gdm^+. Refer to text for the definition of θ and β. Reproduced with permission from Shuching Ou, Di Cui and Sandeep Patel. "Liquid-Vapor Interfacial Properties of Aqueous Solutions of Guanidinium and Methyl Guanidinium Chloride: Influence of Molecular Orientation on Interface Fluctuations." *Journal of Physical Chemistry B.* **2013**, *117 (39)*, 11719-11731. Copyright 2013 American Chemical Society.

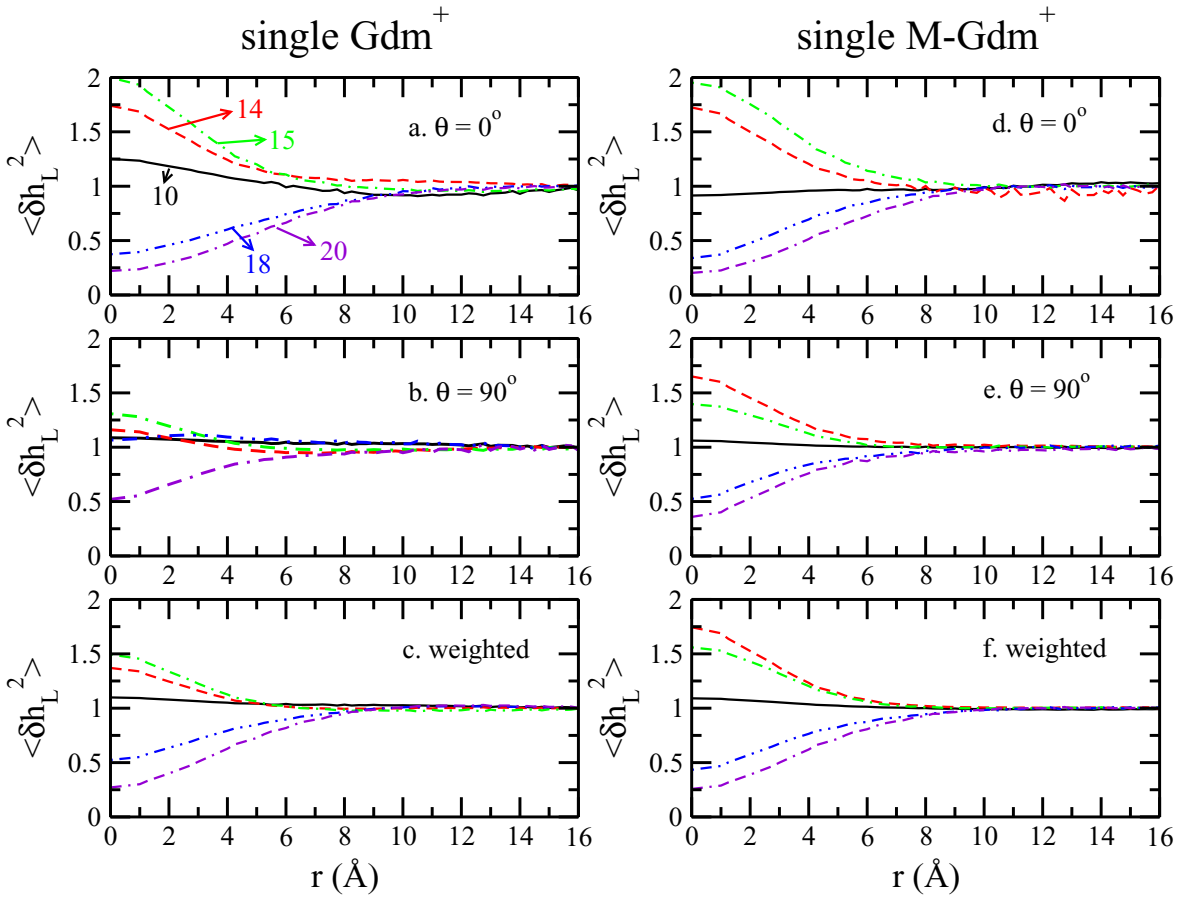

Figure 4.6: Conditional, normalized fluctuation (δh_{L}^2) as a function of r from the center carbon of Gdm^+ or M-Gdm^+. (a) Gdm^+, $\theta = 0$ °; (b) Gdm^+, $\theta = 90$ °; (c) Gdm^+, all orientations with probability weighted; (d) M-Gdm^+, $\theta = 0$ °; (e) M-Gdm^+, $\theta = 90$ °; (f) M-Gdm^+, all orientations with probability weighted. The values shown in Panel a (and applicable to all panels) indicate fluctuation profiles for solute positions of 10.0, 14.0, 15.0, 18.0, 20.0 Å from the center of the bulk solution region of the simulation cell. Reproduced with permission from Shuching Ou, Di Cui and Sandeep Patel. "Liquid-Vapor Interfacial Properties of Aqueous Solutions of Guanidinium and Methyl Guanidinium Chloride: Influence of Molecular Orientation on Interface Fluctuations." *Journal of Physical Chemistry B.* **2013**, *117 (39)*, 11719-11731. Copyright 2013 American Chemical Society.

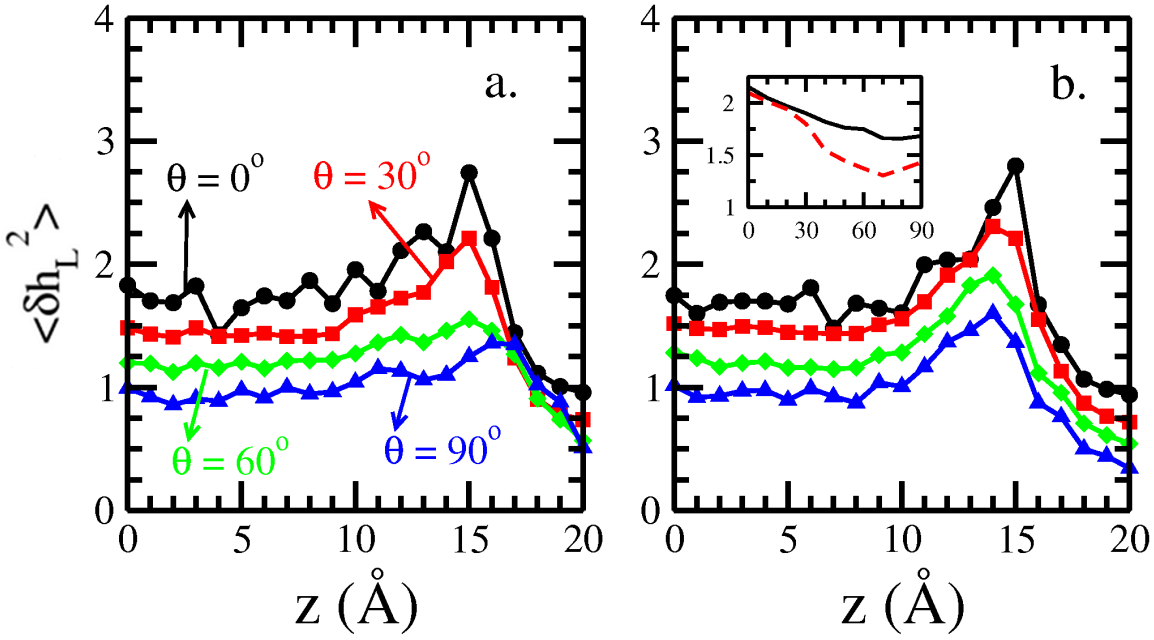

Figure 4.7: The largest, probability weighted, normalized fluctuation (r = 0 Å) as a function of z-position of the (a) Gdm^+ (b) M-Gdm^+. Inset shows the largest conditional fluctuation for each conditional orientation; black solid line is for single M-Gdm^+, while red dashed line corresponds to single Gdm^+. Reproduced with permission from Shuching Ou, Di Cui and Sandeep Patel. "Liquid-Vapor Interfacial Properties of Aqueous Solutions of Guanidinium and Methyl Guanidinium Chloride: Influence of Molecular Orientation on Interface Fluctuations." *Journal of Physical Chemistry B.* **2013**, *117 (39)*, 11719-11731. Copyright 2013 American Chemical Society.

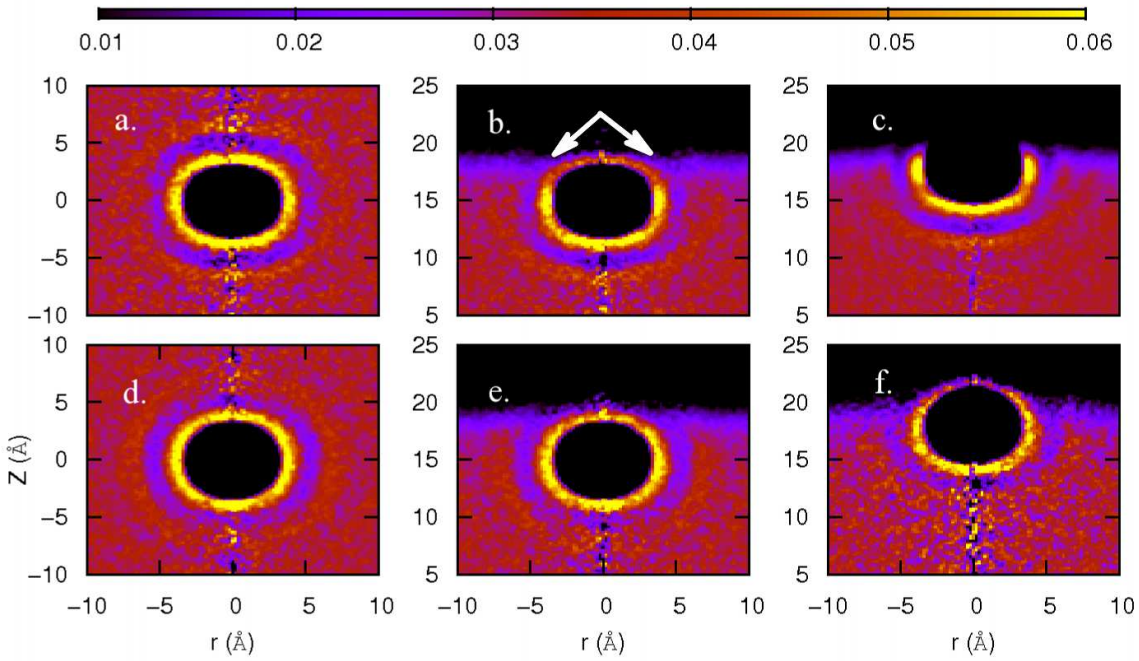

Figure 4.8: Conditional density profiles of single Gdm^+ at different z-position. (a) $z = 0.0$ Å, $\theta = 0$ °; (b) $z = 15.0$ Å, $\theta = 0$ °; (c) $z = 18.0$ Å, $\theta = 0$ °; (d) $z = 0.0$ Å, $\theta = 90$ °; (e) $z = 15.0$ Å, $\theta = 90$ °; (f) $z = 18.0$ Å, $\theta = 90$ °. Reproduced with permission from Shuching Ou, Di Cui and Sandeep Patel. "Liquid-Vapor Interfacial Properties of Aqueous Solutions of Guanidinium and Methyl Guanidinium Chloride: Influence of Molecular Orientation on Interface Fluctuations." *Journal of Physical Chemistry B.* **2013**, *117 (39)*, 11719-11731. Copyright 2013 American Chemical Society.

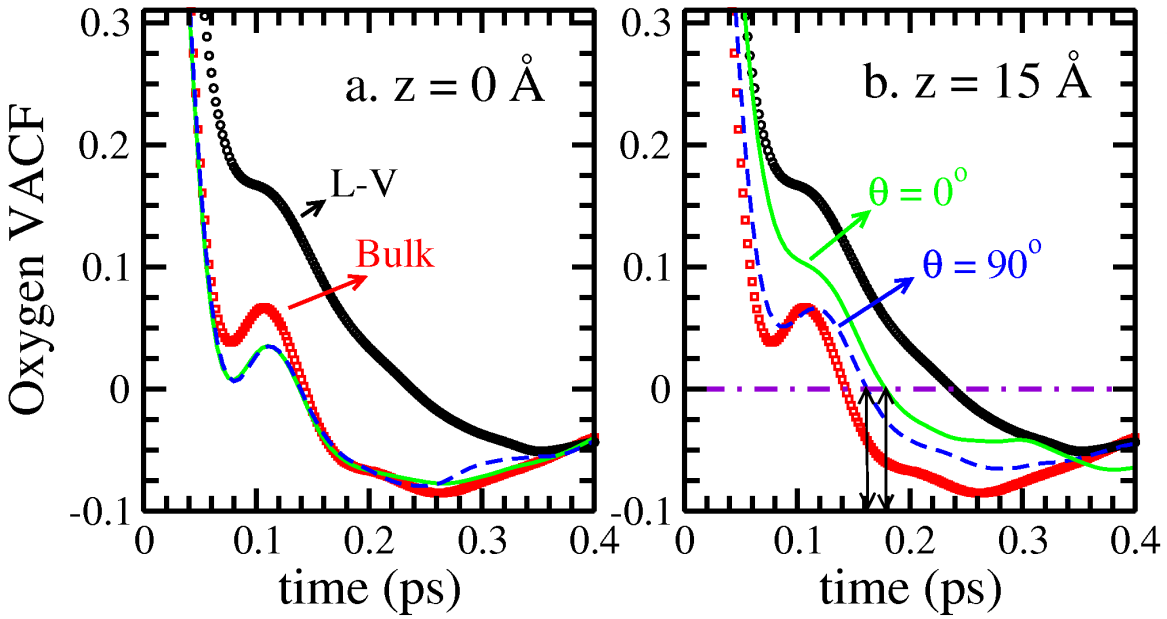

Figure 4.9: Oxygen VACF of water near the Gdm^+ for parallel/perpendicular orientation at (a) bulk ($z = 0$ Å) and (b) the restrained window with largest fluctuation ($z = 15$ Å). Reproduced with permission from Shuching Ou, Di Cui and Sandeep Patel. "Liquid-Vapor Interfacial Properties of Aqueous Solutions of Guanidinium and Methyl Guanidinium Chloride: Influence of Molecular Orientation on Interface Fluctuations." *Journal of Physical Chemistry B.* **2013**, *117 (39)*, 11719-11731. Copyright 2013 American Chemical Society.

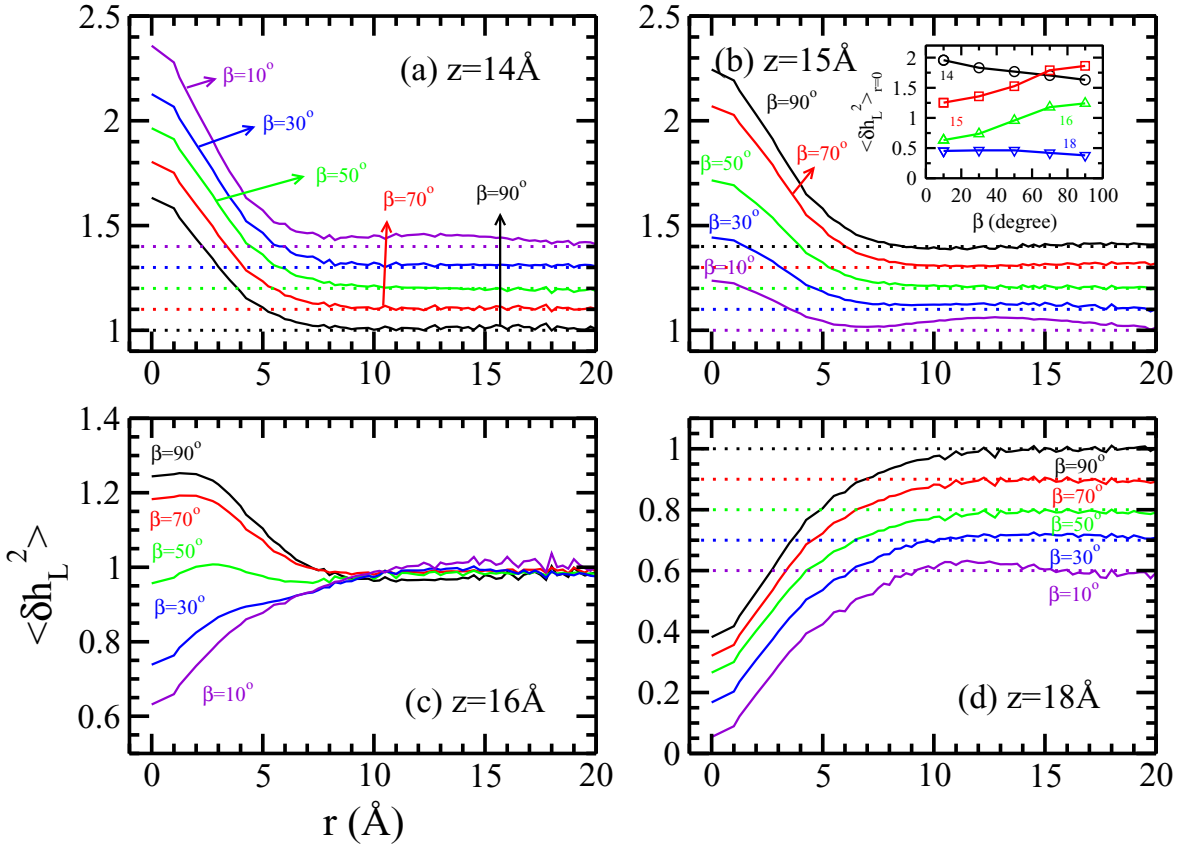

Figure 4.10: β-conditional fluctuation profiles of single M-Gdm$^+$ at different z-position. (a) z = 14.0 Å (b) z = 15.0 Å (c) z = 16.0 Å (d) z = 18.0 Å. Inset shows the $\langle \delta h_{\mathrm{L}}^2 \rangle$ at r = 0 Å from each panel. For clarity, an vertical offset of 0.1, -0.1, -0.1 has been added in window z = 14, 15, 18 Å, respectively. In all panels, the y-axis is the normalized fluctuation, $\langle \delta h_L^2 \rangle$ (dimensionless), and the x-axis is radial distance from the solute center of mass. Reproduced with permission from Shuching Ou, Di Cui and Sandeep Patel. "Liquid-Vapor Interfacial Properties of Aqueous Solutions of Guanidinium and Methyl Guanidinium Chloride: Influence of Molecular Orientation on Interface Fluctuations." *Journal of Physical Chemistry B.* **2013**, *117 (39)*, 11719-11731. Copyright 2013 American Chemical Society.

Chapter 5

ION SPECIFIC INDUCED FLUCTUATIONS AND FREE ENERGETICS OF AQUEOUS PROTEIN HYDROPHOBIC INTERFACES

5.1 Introduction: Connecting Liquid-Vapor Interfaces to Protein Hydrophobic Interfaces

The fundamental nature of interactions between ions, co-solutes, and proteins in aqueous solutions continues to garner attention [301, 302, 303] due to its importance in understanding protein denaturation [1, 2, 3, 4], folding, protein-protein interactions [6] to name a few examples. Hofmeister and others underlined the influence of inorganic salts on protein solubility [20, 21, 22, 23] and stability [304, 249], and eventually classified cosolutes to be either stabilizing (kosmotropic) or destabilizing (chaotropic) [129, 59, 61, 64, 65, 305, 249]. Important theoretical and experimental contributions reported in the literature resulted in the identification of some key factors for the influence of ions/cosolutes on protein stability [306, 1], like protein-cosolute interactions and the excluded volume effect [303, 307]. However, the mechanism by which ions/cosolutes stabilize proteins is not yet totally clear.

At the heart of specific-ion effects as related to protein denaturation is the molecularly-resolved interface between protein and aqueous solution; moreover, the nature of the differences in behavior of cations/anions at such interfaces (including both liquid-vapor interfaces and liquid-solute interfaces) weighs heavily on the interpretation and definition of these processes. Nowaday there are numerous studies regarding ion specific effects as embodied in differential stabilities of (halide) ions at liquid-vapor interfaces [70, 11, 128, 19, 92, 93, 10, 105, 23, 146, 281]. It has been widely accepted that larger halide ions such as I^- and Br^- tend to bind to liquid-vapor interfaces more

strongly and with lower transfer free energies than smaller, more charge-dense, and more strongly-hydrated Cl^- and F^- anions. In our previous chapter, we consider differential perturbations of liquid-vapor interface fluctuations by different anions and conclude that the surface stable ions induces larger interfacial fluctuations compared to the non-surface active species, thus demonstrating a strong correlation with induced interfacial fluctuations and (an)ion surface stability as observed from molecular simulations [92, 93]. Water molecules in the hydration shells of surface stable ions are shown to be more dynamic and less persistent compared to those in proximity to non-surface stable ions. When approaching the liquid-vapor interface, coupling of local solvent around (an)ions with solvent further away and near an interface leads to different perturbations of the interface according to the species, and thus different contributions to interface height fluctuations, and ultimately surface stability via contributions from interfacial entropy arising from surface fluctuations correlations.

However, this ion-specific effect is not necessarily restricted to the liquid-vapor interface; one might consider how the perturbation-inducing properties of different ions may play out generally in the vicinity of hydrophobic interfaces [1]. Heyda et al. [102] examined systems of N-methylacetamide (NMA) in the presence of monovalent cations and anions in water. The larger anions, I^- and Br^-, demonstrated preferential spatial correlation with the hydrophobic methyl group, which supports earlier experiments addressing the importance of the nonpolar methyl groups for the halide ion-NMA interactions [308]. Schweiss et al. studied the interfacial charge formation of self-assembled monolayers (SAMs) of thiol derivatives on gold and found the zeta potential [1] is strongly negative and depends on ion type and concentration [309]. Netz and co-workers investigated the potential of mean force for Na^+, Cl^-, Br^- and I^- to transfer from bulk aqueous solution to a hydrophobic SAM-water interface in an

[1] Zeta potential is the electric potential in the electrical double layer at the location of the shear plane versus a point in the bulk fluid away from the interface. In other words, zeta potential is the potential difference between the dispersion medium (Stern layer) and the stationary layer (diffusion layer) of fluid attached to the dispersed particle.

infinite dilution [310] and found that soft polarizable monovalent anions (I^- and Br^-) tended to accumulate around the hydrophobic interface [311]. Lund et al. probed the distribution of F^- and I^- around a spherical macromolecule using MD simulations [312] and found that when the nanosphere is uncharged and considered as a hydrophobic particle, the strong solvated fluoride ions are repelled while the poorly solvated iodide ions are weakly attracted to hydrophobic surface patches [313]. In the biological content, this ion-specific surface affinity is also ubiquitous. Friedman et al. examined three proteins in NaCl solutions via MD simulations and reported extended duration time near some domains of the proteins [314, 315]. The authors also concluded that binding of cations and anions to protein surfaces is heterogeneous, with the same amino residue demonstrating a wide range of binding probability to a particular ion. This heterogeneity stems from the (locally) heterogeneous environments found on protein surfaces [314, 316, 317], which is largely perturbed and defined by its spatially neighboring residues [318, 319]. Jungwirth and co-workers have further provided volumes of data on the nature of differential, or ion-specific, binding of cations and anions to protein surfaces [320, 321, 91, 313]. Particularly, by using lysozyme in the mixed aqueous solution of KCl and KI, Lund et al. found enhanced I^- density in close vicinity of the hydrophobic groups [321].

The above studies implied a connection of ion-specific behavior at aqueous liquid-vapor interfaces to those of possibly biochemical relevance (protein-water, bilayer-water, etc) [91]. In this chapter, we seek to explicitly address this connection between ideally hydrophobic aqueous liquid-vapor interface and the hydrophobic regions of proteins. Specifically, we will examine the induced interfacial fluctuations of single halide anions (Cl^- and I^-) and single guanidinium cations (with different orientations) as the ions approach the molecularly "large" hydrophobic patch of a rigid protein in aqueous environment. In the spirit of the previous chapters, we also seek to correlate the observed induced interfacial fluctuations to the free energetics (probabilities, or interfacial stability) of the ions near the hydrophobic protein region. We anticipate that similar qualitative trends and behaviors should arise in the biomolecular context as observed

for aqueous liquid-vapor interfaces.

Be that as it may, in the biological systems, due to proteins' inherent chemical and topographical heterogeneity, protein-water (or protein-solvent) interfaces are much more complicated than the model liquid-vapor interfaces. These heterogeneities account for different effective hydrophobicity around protein surfaces [322, 43], spanning the entire spectrum from hydrophilic to hydrophobic [318, 322]. Garde, Chandler and co-workers have done series of work regarding surfaces with different hydrophobicity [322, 43, 323, 324, 317]. By using the water density fluctuation as a measure/signature of hydrophobicity [2] , they found enhanced water density fluctuations (as reflected by the wider probability distributions of water number density) around hydrophobic surfaces. These enhanced water density fluctuations suggest a higher compressibility of hydration shells of hydrophobic surfaces [43, 325, 326], which is of interest because it correlates the volumetric properties of proteins to hydrostatic pressure [43] and the driving forces for assembly near surfaces with different hydrophobicity as well [322]. Additionally, since the long-ranged ion-induced perturbations of aqueous protein interfaces involve the coupling of local hydration shells of the ions with distant hydration shells around protein surfaces, the nature of the ionic hydration shells along with the distinct hydrophobicity of each protein region would affect the extent of induced interfacial fluctuations. Consequently, we would like to further connect this affinity (probabilities) differences of ions around protein surface with different hydrophobicity to their induced aqueous protein interfacial fluctuations correspondingly.

The particular protein we focus on in this study is hydrophobin-II (HFBII), which is a small protein with 71 amino acid residues expressed by filamentous fungi [327, 328]. Briefly the structure can be described as being nearly globular, having a central

[2] We note that the interface height fluctuations we are pursuing in this dissertation are conceptually different from the density fluctuations in their work, while both of them reflect/characterize the nature of hydration water around surfaces. This will be further addressed in the following section.

β barrel structure and a small segment of α helix. The diameter of HFBII is approximately 3 nm. The most notable feature of the protein was that one part of the surface consisted nearly entirely of hydrophobic aliphatic side chains, forming what was called "the hydrophobic patch" [329, 327]. Followed by the spirit of water density fluctuations, Acharya et al. [323] mapped the effective hydrophobic/hydrophilic regions of HFBII by considering the density of small probe hydrophobic solutes in the vicinity of each region of the protein. Their calculations showed that around most hydrophobic region, they observe the largest water density fluctuations whereas the least water density fluctuations were detected around most hydrophilic region. Considering of this, HFBII is an ideal candidate to compare the characters of interfaces with different hydrophobicity.

5.2 Method

Our study will focus on the connection of the ion-specificity at the liquid-vapor interface and protein-solvent interfaces. In this section, we discuss the simulation protocols of the systems including (1) a single $Cl^-/I^-/Gdm^+$ ion at different position relative to the liquid-vapor interface , (2) HFBII with a single Cl^-/I^- ion relative to different regions of the protein, and (3) HFBII with a single guanidinium cation.

5.2.1 Ion Translocation Across Aqueous Liquid-Vapor Interface

To accommodate the parameterized force field for the protein in this study, we chose the ion-water force fields that were not covered in the previous chapters. However, the results of anion-induced interfacial fluctuations are still consistent, as will be shown in the following sections.

5.2.1.1 Single Halide Anion

Molecular dynamics simulations were performed using the CHARMM package [148, 330]. Simulations of liquid-vapor interfaces were performed in the NVT ensemble. Temperature was maintained at T = 300 K using Nosé-Hoover thermostat [260]. A bulk slab consisting of 988 water molecules with a single anion (Cl^-,

I^-) was positioned in the center of the simulation cell. The simulation cell was rectangular with dimensions 24 Å × 24 Å × 100 Å , in which z is the direction normal to the liquid-vapor interface. Water molecules are represented by the nonpolarizable TIP3P model [331], with the O-H bond distance of 0.9572 Å and H-O-H bond angle of 104.52°. Point charges of oxygen and hydrogen atoms are q_{O} = -0.834e and q_{H} = +0.417e, respectively. The Lennard-Jones parameters for water oxygen and hydrogen atoms are $R_{\mathrm{min,O}}$ = 3.5364 Å, ε_{O} = 0.1521 kcal mol^{-1} and $R_{\mathrm{min,H}}$ = 0.449 Å, ε_{H} = 0.046 kcal mol^{-1}. A rigid water geometry is enforced using SHAKE [265] constraints.

The Lennard-Jones parameters for anions with TIP3P were taken from Cheatham et al. [332], which were parameterized in the AMBER force field [333]. We list these parameters in Table 5.1 along with the calculated binding free energies to verify their applicabilities in CHARMM. Non-bonded interactions were gradually switched off at interparticle distance of 11 Å, with a gradual switching between 10 Å (r_{on}) and 11 Å (r_{off}) via the switching function:

$$S(r_{ij}) = \begin{cases} 1 & r_{ij} \leq r_{\mathrm{on}} \\ \frac{\left(r_{\mathrm{off}}^2 - r_{ij}^2\right)^2 \left(r_{\mathrm{off}}^2 + 2r_{ij}^2 - 3r_{\mathrm{on}}^2\right)}{\left(r_{\mathrm{off}}^2 - r_{\mathrm{on}}^2\right)^3} & r_{\mathrm{on}} < r_{ij} \leq r_{\mathrm{off}} \\ 0 & r_{ij} > r_{\mathrm{off}} \end{cases} \tag{5.1}$$

Conditionally convergent long-range electrostatic interactions were treated using Particle Mesh Ewald (PME) [137] approach with a 30 × 30 × 128 point grid, 6th order interpolation, and κ = 0.33. Dynamics were propagated using a Verlet leap-frog integrator with a 1.0 fs timestep. In consistent with the previous chapters, we use the the reversible work (PMF) for transferring single ions/molecules from bulk aqueous environment to the aqueous solution liquid-vapor interface to describe the surface stability of the ions, with the Cartesian z-component of the separation between the water slab center of mass and ion position as the order parameter. We constructed continuous simulation windows with width 1.0 Å spacing with the umbrella sampling technique. In each window, single anion was restrained to z-positions

from 10 Å to 35 Å relative to the water slab center of mass using a harmonic potential $U_{\text{restraint}}(z; z_{\text{relative,ref}}) = \frac{1}{2}k_{\text{restraint}}(z - z_{\text{relative,ref}})^2$ with the force constant of 4 (kcal/mol)/Å^2, this encompassed a range approximately 15 Å below the GDS to approximately 10 Å above it. Total sampling time for each window was 30 ns; properties were calculated from all but the initial 1.0 ns, which was treated as equilibration.

5.2.1.2 Single Guanidinium Cation

Simulations for single Gdm^+ with liquid-vapor interfaces were performed in the NVT ensemble with NAMD 2.9b3 [259, 334]. The temperature was kept constant at 300 K by applying the Langevin friction force scheme with a damping coefficient of 5ps^{-1}. A bulk slab consisting of 1977 TIP3P water molecules with a single Gdm^+ was positioned in the center of the simulation cell. The parameters were retrived from CHARMM22 all-atom force field with CMAP backbone torsion correction term [335]. The simulation cell was rectangular with dimensions 40 Å × 40 Å × 150 Å, with z as the direction normal to the liquid-vapor interface. Periodic boundary conditions were applied in all three spatial directions. A rigid water geometry is enforced using SHAKE [265] constraints. Particle Mesh Ewald (PME) was implemented to treat conditionally convergent long-range electrostatic interactions using a grid of $40 \times 40 \times 150$ points. Non-bonded interactions were gradually switched off at interparticle distance of 12 Å, with a gradual switching between 10 Å and 12 Å via the switching function.

The cation was restrained to z-positions from 0 Å to 30 Å relative to the water slab center of mass using a harmonic potential with the force constant of 4 (kcal/mol)/Å^2, which encompassed a range of 18 Å below the GDS to approximately 12 Å above it [3]. 30 consecutive simulation windows with width 1.0 Å spacing with the umbrella sampling technique were constructed for PMF calculations. From our previous chapters, we noticed that the orientation of Gdm^+ relative to the liquid-vapor

[3] The simulation setup is different from the single spherical ions but consistent with the previous simulations of single Gdm^+/M-Gdm^+ using polarizable CHEQ force field, in order to provide a comparable results between the force fields.

interface led to different degrees of interfacial fluctuations, along with different surface stabilities/affinities. In this chapter, based on the definition of the orientation (the cross product of arbitrary two carbon-nitrogen vectors), we additionally restrained the orientation of the cation by applying a harmonic potential with the force constant of 1000 (kcal/mol)/Å^2 on each carbon-nitrogen vector relative to the positive z-dimension. Consequently, we retrived the (conditional) PMF of the Gdm^+ with only parallel/perpendicular orientation relative to the liquid-vapor interface.

A timestep of 1.0 fs was used to integrate the equations of motion. The production simulation for each window (of each orientation) is 15 ns; properties were calculated from all but the initial 1.0 ns, which was treated as equilibration.

5.2.2 HFBII with Single Ion

Simulations of a single, solvated HFBII were performed with NAMD, version 2.9b3 [334, 259] using the CHARMM22 all-atom force field with CMAP backbone torsion correction term [335]. NPT ensemble simulations were performed using a cubic cell with a box size 60 Å × 60 Å × 60 Å. In this case, we consider only protein-water interfaces by eliminating liquid-vapor interfaces. The initial structure of the protein was constructed using CHARMM-GUI [336]. The protein structure was based on the ultra-high resolution structure at 0.75 Å of hydrophobin HFBII, with PDB code 2B97 [337]. The original crystal structure was actually the dimerization complex of the protein. Only one monomer, composed of 70 residues, was modeled in this study. The protein was placed in the center of the box, with center-of-mass located at (x = 0 Å, $y = 0$ Å, $z = 0$ Å), the rest of the box was filled with 6481 TIP3P water molecules and a single ion (Cl^-/I^-/Gdm^+), transferring from bulk to the protein interfaces. Temperature was maintained by Langevin bath at 300 K, and the pressure was kept constant by Langevin pressure control at 1 atm. A switching distance of 10 Å, non-bonded real-space cutoff of 12 Å and pairlist generation distance of 14 Å were used for the van der Waals interactions. The particle mesh Ewald (PME) method was employed for the calculation of conditionally convergent electrostatic interactions, with the grid

size 60 × 60 × 60 in (x, y, z)-dimensions. The SHAKE algorithm was used to constrain bond lengths involving hydrogen atoms and an integration time step of 1.0 fs was used. The protein was fixed throughout the simulations with other components could move randomly.

A representative snapshot of the simulation system can be found in Figure 5.1 a. HFBII protein was arranged in a way that its largest hydrophobic patch, consisting of VAL18, LEU19, LEU21, ILE22, VAL24, VAL54, ALA61, LEU62 and LEU63 (shown in Figure 5.1 b), was nearly perpendicular to the z-direction. This selection of residues, is common among literature [329, 338, 327, 339]. To study the protein surfaces with different hydrophobicity, we selected a less hydrophobic region (including residues ILE31, ALA32, ASP34, ILE38, ALA41, HSD42, SER45, as shown in Figure 5.1 c) and a hydrophilic region (including residues ASP25, CYS26, LYS27, THR28, ALA58, ASP59, GLN60, as shown in Figure 5.1 d). These selections, though arbitrary, were based on their geometry (nearly flat) and composition of residues. As shown in Figure 5.1 c and d, the less hydrophobic region included less non-polar residues than the hydrophobic patch, while the hydrophilic region was mainly composed of residues other than non-polar ones. For these two scenarios, the simulation conditions remained identical to those in the hydrophobic patch calculations, except that the protein was oriented in a different way such that the corrsponding interface is arranged perpendicular to the positive z-dimension.

The simulation systems for HFBII with single ions are shown in Figure 5.2. We next address other simulation details about the restraints for single halide anions and single Gdm^+ cation separately.

5.2.2.1 Single Halide Anion

A single Cl^-/I^- was added in the solution with one counter ion, K^+, to neutralize the negative charge of the monovalent anion. The K^+ was fixed at position (x = 0 Å, y = 0 Å, z = -15 Å), in which we consider sufficiently far from the surface/region of

interest to prevent from the perturbation induced by K^+. The paramters for ion-water interactions were taken from Cheatham et al. [332].

Similar to the liquid-vapor interface situation, for calculation of PMF, we consider the Cartesian z component of the separation between the center of mass of protein and center of mass of the single Cl^-/I^- as the order parameter for the present umbrella sampling MD simulations. Single Cl^-/I^- was aligned along the z direction, approaching the specific spot on the patch with position $x = 0$ Å and $y = 0$ Å by freezing the orthogonal degrees of freedom along x-axis and y-axis via the use of strong restraining potentials. We center on one specific region of the patch, acknowledging that the heterogeneity of the protein surface necessitates some care in interpreting the results, which we will address further below.

For a meaningful discussion and interpretation of ion-induced fluctuation (interface fluctuation in addition to the level present in pure water) as the ion approaches the interface, one reference location with fixed position has to be defined. x and y components of the ion was restrained at $x = 0$ Å, $y = 0$ Å with a force constant of 1000 (kcal/mol)/Å^2. Along the z-axis, we constructed 46 continuous umbrella sampling windows with width 0.2 Å along the positive z-direction ranging from area around protein-solvent interface to bulk water region. The spans of the windows going from interfacial region to bulk region (unit in Å) were: [16.0:16.2], [16.2:16.4], [16.4:16.6] ..... [24.4:24.6], [24.6:24.8], [24.8:25.0]. We consider this range of ion position (from 16 Å to 25 Å) sufficient to probe the differences of single ion around interface and that in bulk water region, while minimizing the number of windows that is required to construct. In each simulation window, a harmonic restraint potential with force constant of 10 (kcal/mol)/Å^2 was applied on Cartesian z component of the ion. The first 2 ns was allowed for equilibration before a total of 20 ns production data was generated for each window.

For comparison, we performed another set of simulations to compute the PMF of the anion approaching the hydrophobic patch using average force integration method; in these simulations, both anion and protein are held fixed so as to realize a series of

center of mass separation distances; the PMF is then obtained by integration of the average force along the order parameter (i.e., z) obtained from simulation trajectories. Furthermore, to attempt to consider effects of protein motion on ion-induced interface fluctuations, we performed simulations with protein under restraint conditions instead of atom-fixed constraints. HFBII was placed in the center of box with exactly the same starting structure as in the fixed/rigid scenaraio. During the simulation, the protein was strongly restrained to remain in a single orientation and its center of mass at a specific position, chosen as (x = 0 Å, y = 0 Å, z = 0 Å) via the use of strong restraining potentials. Using NAMD's collective variable infrastructure, HFBII's center of mass was restrained at (x = 0 Å, y = 0 Å, z = 0 Å) using a force constant of 5000 (kcal/mol)/Å^2, and its orientation was restrained about the crystal based orientation using a harmonic restraint potential with force constant of 5000 (kcal/mol)/Å^2. Single Cl^-/I^- was fixed along positive z axis, starting from z = 16 Å to z = 25 Å, a total of ten continuous windows with width 1.0 Å. We note that PMF calculations will not be concerned in the restrained protein case since it requires extensive simulation time for a well-converged PMF with flexible protein. Instead, we are only interested in the comparison of ion-induced interfacial fluctuations of total fixed protein and restrained moving protein as Cl^-/I^- locates at particular separations along the reaction pathway.

5.2.2.2 Single Guanidinium Cation

A single Gdm^+ cation was placed in the system along the reaction pathway (center-of-mass distance between HFBII and the Gdm^+ cation) with a fixed Cl^- (at x = 0 Å, y = 0 Å, z = -15 Å) as the counter ion. The parameters were obtained from CHARMM22 force field [4].

For PMF calculations, we also use the center-of-mass difference between HFBII and Gdm^+ as the order parameter, with the simulation windows spanning from 15.4 Å

[4] Here the parameters for Cl^- were also from CHARMM22 force field instead of the parameters from Cheatham et al. However, since the Cl^- is sufficiently far from the hydrophobic patch, we consider this difference negligible.

to 25 Å, with the width 0.2 Å along the positive z-direction. Gdm^+ and HFBII are totally fixed throughout the simulation, and the PMF was computed via force integration method. The first 2 ns was allowed for equilibration before a total of 15 ns production data was generated for each window. In order to consider the orientational effects of Gdm^+, we specifically studied three configurations ("parallel", "perpendicular-x" and "perpendicular-y") of Gdm^+ plane relative to the protein patch. Since the hydrophobic patch is oriented perpendicularly to z-axis in this work, the "parallel" configuration then refers to the normal vector axis of Gdm^+ is along the z-axis, as illustrated in Figure 5.2 b; the "perpendicular-x" and "perpendicular-y" configurations then indicate the respective dimension of the normal vector of the Gdm^+, as shown in Figure 5.2 c and d. Here, although the protein patch is commonly considered "flat", it still has some curvature. Hence strictly speaking, the actual "parallel" or "perpendicular" orientations of Gdm^+ plane relative to the protein patch are not applicable. However, in this work, we aimed to study the contrasting hydration properties and surface fluctuations induced from different partition of Gdm^+ (i.e., water-depleted flat faces versus the side of the cation) with the hydrophobic patch of the protein. Therefore in this convention, "parallel orientation" simply indicates that Gdm^+ has more overlap with the protein patch in terms of their projection to xy-plane, relative to the "perpendicular orientation".

5.2.3 Calculating Surface Height Fluctuations

In the previous chapters, we have already discussed the protocol to construct instaneoue liquid-vapor interface. In brief, we set up series of grid points in the simulation box, sum the distance-based density contribution of water molecule in the system as the instaneous density of each grid point. Then the interface is determined as the $(d-1)$-dimensional manifold with a reasonable constant value c.

In practice, some differences arise to construct the liquid-vapor interface and liquid-protein interface in this work considering the shape of the liquid-vapor interface is flatter while protein-water interface possesses some curvature. Therefore, we select

Cartesian coordinate system to construct the liquid-vapor interface and spherical coordinate system for protein-water interface. For the liquid-vapor interface, coordinate (x, y, z) for each grid point in space is set up and the surface is obtained as the manifold by setting $\rho(x, y, z) = \rho_{\text{bulk}}/2$. That is, for a specific (x, y) coordinate set in 3-dimensional space, it defines a line which is parallel to the z-axis. Along this line, if water density of one point satisfies condition $\rho(x, y, z) = \rho_{\text{bulk}}/2$, then this point is assigned to the interface. This instantaneous surface is denoted as ($h_{\text{t}}(x, y)$, at time t). We can average these instantaneous surfaces to obtain the mean surface $\langle h(x, y)\rangle$ and furthermore, subtracting the mean values from the $h_{\text{t}}(x, y)$, we obtain $\delta h_{\text{t}}(x, y)$ as surface height and the height fluctuations $\langle \delta h^2(x, y)\rangle$.

For protein-water interface, grid points in space are defined by (r, θ, ϕ) and for a specific (θ,ϕ) coordinate set in the spherical system, it defines a radius vector. r is the radical distance of end point of the radius vector from the origin $(0, 0, 0)$ (which overlaps with the center-of-mass of the protein); θ is polar angle, which is defined as intersection angle between the radius vector and the positive z vector; and ϕ is azimuthal angle defined by the positive x dimension and orthogonal projection of the radius vector on xy plane. The spherical coordinates (r, θ, ϕ) of a point could be derived from its Cartesian coordinates (x, y, z) by the following formulas: $\mathbf{r} = \sqrt{x^2 + y^2 + z^2}$, $\theta = \arccos(\frac{x}{r})$ and $\phi = \arctan(\frac{y}{x})$. Points are defined to belong to the interface if $\rho(r_0, \theta, \phi) = 0.6\rho_{\text{bulk}}$ [5]. We note that other parameter sets, ξ and d remain the same. Correspondingly, instantaneous protein interface can be expressed as $(h_{\text{t}}(\theta, \phi))$, mean surface as $\langle h(\theta, \phi)\rangle$, surface height as $\delta h_{\text{t}}(\theta, \phi)$ and height fluctuation as $\langle \delta h^2(\theta, \phi)\rangle$.

We evaluate the inherent fluctuations (with the absence of ions) of different interfacial regions of the protein as reference. Figure 5.3 shows a colored map of HF-BII protein interface based on the magnitude of interface fluctuations in TIP3P water. The color scheme from red to blue represents fluctuation spectrum from higher to lower

[5] We use a different constant value c here compared with liquid-vapor interface case because this choice will result in a more unambiguous construction of protein-solvent interface.

values. Since there are no other impurities in the system, the inherent interface fluctuations are derived from the thermal fluctuations of the water. As shown in Figure 5.3 a, regions defined as the hydrophobic patch possess the largest fluctuations while the selected hydrophilic interfaces in Figure 5.3 d manifest the lowest fluctuations. The less hydrophobic interface (Figure 5.3 c) displays a moderate fluctuation. This suggests that the magnitude of interface fluctuation correlates well with the surface hydrophobicity. This is consistent with Garde's insights [322, 43, 323, 324, 317] that density fluctuations are enhanced near hydrophobic surfaces while reduced with increasing hydrophilicity. This enhanced density fluctuation is explained as a consequence of more facile cavity formation, increased compressibility of hydration water, and more favorable binding of hydrophobic solutes. Although in this work the fluctuation we address is based on the aqueous protein interface height, which is not exactly the same as water density fluctuation Garde et al. applied, it reflects similar information about the malleable nature of the water around hydrophobic patch, considering that the aqueous protein interfaces we construct were based on the coarse-grained solvent densities at each space-time point.

5.3 Single Halide Anion: PMF and Surface Fluctuations

5.3.1 Validation: Anions at Liquid-Vapor Interfaces

We start by looking at the free energetics of single Cl^-/I^- across the liquid-vapor interface. Results of PMF for Cl^- and I^- are shown in Figure 5.4 a. For clarity, we added a vertical offset of 0.1 kcal/mol for the Cl^- case. To better compare the interface stability between the two anions, in Figure 5.4 a we emphasized the PMFs around the interfacial region while the whole PMFs along the reaction pathway can be found in the inset. The PMF is defined to be zero in the bulk (which is determined by window $z = 10$ Å). I^- has a slight PMF minimum (≈ 0.05 kcal/mol) prior to the GDS (Gibbs dividing surface is around $z = \pm 25.5$ Å in this case). Due to the uncertainty reported, whether I^- shows surface stability is ambiguous. However, we notice that there is a barrier (around $z = 19$ Å) prior to the PMF minimum, which

is also observed in other studies [10, 92]; as a result, although being less explicit than the interfacial stability reported in experiments and other force fields [70, 11, 128, 19, 93, 92], qualitatively we consider that I^- exhibits a surface-stable state in the current simulations. In contrast, Cl^- is repelled from the L-V interface in the current and other force fields [92]. Consequently, we consider Cl^- to be interface unstable, and I^- as having liquid-vapor interface stability with the current force field, consistent with the previous chapter. In this work, we stress that we are not focusing on the exact values of free energetics of single Cl^-/I^- adsorption at the liquid-vapor interface, but rather we want to emphasize the interfacial stability difference between Cl^- and I^- and related physical and structural properties. More importantly, we would like to connect these behaviors of ion-specific at aqueous liquid-vapor interfaces to those of more general aqueous protein hydrophobic interfaces. The nonpolarizable water model and nonpolarizable protein parameters combination would clarify these issues with the benefit of saving computational resources compared with the polarizable force fields. In light of this, we argue that the current force field we are applying is sufficiently robust and appropriate.

In previous chapters, it is found that the species demonstrating an interfacial stability appear to enhance liquid-vapor interfacial fluctuations significantly, while those that show no interfacial stability induce no further fluctuation (or may even suppress levels of fluctuations). Here we explore the differences in interfacial fluctuations for the two anions discussed in the current simulations. From our previous chapters, the geometry of the fluctuation $\langle \delta h^2(x,y) \rangle$ is radially symmetric, with the largest value at the center $x = 0$ Å, $y = 0$ Å (right towards the ion). For convenience, we use $\langle \delta h^2(x=0, y=0) \rangle$ to compare the magnitude of interface fluctuations when Cl^-/I^- are restrained at different z-positions, with the result shown in Figure 5.4 b. The fluctuation profile is normalized by the fluctuation value in pure water (i.e., the system in the absence of the ion, which has a value of 0.77 Å^2). In this convention of normalized surface fluctuation ($\langle \delta h_{\mathrm{L}}^2 \rangle$) we extract the ion-induced contribution from each species at different z-position. When $\langle \delta h_{\mathrm{L}}^2 \rangle$ equals 1, the effect of ion is zero; when $\langle \delta h_{\mathrm{L}}^2 \rangle > 1$,

the surface height fluctuation is enhanced relative to pure water with the presence of ion; when $\langle \delta h_L^2 \rangle < 1$, the surface height fluctuation is suppressed. No obvious enhancement of surface fluctuations is associated with Cl^-; on the other hand, I^- induces larger fluctuation, with the maximum normalized fluctuation value around 1.5 at the location of $z = 21$ Å, which is before the position of the free energy minimum. Also presented in the inset is the time profile of $\langle \delta h_L^2(x = 0, y = 0) \rangle$ for I^- at the window $z = 21$ Å (which possesses the largest surface fluctuation) to show the convergence of the fluctuation.

Previously, by studying a wide variety of force fields (polarizable and nonpolarizable), our results [92] suggest a threshold value of the maximum normalized interfacial fluctuations about 1.5 dividing those ions that are interfacially stable and those that are not. The largest normalized fluctuation and ΔG in current work for I^- are 1.55 (unitless) and -0.03 kcal/mol, just barely placing it on the critical/transitional position in Figure 3.6. For Cl^-, we found the maximum fluctuation is 1.1 and the corresponding $\Delta G = 0.52$ kcal/mol, which falls in the quadrant for non-surface stable species. It indicates that in terms of the surface stability, the current force fields for anionic behavior is consistent with other force fields. The differential behavior of the two ions at the pure aqueous liquid-vapor interface, consistent with previous studies, thus provides the control needed to interpret the simulations in a protein context.

5.3.2 Free Energetics for Anions with Protein Surfaces

The umbrella sampling molecular dynamics PMF for both anions approaching the hydrophobic patch are shown in Figure 5.5 a; large values of the x-axis represent large separation of anion and protein center-of-mass, and the PMF's are referred as zero at large separation. For Cl^-, there is a small barrier around $z = 19.5$ Å, followed by a shallow minimum around $z = 18.5$ Å; a similar trend is seen for I^-, with a small barrier around $z = 20.5$ Å and a minimum afterward. For Cl^-, the PMF minimum is -0.06±0.05 kcal/mol; for I^-, it is -0.08±0.04 kcal/mol (as emphasized in the inset with the uncertainties). In light of the uncertainty estimates, both Cl^- and I^- exhibit little

stabilization at the hydrophobic patch. However, as the single Cl^-/I^- draws near the interface, significant differences arise. The Cl^- PMF starts to increase monotonically; the I^- PMF shows a slightly more complex trend. Unlike the situation of Cl^-, the PMF profile of I^- shows a second minimum, which is a little more repulsive (0.20±0.04 kcal/mol) than the first one. At this second minimum position, the free energetic difference between Cl^- and I^- is about 0.78±0.09 kcal/mol, even with the consideration of the uncertainty. This implies that close to the hydrophobic protein interface, I^- tends to be more interfacial stable than Cl^-, although compared with bulk, neither of them displays the stabilization effect around the interface within the context of the current force field.

We next process single Cl^-/I^- approaches the aqueous protein interfaces with different hydrophobicity. Figure 5.5 b presents the PMF for single Cl^-/I^- approaching the less hydrophobic protein-solvent interfaces. The PMF shows a minimum of -0.06±0.04 kcal/mol for the single Cl^- and -0.16±0.04 kcal/mol for the single I^- at position around 20 Å for both, which is further emphasized in the small inset. The main differences in PMF between Cl^- and I^- appear in the range from $z = 15.5$ Å to $z = 17.0$ Å. Unlike the Cl^- PMF in this range, which continues increasing, there is a minimum in the PMF profile for I^-. Consistently, the PMF for I^- shows slightly higher stability than that of Cl^- in this range. Overall, the free energetic signature of I^- near the less hydrophobic region is similar to the case of hydrophobic patch. Figure 5.5 c shows the PMFs for Cl^- and I^- approaching the hydrophilic region. The PMF shows a global minimum of -0.35±0.06 for single Cl^- and -0.24±0.05 for single I^- at position 14.7 Å and 15.1 Å respectively as they approach the hydrophilic protein-solvent interfaces. They suggest a modest stabilization effect from both Cl^- and I^- as they are in the vicinity of the hydrophilic region around protein interfaces.

In summary, the PMF as single Cl^-/I^- approaches three different regions on the protein interfaces with different hydrophobicity, we find significant differences arising as single Cl^-/I^- is close to the interfaces from $z = 14$ Å to $z = 17$ Å. For Cl^-, when it is

close to the hydrophobic and less hydrophobic region, there are (effectively) no free energy minima, with the free energy values being positive/repulsive. For I^-, although the free energy values are still positive/repulsive, they are lower (with the largest difference about 1 kcal/mol) than those of Cl^-. Minima are observed in this region for the I^- but not for Cl^-. However, around hydrophilic interfaces, both Cl^- and I^- have minima. This reflects the fact that for both Cl^- and I^-, there are more free energetic advantages as they are close to the hydrophilic regions, compared with the hydrophobic ones of HFBII protein, which may due to the favorable direct anion-charged residue interactions around the hydrophilic protein interfaces. Interestingly, our results of PMF for Cl^-/I^- when they are around hydrophobic and hydrophilic residues of HFBII protein follow the similar trend for the previous published work by Lund et al. [312]. They compared the free energetics of F^- and I^- around a spherical model macromolecule. Here, F^- is a small, highly charge-dense and fully hydrated anion similar to Cl^-. They suggest that when the macromolecule is uncharged and considered as a hydrophobic particle, I^- has more free energy advantage than F^- for being near the interface. When the macromolecule is positive charged and considered as a hydrophilic particle, the trend reverses, F^- is more favorable around the macromolecule. Also, comparing the free energetics of the same anion around the hydrophobic and hydrophilic sphere, Lund et al. find that both F^- and I^- are more stable around the hydrophilic particle.

Since the two anions display distinct free energy profiles nearing the interface, we next consider the induced fluctuations associated with the approach of these ions in the spirit of earlier chapters.

5.3.3 Surface Fluctuation

Unlike the liquid-vapor interface, due to the heterogeneous features of the protein surface, the extent of induced fluctuation is not perfectly symmetric. However, judging from Figure 5.6, we could find that ($x = 0$ Å, $y = 0$ Å), which corresponds to ($\theta = 0$, $\phi = 0$), is a feature point displaying largest induced fluctuations compared with other regions on protein surface as anions locate at interested separations ($z = 18$ Å).

To better illustrate the change in interface fluctuation magnitude as single anions move toward the point ($x = 0$ Å, $y = 0$ Å), we plot $\langle \delta h^2(x = 0, y = 0) \rangle$ along the reaction pathway in Figure 5.5 d-f.

Shown in Figure 5.5 d, as single Cl^-/I^- approach the hydrophobic patch, ion-induced perturbations of the aqueous interface around protein surface are more pronounced. Right above the position ($x = 0$ Å, $y = 0$ Å) where single anion approaches the hydrophobic patch, we notice that fluctuations induced by I^- are much larger than those induced by Cl^-. As single anions move closer to the interface ($z = 16$ Å), this large difference of fluctuation between Cl^- and I^- lessens. These features are similar with what we discovered when the single anions approach liquid-vapor interfaces. When the ion is far from the protein, i.e., the bulk state ($z = 25$ Å), $\langle \delta h^2(x = 0, y = 0) \rangle$ is around 0.19 $\mathring{A}^2$ for both Cl^- and I^-, which corresponds to the protein interface inherent fluctuation in the pure water due to the thermal fluctuations. We use the same convention to normalize surface fluctuation by defining the fluctuations when the ion is far from the interface as the normalization factor, and define $\left\langle \delta {h_L}^2(x = 0, y = 0) \right\rangle$ as the normalized fluctuation value, as presented in Figure 5.5 g. For Cl^-, only slight enhancement of fluctuation was observed at $z = 17.5$ Å, with a normalized value of 1.36. In stark contrast, for the case of I^-, onset of enhanced fluctuation relative to the bulk occurs at $z = 22$ Å. As I^- moves closer to the hydrophobic patch, induced fluctuation continue increasing and this enhancement reaches a maximum with a normalized value around 3.0 while I^- is located at $z = 18$ Å. Finally, the fluctuation is lower compared to the bulk when the anion is close enough to the interface. Comparing the trends of surface fluctuation as single Cl^-/I^- move toward the hydrophobic protein interface and liquid-vapor interface, we find that in both cases the fluctuation is enhanced with presence of I^-; however, there is only marginal perturbation of the interface by Cl^-.

Again, we consider this results manifest from the different malleability hydration shells of Cl^-/I^-. Cl^- presents a more rigid hydration environment, thus decreasing the efficacy of promoting interfacial fluctuations; I^-, in contrast, possesses the first hydration shell that is weakly-bound and less-ordered, so that its solvation shell has

more tendency to couple with the protein interface, consequently inducing a larger interface fluctuation. In the previous chapters, we have demonstrated a connection between liquid-vapor interfacial stability of chemical species and the extent to which the presence of these molecular species in the vicinity of the interface induces collective fluctuations of the interface in addition to the level inherent in pure water due to thermal motion. Here, we would like to also use the induced protein interface fluctuation difference for Cl^- and I^- to explain their deviations in free energy of transferring to the hydrophobic patch. When the ion is approaching the interface, due to partial dyhration, favorable interaction energy between ion and water is reduced, therefore increases the free energy enthalpically. However, for the I^-, since larger interface fluctuations are induced as the ion approaches, this provides a favorable surface entropy contribution/compensation. This advantageous increase of entropy will compensate for the unfavorable enhancement of enthalpy, resulting the decrease of total free energy at some point; for the Cl^- case, due to the negligible enhancement of induced interface fluctuation, the entropic contribution is not sufficient for balancing the enthalpic loss, so the total free energy keep increasing as the ion moves toward the protein.

Figures 5.5 e and f show fluctuation profiles as Cl^-/I^- approach the less hydrophobic and hydrophilic protein interfaces. We note that the fluctuations for the anion far from the protein interfaces, which are also the inherent fluctuation values as the normalization factors, are distinct. For the hydrophobic patch, this value is 0.19 $Å^2$; for the less hydrophobic and hydrophilic regions, the inherent values are 0.11 $Å^2$ and 0.067 $Å^2$, respectively. Again this is conceptually consistent with Garde's argument that density fluctuations are enhanced near hydrophobic surfaces while reduced with increasing hydrophilicity [322, 43, 323, 324, 317]. In the case of less hydrophobic interface (Figure 5.5 e), the anion-induced behavior is qualitatively consistent with the case of anion approaching the hydrophobic patch (Figure 5.5 d), for both Cl^- and I^-. As single Cl^-/I^- moves closer to the less hydrophobic interface, I^- induces more interfacial fluctuation than Cl^-, especially in the range from z = 18 $\mathring{A}$ to z = 19 $\mathring{A}$.

Intriguingly, the largest, normalized fluctuation for I^- near the less hydrophobic interface (Figure 5.5 h, about 3.2) is greater than the largest, normalized fluctuation for I^- near the hydrophobic patch (Figure 5.5, about 3.0). However, in terms of the absolute magnitude, the difference (between the largest fluctuation and the state when anion is in the bulk) induced by I^- near the less hydrophobic interface is 0.25 $Å^2$, which is less than the value of 0.35 $Å^2$ for I^- at the hydrophobic patch.

In the case of the hydrophilic interface (Figure 5.5 f), both Cl^- and I^- have inappreciable effect on hydrophilic interfacial fluctuations. Although I^- may induce a little larger fluctuation compared with Cl^- as it moves closer to the interface, the differences are quite small and neglgible. In this picture, our suggestion is that the extent of the difference is highly related to the nature of the protein interface. The hydrophilic interface borders a rigid water environment that is difficult to couple with both the hydration shells of Cl^- and I^-. Consequently, Cl^-/I^- approaching the hydrophilic interface induce marginal interfacial fluctuations, and the difference between induced fluctuations of the two anions is less; however, for the hydrophobic interface and less hydrophobic interface we defined, the water shells around these regions are malleable, so they can exchange solvation water with that of I^-, which also possesses a less rigid solvation shell. However, due to the more severe ordering of water around Cl^-, it is not possible for water around hydrophobic interface to perturb the solvent around Cl^-. Therefore, as Cl^- and I^- approach this type of hydrophobic interface, significant differences appear in their ability to induce hydrophobic interfacial fluctuations.

5.3.4 The Effect of Protein Flexibility

Since the real proteins in biological system are not motionless, it is meaningful to address whether the different perturbations of interfacial fluctuations induced by Cl^- and I^- persist with the protein flexibility. Instead of freezing all protein atoms, we allow modest vibrational degrees of freedom of the protein, as discussed in the Method section. For the convenience of evaluating the interface fluctuation around specific

regions of the protein in the external coordinate system without worrying about translation and rotation of the protein in space, translational and rotational motions of the protein were first removed from the MD trajectory by using 'MERGE ORIENT' module of CHARMM. The root-mean-square deviation (RMSD) values based on the backbone protein atoms are less than 2.5 Å in all cases as Cl^-/I^- locate around protein surface and in the bulk. Aqueous protein interface was constructed using new trajectories based on the same protocol in Method section. Figure 5.7 shows the hydrophobic interface fluctuation profiles at $x = 0$ Å and $y = 0$ Å as a function of z-position of Cl^- and I^- approaching the flexible protein. When the single anion is far from the patch, fluctuation is about 0.3 $Å^2$ for both anions, higher than the inherent fluctuation of the interface around the fixed protein, which is about 0.2 $Å^2$. This indicates that the inherent fluctuation of the protein interface is not only derived from thermal motion of water, but also from that of protein itself. Consistent with the fixed protein outcomes, I^- induces larger fluctuations than Cl^- nearing the hydrophobic patch, with the maximum value of 0.56 $Å^2$ higher than that of Cl^- 0.43 $Å^2$ at the location of $z =$ 20 Å.

5.4 Single Guanidinium Cation: PMF and Surface Fluctuations

Results of PMF for Gdm^+ approaching liquid-vapor interfaces are shown in Figure 5.8 a. A vertical offset of 1 kcal/mol is added between the conditions for clarity. The PMF is defined to be zero when the cation is in the bulk, which is determined by window $z = 0$ Å. Consistent with the previous results, the parallel orientation shows a minimum of -0.47 kcal/mol (the uncertainty is about 0.1 kcal/mol) prior to the GDS, while the perpendicular orientation displays no surface stability at the liquid-vapor interface. Overall, when there is no orientational restraint applied on the Gdm^+, no surface stability is found near the interface. The corresponding, normalized fluctuation profiles using $\langle \delta h_L^2(x = 0, y = 0) \rangle$ as functions of the cation restained z-position, are presented in Figure 5.8 b. The normalization factor here is 1.32 $Å^2$. It is evident that the parallel orientation possesses a significant enhancement of $\langle \delta h_L^2 \rangle$ (up to about 2.1

when $z = 14$ Å), while the perpendicular orientation shows no enhancement.

The PMF's and corresponding interface fluctuation of Gdm^+ approaching the HFBII hydrophobic patch are shown in Figure 5.9. We reiterate that the orientations (parallel, perpendicular-x and perpendicular-y) are simply defined via the normal vector of the Gdm^+ plane, and are approximate configurations relative to the hydrophobic patch. As the cation approaches the patch, the parallel configuration has a significant PMF minimum with a value of -2 kcal/mol, near $z = 15.8$ Å, as displayed in Figure 5.9 a. This feature is similar with I^- (Figure 5.5 a). The perpendicular-y configuration shows a slight minimim (at $z = 16.4$ Å) after a barrier ($z = 17.4$ Å), but still positive throughout the reaction pathway. The PMF of perpendicular-x configuration increases monotonically. In general, the features of both perpendicular orientations are similar with the case of Cl^- as the ion approaches the hydrophobic patch. The induced fluctuations of the different orientations are also consistent with our previous argument, as presented in Figure 5.9 b. The parallel orientation induces up to 5 times of the inherent interfacial fluctuation (0.19 $Å^2$), while the perpendicular orientations can induce much smaller fluctuations.

As discussed in the previous chapers, these different effects of fluctuations are originated from different "malleability" of the solvation shells. Due to its planarity, aromaticity, and nonuniform charge distribution, the faces of the Gdm^+ cation are hydrophobic and weakly hydrated, with guanidinium forming hydrogen bonds with water molecules exclusively in the plane [288]. Consequently, as a configuration with "higher hydrophobicity", the parallel orientation of Gdm^+ is preferred to reside in the vicinity of the hydrophobic patch. Similarly, England et al. did a study of hydrophobic dewetting [6] between nonpolar plates in GdmCl and urea aqueous solutions via MD simulations. They found that both GdmCl and urea stabilize the liquid phase between

[6] Dewetting is the evacuation of the liquid phase between two hydrophobic surfaces that takes place when the interplate separation becomes small enough that the surface tension of the liquid next to the plates overwhelms the bulk pressure of the surrounding bath.

the plates, and that Gdm^+ does so by flattening itself against the hydrophobic surfaces of the plates [286]. Godawat et al. also observed the same coating phenomenon in a simulation of the solvation of a model hydrophobic polymer [340].

Unlike the guanidinium cation, although urea appears to be more likely to aggregate into nanosized clumps [297, 286], both England et al. [286] and Zangi et al. [63] demonstrated that urea also stabilizes a hydrophobically confined liquid phase against dewetting. Koishi et al. showed that, near the surface of a hydrophobic plate, urea tends to show weaker surface stability and orientational dependence compared with guanidinium cation [295]. It will then be interesting to study the effect of urea with biologically hydrophobic interfaces, in order to provide more insights to our argument.

5.5 Discussion and Conclusions

Building upon the insights gained from the vast studies of specific ion behaviors at aqueous liquid-vapor interfaces, we have presented here a discussion regarding the unique fluctuation inducing properties of two anions as well as two orientations of Gdm^+ for which the degree of induced interfacial fluctuations correlates with stability at the interface. Our major conclusions are for hydrophobic protein-water interfaces, and this particular nature of the interface is chosen as it is a logical extension of the ideally hydrophobic interface presented by the aqueous liquid-vapor context. At the interface between a hydrophobic region of a protein, in this case HFBII, and the aqueous solvent, we find that I^- (as a less charge-dense species with more malleable solvation shell) has a stronger surface stability and larger induced fluctuations than Cl^-, which recapitulate the signature of liquid-vapor interfaces. These behaviors, at the hydrophobic interface, are related to the coupling of local hydration water in the vicinity of the protein with the hydration water around the individual anions; specifically, the differential ability of the water environments to couple with one another in the case of Cl^- and I^- leads to the specific-ion behavior as it is related to induced interfacial fluctuations. At the hydrophilic interfaces, both anions display similar behaviors in terms of surface stability and induced interface fluctuations. These differences offer a view of

the anions as having different characters in different contexts. Where strong local interactions are not dominant, as in the case of hydrophobic surfaces that inherently holds higher fluctuations (i.e., higher solvent density fluctuations [341, 43]), the anions tend to differentiate themselves based on their "hydrophobicity"; the large, less charge-dense iodide has a higher propensity to associate with hydrophobic regions due to its inherent higher "hydrophobicity". On the opposite, the smaller, more charge-dense, less hydrophobic chloride does not show surface stability at a hydrophobic interface. In the case of hydrophilic interfaces presenting highly polar and charged species, the strong charge-dipole and charge-charge interactions dominate and equalize the stabilities and interface perturbing effects of both anions.

We further studied three specific orientations of a single guandinium cation (parallel, perpendicular-x and perpendicular-y, depending on the dimensionality of the Gdm^+ normal vector) relative to the hydrophobic patch of HFBII. Qualitatively consistent with the results near liquid-vapor interfaces, the parallel configuration, due to the nature of weak hydration on the Gdm^+ face, the corresponding hydrophobicity is higher, hence induces more interface fluctuation along with a -2 kcal/mol surface stability as the cation approaches the hydrophobic patch. On the other hand, the perpendicular configurations induces less interface fluctuation and show no surface affinity at the hydrophobic interface. In the biological context, our results suggest that the hydrophobic effect/association, rather than the electrostatic interactions, is a more plausible driving force for denaturing proteins.

This mechanism of surface stabilization and resulting association being dominated by dispersion interactions, or say, hydrophobic effects, rather than electrostatic interactions, are also found in other studies [342, 343, 344]. In some literature, one may discribe that dispersion interactions are the key elements to the denaturation or surface stabilization [340, 345, 343]. Jungwirth and co-workers used Gdm^+-Gdm^+ and a control group, NH_4^+-NH_4^+, to study the like-charge pairing in water using ab initio molecular dynamics (AIMD). Their results revealed that only guanidinium cations were able to form the contact pairs despite direct electrostatic repulsion, which served

as a strong evidence for van der Waals interactions in Gdm^+ stacking [342]. Godawat et al. used a model hydrophobic chain in GdmCl solution and pointed out that, it is the coating of the polymer with the co-solvent, and the resulting favorable dispersion interactions, that energetically stabilizes the expanded coil state [340]. Usually it is not informative to try to distinguish between the dispersion interactions or modulation of the hydrophobic effect, as they often reflect two sides of one thing in studies [343] [7].

[7] In all cases in which stronger dispersion interactions between co-solvent and solute were observed, we average over the thermal ensemble of system configurations sampled during simulations. That is, these interactions are computed for typical distributions of particles in space at thermodynamic equilibrium. At equilibirum, hydrophobic species are expected to reside closer to a nonpolar surface than they would to water, or than water would to the surface. Since van der Waals interactions are only repulsive at extremely short ranges, the increased proximity associated with the hydrophobic effect should be considered as a more favorable interaction energy between the hydrophobic species and the nonpolar surface.

Non-Bonded Parameters	σ (Å)	ε (kcal/mol)
Cl^-	5.026	-0.0355910
I^-	5.720	-0.0536816
K^+	3.410	-0.1936829
Single Water-Ion Binding Distances	Cheatham (Å)	this work (Å)
K^+	2.66	2.66
Na^+	2.29	2.29
Cs^+	3.00	2.98
Cl^-	3.09	3.13
I^-	3.48	3.50
Single Water-Ion Binding Energies	Cheatham (kcal/mol)	this work (kcal/mol)
K^+	-18.51	-18.52
Na^+	-24.29	-24.30
Cs^+	-15.08	-15.10
Cl^-	-14.26	-14.15
I^-	-11.34	-11.37

Table 5.1: LJ parameters for ions applied in this work along with the verification. For the case of single water-anion binding case, there are two geometries for the binding structure, one is C_s, another is C_{2v}; the binding distances and binding energies for Cl^- and I^- shown here are from C_s geometry. Reproduced with permission from Di Cui, Shuching Ou, Eric R. Peters and Sandeep Patel. "Ion-Specific Induced Fluctuations and Free Energetics of Aqueous Protein Hydrophobic Interfaces: Towards Connecting to Specific-Ion Behaviors at Aqueous Liquid-Vapor Interfaces." *Journal of Physical Chemistry B.* **2014**, *ASAP*, DOI: 10.1021/jp4105294. Copyright 2014 American Chemical Society.

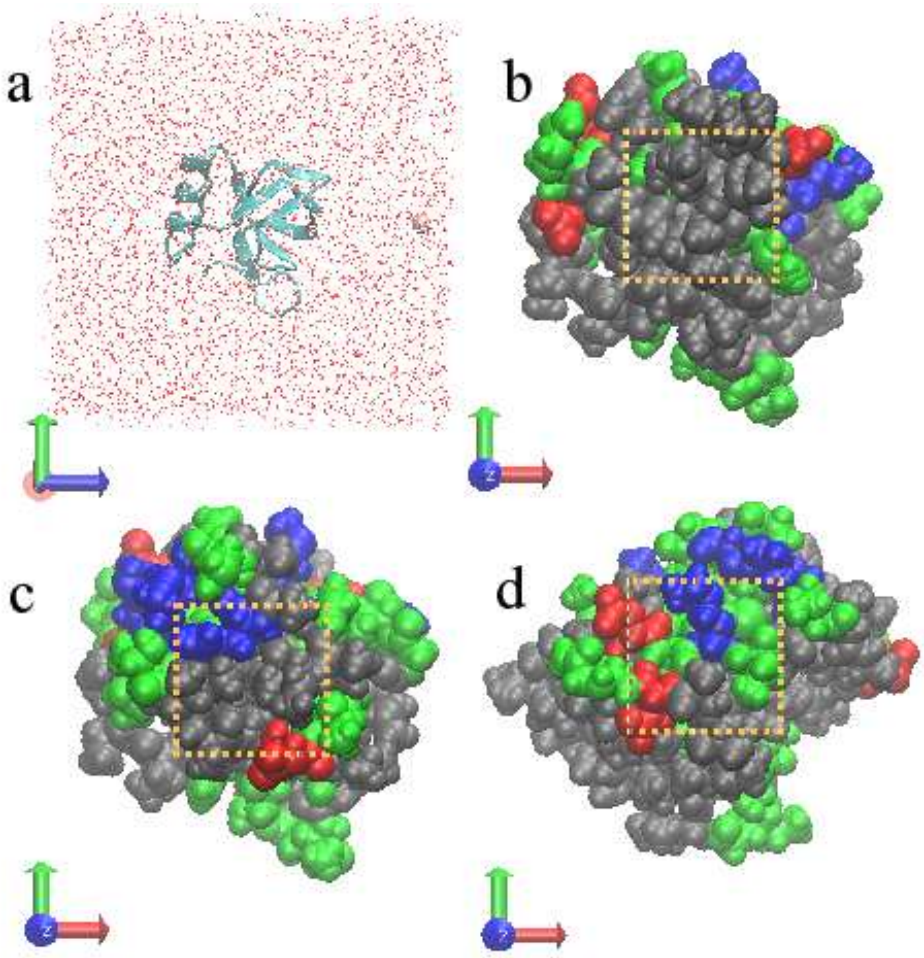

Figure 5.1: (a) Representative snapshots of the system used in this study. (b) Representation of the hydrophobic interface defined in this study, including residues VAL18, LEU19, LEU21, ILE22, VAL24, VAL54, ALA61, LEU62 and LEU63. Non-polar residues are reprsented in grey; basic residues are blue; acidic residues are red; and finally, green for uncharged hydrophilic residues. Dash orange boxes roughly select the region of interest. (c) Representation of the less hydrophobic interface defined in this study, including residues ILE31, ALA32, ASP34, ILE38, ALA41, HSD42, SER45. (d) Representation of the hydrophilic interface, including residues ASP25, CYS26, LYS27, THR28, ALA58, ASP59, GLN60. Reproduced with permission from Di Cui, Shuching Ou, Eric R. Peters and Sandeep Patel. "Ion-Specific Induced Fluctuations and Free Energetics of Aqueous Protein Hydrophobic Interfaces: Towards Connecting to Specific-Ion Behaviors at Aqueous Liquid-Vapor Interfaces." *Journal of Physical Chemistry B.* **2014**, *ASAP*, DOI: 10.1021/jp4105294. Copyright 2014 American Chemical Society.

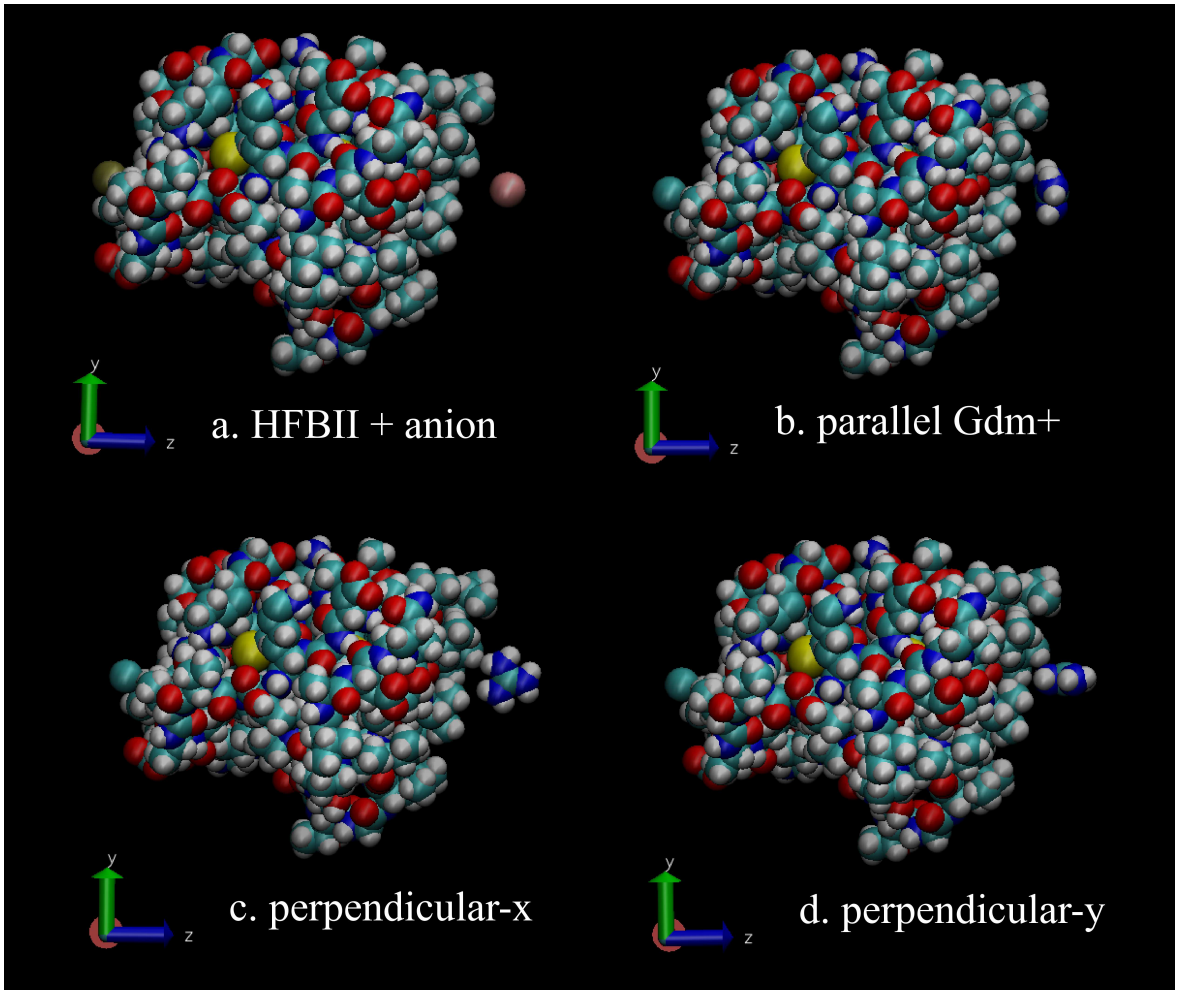

Figure 5.2: Representative snapshots of the HFBII with single ion system. For clarity, water molecules are not shown. (a) HFBII with single Cl^-/I^-. The anion is fixed throughout the simulations. (b) HFBII with single, "parallel" Gdm^+. (c) HFBII with single, "perpendicular-x" Gdm^+, the normal vector of Gdm^+ is along x-axis. (d) HFBII with single, "perpendicular-y" Gdm^+, the normal vector of Gdm^+ is along y-axis. Refer to the main text for the discussion of the orientations of Gdm^+. Reproduced with permission from Di Cui, Shuching Ou, Eric R. Peters and Sandeep Patel. "Ion-Specific Induced Fluctuations and Free Energetics of Aqueous Protein Hydrophobic Interfaces: Towards Connecting to Specific-Ion Behaviors at Aqueous Liquid-Vapor Interfaces." *Journal of Physical Chemistry B.* **2014**, *ASAP*, DOI: 10.1021/jp4105294. Copyright 2014 American Chemical Society.

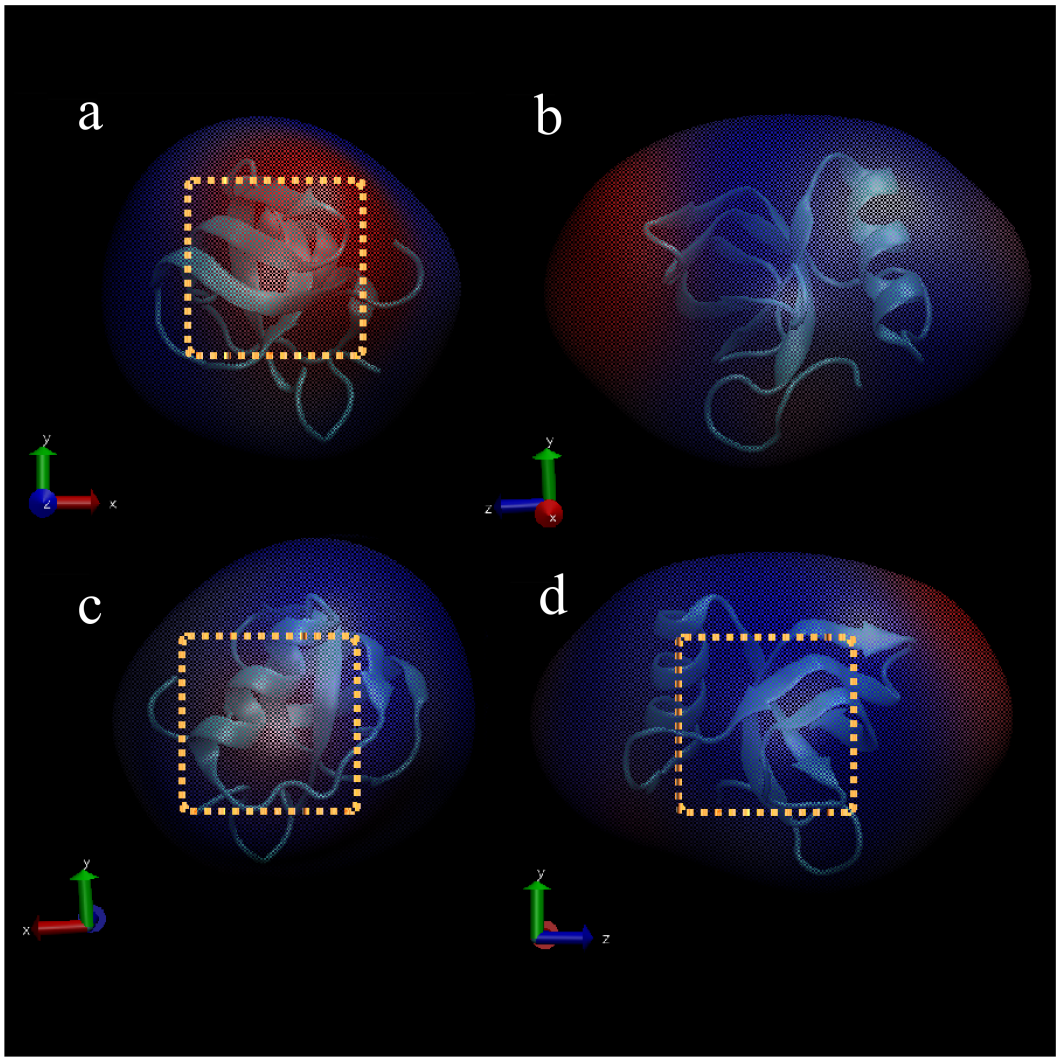

Figure 5.3: Inherent interface fluctuations of HFBII. For a, b, c and d, each one depicts one side of the protein interface with a rotation of 90° respectively. Red colour represents larger fluctuations, while blue colour represents smaller fluctuations. The highlight regions in a, c and d corresponds to the hydrophobic, less hydrophobic and hydrophilic regions defined in this study. Reproduced with permission from Di Cui, Shuching Ou, Eric R. Peters and Sandeep Patel. "Ion-Specific Induced Fluctuations and Free Energetics of Aqueous Protein Hydrophobic Interfaces: Towards Connecting to Specific-Ion Behaviors at Aqueous Liquid-Vapor Interfaces." *Journal of Physical Chemistry B.* **2014**, *ASAP*, DOI: 10.1021/jp4105294. Copyright 2014 American Chemical Society.

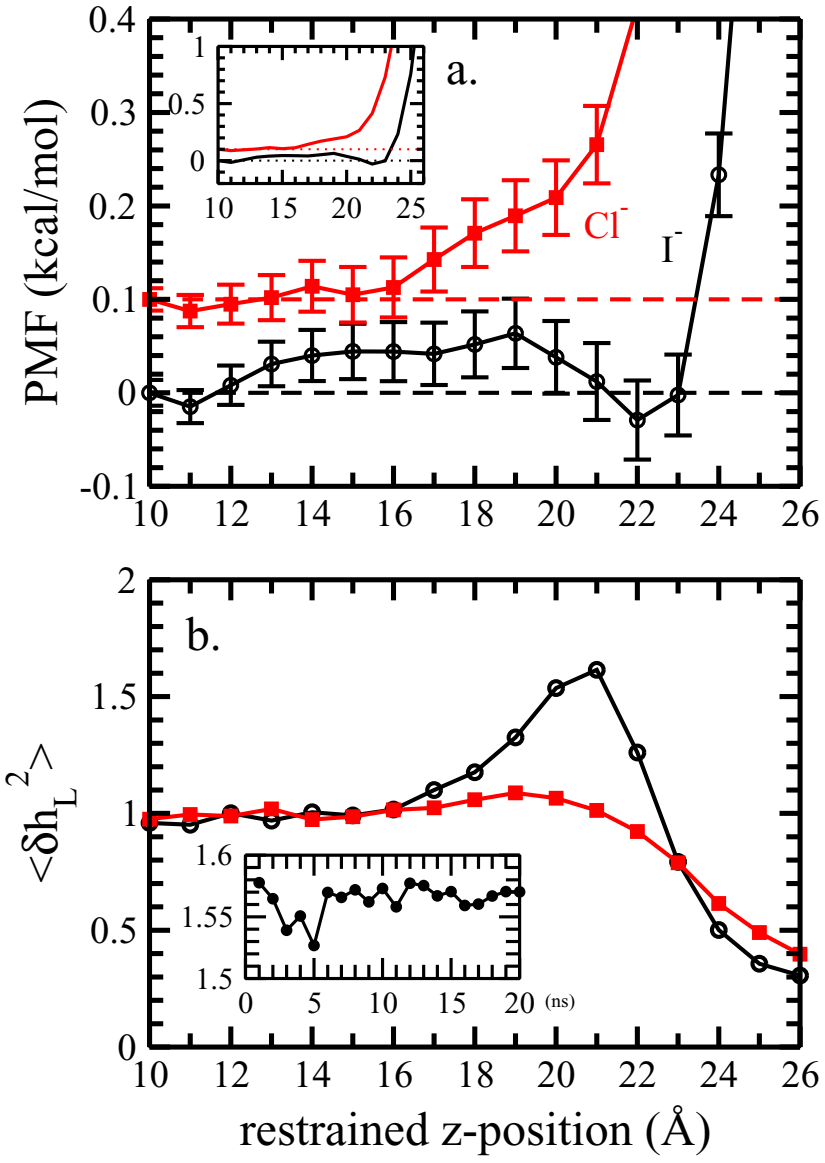

Figure 5.4: (a) PMF of single Cl^-/I^- approaching the liquid-vapor interface in TIP3P water. (b) Normalized liquid-vapor interface fluctuation at ($x = 0$, $y = 0$) as a function of anion restrained position for Cl^- and I^-. The inset shows the time evolvement of the largest fluctuation (at window $z =$ 21 Å). Reproduced with permission from Di Cui, Shuching Ou, Eric R. Peters and Sandeep Patel. "Ion-Specific Induced Fluctuations and Free Energetics of Aqueous Protein Hydrophobic Interfaces: Towards Connecting to Specific-Ion Behaviors at Aqueous Liquid-Vapor Interfaces." *Journal of Physical Chemistry B.* **2014**, *ASAP*, DOI: 10.1021/jp4105294. Copyright 2014 American Chemical Society.

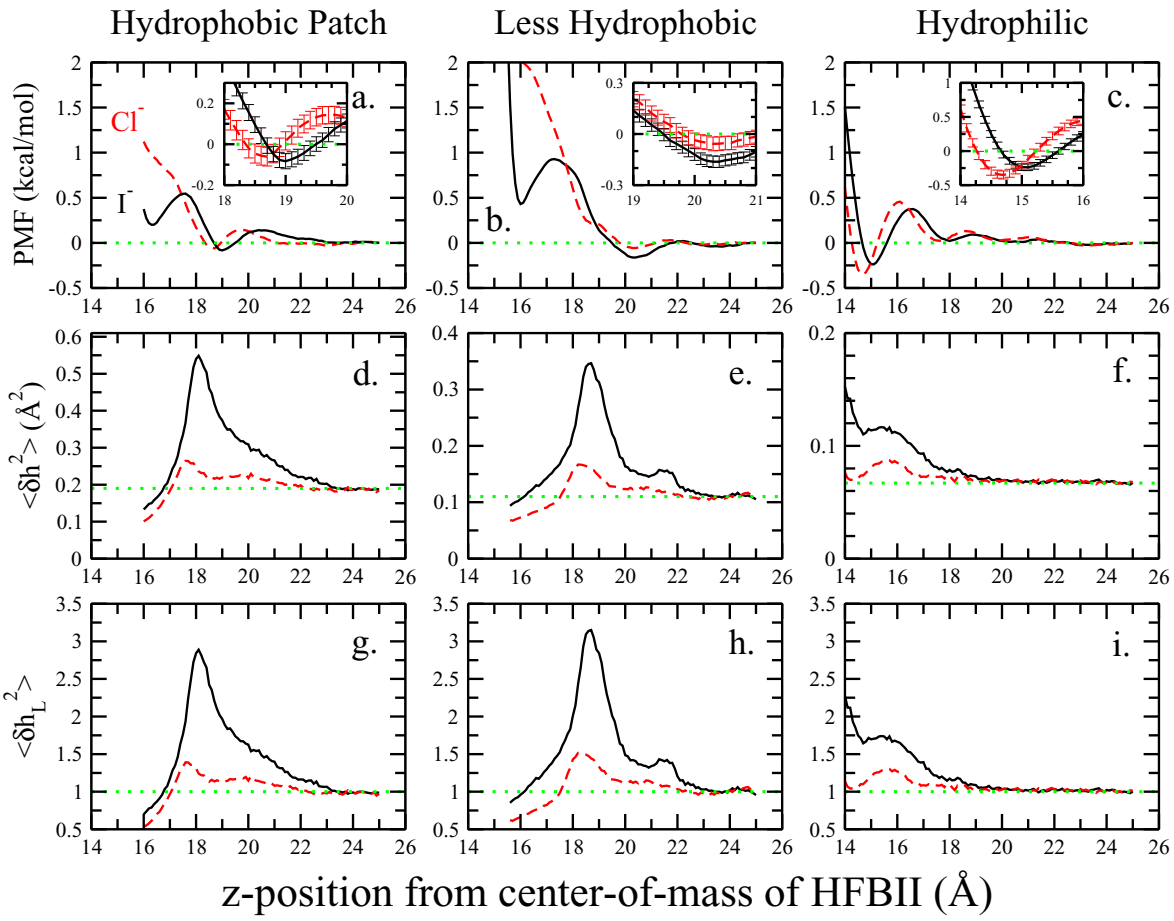

Figure 5.5: PMF for single Cl^-/I^- approaching the protein-solvent interface of (a) the hydrophobic patch (b) the less hydrophobic region (c) the hydrophilic region. Interfacial fluctuation at ($x = 0$ Å, $y = 0$ Å) as a function of anion restrained position for Cl^- and I^-, in the vicinity of (d) the hydrophobic patch (e) the less hydrophobic region (f) the hydrophilic region. (B) Normalized interfacial fluctuation at ($x = 0$ Å, $y = 0$ Å) as a function of anion restrained position for Cl^- and I^-, in the vicinity of (g) the hydrophobic patch (h) the less hydrophobic region (i) the hydrophilic region. The normalization factors are 0.19 Å^2, 0.11 Å^2 and 0.067 Å^2 for the hydrophobic patch, less hydrophobic region, and hydrophilic region, respectively. Reproduced with permission from Di Cui, Shuching Ou, Eric R. Peters and Sandeep Patel. "Ion-Specific Induced Fluctuations and Free Energetics of Aqueous Protein Hydrophobic Interfaces: Towards Connecting to Specific-Ion Behaviors at Aqueous Liquid-Vapor Interfaces." *Journal of Physical Chemistry B.* **2014**, *ASAP*, DOI: 10.1021/jp4105294. Copyright 2014 American Chemical Society.

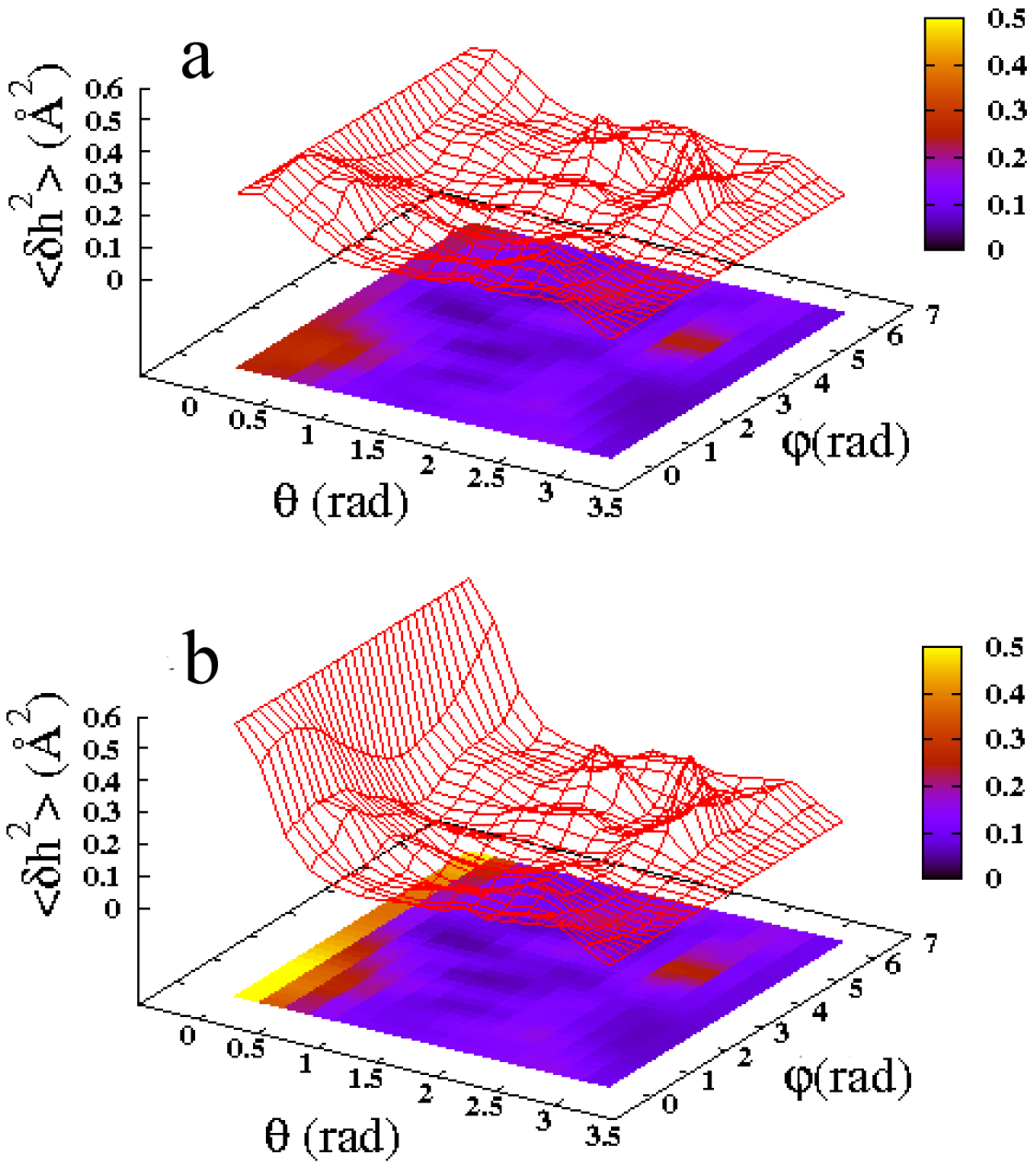

Figure 5.6: Average aqueous protein surface fluctuation $\langle \delta h^2(\theta, \phi) \rangle$ for (a) Cl^- locates at $z = 18$ Å (b) I^- locates at $z = 18$ Å. Reproduced with permission from Di Cui, Shuching Ou, Eric R. Peters and Sandeep Patel. "Ion-Specific Induced Fluctuations and Free Energetics of Aqueous Protein Hydrophobic Interfaces: Towards Connecting to Specific-Ion Behaviors at Aqueous Liquid-Vapor Interfaces." *Journal of Physical Chemistry B.* **2014**, *ASAP*, DOI: 10.1021/jp4105294. Copyright 2014 American Chemical Society.

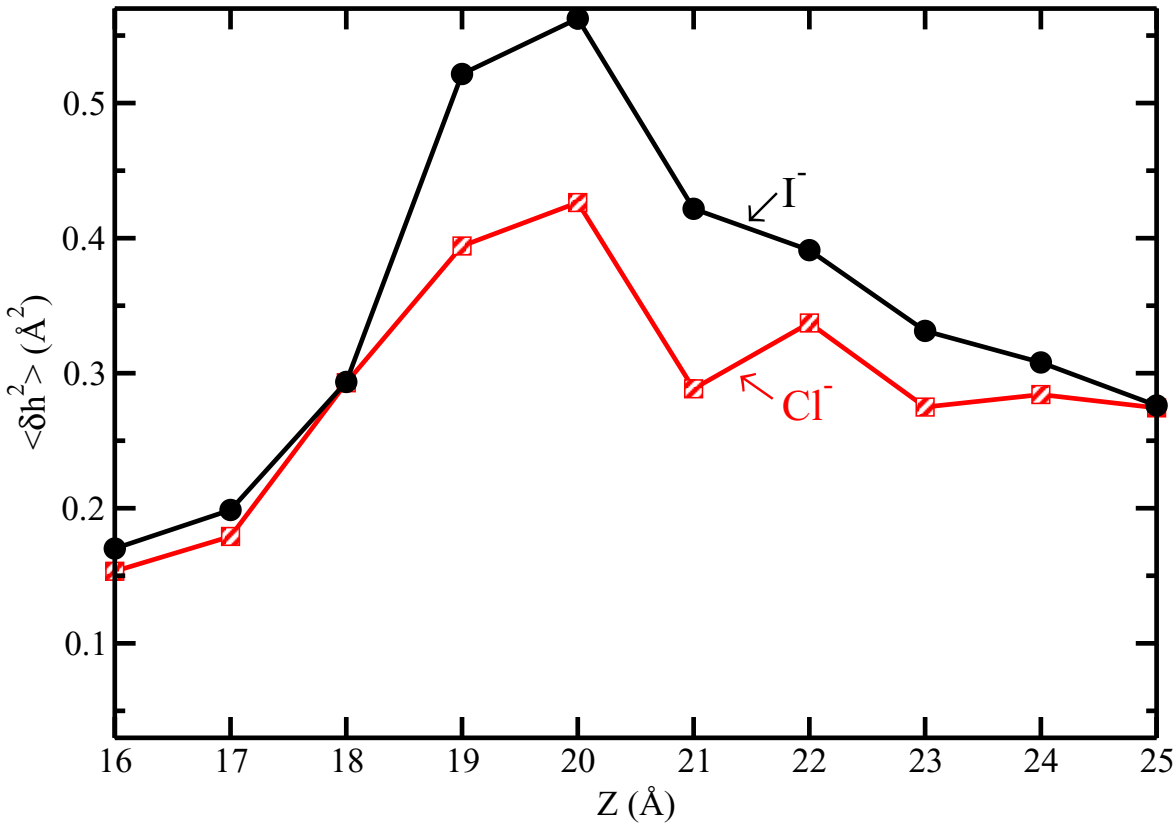

Figure 5.7: Hydrophobic interface fluctuation at (x = 0 Å, y = 0 Å) as a function of anion z-position for Cl^- and I^- with the protein flexibility. Reproduced with permission from Di Cui, Shuching Ou, Eric R. Peters and Sandeep Patel. "Ion-Specific Induced Fluctuations and Free Energetics of Aqueous Protein Hydrophobic Interfaces: Towards Connecting to Specific-Ion Behaviors at Aqueous Liquid-Vapor Interfaces." *Journal of Physical Chemistry B.* **2014**, *ASAP*, DOI: 10.1021/jp4105294. Copyright 2014 American Chemical Society.

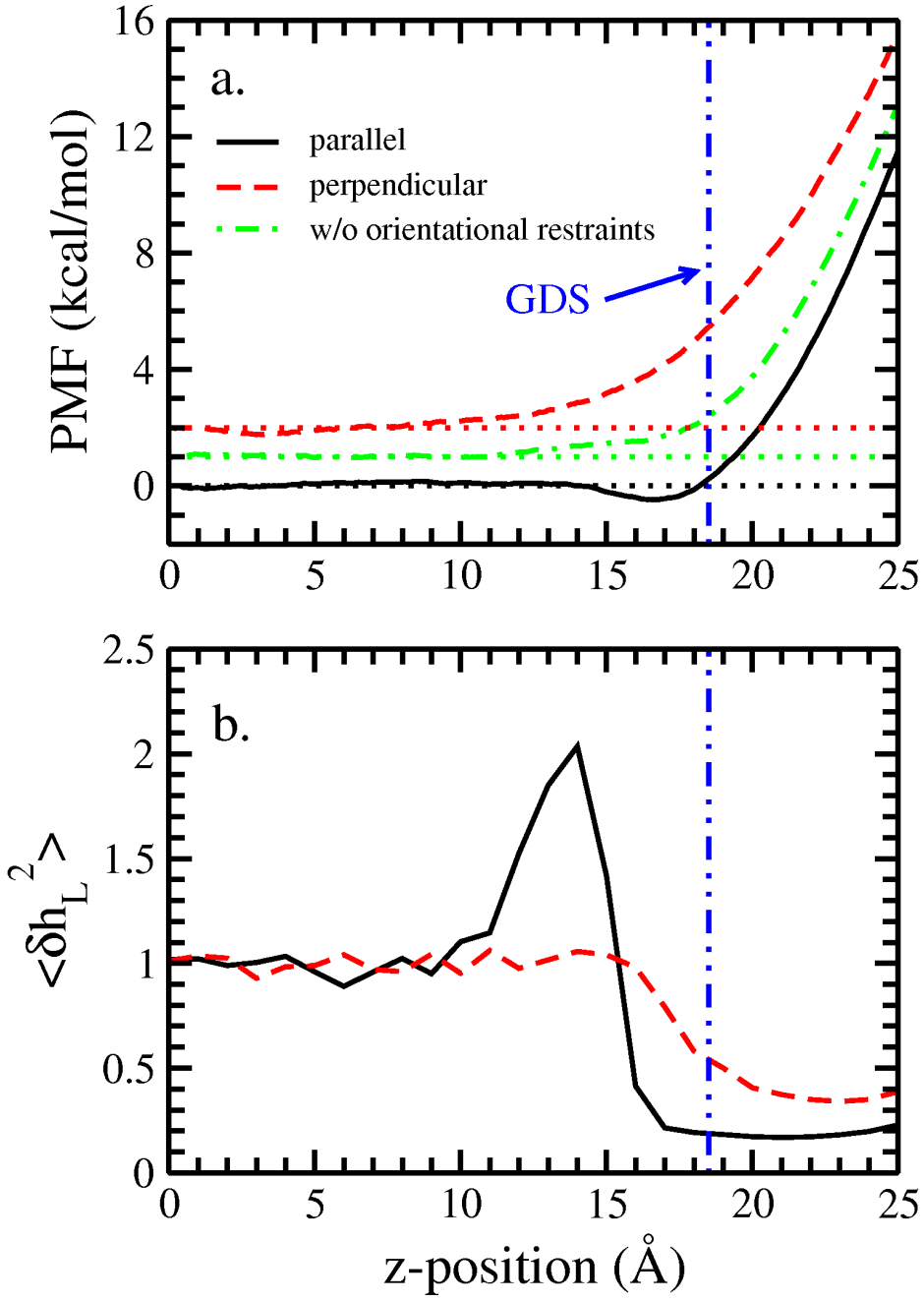

Figure 5.8: (a) PMF of single Gdm^+ approaching the liquid-vapor interface in TIP3P water. For clarity, a vertical offset of 1 kcal/mol is added. (b) Liquid-vapor interface fluctuation at ($x = 0$, $y = 0$) as a function of cation restrained position.

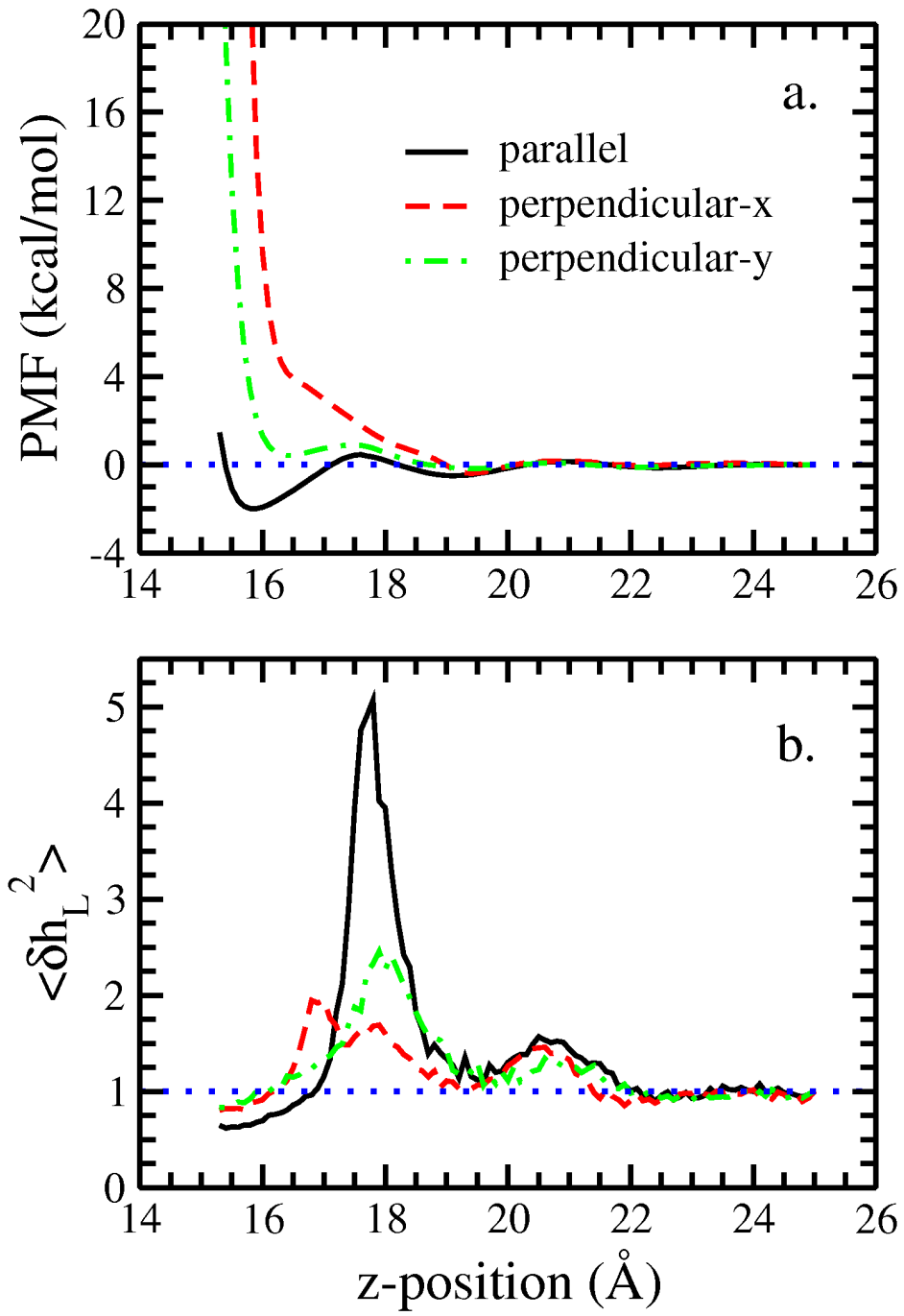

Figure 5.9: (a) PMF of single Gdm^+ approaching the HFBII hydrophobic patch. (b) Normalized interface fluctuation at ($x = 0$, $y = 0$) as a function of cation restrained position. Refer to the main text for definitions of the Gdm^+ orientations.

Chapter 6

SPECIFIC ION EFFECTS ON NANOMETER-SCALE HYDROPHOBIC ASSEMBLY

6.1 Introduction

Hydrophobic interactions, or the attractive forces between nonpolar groups in water, are inherent in a wide variety of fundamental and biological processes [34, 35, 36, 37, 38, 39, 40, 346]. Controlling assembly (either preventing it or exploiting it to create extended structures) often requires the addition of solubilizing intermediates. How these additives influence the hydrophobic assembly, directly or indirectly, is then the central issue to understanding/explaining considerable fundamental questions. For example, in the case of single-walled carbon nanotubes (SWNTs), recent research has focused on preventing the assembly/aggregation of SWNT's in solution, by involving addition of surfactants or surfactant-like dispersants [35, 34, 347, 348]. These additional molecules effectively present a barrier for close contact between SWNT's, thus affording some control of aggregation behavior.

Numerous experimental and theoretical studies suggest that an increased ionic charge density [1] amplifies the hydrophobic interaction between nonpolar solutes [65, 21, 304]. This behavior is related to decreasing the solubility of hydrophobic molecules, known as having a "salting-out" effect, along with the opposite phenomenon, known as "salting-in". Using the association of two model hydrophobic plates, Zangi et al. reported salting-out as being entropically-driven by ions with high charge density (the effect increasing with charge density) [63, 349], and less polarizability, that form strong hydration complexes away from the hydrophobic surfaces, whereas salting-in, is caused

[1] The ionic charge per unit ionic volume.

by ions with lower charge density, and greater polarizability, that exhibit preferential binding at the hydrophobic surfaces and stabilized by entropic or enthalpic effects. The mechanism of salting-out (phase separation of amphiphilic molecules from aqueous solution) has been further studied using NaCl and t-butanol [350]. In relatively concentrated solution, the t-butanol molecules tend to form loose dimers through hydrophobic interactions of their methyl groups with no noticeable interaction between their alcohol groups [351]. Introduction of NaCl causes the further interaction of the butanol residues indirectly through their alcohol groups, due to their mutual interaction with the anions, and increasing both the tendency for further amphiphilic clustering and tendency for phase separation. Nelson and Schwartz investigated the effects of ions taken from opposite ends of the Hofmeister series (F^- and SCN^-) on the dynamics of a hydrophobic probe molecule at a hydrophobic self-assembled monolayer (SAM)/aqueous interface [25]. They found that the adsorption rate of the probe molecule to the SAM increased systematically in the presence of F^- anions, which are expected to increase hydrophobic interactions.

It should be noticed that hydrophobic interaction is highly sensitive to the length scale of the solutes, especially the thermodynamic driving force acting between the hydrophobes [352]. Since water has extensive hydrogen bonding network, one would think that the attractive force between two nonpolar solutes in water originates from the inability of water molecules next to the solute to form as many hydrogen bonds as it can in bulk water, thus enthalpically driven. However, measurements of the thermodynamics of solvation demonstrated that the forces between nonpolar organic compounds in water are induced by entropy, especially followed by the observation that the strength of the hydrophobic interaction increases with temperature. In 1973, Stillinger proposed that water molecules around small hydrophobic solutes can maintain their hydrogen bonding network, but not around large hydrophobes [353]. In the small-scale regime the hydrogen bonds are not lost for the presence of the solute but it cost entropy for water to maintain them; in the large-scale regime, the water hydrogen bonding network cannot persist anymore and enthalpy is brought into play. Based on

this idea, Lum, Chandler, and Weeks (LCW) later predicted that the crossover of driving force (enthalpic or entropic) between small and large regime occurs on nanometer length scale [354]. This crossover length is about the range of interactions between water molecules in the bulk. Subsequent computer simulations reported that the excess Gibbs (free) energy of solvation of small hard-sphere solutes (i.e., formation of cavities) in water scales approximately with the solute's volume, whereas the excess Gibbs energy of large solutes scale with solute's surface area [355]. Huang and Chandler reported that when the radii of the solute is larger than 1 nm, the entropy change of solvation is positive for all liquid temperature and roughly temperature independent; on the other hand, when the solute size is smaller than 1 nm, the temperature dependence is nonmonotonic, and the entropy change of solvation has a maximum that moves to lower temperature as the size of the solute increases [355].

In the present study, we explore hydrophobic surfaces at the nanoscale, since it is the reasonable/comparable scale to the biomolecular surfaces. In the spirit of previous chapters, the focus here is to demonstrate how the hydrophobic interaction between nonpolar solutes is amplified or reduced by the addition of inorganic salts to the aqueous solution, considering the different hydrophobic nature and specific hydration properties of ions, along with their temperature dependencies. We selected single-walled carbon nanotubes as our model hydrophobic solutes to probe the nature of interactions of ions with SWNTs in the context of the effects of ions on the energetics of assembly. Furthermore, as an extension, we adopt the use of Graphical Processing Units (GPUs) as a new platform for molecular simulations of fully atomically resolved systems [356, 357, 358, 359, 360, 361, 362, 363]. Specifically, we use GPU resources to extend the sampling times of our all-atom systems in order to compute well-converged potentials of mean force (vis-a-vis, free energies or reversible work) that require substantial sampling for statistical precision. We use current state-of-the-art algorithms for treatment of electrostatics and short-range dispersion interactions, in order to faithfully retain the quality of well-validated force fields in our studies.

6.2 Method

In this chapter we studied the hydrophobic association between two single-walled carbon nanotubes in aqueous salt solutions. The first part compared the free energetics (PMF) of tubes in 3 m NaCl and NaI solutions, along with the control, i.e. tubes in pure water. The second part used GPUs to focus on the temperature effects on tube association in 3 m NaI solution.

6.2.1 Effect from Different Anions

Molecular dynamics simulations were performed using the CHARMM molecular simulation package [148]. We chose to perform canonical ensemble (NVT) simulations using the geometry shown in Figure 6.1; the central simulation cell consists of two liquid-vapor interfaces. This geometry allows the solvent density to relax in response to the presence of the SWNT's. With respect to calculation of potentials of mean force, to be discussed further below, the methodology adopted in this work has been shown to reproduce the results for large hydrophobe association free energetics using constant pressure molecular dynamics simulations [181]. Temperature was maintained at T = 300 K using a Nosé-Hoover thermostat [260]. The simulation cell was rectangular with dimensions of $L_{\mathrm{x}} = 40$ Å, $L_{\mathrm{y}} = 40$ Å and $L_{\mathrm{z}} = 150$ Å, in which z is the direction normal to the liquid-vapor interface. Two (10,10) single wall carbon nanotubes are parallel and oriented along the x-direction. The SWNTs are constructed with the Nanotube Modeler package [364]. Each (10,10) SWNT it is comprised of 400 carbon atoms with the bond length of 1.421 Å [365]. The diameter (D) and the length (l) of each tube are 13.56 Å and 24.0 Å, respectively. Throughout the simulation the positions of all tube atoms were fixed. The Lennard-Jones (LJ) parameters of the tube atoms were $\varepsilon = 0.0663$ kcal/mol, $R_{\mathrm{min}} = 4.0195$ Å; however, the interactions among atoms on the same tube were excluded. The water-carbon interactions were fixed to be $\varepsilon_{\mathrm{ij}} = 0.1015$ kcal/mol, $R_{\mathrm{min}} = 3.7793$ Å. These parameters are adopted from previous studies [366], which have been validated to model hydrophobic effects in understanding the nature of surface friction in nanoscale fluid transport. Although

the addition of a water hydrogen-tube LJ interaction may influence the structure of water near the tubes, the inclusion of this term seems arbitrary as the water model used in this study and many other previous study [367, 284, 63, 346, 181, 111] do not include LJ interactions. For two SWNT's in pure water, a bulk slab consisting of 4800 water molecules, which are represented by the extended simple point charge (SPC/E) model [261], results in two liquid-vapor interfaces. To generate 3 m salt solutions, 504 water molecules were replaced randomly with 252 pairs of anions and cations (yielding a final system of 4296 SPC/E water molecules, 252 anions, 252 cations). The molar concentrations used throughout this work are only approximate concentrations since they depend on the actual physical volume of the solution, which fluctuates slightly since there are liquid-vapor interfaces. The actual molality (moles of ion over the mass of water) of both 3 m solutions is 3.255 mol kg^{-1}; we retain the approximate molar concentrations for convenience. Representative snapshots of a 3 m NaCl system are shown in Figure 6.1. In order to obtain the potential of mean force (PMF) as a function of the separation between two SWNTs, we define the order parameter, d, as the distance between the center of the tubes (i.e., the distance between the center axes of the tubes). In this study we sample more than 40 separations/windows between 16.4 Å and 26.0 Å center of mass distance.

For the SPC/E water the LJ parameters are ε_{OO} = 0.1554 kcal/mol, $R_{\min}$ = 3.5537 Å and are assigned only to the oxygen atom of water. Point charges of oxygen and hydrogen atoms are q_O = -0.8476e and q_H = +0.4238e, respectively. Ions were treated as non-polarizable particles with interaction parameters based on those by Fyta et al. [266] which have been shown to reproduce experimental solvation free energies and the osmotic coefficients. All the LJ parameters are summarized in Table 6.1.

The non-bond interactions were treated via the standard Lennard-Jones "12-6" potential

$$E_{LJ} = \sum_{ij} \varepsilon_{ij} \left(\frac{R_{\min,ij}^{12}}{r_{ij}^{12}} - 2\frac{R_{\min,ij}^{6}}{r_{ij}^{6}} \right) \tag{6.1}$$

The parameters of ion-tube and ion-water interactions were determined by the combination rules:

$$\varepsilon_{ij} = \sqrt{\varepsilon_i \varepsilon_j}, \quad R_{\min,ij} = \frac{R_{\min,i} + R_{\min,j}}{2} \tag{6.2}$$

Lennard-Jones interactions were gradually switched off at interparticle distance of 12 Å, with a gradual switching between 11 Å (r_{on}) and 12 Å (r_{off}) using the switching function:

$$S(r_{ij}) = \begin{cases} 1 & r_{ij} \leq r_{\text{on}} \\ \frac{\left(r_{\text{off}}^2 - r_{ij}^2\right)^2 \left(r_{\text{off}}^2 + 2r_{ij}^2 - 3r_{\text{on}}^2\right)}{\left(r_{\text{off}}^2 - r_{\text{on}}^2\right)^3} & r_{\text{on}} < r_{ij} \leq r_{\text{off}} \\ 0 & r_{ij} > r_{\text{off}} \end{cases} \tag{6.3}$$

In considering the force field to use for this study, our philosophy is to attempt to apply models developed and validated to some degree based on considerations of the hydration free energy of ions in pure water. We believe that consideration of ionic solutions requires attention to this chemical aspect of the physics of these systems. We acknowledge that the precise absolute values of hydration free energies are fraught with assumptions necessarily arising from the inseparability, in reality, of electroneutral anion-cation pairs. Furthermore, the nature of the water-hydrophobe interface is also critical when considering simulations of the nature presented here, and within this context, we have chosen force fields that, again, have been validated with the nature of this interface in mind.

Conditionally convergent long-range electrostatic interactions were treated using Particle Mesh Ewald (PME) [137] approach with a 40 × 40 × 150 point grid and $\kappa = 0.330$. SHAKE [265] was used to maintain the rigid geometry of each water molecule. Dynamics were propagated using a Velocity-Verlet integrator with a 1.0 fs timestep under 3D periodic boundary conditions. The sampling time for each window was at least 11 ns with 3 replicates. Properties were calculated from all but the first 1 ns, which was treated as equilibration, resulting in more than 30 ns per window for data analyses.

6.2.2 Temperature Effects on Hydrophobic Association

Molecular dynamics simulations were performed using a custom-developed code, FEN ZI [368, 369]. Essentially the simulation protocol was the same with the systems in CHARMM; here we only address the major difference. The system was extended along z-dimension with the identical geometry, yielding 6264 SPC/E water molecules along with 368 pairs of ions (Na^+ and I^-), which retained the same concentration of 3 m. The simulation cell was 40 Å × 40 Å × 200 Å, Temperature was maintained constantly from 300 K to 360 K (with 10 K spacing) using a Nosé-Hoover thermostat [260]. Ion-water and ion-tube interactions are identical as listed in Table 6.1. The r_{on} and r_{off} for the switching function are 10 and 12 Å, respectively. Conditionally convergent long-range electrostatic interactions were treated using Particle Mesh Ewald (PME) [137] approach with a 40 × 40 × 200 point grid and $\kappa = 0.330$. SHAKE algorithm [265] was also used to maintain the rigid geometry of each water molecule. Dynamics were propagated using a Velocity-Verlet integrator with a 1.0 fs timestep under 3D periodic boundary conditions. The sampling time for each simulation window was at least 150 ns. Properties were calculated from all but the first 5 ns, which was treated as equilibration, resulting in more than 145 ns per window for data analyses.

The simulations were run on two GPU clusters, a local GPU cluster at the University of Delaware and a XSEDE GPU cluster called Keeneland (KIDS) at Oak Ridge National Lab. The local cluster includes 48 dual six-core compute nodes (576 cores), 96 Fermi S2070 GPU systems, four GPUs per node. The cluster utilizes both an Infiniband fabric and a Gigabit Ethernet interconnect. KIDS is a HP SL-390 (Ariston) cluster with Intel Westmere hex-core CPUs, NVIDIA 6GB Fermi NVIDIA M2070 GPUs, and a Qlogic QDR InfiniBand interconnect. The system has 120 nodes with 240 CPUs and 360 GPUs, three GPUs per node.

6.2.3 Hydrophobe-Solvent Surface Fluctuation

From individual snapshot/configuration we can construct the coarse-grained instantaneous surface defined by Willard and Chandler [246]. Gaussian mass distributions are assigned to each water oxygen atom (or ion):

$$\Phi(\mathbf{r};\xi) = (2\pi\xi^2)^{-d/2} exp(-r^2/2\xi^2) \tag{6.4}$$

where r is the magnitude of $\mathbf{r}$, ξ is correlation length, and d stands for dimensionality. We use correlation length = 3 Å, which is roughly the size of a single water molecule in the bulk, to assign the Gaussian mass to each water oxygen. However, unlike the water, the total number of ions is less, as a result we need to consider a larger correlation length (6 Å) to render the coarse-grained surface (the choice of 6 Å is included in Appendix C). At space-time point $\mathbf{r}$, t, we have the coarse-grained density as

$$\bar{\varrho}(\mathbf{r},t) = \sum_i \Phi(|\mathbf{r} - \mathbf{r}_i(t)|;\xi) \tag{6.5}$$

The interface is then determined as the $(d-1)$-dimensional manifold with a constant value c.

In the case of liquid-vapor interface, the surfaces are often orthogonal to an normal vector (z-axis), coordinate (x, y, z) for each grid points in space is set up and the surface is obtained as the manifold by setting $\varrho(x, y, z) = \varrho_{bulk}/2$ (based on the usual definition of Gibbs dividing surface). The mean surface of all the instantaneous surfaces is then described as the function $\langle h(x, y)\rangle$. Subtract the mean values from the instantaneous $h_{\mathrm{t}}(x, y)$, we obtain $\delta h_{\mathrm{t}}(x, y)$ as surface height and the height fluctuations $\langle \delta h^2(x, y)\rangle$. Owing to the cylindrical geometry of nanotubes, we set up a series of (ρ, θ, l) (cylindrical) based grid points and treat ρ as the tube-water surface height, as shown in Figure 6.1 d. ρ is radical distance of end point of the radius vector from the tube axis with the range 6.8 Å $\leq \rho \leq$ 20 Å since we are interested in the tube-water surface outside the tube; θ is polar angle, which is defined as intersection angle between the radius vector and the positive y-vector with the range to ensure that only the hemisphere of interest is selected (facing the bulk: $0 \leq \theta \leq \pi$ or intertube region:

-$\pi \leq \theta \leq 0$); l is the position along x-dimension with -11 Å $\leq l \leq$ 11 Å [2]. In practice, we set 66 × 18 × 22 grid points along (ρ, θ, l), which gives a resolution of (0.2 Å,10°,1 Å) in each dimension. The tube-water and tube-ion surfaces are defined as 3/4 bulk density of the corresponding species. We use a different constant value c here compared with liquid-vapor interface case to avoid the ambiguity during constructing the tube-solvent interface. We note that in the current convention, instantaneous tube-solvent interface is then expressed as $h_{\mathrm{t}}(\theta, l)$, mean surface as $\langle h(\theta, l)\rangle$, and the surface height fluctuation as $\langle \delta h^2(\theta, l)\rangle$.

6.3 Hydrophobes in Different Aqueous Solutions

In this section, we start with the spatial distributions of inorganic monovalent salts (NaCl and NaI) relative to the carbon nanotubes, to verify the current force field does reproduce the behaviors near hydrophobic surfaces. Then we will exmaine the dispersion stability between nanotubes, along with the decompositions of contribution from each component. The fact that I^- has stronger surface affinity to directly attach the nanotubes while Cl^- does not, indicates that qualitatively the (mechanical) mechanism to promote/reduce the hydrophobic association is ion specific.

6.3.1 Density Profile

Basially, the spatial distributions of species include three different regions due to our system setup: intertube, intra-tube and the bulk solvent. We will discuss the spatial distribution of each region separately.

We start with computing radial number density profiles of water molecules and ions about the tube to contrast the properties near the hydrophobes and in the bulk solvent. We restricted sampling for these profiles to a half cylinder on the side of the tube extending into the bulk solution. This prevents sampling between the SWNTs (i.e., the inter-tube region), where the distributions will contain interference effects from

[2] Although the actual tube range is ±12 Å, we only selected the range between ±11 Å for analyses to avoid the edge effect at the tube terminals

the other tube. After each half cylinder is considered (for each tube) the symmetry of the two-tube system allows us to combine the sampling volumes into a full cylinder. Also, we limited the length of the sampling cylinder to $-l' \leq x \leq l'$ ($l' = 11.0$ Å), which is shorter than the tube length. Although being slightly reduced from the true length of the tube, it can avoid artifacts arising from the edge of the tubes. So the radial density profiles ($\rho(r)$) can be written as:

$$\rho_i(r) = \frac{N_i}{4\pi l' r dr} \tag{6.6}$$

i is the atomic/molecular species, N_i is the corresponding number of species i within the region $r - dr/2$ to $r + dr/2$.

Figure 6.2 shows the radial density profiles of water oxygen atoms and ions as a function of r which is relative to the center of the tube axes (at $r = 0.0$ Å). In Figure 6.2 a, all the values are scaled by dividing by $\rho_{\text{bulk}} = 0.0334$ Å^{-3}, which is the density of water molecules in pure SPC/E bulk. The radial density profiles for pure water (solid line), water in 3 m NaCl (red dashed line), and water in 3 m NaI (green dot-dashed line) are qualitatively similar. Water density is enhanced in the vicinity of the tube, both inside and outside the tube, and follows the trend of $\rho_{\text{water,pure}} > \rho_{\text{water,NaCl}} > \rho_{\text{water,NaI}}$, as presented in the insets of Figure 6.2 a. For the region outside the tube ($r > 9.0$ Å), we observe that the pure SPC/E system has higher number density throughout the profile, which is not surprising, since there are more water molecules in the pure SPC/E system. However, unlike the significant difference between $\rho_{\text{water,pure}}$ and $\rho_{\text{water,NaI}}$ from the first layer (~ 10.1 Å), the difference between $\rho_{\text{water,pure}}$ and $\rho_{\text{water,NaCl}}$ becomes larger at the second layer (~ 13.0 Å). These differences are largely influenced by ion density in the vicinity of the tube surface as well as in bulk solution. We address this next. Figure 6.2 b shows the actual radial density profiles of ions. I^- in 3 m NaI solution (green dashed line) shows significant enhancement adjacent to the tube-water interface and tends to show anisotropic solvation structure near the hydrophobic surfaces [111, 272, 122, 103, 143], subsequently displacing water near the tubes and resulting in the reduced water density in the NaI solution. The reduced water density

correlates with the enhanced iodide anion density. These qualitative behaviors conform to the behavior of this particular iodide anion model to slightly favor the hydrophobic liquid-vapor interface reported in the previous chapter. Cl^- ion is not as enhanced near the tube at small r, thus explaining the similarity between water number density profiles in pure water and NaCl solution. However, owing to the increased density of Cl^- around $r = 13.5$ Å, $\rho_{\text{water,NaCl}}$ eventually decreases, converging with $\rho_{\text{water,NaI}}$.

We also notice that although we use Na^+ as cations in both salt solutions, the magnitude of the radial density profiles are significantly different; Na^+ in the NaI solution is enhanced in the vicinity of the tube relative to in NaCl. This behavior will be addressed later in this work.

For the intra-tube region, taken to be the region inside the tube ($r < 4.0$ Å), we observe that near the very center of the tube, $\rho_{\text{water,pure}}$ shows the lowest density among the three systems. The average number of intra-tube water molecules ($\langle N_{\text{intra-tube,water}} \rangle$), anions ($\langle N_{\text{intra-tube,anion}} \rangle$) and cations ($\langle N_{\text{intra-tube,cation}} \rangle$) are summarized in Table 6.2. These values are calculated as direct averages of the number of species in the tube normalized by the number of observations. Alternatively, though not done here, one can integrate the radial density profiles to obtain the equivalent value. Uncertainties included in the parentheses are determined from the standard deviations of $\langle N_{\text{intra-tube}} \rangle$. The average number of intra-tube water molecules is greatest for the pure SPC/E system and least for the NaI solution; we attribute the latter observation to an increased number of intra-tube ions/ion pairs which displace water molecules from this intra-tube volume. However, since the number of intra-tube ions is low (about or less than one ion pair within the tube per snapshot), the number of intra-tube water molecules does not vary much among the systems.

In order to investigate the behavior of water molecules and ions within the inter-tube region, we define a rectangular sampling volume, as illustrated in Figure 6.1 b and c. We emphasize that the inter-tube region only includes the region between tubes, excluding the region inside the tubes. The length (L) of the box is along the x-axis and identical with the cylinder used to sample for the radial density profiles, which

makes $L = 22.0$ Å; the width (W) is along the z-axis and determined by subtracting from the tube separation (d) with the tube diameter ($D = 13.56$ Å). Finally, the height (H) equals $D - 2\ R_{\mathrm{min,OC}}$ and projects along the y-axis. The choice of this sampling region is not unique; we provide further analysis and an alternative scheme in the Appendix D. Results are self-consistent using both sampling volumes. The average numbers of water oxygen atoms ($\langle N_{\mathrm{inter-tube,water}} \rangle$), anions ($\langle N_{\mathrm{inter-tube,anion}} \rangle$) and cations ($\langle N_{\mathrm{inter-tube,cation}} \rangle$) in the rectangular box as functions of d are shown in Figure 6.3. From Figure 6.3 a and the inset, the number of inter-tube region water molecules in NaI solution is ostensibly less compared to that in the NaCl and pure water systems. This correlates with the water densities in the outer regions. We also notice that at $d \sim 19.4$ Å and 22.0 Å, $\langle N_{\mathrm{inter-tube,water}} \rangle$ shows dramatic increases, indicating energy barriers around these intertube separation, which will be discussed in detail in the following section.

In Figure 6.3 b we observe that I^-, despite being the larger ion (based on van der Waals dimension as well as considering the single ion in its bulk-solution extended solvation shell), enters this region at lower separation distances (21.0 Å) than chloride (21.6 Å). This is attributed to the stronger solvation of chloride (more favorable absolute hydration free energy compared to iodide) which would prevent it from entering this region without significant room to accommodate its hydrating waters. Despite the fact that same cation is used in both salt solutions, the sodium density is noticeably higher outside the tube (Figure 6.2 c) and within the tube (Table 6.2) in the NaI solutions. Interestingly, the features of the sodium ions qualitatively mimic those of the corresponding anions. This increased affinity of Na^+ suggests some extent of ion pairing that works to raise the stability of the ions in each region. Ottosson et al. observed a similar enhancement of sodium density in NaI solutions (relative to those of NaCl solutions) in their study of ions at the air-water interface [370] and attributed this difference to the need for cation density to balance the adsorbed anion density.

6.3.2 Free Energetics of Nanotube Association and Decompositions

The effect of inorganic ions on the free energetics of nanotube association is now considered. The potential of mean force (PMF) for nanotube association following an order parameter that brings the parallel-oriented tubes from an infinite-separation, dissociated state to the associated, contact state is calculated directly from the average forces acting on a tube:

$$W(\xi) = -\int \langle F(\xi) \rangle \, d\xi \tag{6.7}$$

where ξ is the order parameter taken as the separation distance between the center of mass of the two SWNTs. We consider the average of forces $\langle F(\xi) \rangle$ acting on each SWNT over the sampled configurations at each separation distance; the average force used in the integration is the average of the values for the two SWNTs after negating the forces acting on the SWNT located in the negative z-region of the simulation cell. All profiles of the PMF are shifted such that $W(\xi_{\text{dissociated}}) = 0$ kcal/mol. We show the PMFs for pure SPC/E and 3 m salt solutions in Figure 6.4. Numerical results are summarized in Table 6.3 and denote the difference in PMF from dissociated state to the global minimum:

$$\Delta W = W(\xi_{\text{contact}}) - W(\xi_{\text{dissociated}}) \tag{6.8}$$

where $\xi_{\text{contact}} \sim 16.9$ Å (position of tube contact minimum) and $\xi_{\text{dissociated}} = 26.0$ Å (dissociated distance). PMF results are shown in Figure 6.4 a. The error bars are obtained from standard deviations between three independent replicates. For clarity, in the inset of Figure 6.4 a, which shows the minimum region of the profiles near the contact distance, we applied a vertical offset of +2 kcal/mol for the case of 3 m NaI.

Addition of salts results in a more favorable PMF for tube association relative to pure SPC/E. The increase in stability is on the order of 4 kcal/mol. This difference, though statistically significant, is roughly 9% of the free energy well-depth in pure water. Whether this makes a substantital difference in the context of SWNT association in salt versus pure aqueous solutions is debatable as the difference is rather small.

The salt solutions indicate a slightly higher stability of the contact state may be due to several reasons. The most direct is that the density of molecular species that contribute destabilizing forces to association is reduced in the case of the salt solutions. As shown in Figure 6.2 a, water density in the salt solutions (both in the direct vicinity of the tubes as well as in the bulk solution at larger distances from the tubes) is non-trivially reduced. As will be discussed further below, the contribution from water in this region is destabilizing towards hydrophobe assembly; thus, reducing this effect, as well as increasing the stabilizing contributions from ions (to be discussed further below as well) lead to the overall increased stability of the contact state in the salt solutions. Furthermore, we consider fairly concentrated solutions in our study, ostensibly 3 m, thus providing a strong driving force for stabilization of the contact state; 1 m solutions (data not shown) exhibit essentially little or no enhanced stability of the contact state. Thus, by using the higher concentration in this study, we are able to dissect the influence of the different ions because the overall effect is sufficiently large.

We return to issues of the conferred stability from density and spatial distribution effects in more detail below. We note a recent study demonstrating fast aggregation kinetics of single-walled nanotubes in millimolar concentration ranges of NaCl and $CaCl_2$ [371]. Though the present concentration of salt is much higher than the concentrations probed in earlier studies, the present conditions are above what is termed the critical coagulation concentration (CCC in Reference [371]) at which point the aggregation kinetics of SWNT's plateau to constant rates (diffusion limited in this fast range); we note that earlier studies of aggregation kinetics of SWNT's model the process in the formalism of Derjaguin, Landau, Verwey, and Overbeek (DLVO) theory [372, 373]. Our results recapitulate qualitative aspects of that model treatment in the high concentration limit.

Artifacts arising from simulation protocol may give rise to the observed enhanced contact-state stability. The potentials used in this study as well as the fact that long-range Lennard-Jones corrections are not included explicitly may be at play.

With respect to the latter of the two effects just mentioned, one can envision that attractive forces from species separated from the tubes well beyond the cutoff distance will contribute to destabilizing the contact state by attracting (i.e. "pulling on") the tubes. In order to semi-quantitatively investigate the effect of long-range forces, we re-analyzed the simulation trajectories in terms of the total forces on the tubes using longer cutoffs (again, only for the purpose of computing the force on the tubes); of course, the ensemble of states do not exactly correspond to the states one would encounter using explicit long-range contributions during the actual molecular dynamics simulations. This is similar to the semi-quantitative corrections applied by several groups to account for long-range corrections to the Lennard-Jones interaction during hydration free energy calculations [374]. The results are shown in detail in the Appendix E. In summary, we find that the long-range forces for all systems (SWNT's in pure water, NaI solution, and NaCl solution) contribute destabilizing forces (as one would expect) in all cases, and in roughly equivalent amounts. Thus, the PMF's for all cases would be shifted to higher values for all systems. Importantly, the relative stability of the contact state in the three systems would not be changed (based on this analysis). We thus conclude that long-range effects are not the major contributor for the enhanced stability of the contact state in the salt solutions.

Finally, we note that the inversion of stability of the contact relative to pure water may result from inadequacy of the water-ion-tube potentials. If the combination of ion-water potentials predicts lower solution density compared to experimental data, the simulations will underestimate destabilizing forces arising from molecular species in the bulk. We do find that for the 1 m salt solutions (excluding SWNT's) simulated using NPT (constant pressure and temperature) molecular dynamics calculations, the bulk aqueous salt solution densities are predicted to be lower than the experimental values at 298 K and 1 atmosphere pressure conditions. The predicted densities for NaCl and NaI solutions are 1.019 g/mL and 1.094 g/mL, respectively. The experimental data are 1.04 and 1.11 g/mL, respectively [375].

We now explore contributions of individual species to the overall potential of

mean force, and attempt to connect the nature of this contribution to spatial distributions of the individual atomic species. This is particularly relevant in order to connect the different properties of the halides, as embodied in their distributions relative to the hydrophobic species of interest in the context of specific-ion effects, to the particular contribution the ionic species makes to the stability of the contact state. We note that the difference in PMF's between 3 m NaI and 3 m NaCl is small and within the associated uncertainty.

To explore the origins of the differences in the potential of mean force, we determine individual contributions to the PMF as:

$$\Delta W = \Delta W_{\text{tubes}} + \Delta W_{\text{water}} + \Delta W_{\text{Na}^+} + \Delta W_{\text{X}^-} \tag{6.9}$$

where each contribution is calculated from the forces on the tubes arising from each component and $X^- = Cl^-, I^-$. Results are shown in Figure 6.4 b-d respectively, the error bars are computed via the same method as the total PMF; numerical values are shown in Table 6.3. Since the tube coordinates are fixed throughout the course of the simulation for each separation distance and the tube-tube interactions are the same in all systems, the tube contribution to the PMF is identical in all systems. Therefore, any differences in the PMF for our systems are solvent (water and ions) driven. We thus focus the remaining discussion and analyses on the effects of water and ions. Water represents the largest effective contribution (in magnitude) to the PMF, as shown in Table 6.3 and Figure 6.4 b, the latter showing the water contributions to the PMFs in each system. In the case of pure SPC/E, the water contribution to the PMF has a global maximum ($\sim$ 19.4 Å) corresponding to the position of the desolvation maximum in the PMF curve, and a local maximum at $\sim$ 21.8 Å, which have been expected from the discussion in the previous section. In consideration of describing the relationship between the structure of water and these barriers, the spatial density distribution of water oxygen atoms near the SWNTs is shown in Figure 6.5.

Each density map is integrated over the reduced tube length (between $\pm$11.0

Å) based on the previous discussion, and can be written as Equation 6.10:

$$\rho_i(y,z) = \int_{-l'}^{l'} \rho_i'(x,y,z)dx \tag{6.10}$$

where $\rho_i'(x,y,z)$ represents the number density of a given species i at position (x,y,z). The layers shown in each panel depict the fluctuations of radial density profile (in Figure 6.2) in a more intuitive way. In Figure 6.5 a and b, the most evident difference happens at the very center of the region between the SWNTs. The white region, which corresponds to the first peak shown in the radial density profile of water, is "broken" at $d = 19.3$ Å and "connected" at $d = 19.5$ Å; similarly, the purple/pink region, which corresponds to the first minimum, "breaks" at $d = 21.6$ Å and "connects" at 22.0 Å. This behavior demonstrate that the energy barriers of PMF are modulated by the interference and reconstruction of water structures, which is also proposed by Li et al. [376]. Alternatively, these distances correspond to dewetting events. The barriers in the water contribution (which transfer to the overall PMF curve) reflect the work needed to evacuate layers of water molecules in a manner that allows the remaining inter-tube volume to accommodate the particular numbers of water molecules. This behavior appears to be universal among explicitly non-polarizable water models which do not allow environment-dependent variation of molecular dipole moments or atomic partial charge distributions.

The contribution to the PMF from water in the pure SPC/E system is repulsive in general. This agrees with published work by Li et al. [377, 376] on carbon nanoparticles in water, Choudhury and Pettitt's work on graphene in water [378], and Uddin et al. on carbon nanotubes in water/surfactant systems [55]. The features (barriers and minima) of the water contribution in all systems are summarized in Table 6.4. Comparing the water contributions in the pure SPC/E and 3 m solutions, we observe that the destabilizing water contribution in 3 m NaCl and NaI solutions are reduced by 6 and 4 kcal/mol, respectively, at the second barrier (ΔW_{water}) occurring at tube separation of $\sim$ 19 Å. The difference between the PMF at the local minimum at $\sim$ 20.5 Å and the value of the dissociated distance ($\Delta W_{\text{water}}^{\dagger}$) is positive in pure SPC/E but negative

in the salt solutions. Furthermore, the barriers in the water contribution at $d \sim 22$ Å and ~ 19 Å are systematically lower in the salt solutions compared to the pure water case. Admitting that the barriers arise from dewetting transitions, the barriers for the salt solutions are reduced as less water is involved. The profiles of water number at various inter-tube distances demonstrates the reduction in water in this volume.

We suggest the effects of the spatial distribution of ions on water density in the vicinity of the tubes to explain the less destabilizing water contribution to the overall PMF in the salt solutions. When an ion or water molecule is immediately adjacent to the outer surface of the tube, there is a repulsive force between the ion/molecule and the tube. The repulsive nature is explained as a result of the separation distance being on the repulsive wall of the Lennard-Jones potential; the ion/molecule is "pushing" the tube away. For ionic or molecular species on the bulk solution side of a tube, this effect leads to a stabilizing force for tube-tube assembly; when species are on the inter-tube side of a tube, the effect is opposite and leads to destabilization of the contact state. This will be shown explicitly for the case of anions further below. Separations of the ion/molecule further from the tube (but still within the simulation cutoff), attract the tube, thus destabilizing the contact state. Since the cutoff for Lennard-Jones interactions is finite in the simulation, effectively all forces on the tube from species beyond the first solvation shell are destabilizing to the contact state. Thus, by lowering the density of species further away from the tube, one effectively is reducing the destabilizing contributions to the potential of mean force (i.e., less work is needed to bring the tubes together to the contact state). Thus in Figure 6.4 b, relative to the pure water system, the water contribution in the salt solutions is lower. In particular, once the inter-tube region is evacuated of water at tube separations smaller than 19 Å, the water directly in the first solvation shell of the tube (on the bulk solution side of the tube) works to force the tubes together (working to stabilize the contact state). This explains the rapid falloff in the water contribution to the PMF in Figure 6.4 b. Furthermore, since the bulk density of water in the salt solutions is lower than in pure water, the forces from these far water molecules working to pull

the tubes apart is lessened, again contributing to the observed behavior of the water contribution relative to pure water. Finally, the water contribution is more stabilizing (approaching the contact state at tube separations less than 19 Å) in the NaCl solution than in the NaI solution. This is because in the NaCl system, water is not displaced from the first solvation shell of the tube to as much an extent as in the NaI system. Thus, the force from water acting to push the tubes together is greater in the NaCl system compared to the NaI system. The differences in water density relevant to this discussion, we reiterate, are highlighted in Figure 6.2 a.

As shown in Figure 6.4 c, d and Table 6.3, both anions and cations show positive contribution to the PMF in general. Sodium cations contribute a stronger repulsive force ($\Delta W_{\mathrm{Na^+}} \sim 1.5$ kcal/mol) in NaCl and NaI similarly. While chloride contributes ~ 4 kcal/mol to the PMF, iodide adds less than 0.1 kcal/mol. In fact, iodide appears to stabilize ($\Delta W_{\mathrm{anion}} < 0$) at d less than the contact distance. To investigate this non-intuitive behavior, we compute the z-component of the total force from the individual anions on all the tube atoms ($\langle F_{\mathrm{z,anion}} \rangle$) as a function of the positions of anions. We first determine the force on the tube from an anion at a Cartesian position (x, y, z), $F'_{\mathrm{z},i}(x, y, z)$, and then integrate over the length of nanotube to obtain an average force that depends only on the y and z positions of the individual anion. The integrated force map is:

$$\langle F_{\mathrm{z},i}(y, z) \rangle = \left\langle \int_{-l'}^{l'} {F_{\mathrm{z},i}}'(x, y, z) dx \right\rangle \tag{6.11}$$

where ${F_{\mathrm{z},i}}'(x, y, z)$ corresponds to the sum of the forces applied on all tube atoms from given species i at position (x, y, z). Shown in Figure 6.6 are the results in NaI and NaCl solutions at $d = 16.4$ Å and 19.4 Å. From the perspective of anions residing in the hemisphere facing the bulk solution, a negative value in the figure denotes that the net force in z-direction for the corresponding anion at position (y, z) is repulsive and "pushes" the tubes to associate, while a positive value indicates an attractive net force that "pulls" the tubes apart. The opposite holds for anions within the inter-tube region. The figures are symmetrized by averaging forces from both tubes. We

therefore can increase the statistics since the tubes are equivalent about the center of the simulation cell.

6.3.3 Force Map: Spatial Distribution of Ions

In order to explain the connection between the force and spatial distribution of anions, we further multiply the density map of anion with the force map, as presented in Figure 6.7. For further clarity, we show in panel a (3 m NaI solution with $d = 16.4$ Å, the z-components of the tube axes are $\pm$ 8.2 Å) one way to divide the profiles into three regions: Region 1 represents $z \leq$ -8.2 Å; Region 2 corresponds to the region -8.2 Å $< z <$ 8.2 Å; Region 3 denotes the region $z \geq$ -8.2 Å. We observe that in all cases, there is a "half ring" of stabilizing anions directly adjacent to the tubes in Regions 1 and 3; the stabilization by iodide is greater than chloride as indicated by the stronger dark bands in Regions 1 and 3. The inner rings of stabilizing ions are enclosed by an outer destabilizing layer in Region 1 and Region 3; these are ions further away from the tube nearing the bulk region. Due to chloride anion's spatial preference of being in the bulk region, its outer destabilizing layer is greater than iodide. These distinct "types" of anions are present at both short and long tube separations (comparing panel a versus b for iodide, and panel c versus d for chloride). We now use this figure to explain the anion contribution in Figure 6.4 c.

At large separations, both anions exhibit neutral behavior towards nanotube association; the contributions to the PMF are on the order of $\sim$ 0.1 kcal/mol. From Figure 6.7 d, in the bulk regions (Regions 1 and 3), the stabilizing forces from the anions in direct contact with the tube are small, therefore leaving strong destabilizing forces from anions in the bulk. In the inter-tube region, although there are relatively few chloride anions, we still observe some stabilizing net forces in Region 2. With decreasing tube separation, chloride ions are expelled from the inter-tube region, thus driving this contribution to even smaller on average at small separations (and then at the contact state); since the majority of chloride density is in the bulk solution (there is no significant enhanced density of chloride anions at the tube surface), the net force

becomes destabilizing and the chloride PMF manifests as a monotonically increasing curve up to the contact state.

Primarily because of the significantly different spatial distribution of iodide anions, the iodide PMF manifests in quite a different curve. At large tube separations, the iodide anions directly adjacent to the tube in Regions 1,3 and Region 2 contribute equivalent, but opposite forces. The overall effect at this separation from ions directly in contact with the tube is marginally destabilizing. Offsetting this stability is the contribution from iodide anions in the bulk, thus leading to a slight destabilizing net force at large separations. Finally, nearing the contact state (short tube separations), the iodide density in the inter-tube region decreases as the anions are expelled from the region. This weakens the destabilizing force on the tubes in Region 2, which manifests as a slightly negative contribution to the PMF at contact state distances. Starting at the maximum in the iodide PMF contribution curve at 20 Å and moving towards the contact state, the expulsion of iodide anions from the inter-tube region coupled with the accumulation of these anions at the tube's outer surface (bulk-facing surface) leads to the gradual transition of the iodide PMF from positive to marginally negative values at the contact state. Since iodide hydration is not favored, the contribution from iodide in bulk solution (further way from the tubes) does not significantly increase so as to offset the stabilizing contributions from ions in direct contact with the tube. The barrier in the iodide PMF arises from the work required to expel iodide from the inter-tube region. This is the same phenomena associated with the barriers in the water contribution to the PMF. Thus, to reiterate, we suggest that the contributions from the anions to the overall PMF for SWNT association are significantly different and arise from the spatial distributions of the different species. This is again another manifestation of specific-ion effects in condensed phase heterogeneous environments.

Due to the presence of L-V interfaces and specific-ion interfacial stabilities of the iodide and chloride anions, the absolute ion densities in the bulk region, where the SWNTs are located, are slightly different, as exhibited in the inset of Figure 6.2 b. In a closed NPT or NVT ensemble simulation (with no liquid-vapor interface), the bulk

anion concentrations would be closer in value in the absence of a liquid-vapor interface to lead to interfacial enhancement of the iodide compared to the chloride anion. Thus, we address the implications of this difference on the general conclusions relating to the contributions of the anions to the total PMF. Specifically, we demonstrate by using artificial scaling of anion densities in the bulk and vicinal regions that the net z-direction force does not change sign, even with the application of extreme, non-realistic scaling regimes. By showing that the sign of the force is not altered for two different tube separations, we demonstrate that the slight differences in bulk anion densities do not alter the conclusions about the nature of the contributions of the two different anions to the potential of mean force. We remind the reader that the z-direction force used in the following discussion is simply a function of the position with respect to the tube, and can be thought of as a force per atom density within a small sampling volume around the tube. By multiplying this force density by the (scaled) atom density, we obtain the z-direction force under the varying conditions just described (i.e., scaled or non-scaled, the latter being the original density). From Figure 6.2 and Figure 6.7 we can separate the anions into bulk anions (in Region 1 or 3, and 17.0 Å away from the tube axis) and non-bulk anions (in Region 2 or within 17.0 Å to the tube axis). From Figure 6.2, we see that 17.0 Å is the radial distance at which the bulk liquid regime begins based on the plateauing of the anion densities. Therefore the total forces (only the z-components are considered) can be written as:

$$\sum F_z = \alpha \sum_{\text{non-bulk}} F_z(y,z)\rho_{\text{non-bulk}}(y,z) + \beta \sum_{\text{bulk}} F_z(y,z)\rho_{\text{bulk}}(y,z) \tag{6.12}$$

By varying scaling parameters α and β, we can see how the resulting variation of anion densities may affect tube association free energetics through the forces. Increasing α increases the density in the vicinal region (in the immediate vicinity of the tube), and increasing β increases the density in the bulk region. Figure 6.8 a and b show the $\sum F_z$ as a function of α and β for I^- and Cl^- at $d = 16.4$ Å. It is evident that within the range of ($1 \geq \alpha \geq 2$, $1 \geq \beta \geq 2$), the total forces from all the I^- remain stabilizing (facilitating tube association), while the total forces from all the Cl^- remain

destabilizing (facilitating tube dissociation). We project the surface onto the case of $\beta = 1$, which means no scaling for bulk anions, as shown in Figure 6.8 c. By increasing α we basically increase the number of anions in vicinity to the tubes. The different slopes between I^- and Cl^- further emphasize how the specific-ion effects tube association. In panel d we project the surface into the case of $\alpha = 1$, where scaling is only applied on the bulk anion density. Both I^- and Cl^- show the trend of increasing of repulsiveness, however, within the extreme range of densities chosen for this analysis, I^- consistently presents a favorable contribution to tube association. This suggests to us that the mechanistic picture of the role of differences in spatial distribution of anions will remain qualitatively the same for all densities. This analysis has not addressed the question of how changes in anion density will affect the depth of the PMF in the ionic solutions relative to the value in pure water. A more specific answer to this question is complicated by the fact that increasing the bulk density of iodide, for instance, will also tend to increase somewhat the near-tube density. Since the two density regions offer opposing contributions to the stability, it is difficult to precisely characterize the net effect.

Finally, we address the form of the water contribution to the PMF in panel b of Figure 6.4. We observe that in all cases (pure water, NaI solution, and NaCl solution) the water PMF exhibits a dramatic reduction nearing the contact state. This signifies that as the inter-tube region (Region 2) is dewetted, the destabilizing forces from water molecules adjacent to the tube in Region 2 vanishes. Water that is expelled is either accumulated adjacent to the tubes in Regions 1 and 3 (and is thus stabilizing the contact state), or returns to the bulk regions further from the tube. The reduction is greater in the NaCl system because more water accumulates at the surface of the tube in Region 1 and 3; since the chloride is preferentially solvated relative to iodide, expelled water molecules contribute more to stabilizing the contact state in the chloride solution than in the iodide solution. Furthermore, by virtue of a lower water density in the chloride system compared to that in the iodide system, water molecules contribute less destabilizing forces in the former case, and again in this manner contribute more

to stabilizing the contact state.

6.3.4 Enthalpic and Entropic Contribution

We consider decomposition of the total PMF into enthalpic and entropic components to assess the relative contributions of these thermodynamic quantities to the overall association free energetics. In particular, we are interested in the solvent induced contributions to the PMF, where we take the solvent to include all species except the tubes. Thus, the solvent induced enthalpy includes interactions between tubes and all other non-tube species, as well as interactions between all non-tube species (including self-interactions between non-tube species). Effectively, the tube-tube interaction energy is excluded. For each separation, the enthalpy is computed as the difference of the average interaction potential energy of the dissociated state and the state at the particular SWNT separation of interest; this reflects the fact that the enthalpy is referenced to the dissociated state as is the potential of mean force. The Gibbs energy change (considering the equivalence of the Gibbs and Helmholtz potentials by neglecting small ambient-condition P-V contributions to the former), ΔG has been computed via Equation 6.8. By subtracting the direct tube-tube Lennard-Jones interaction, we obtain the solvent-induced free energy for the state defined by a particular separation of the tubes; this is called ΔW_{solv}. In our system the volume change between the contact state and dissociated state is negligible, therefore the change in enthalpy (ΔH) is obtained as a difference in potential energy of the system at a particular tube-tube separation and that at the largest separation (dissociated state). To be consistent with ΔW_{solv}, we compute the total interaction energy between tubes and all other components of the system (which we consider the solvent: water, anions, and cations as relevant); this also includes interaction energy between elements of the solvent (water-ion, ion-ion, water-water).

The total enthalpic change can be written as:

$$\Delta H = -\sum_i \sum_j \Delta H_{ij} \tag{6.13}$$

where i, j indicate each component in the given system. Since the tube-tube interaction is independent of the systems, we only look at the solvent induced enthalpic changes (ΔH_{solv}), which can be obtained by subtracting the direct tube-tube potential part from the overall enthalpic change. The entropic change is therefore determined from $-T\Delta S_{\text{solv}} = \Delta G_{\text{solv}} - \Delta H_{\text{solv}}$ [284]. The results of these thermodynamic properties of pure water, 3 m NaCl and 3 m NaI systems are shown in Figure 6.9 a-c; further comparison of the same thermodynamic property among the three systems plotted on the same graph are presented in panels d-f of Figure 6.9. Figure 6.9 a shows the variation of free energy, enthalpy, and $-T\Delta S$ with tube separation for the tubes in pure water. Panels b and c show the same for 3M NaCl and NaI, respectively. In all cases, the solvent-induced contribution to the free energy is positive and destabilizes the contact state. Thus, the entire free energy stabilization of the contact state in our model system arises from the tube-tube enthalpy (interaction energy) arising from the Lennard-Jones potential. Moreover, the major solvent-induced free energy is driven by a repulsive enthalpy of interaction in all systems. Finally, the added stability of the contact state in the aqueous salt solutions, it appears, arises from the lower enthalpy of the solvent at the contact state. This behavior is most likely potential dependent as other studies may demonstrate higher enthalpic contributions for the salt solutions. These trends are further demonstrated in panels d-f of Figure 6.9. Panel e further highlights the dominant role of enthalpy as the driver of the added stability of the contact state in salt solutions. The added stability of hydrophobes in salt solutions, specifically NaCl solutions, has been described in detail by Athawale et al. [379].

The solvent-induced contribution to enthalpy can be further split into the change in tube-solvent interaction ($\Delta U_{\text{tube-solv}}$) and the remaining contribution from the change in solvent-solvent interactions and other mechanical work (ΔH_{rem}). When all the quantities are referenced to the values at the dissociated distance $d = 26.0$ Å, we have

$$\begin{aligned} \Delta U_{\text{tube-solv}}(d) &= U(d) - U(d_{\text{dissociated}}) \\ &= \Delta U_{\text{tube-water}}(d) + \Delta U_{\text{tube-anion}}(d) + \Delta U_{\text{tube-cation}}(d) \end{aligned} \quad (6.14)$$

The results of $\Delta U_{\text{tube-solv}}$ and ΔH_{rem} as functions of d are shown in Figure 6.10. From Figure 6.10 a, $\Delta U_{\text{tube-solv}}$ of all the systems are nearly zero at large intertube separation. At $d = 19.4$ Å and 21.8 Å, which correspond to the critical distances that water molecules form the monolayer and bilayer structures, the changes in $\Delta U_{\text{tube-solv}}$ are considerable. As the intertube separation reduces, $\Delta U_{\text{tube-solv}}$ becomes more unfavorable and contributes significantly to the unfavorable ΔH_{solv}. This behavior is similar with Choudhury et al.'s study [378] using two planar solutes, while in their case, due to the expulsion of water between the solutes, the interactions of the confined water with the solutes decrease, therefore leads to the increase of $\Delta U_{\text{tube-solv}}$ at small intersolute separation. However, owing to different geometry and larger surface area in our system, $\Delta U_{\text{tube-solv}}$ keeps increasing below $d = 19.4$ Å, while in their case $\Delta U_{\text{tube-solv}}$ eventually becomes a constant at small intersolute separation. We also notice that in the case of 3 m NaCl solution, changes in the direct tube-solvent interactions contribute to destabilizing the contact state more than in the case of 3 m NaI and pure water systems. Since the ΔH_{solv} in pure water is more destabilizing than the cases in salt solutions, it indicates that the remaining contributions from solvent-solvent interactions and from the pressure-volume work ($P\Delta V$) in pure water have to be even more destabilizing. In this study, we consider the $P\Delta V$ term negligible and therefore the solvent-solvent interactions dominate the ΔH_{rem}. The results shown in Figure 6.10b suggest less favorable solvent-solvent interactions in pure water, which may be due to the reorganization of more expelled water molecules from the intertube region into the bulk. The solvent enthalpy is more favorable in the NaCl system; since chloride anion is preferentially solvated relative to iodide, the added enthalpic stabilization of the system (within the context of the current force field) with chloride ions present is reasonable. Iodide ions preferentially segregate to the tube-water interface (and the liquid-vapor interface). Thus, the changes in enthalpy for the pure water and NaI systems can reasonably be considered to be equivalent. This is borne out by the results of Figure 6.10 b.

To explore the nature of the contributions to enthalpy and entropy arising from interactions involving components of the salts (chloride, iodide, and sodium), we further

investigate the individual contribution to these thermodynamic properties by decomposing the enthalpic changes using the following relation which ascribes an enthalpy change for a species i that is determined from its interactions with all other components of the system. ΔH_{Iodide}, for instance, represents the difference in the interaction energy involving iodide ion between the contact and largest separation states and can be written as:

$$\Delta H_{\text{Iodide}} = \Delta H_{\text{Iodide-tube}} + \Delta H_{\text{Iodide-water}} + \Delta H_{\text{Iodide-Iodide}} + \Delta H_{\text{Iodide-Sodium}} \quad (6.15)$$

The results of ΔH_{ion} and $-T\Delta S_{\text{ion}}$ as functions of d in salt solutions are shown in Figure 6.11. For clarity, vertical offsets of -2 and -1 kcal/mol are imposed for the entropic contribution in anion and cation, respectively. Considering the anions first, Figure 6.11a demonstrates that the stabilization of the contact state by iodide ion is facilitated by a larger entropy gain associated with iodide. Both chloride and iodide show destabilizing enthalpic contributions, of about the same magnitude as well. At the contact state, the enthalpic and entropic contributions of the iodide-induced profiles almost exactly cancel. The entropically stabilizing effects of iodide arise from the fact that segregation of iodide at the interfaces increases the overall entropy of the system through the increased configurational volume available to water. We stress that this is a qualitative argument for the stability conferred to the contact state by the iodide anion. In the case of iodide, release of water and the limited iodide between the tubes, in conjunction with the enhancement of iodide density at the tube surface, thus favors the contact state. The sodium essentially exhibits an enthalpic destabilization, with a slight decrease in entropy due to the structuring of water around the relatively small sodium ion once it is released into the bulk regions at the tube contact state.

6.4 Temperature Effects of Carbon Nanotube Association

In this section we continue to probe the effects of simple inorganic salt solutions, sodium iodide (NaI), on the energetics of assembly in such systems, and provides a reference point from which to consider systems where salts are used in combination

with larger dispersants (i.e., surfactants, polymers, etc.) in order to effect desired physical behaviors leading to desired physical properties and structures, using GPU-based resources. Particularly, we are interested in the temperature dependence of the free energetics of association, and how the contributions of water and ions change with temperature, as well as the hydrophobe-solvent interfacial fluctuation.

6.4.1 Free Energetics of Nanotube Association and Decompositions

We start by considering the free energetics of nanotube association and its decomposition into enthalpic and entropic components to assess the relative contributions of these thermodynamic quantities. The method for PMF calculation has been discussed as Equation 6.7. We show the PMFs for 3 m NaI solutions at different temperature in Figure 6.12 a. Inset shows the minimum region of the PMF profiles. Numerical results (ΔW_{total}) are summarized in Table 6.5. We also include $\Delta W^b = W(\xi_{\text{peak}}) - W(\xi_{\text{dissociated}})$ as the value from the dissociated state to the first barrier (which is usually treated as the desolvation barrier for hydrophobic association process). The increase in stability, as represented with ΔW_{total}, is linear in temperature with a slope -0.071 kcal mol^{-1} K^{-1}. This slope is consistent with the slope of stability for nanotubes in pure SPC/E (in the absence of ion), which is not surprising since the water dominates the contribution to the PMF. The barrier (ΔW^b) is seen to shift slightly toward larger ξ and exhibits a similar temperature dependence with a weaker slope -0.058 kcal mol^{-1} K^{-1}. Interestingly, in another study using two hydrophobic plates (diameter $\sim$ 21 Å) with the same water model performed by Zangi and Berne [284], their slope of stability (-0.032 kcal mol^{-1} K^{-1}) is smaller than our result [3]. In an early work by Mancera and Buckingham, they reported the aggregation

[3] In Reference [284], the largest difference between the free energy changes, ΔG(T = 280 K) - ΔG(T = 340 K) $\approx$ 8 kJ/mol, which roughly gives the slope = -0.032 kcal mol^{-1} K^{-1}. Although the highest temperature (360 K) did not induce the most favorable contact state, 8 kJ/mol is barely larger than the error of free energies reported. Their conclusion was that the change in free energy for plate association is weakly temperature dependent.

of ethane in aqueous solution has a different tempendence with temperature, in which they found at the intermediate 317 K ethane particles have the maximum tendency to aggregate [380]. Although not the main scope in this study, this might be related to the difference in solute size between ethane with the model hydrophobes in Zangi's and our work, since the thermodynamic driving force (enthalphic or entropic) is length-scale dependent [355, 346].

From the previous discussion, the non-solvent contribution (i.e., force from the other carbon nanotube) is identical for all environments, we therefore consider ΔW_{solv}, ΔH_{solv} and ΔS_{solv} between dissociated state ($d = 26$ Å) and contact state ($d = 16.9$ Å) as functions of temperature in Figure 6.12 b and c, to address their temperature dependencies. The (decorrelated) uncertainties of ΔH_{solv} were obtained from block averages method [279]. We notice that values of ΔW_{solv} and ΔH_{solv} are positive for the temperature range in this work. Both Gibbs free energy change and enthalpic change are less repulsive at higher temperature, with a stronger slope/dependence in magnitude for ΔH_{solv} than ΔW_{solv} to the temperature. This negative slope of enthalpic change with temperature is similar to that observed in the folding of proteins [381, 382, 383], although our simulations were under the condition of constant volume. A larger slope in magnitude for ΔH_{solv} than ΔW_{solv} indicates a compensation in entropic change. At high temperature, the ΔS_{solv} term is almost zero, consequently the association process is dominated by enthalpy; at low temperatures, ΔS_{solv} becomes 5 times larger and there is more entropic contribution to the association. Similarly, Lüdemann et al. [384] studied the hydrophobic interactions of two methane-like particles in water and found that at 300 K the association is controlled by entropy, while the internal energy takes over and dominates at high temperature. Here we will not argue whether the association process at the low temperature is dominated by enthalpic or entropic contribution, since the origin of that depends on the strength of solvent-tube interactions (i.e., the force fields) [284]. In our system, the solvent includes water, anions and cations, the situation is therefore more complicated. However, our main goal here is to reflect that the temperature dependencies of the three thermodynamic quantities in this work are

similar to other studies at the nanometer scale qualitatively [284, 378]. It implies that the parameters in this study are reasonable and also that there are underlying global similarities in the descriptions of atomic-level interactions.

Our next question is then, what is the temperature dependence of each component in the solvent? By using the same method in previous discussion, individual solvent-induced contributions to the PMF can be decomposed and are displayed in Figure 6.13; numerical values for individual component to ΔW_{solv} are listed in Table 6.5. As the temperature increases, ΔW_{water} becomes less positive/repulsive/destabilizing. On the other hand, ΔW_{I^-} is negative/stabilizing at low temperature (which is consistent with our previous result), but becomes destabilizing at high temperature. ΔW_{Na^+} shows no significant difference throughout the temperature range in this work (≈ 1.3 kcal/mol).

We take water contribution as an example to explain this difference of temperature dependence among the three species from the mechanistic point of view, with the density-weighted force map in previous section. In our system, tube atoms are neutral, therefore only van der Waals forces are considered for tube-water interactions. Shown in Figure 6.14 a and b are $\langle F_{\text{z,water}}(y,z)\rangle$ at $d = 16.4$ Å and 19.4 Å. Here we emphasize that the force map is only related to how different tube separation effects the water spatial distribution, and is independent from the temperature. From the perspective of waters residing in the hemisphere facing the bulk solution, a negative value in the figure denotes that the net force in z-direction for the corresponding water at position (y,z) is repulsive and "pushes" the tubes to associate (stabilizing), while a positive value indicates an attractive net force that "pulls" the tubes apart (destabilizing). The opposite holds for waters within the intertube region. The figures are symmetrized by averaging forces from both tubes to increase the statistics since the tubes are equivalent about the center of the simulation cell. We can then categorize the "stabilizing water" and "destabilizing water" based on the spatial position of the water molecule. Since the force map is independent from the temperature, the difference in density-weighted forces between two temperature is then determined by the difference of density maps.

The difference of densities for water oxygen between 300 K (low temperature) and 360 K (high temperature), which can be written as $\rho_{i,300\mathrm{K}}(y,z) - \rho_{i,360\mathrm{K}}(y,z)$, are shown in Figure 6.14 c and d, for the tube separation $d = 16.4$ Å and 19.4 Å, respectively. The difference of spatial density-weighted force map is then the product of panel a and c (or panel b and d), as presented in Figure 6.14 e and f. In Figure 6.14 a and b, the major difference is the strongly repulsive/destabilizing water band at the intertube region for $d = 19.4$ Å; on the other hand there is an evident excess of water in this intertube region at low temperature (as presented in Figure 6.14 d). Meanwhile, due to more "destabilizing" water in the intertube region at 300 K, water is then anticipated to apply more repulsive/destabilizing contribution in sum. We admit that without actually summing up the force, the current force map may not be quantitatively sufficient to explain the difference of solvent-induced PMFs; what we are suggesting is that the contributions from the waters/anions to the PMF for nanotube association are different and arise from the spatial distributions of each species at the different temperature. This differences in spatial distribution for the bulk environment, in the vicinity of the nanotubes, and the intertube regions, are then studied in the following sections as to manifest the origin of the temperature dependence of nanotube association.

6.4.2 Solvent Structure: Tube Center to Solution Bulk

In this section we will study the waters/ions residing in the hemisphere facing the bulk solution, as a reference/baseline for the behavior and structure of the solvent at different temperature. We start with radial number density profiles of water molecules and ions about the tube using Equation 6.6. Figure 6.15 shows the radial density profiles of water oxygen atoms and ions as a function of r which is relative to the center of the tube axes (at $r = 0.0$ Å).

In Figure 6.15 a, we observe enhanced water density in the first solvation shell of the nanotubes. This is consistent with a preponderance of published data concerning first solvation shell ordering around large hydrophobes. At higher temperatures, the structuring is reduced, though even up to 360 K the first shell retains a significantly

enhanced density relative to the bulk. This effect may be attenuated with modified interaction potentials between water and hydrophobic moiety, but the essence of the physical effect will remain as long as physically relevant interaction energies/forces are incorporated in the force fields. We believe that the models for water-hydrophobe interactions applying here are well-tuned for this interface. Figure 6.15 b shows the density of I^- in the same regions corresponding to Figure 6.15 a for water; the temperature dependence is similar to that of water. As the anion replaces water molecules in the immediate vicinity of the tubes, the cation is forced to the next outer solvation layer, thus creating an electrical double layer in the immediate vicinity of the tube, as shown in Figure 6.15 c. The density of the cation is substantially lower than exhibited by the anion near the nanotube surface. Furthermore, we observe that the cation is more probable to reside in the nanotube interior ($r < 4.0$ Å, intra-tube region) as demonstrated by the density profiles of Figure 6.15 c. This is not surprising since the cation, being smaller, is also well solvated and does not lose its local hydration shell upon entering the intra-tube region. For this intratube region, the average number of water molecules ($\langle N_{\mathrm{intra-tube,water}} \rangle$), anions ($\langle N_{\mathrm{intra-tube,anion}} \rangle$) and cations ($\langle N_{\mathrm{intra-tube,cation}} \rangle$) are summarized in Table 6.6. These values are calculated as direct averages of the number of species in the tube normalized by the number of observations. Uncertainties included in the parentheses are determined from the standard deviations of $\langle N_{\mathrm{intra-tube}} \rangle$. The average number of intratube water molecules is greatest at 300 K and follows the same temperature dependence as the first solvation shell; however, the average numbers of ions are low (about or less than one ion pair within the tube per snapshot) and they are not very sensitive to the system temperature. Mimicking the interfacial propensities on the bulk solvent side of the tubes, we see that the anion, even when in the nanotube interior, displays enhanced density at the edge of the intra-tube volume, while the cation resides in the interior where it is well-solvated.

We next present the surface fluctuations of coarse-grained tube-water surfaces and tube-ion surfaces for the bulk sides of the tubes, to discuss the interfacial propensity of each species at different temperature, as an application of the fluctuation analyses.

By tube-ion surface, we mean the interface formed between the tube and the ions taken to be a solvent-like medium in the absence of water. Ideally, because of the cylindrical symmetry of the tube, the surface fluctuation should be identical and independent from θ and l, except for the regions near the termini/edges of the tube. To represent the fluctuation values and prevent edge effects, we show the $\langle \delta h^2(\theta, l) \rangle$ as an average in the region -5 Å $\leq l \leq$ 5 Å and 85° $\leq \theta \leq$ 95°. The uncertainties were obtained via standard deviation. The results for tube-water and tube-ion fluctuations at different temperature are shown in Figure 6.16 a and b. A few salient features are noteworthy in this figure: (i) generally, the magnitude of tube-ion fluctuations is larger than tube-water fluctuations. (ii) All the solvent components show enhanced fluctuations as the temperature increases, however, in terms of the absolute magnitude of the difference (between 300 K and 360 K), the difference in tube-I^- ($\approx$ 1.6 Å^2) is the greatest, then the difference in tube-water ($\approx$ 0.4 Å^2), and tube-Na^+ is rather modest ($\approx$ 0.3 Å^2). If we consider the relative magnitude of each component (normalized with the inherent fluctuation at 300 K), we have tube-water (53%) > tube-I^- (34%) > tube-Na^+ (4.6%). Therefore, the results suggest that tube-Na^+ shows basically no temperature dependence, while tube-I^- and tube-water are dependent on temperature. Interestingly, this is consistent with what has been observed in the PMF and radial density profile.

We use the deformability/malleability of solvent shell to explain these features. From Figure 6.2 a, the density ratio between the first peak (r = 10.1 Å) and the first minimum (r = 11.7 Å) of water is 0.095 Å^{-3}/0.015 Å^{-3} = 6.33; from Figure 6.2 b this ratio for I^- is 0.0031 Å^{-3}/0.00095 Å^{-3} = 3.26; and for Na^+ this ratio is 0.0022 Å^{-3}/0.0015 Å^{-3} = 1.47. The ratios demonstrate different manners in which the solvation shells of the nanotubes couple with the solvent component at the interface. Water retains the strongest, least ambiguous, well-defined solvation shells, and does not support the intermixing with water from outer shells, therefore the tube-water interface is the least malleable. I^- holds the second strongest ordered solvation shells while Na^+ is the weakest, subsequently the tube-ion surfaces are more deformable. As the temperature increases, the ratios for water and I^- decrease (as highlighted in the

insets), their malleabilities of solvation shells are increased, subsequently the corresponding fluctuations rise. In the case of Na^+, the ratio between the first peak and the first minimum is insensitive to the temperature, hence no significant temperature dependence is observed.

Previously, we investigated the connection between the stability of a solute at the liquid-vapor interface and corresponding interface fluctuation. The fluctuation can be separated into water inherent and solute-induced contributions. When temperature increases, the enhancement of inherent thermal water surface fluctuation raises, thus reduces the impact of any solvent structural perturbation induced by the solute [93]. This behavior accompanies with the disappearance of (adsorption) free energy minimum of surface stable species near the interface. In this study, this behavior is shown as the reduction of the first peak of anion density (Figure 6.15 b) as the temperature elevates.

As we suggested, the structure of water molecules is important in explaining the temperature dependencies of fluctuations and PMF; we consider the hydrogen bonding network and geometric configurations at hydrophobic surfaces next. Specifically, we investigate hydrogen bonding numbers (average hydrogen bonds per molecule, $\langle N_{\mathrm{HB}} \rangle$) and the angular tetrahedral parameters (q, to be defined further below) at various locations. Two water molecules were considered hydrogen bonded if the oxygen-oxygen distance is less than 3.5 Å and the HO$\cdots$O angle is less than 30° [180, 181, 110]. The average number of hydrogen bonds, normalized by the number of hydrogen bonds in the bulk for T = 300 and 360 K for the configuration $d = 16.4$ Å, are shown in Figure 6.17 a as functions of r using the same cylindrical sampling volume that we used to compute the radial density profiles. In aqueous salt solutions, due to the presence of ions, the average hydrogen bonds per water molecule in the current solvent bulk is less than the pure water bulk (about 3.5 hydrogen bonds per water molecule for SPC/E). The inset shows the numbers of hydrogen bonds per water molecule in the bulk at the temperatures in this work. The uncertainties were obtained via standard deviation. As the temperature increases, less hydrogen bonds are formed for bulk water. In the

intra-tube region, water tends to hold more hydrogen bonds than water in the bulk region. This should not be surprising since on average only 1-2 ions are found in this region, the equivalent concentration is about half compared to the bulk, consequently the hydrogen bonding network is less affected by the ions. In the vicinity of the nanotubes, we found a slight enhancement followed by a depletion of hydrogen bonds; as the temperature elevates, the number of hydrogen bonds at the interface is reduced. Considering the deformation of hydrogen bonding network as a result of lack of strong electrostatic interaction between hydrophobe and water, water-water interactions are therefore more important in shaping the orientation of water molecules [385]. Since the loss of hydrogen bonds is more likely to happen when there is another partner (i.e., another water molecule in our case) in the neighborhood to exchange the bond with, the location near the tube surface (which is considered liquid-vapor like) can promote the maximization of hydrogen bonding. However, the incompatibility of the tube surface with the tetrahedral network induces a distortion in the donor-acceptor angle for the water at the interface than in the bulk [284]. With increased temperature, the rotational mobility of water increases. At high temperature, the water molecules in the bulk are correlated and therefore have to maintain a certain degree of tetrahedral network connectivity; however, the orientational preference of water near the tubes limits the ability to simultaneously rotate and maintain hydrogen bond connectivity.

We next apply the conditional tetrahedral parameter (q) introduced by Godec et al. [183] to describe the configurations of water near the nanotubes. For a tetrahedral configuration there are five points: the four vertices of the tetrahedron and the center. In a perfectly tetrahedral arrangement, all the angles between bonds hold the same value, and the cosine of this angle is -1/3. However, in the vicinity of the tubes, water molecules may not have four nearest hydrogen-bonded neighbors. Physically, at least two neighboring water molecules are necessary for a meaningful evaluation of tetrahedral order. The generalized form of the conditional tetrahedral parameter can

therefore be written as:

$$q_i = 1 - \frac{1}{N(N-1)} \frac{9}{8} \sum_{j=1}^{N-1} \sum_{k=j+1}^{N} (\cos \psi_{j,k} + \frac{1}{3})^2 \tag{6.16}$$

where $\psi_{j,k}$ is the angle subtended at the central water between the j_{th} and k_{th} bonds. N is the number of neighboring water molecules with $2 \leq N \leq 4$. The squaring ensures the contribution from each inter-bond angle is always greater than or equal to zero. The normalization factor is chosen so that $q_i = 1$ when the configuration is perfectly tetrahedral (all the cosine values are -1/3); $q_i = 0$ indicates the extreme non-tetrahedral arrangement. The average tetrahedral order parameter, q, normalized by the corresponding bulk values (q_{bulk}) for T = 300 and 360 K at the separation d = 16.4 Å, are shown in Figure 6.17 b as functions of r using the same cylindrical sampling volume that we used to compute the radial density and hydrogen bond profiles. The inset shows q_{bulk} values as a function of temperature, the uncertainties were obtained via standard deviation. Consider the radius of the nanotube is roughly 6.8 Å, the tetrahedrality of water molecules shows slight enhancement extending up to 5.5 Å from the tube atoms. At 300 K, q reaches a maximum of 0.97, which is about $1.1 q_{\text{bulk}}$. q_{bulk} is not sensitive to temperature, gives only 0.95% difference between 300 K and 360 K, while $\langle N_{\text{HB,bulk}} \rangle$ gives 7.26% difference between these two temperatures. Qualitatively, our results with temperature dependence are consistent with the experiment performed by Davis et al. [386]. The authors reported temperature-dependent Raman scattering measurements to investigate the hydrophobic hydration shells of linear alcohols. At low temperatures, the hydration shells were found to hold a hydrophobically enhanced water structure with greater tetrahedral order along with fewer weak hydrogen bonds than the surrounding bulk water. By increasing the temperature the structure is replaced by a less ordered structure with weaker hydrogen bonds than bulk water.

6.4.3 Solvent Structure: Intertube Region

We next study the solvent structure of the intertube region. To investigate the behavior of water molecules and ions within the intertube region, we use the rectangular

sampling volume defined in the previous discussion, as illustrated in Figure 6.1 b and c. The average numbers of water oxygen atoms ($\langle N_{\text{inter,water}} \rangle$), anions ($\langle N_{\text{inter,anion}} \rangle$) and cations ($\langle N_{\text{inter,cation}} \rangle$) in the rectangular box as functions of d are shown in Figure 6.18. Insets show focused view of the dramatic increase of $\langle N_{\text{inter,water}} \rangle$. As temperature increases, the number of intertube water is reduced. The plateaus in Figure 6.18 a suggest the existence of stable solvation shells at particular tube separations, and are also found in other instances of hydrophobic association [387, 378]. We plot the water oxygen density profile along z-dimension at 300 K and 360 K in Figure 6.19 to illustrate this behavior. Each $z \sim z+dz$ region has the same x and y-dimension length resulting in a sampling volume of $L \times H \times dz$. The second solvation shell of water only appears at the largest separation, therefore the total number of $\langle N_{\text{inter,water}} \rangle$ is determined by the first solvation shell. At the same tube separation, the density of water at low temperature is substantially larger than the density at high temperature, which correlates with the water densities in the outer regions. Giovambattista et al. also found the same behavior for the water confined between two hydrophobic plates [388]. The effective hydrophobicity of the tube decreases as temperature decreases, consistent with the suppression of the vapor phase upon cooling. The numbers of anion and cations in the intertube region are not sensitive to the temperature, as shown in Figure 6.18 b and c. We should point out that the difference of $\langle N_{\text{inter,water}} \rangle$ in our system is very small (less than 3 water molecules at $d = 22.0$ Å); meanwhile, even at the largest separation, only 1.3 pairs of ions are observed, resulting in an equivalent concentration also about half compared to the bulk environment.

We next address the surface fluctuation for intertube region. Due to the scarcity of ions in this region, we only focus our discussion on the tube-water interface fluctuation. The results for tube-water fluctuations for various tube separations at 300 K and 360 K are shown in Figure 6.20. At the dissociated state, we found $\langle \delta h^2(\theta, l) \rangle \sim 0.65$ Å^2 at all temperatures, which results from the small discrepancy of effective concentration/environment in this confined region as discussed. Also because of the lower effective concentration in this region, we found a smaller $\langle \delta h^2(\theta, l) \rangle$ value relative to

the fluctuation at the outer sides (as shown with red dashed lines, along with the uncertainties, which are plotted as dotted lines). In the biological content, ofttimes by measuring the unfolding transition, we can determine the role of salt concentration in protein stability. Date and Dominy reported that the protein stability (as depicted by the unfolding free energy) is primarily exerted by the screening of surface charge-charge interactions at lower salt concentrations, but dominated by the non-polar solvation (which, is often characterized as hydrophobic effects in aqueous solvents) at higher concentrations [389]. As the concentration of the solvent raises, surface tension increases and strengthens the hydrophobic effect. In our case, the contraction of concentration in the intertube region leads to less hydrophobicity and less induced interface fluctuations. In Figure 6.21, we include our results of $\langle \delta h^2(\theta, l) \rangle$ of the sides facing the outer region, at different concentration (0 m, 1 m, 3 m) of NaI aqueous solution to support this argument.

It is worth noting that a crossover of $\langle \delta h^2(\theta, l) \rangle$ (relative to the outer side fluctuation) happens between $d = 22.0$ Å and 23.0 Å (we do not consider the crossover between $d = 21.0$ Å and 22.0 Å due to the large uncertainties observed at their intermediate separations). First, at these separations, less than 0.5 pairs of ions are observed (refer to Figure 6.19 b and c). Consider there are ~ 20 water molecules in the intertube region, the "crossover" should be dictated by the water behavior. Again we use the "malleability" of solvation shell to explain this "crossover" of fluctuations. From Figure 6.19 a, when $d = 22.0$ Å and 23.0 Å, the intertube densities are similar; but the ratio between the density peak and density minimum (i.e. $z = 0$ Å) considerably different, as listed in Table 6.7. The shell "malleability" for $d = 23.0$ Å is therefore weaker than the the case $d = 22.0$ Å, as a consequence the fluctuation for $d = 23.0$ Å is less. Recall that for the outer sides of the tubes, we have a ratio ~ 6.33 for the water solvation shell in the bulk side of the tube. This value (6.33) is between the ratios at $d = 22.0$ Å and $d = 23.0$ Å (both in low and high temperature scenarios), therefore a "crossover" behavior should be expected. This argument also holds when we compare the ratio at the same separation but different temperature. At $d = 22.0$ Å, the ratio

for 300 K ($\sim$ 2.76) is larger than the ratio for 360 K ($\sim$ 1.94), therefore the the former solvation shell is more rigid and holds a smaller fluctuation; meanwhile, at $d = 23.0$ Å, the ratio for 300 K ($\sim$ 22.76) is substantially greater, in consequence its corresponding fluctuation value is significantly lower.

We next address the hydrogen bonds and tetrahedrality of the water molecules as functions of z in the intertube region. Same sampling volume ($L \times H \times dz$) is used as we discussed in intertube densities. The results of $\langle N_{\mathrm{HB}} \rangle / N_{\mathrm{HB,bulk}}$ and q/q_{bulk} at various tube separations at 300 K and 360 K are shown in Figure 6.22 and Figure 6.23. Usually, under the confinement of hydrophobes, the (SWNT) walls do not form any hydrogen bonds with water molecules, the average number of hydrogen bonds per molecule in the confined system is expected to be smaller than in bulk environment [390, 391]. The addition of salts has little effect on the O-H and H-H structures but still distorts the arrangement of the water network [392]. Therefore the relatively lower concentration in the intertube region has less effects on hydrogen bond breaking (when $d > 21.0$Å), as shown in Figure 6.22. This concentration dependence of hydrogen bonding profile is consistent with the neutron diffraction data from monovalent ionic solutions reported by Mancinelli et al. [83]

For intertube water tetrahedrality, at small separation ($d < 22.0$ Å) all the $q(z)$ is smaller than the bulk value. When $d = 22.0$ Å (for both low and high temperatures) we observe that the largest $q(z)$ (at $z = 0$ Å) barely coincides with the bulk value. At $d = 23.0$ Å, strongly enhanced q (even larger than the q_{bulk}) is discovered in the intertube region, indicating a highly-ordered structure of water molecules. Again, we use the idea of equivalent concentration in the intertube region to explain this behavior. From Figure 6.18, below the separation of 21 Å, the presence ion is not found. There are also very limited amount of water in the intertube region to introduce a nice, tetrahedral structure. As the tube separation increases, this region allows the entry of ions, with a lower equivalent concentration relative to the bulk. The corresponding tetrahedral structure among water molecules are therefore less perturbed by the ions, in agreement with Galamba's results of tetrahedrality of water in different concentration

of aqueous salt solutions [86]. Another feature at $d = 23.0$ Å is that, considering q_{bulk} being insensitive to the temperature, we have $q(z)$ reduced for all values of z as temperature increases, suggesting that the water local structure becomes less ordered (ice-like) in this respect, in consistence with the temperature dependence reported by Giovambattista et al. using two hydrophobic plates [388]. However, due to the geometry of nanotubes and the resulting intertube environment, we found no plateaued profile nor the widening profiles in $q(z)$ upon cooling [393, 388].

6.5 Conclusions

In this chapter, we investigate how salt solutions of Cl^- and I^- ions influence the magnitude of the association between two carbon nanotubes, in order to study how ion-specificity affects the hydrophobic association. Specifically, we address how the differences in the contributions of the two anions arise from the perspective of the significantly different spatial distribution of ions around the nanotubes. To accomplish this, we have used molecular dynamics simulations to calculate the potential of mean force between two nanotubes in aqueous salt solutions as a function of the distance between the tube axes.

The present results indicate that both the Cl^- and I^- salt solutions marginally stabilize the hydrophobic contact state, although the contributions of the anions in this process are drastically different. We stress that the dominant stabilizing factor, leading to the deep potential of mean force minimum, is the tube-tube interaction energy; in the salt solutions, the combined effects of anion, cation, and water lead to further overall marginal enhancement in the stability of the contact state. We address this interplay between the various components in the salt solutions. At large tube separations, both the Cl^- and I^- solutions show very little difference in that both anions contribute relatively little to the PMF. As the intertube distance decreases, the segregation of the larger, less strongly-hydrated I^- anion to the nanotube surface coupled with the emptying of the intertube region by I^- anion (as well as water) leads to the iodide presenting a net stabilizing force on the tubes. The proximity of the

iodide anions to the tube surface (asymmetrically) effectively pushes the two tubes together. Cl^-, on the other hand, is not surface active and contributes destabilizing, longer-ranged dispersion forces that effectively pull the tubes apart. That we observe almost an equivalent stabilization of the tube contact state in the two salt solutions despite the differences in the contributions from the anions is reconciled by considering the associated differences in water contributions to the potential of mean force. In the case of I^- solutions, water is driven further away from the tube surface because of iodide anions segregating to the surface; the force contributed by water further away is to pull the tubes toward the water and away from one another, thus destabilizing the contact state. In the Cl^- solutions, much less water is expelled from the immediate vicinity of the tubes; water thus exerts a greater net destabilizing force in the iodide solutions compared to that in the chloride solutions. These factors in aggregate lead to the stabilization of the contact state in both NaCl and NaI relative to that in pure water.

We further studied the effect of temperature on the interfacial properties of carbon nanotube assembly in 3 m NaI aqueous solution using GPU-enabled molecular dynamics simulations (FEN ZI). Decomposition of solvent-induced PMF into changes in enthalpy and entropy suggests that all three thermodynamical quantities decrease with increasing temperature. At the highest temperature (360 K) in this work, we found barely any entropic contribution to the free energetics. Further decomposition of PMF into each solvent component (water, I^- and Na^+) implies that as the dominant component, water contributes to the tube association in a less destabilizing manner as the temperature increases. I^- shows reversed trend, and Na^+ presents no dependence on temperature. From the mechanistic point of view, this difference in force contribution originates from differences in spatial distribution of the various system species.

In order to illustrate these different dependencies to the temperature, we examined the spatial distribution and the structure of the solvent in different regions: intertube, intra-tube, along with the outer-tube region extending from the tube surface

to the solvent bulk. For the outer side of the nanotubes, by calculating the fluctuation of coarse-grained tube-solvent surfaces, we found that proportionally, tube-water fluctuation exhibits the strongest temperature dependence. Tube-I^- fluctuation also shows similar but weaker dependence to the temperature, while tube-Na^+ shows no dependence in general. These characteristics are discussed via the malleability of their corresponding solvation shells. Hydrogen bonding profile and tetrahedrality of water arrangement are also computed to describe the structure of solvent at different temperatures. The analysis of hydrogen bonding in the vicinity of the nanotubes suggests an orientational preference of water molecules, implying a higher orientational order relative to the bulk water. It is worth noting that, grid-based surface height fluctuation can also be a method to estimate the surface entropy. The greater fluctuation of tube-solvent surfaces at higher temperature indicates a possibly higher surface entropy. These two contributions to the entropy change counteract with each other and result in the low entropy change (~ 0) at high temperature, in agreement with Zangi et al.'s study using two hydrophobic plates [284]. The hydrophobic confinement induces a relatively lower concentration environment in the intertube region, therefore causing different behavior depending on the tube separation. At the separation = 23.0 Å the malleability of water solvation shell reduces (weaker than the solvent bulk side), consequently generates smaller interface fluctuation; on the other hand, at separation = 22.0 Å the malleability of water solvation shell increases (stronger than the outer side), therefore a "crossover" of fluctuation is observed at the intermediate tube separation. This implies a comparative malleability of solvation shell or similar environment of "hydrophobicity" at a critical separation.

	$R_{\min}$ (Å)	ε (kcal/mol)	q (e)
O	3.5537	0.1554	-0.8476
Cl^-	4.9340	0.1	-1
I^-	5.9872	0.0377	-1
Na^+	2.9004	0.1	1
Tube[a]	4.0195	0.0663	0

Table 6.1: Parameters used in the simulation. [a] The LJ parameters for oxygen-tube interaction are fixed to be $\varepsilon_{ij} = 0.1015$ kcal/mol, $R_{\min} = 3.7793$ Å. Reproduced with permission from Shuching Ou, Sandeep Patel and Brad A. Bauer. "Free Energetics of Carbon Nanotube Association in Pure and Aqueous Ionic Solutions." *Journal of Physical Chemistry B.* **2012**, *116 (28)*, 8154-8168. Copyright 2012 American Chemical Society.

	$\langle N_{\text{intra-tube,water}} \rangle$	$\langle N_{\text{intra-tube,anion}} \rangle$	$\langle N_{\text{intra-tube,cation}} \rangle$
Pure SPC/E	51.10(15)	-	-
3 m NaCl	50.32(22)	0.24(12)	0.66(16)
3 m NaI	49.02(52)	0.47(15)	1.07(16)

Table 6.2: Average number of water molecules, anions and cations within the tube. Values in parentheses denote the uncertainty in the last reported digit as determined from the standard deviation. Reproduced with permission from Shuching Ou, Sandeep Patel and Brad A. Bauer. "Free Energetics of Carbon Nanotube Association in Pure and Aqueous Ionic Solutions." *Journal of Physical Chemistry B.* **2012**, *116 (28)*, 8154-8168. Copyright 2012 American Chemical Society.

	ΔW_{tube}	ΔW_{water}	ΔW_{anion}	ΔW_{cation}	ΔW_{total}
Pure SPC/E	-62.17	17.14(6)	-	-	-45.03(6)
3 m NaCl	-62.17	7.59(32)	3.83(5)	1.52(3)	-49.24(38)
3 m NaI	-62.17	11.55(49)	0.07(3)	1.33(1)	-49.22(51)

Table 6.3: Decomposition of potential of mean force into contributions from water, tubes, anions, and cations. Values in parentheses denote the uncertainty in the last reported digit as determined from the standard deviation. Reproduced with permission from Shuching Ou, Sandeep Patel and Brad A. Bauer. "Free Energetics of Carbon Nanotube Association in Pure and Aqueous Ionic Solutions." *Journal of Physical Chemistry B.* **2012**, *116 (28)*, 8154-8168. Copyright 2012 American Chemical Society.

	ΔW_{water}	$\Delta W^{\dagger}_{\text{water}}$	$\Delta W^{\ddagger}_{\text{water}}$
Pure SPC/E	19.01(2)	1.35(8)	-1.41(6)
3 m NaCl	13.00(28)	-1.83(14)	-1.49(15)
3 m NaI	14.97(40)	-0.34(27)	-1.12(12)

Table 6.4: Summary of key features from PMFs in Figure 6.4 b. ΔW_{water} refers to the difference of water contribution (to the PMF) between global maximum and value at the dissociated distance, $\Delta W^{\dagger}_{\text{water}}$ corresponds to the difference between the first local minimum and value at the dissociated distance, $\Delta W^{\ddagger}_{\text{water}}$ shows the difference between the global minimum and value at the dissociated distance, respectively. All units are in kcal/mol. Values in parentheses denote the uncertainty in the last reported digit as determined from the standard deviation. Reproduced with permission from Shuching Ou, Sandeep Patel and Brad A. Bauer. "Free Energetics of Carbon Nanotube Association in Pure and Aqueous Ionic Solutions." *Journal of Physical Chemistry B.* **2012**, *116 (28)*, 8154-8168. Copyright 2012 American Chemical Society.

	ΔW_{tube}	ΔW_{water}	ΔW_{anion}	ΔW_{cation}	ΔW_{total}	ΔW^{b}
300 K	-61.69	14.31	-0.25	1.28	-46.35	7.26
310 K	-61.69	13.51	-0.13	1.29	-47.02	6.77
320 K	-61.69	12.41	-0.072	1.30	-48.07	5.94
330 K	-61.69	11.81	0.021	1.28	-48.58	5.50
340 K	-61.69	10.99	0.13	1.29	-49.28	4.85
350 K	-61.69	10.25	0.21	1.27	-49.97	4.29
360 K	-61.69	9.56	0.29	1.23	-50.61	3.85

Table 6.5: Decomposition of potential of mean force into contributions from water, tubes, anions, and cations. Values in parentheses denote the uncertainty in the last reported digit as determined from the standard deviation.

	$\langle N_{\text{intra-tube,water}} \rangle$	$\langle N_{\text{intra-tube,anion}} \rangle$	$\langle N_{\text{intra-tube,cation}} \rangle$
300 K	51.96(27)	0.42(7)	1.05(8)
310 K	50.16(20)	0.45(6)	1.05(7)
320 K	49.41(19)	0.45(4)	1.03(5)
330 K	48.66(21)	0.47(5)	1.01(5)
340 K	47.92(19)	0.48(4)	0.99(5)
350 K	47.20(18)	0.48(4)	0.96(5)
360 K	46.45(19)	0.49(4)	0.94(5)

Table 6.6: Average number of water molecules, anions and cations within the tube. Values in parentheses denote the uncertainty in the last reported digit as determined from the standard deviation.

	$\rho_{o,max}$	$\rho_{o,min}$	$\rho_{o,max}/\rho_{o,min}$
300 K			
$d = 22.0$ Å	0.069	0.025	2.76
$d = 23.0$ Å	0.117	0.005	22.76
360 K			
$d = 22.0$ Å	0.056	0.0029	1.94
$d = 23.0$ Å	0.092	0.0098	9.35

Table 6.7: Features of the intertube water densities in Figure 6.19. The units for $\rho_{o,max}$ and $\rho_{o,min}$ are Å^{-3}. Reproduced with permission from Shuching Ou, Sandeep Patel and Brad A. Bauer. "Free Energetics of Carbon Nanotube Association in Pure and Aqueous Ionic Solutions." *Journal of Physical Chemistry B.* **2012**, *116 (28)*, 8154-8168. Copyright 2012 American Chemical Society.

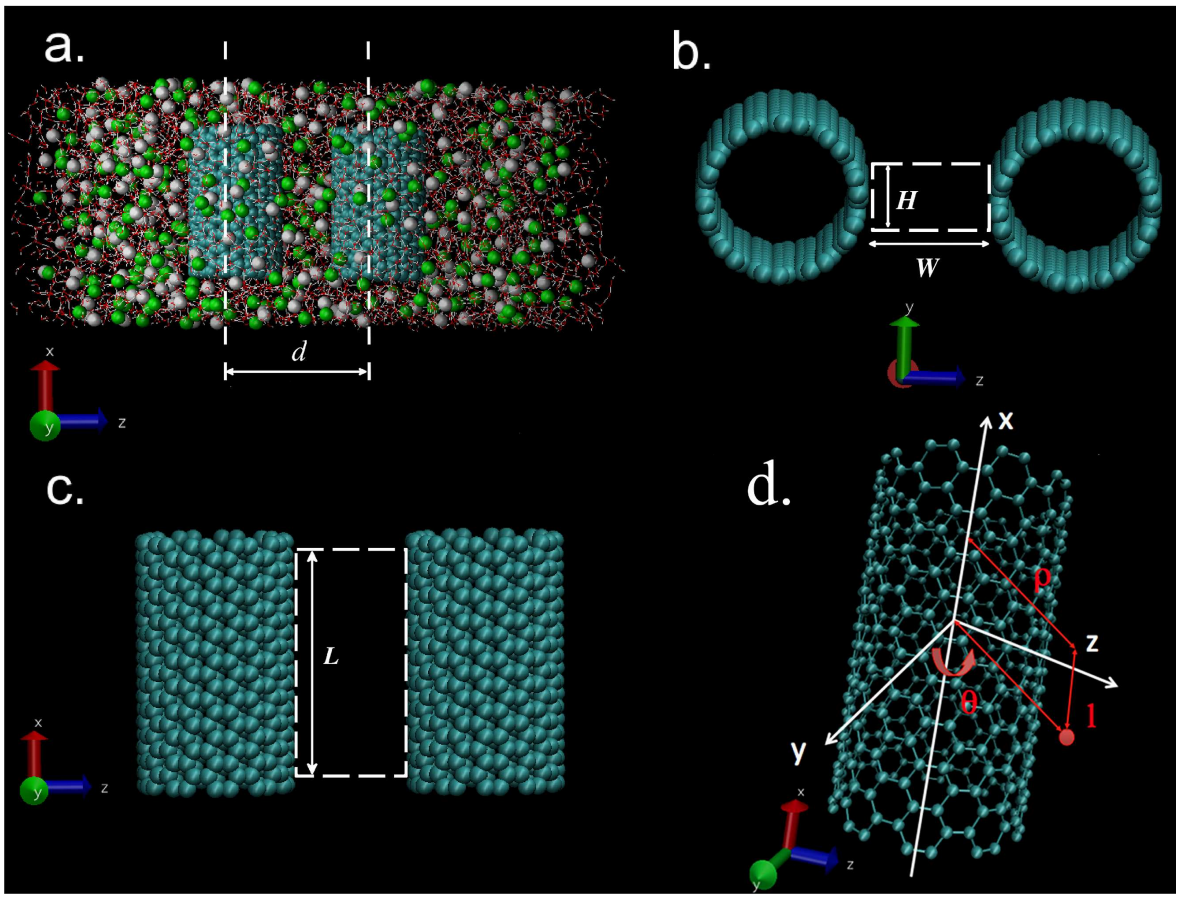

Figure 6.1: Representative snapshots of the 3 m NaCl system used in this study; separation (d) is 26.0 Å, which is defined by the distance between the center axes of the tubes. The diameter (D) and the length (l) of each tube are 13.56 Å and 24.0 Å, respectively. Atom types can be distinguished by the following color code: O (red), H (white), Cl^- (green), Na^+(gray), tube atoms (blue). (a) Side profile showing the relative solvation of the tubes in the normal and lateral directions. Projection of unsolvated tubes on (b) $y-z$ and (c) and $x-z$ plane. Dashed rectangular boxes in (b) and (c) define the confined region used in following analysis. The definition of the dimensionalities (L, W, H) is given in the text. (d) Illustration of grid points for surfacce fluctuation analyses using cylindrical coordinates. Reproduced with permission from Shuching Ou, Sandeep Patel and Brad A. Bauer. "Free Energetics of Carbon Nanotube Association in Pure and Aqueous Ionic Solutions." *Journal of Physical Chemistry B.* **2012**, *116 (28)*, 8154-8168. Copyright 2012 American Chemical Society.

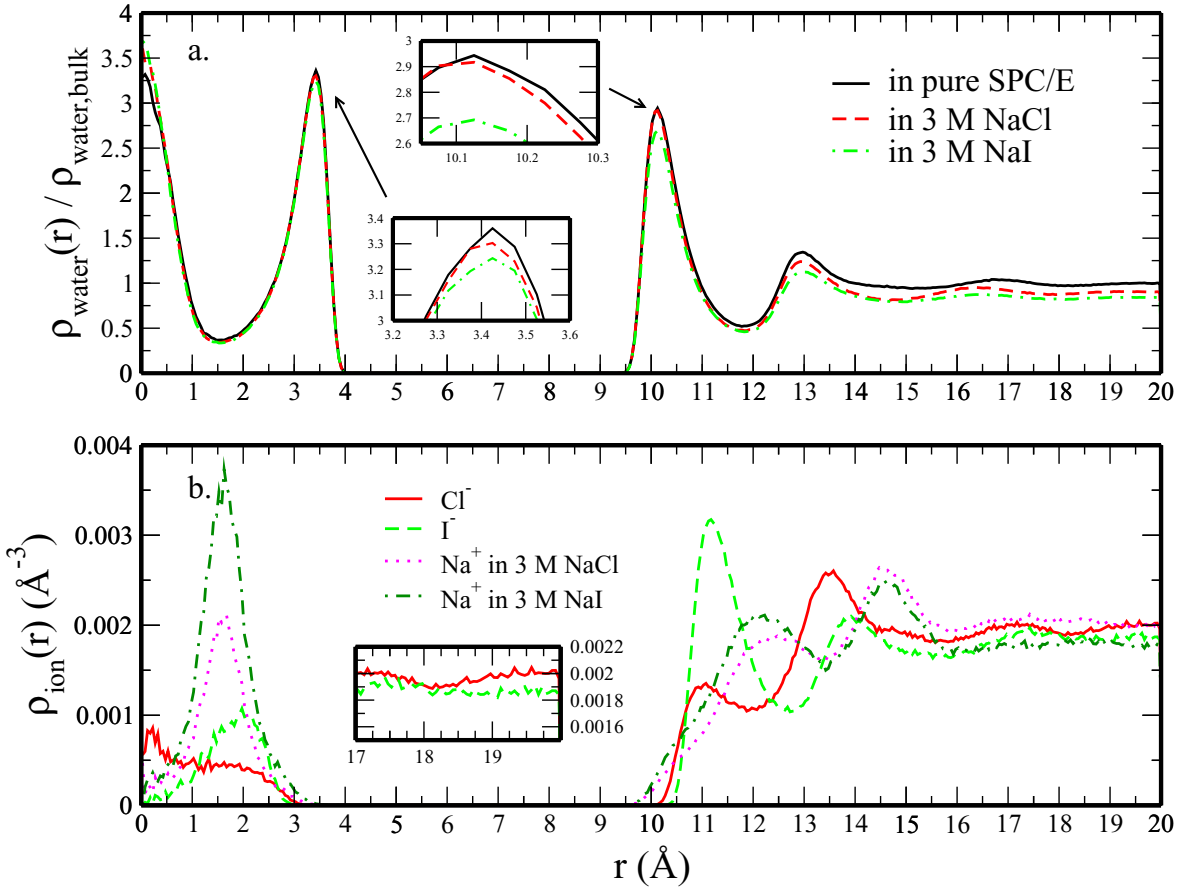

Figure 6.2: Radial number density profiles of (a) water molecules and (b) ions at $d =$ 19.4 Å. For panel a, all the values are scaled with $\rho_{bulk} = 0.0334$ Å^{-3} (the density of water molecules in bulk for pure SPC/E). Insets focus on the number density in the vicinity of the tube wall. For panel b, all the values are the actual densities of ions in bulk for 3 m solutions. Inset in panel b highlights the bulk densities of anions. Reproduced with permission from Shuching Ou, Sandeep Patel and Brad A. Bauer. "Free Energetics of Carbon Nanotube Association in Pure and Aqueous Ionic Solutions." *Journal of Physical Chemistry B.* **2012**, *116 (28)*, 8154-8168. Copyright 2012 American Chemical Society.

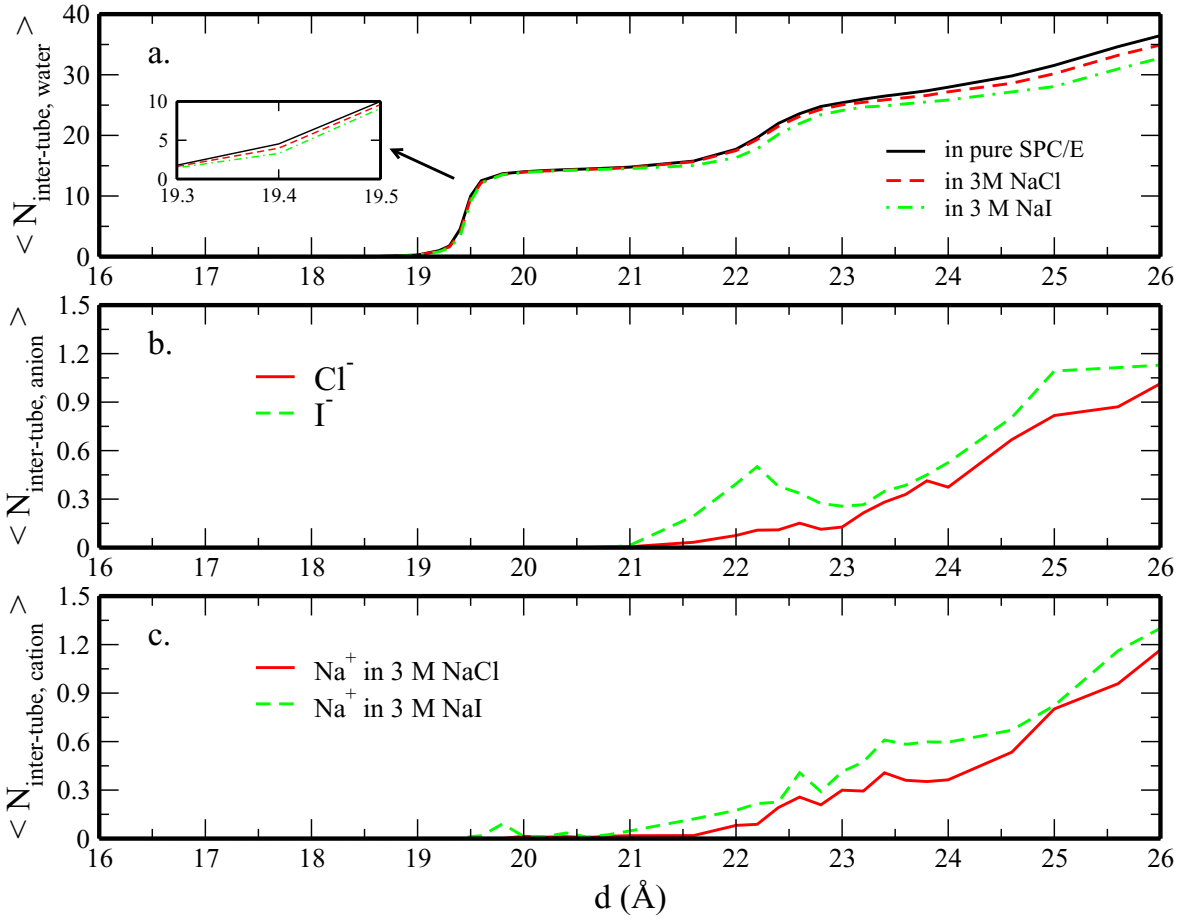

Figure 6.3: Average number of (a) water molecules, (b) anions, and (c) cations of the confined region in pure water and 3 m NaX (X = Cl, I) solutions. Insets in panel a show focused view of the density peaks. Reproduced with permission from Shuching Ou, Sandeep Patel and Brad A. Bauer. "Free Energetics of Carbon Nanotube Association in Pure and Aqueous Ionic Solutions." *Journal of Physical Chemistry B.* **2012**, *116 (28)*, 8154-8168. Copyright 2012 American Chemical Society.

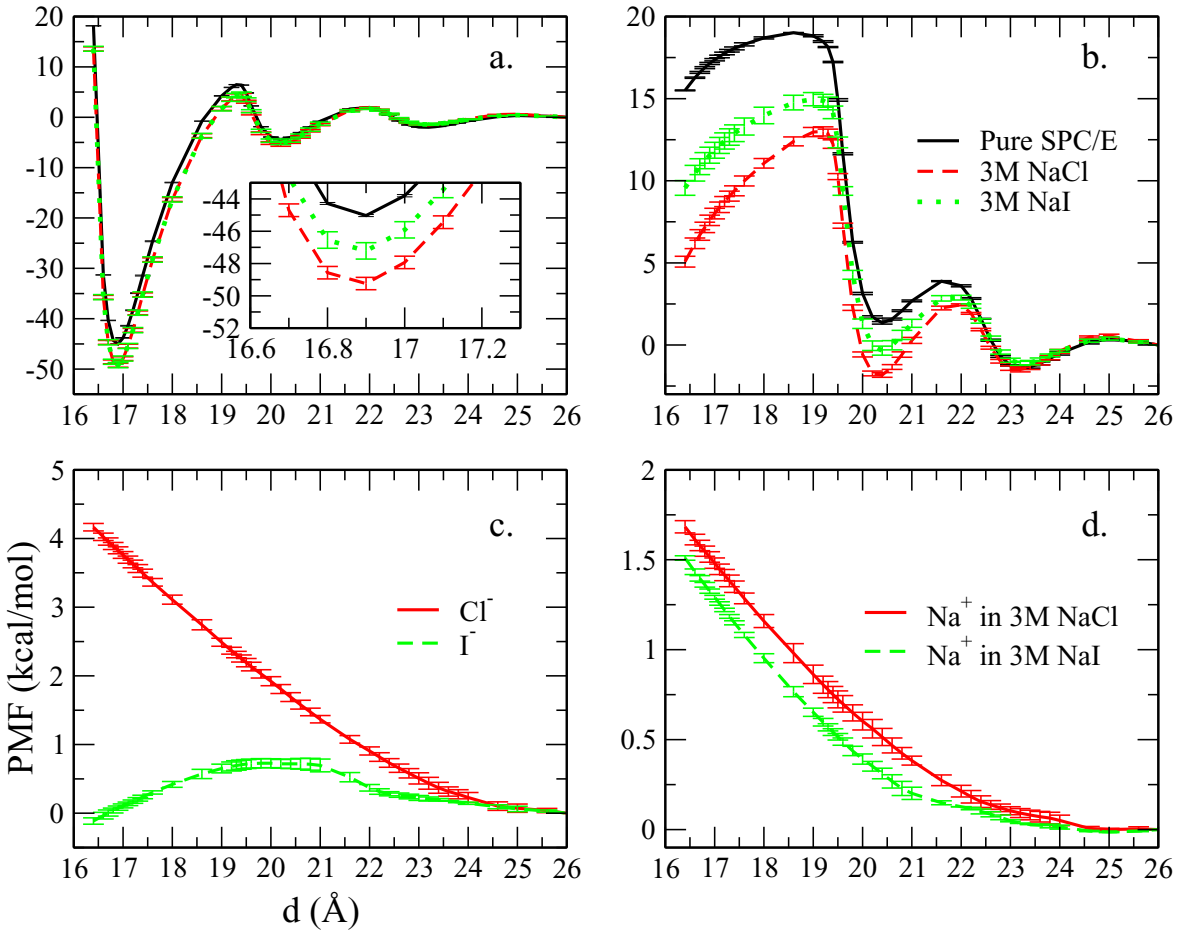

Figure 6.4: (a) Total potential of mean force for tube association in pure SPC/E, 3 m NaCl, and 3 m NaI solutions. The inset shows the minimum region of the profiles. For clarity, in the inset a vertical offset of 2 kcal/mol is imposed for the case of 3 m NaI. The additional panels correspond to the decomposition of (b) water (c) anion and (d) cation contributions. The error bars are obtained from standard deviations among three independent replicates. Reproduced with permission from Shuching Ou, Sandeep Patel and Brad A. Bauer. "Free Energetics of Carbon Nanotube Association in Pure and Aqueous Ionic Solutions." *Journal of Physical Chemistry B.* **2012**, *116 (28)*, 8154-8168. Copyright 2012 American Chemical Society.

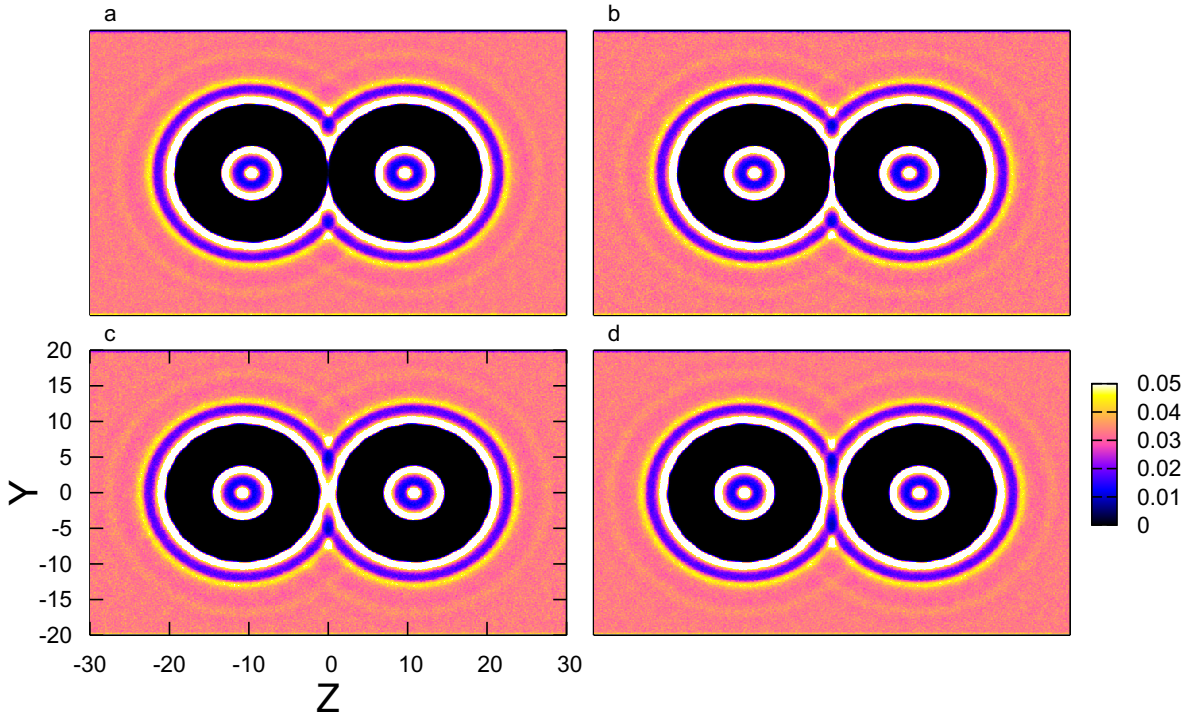

Figure 6.5: Density distribution of water molecules at location (y, z) around the carbon nanotubes, with the intertube separations (a) $d = 19.3$ Å (before first barrier), (b) $d = 19.5$ Å (after first barrier), (c) $d = 21.6$ Å (before second barrier), (d) $d = 22.0$ Å (after second barrier). Reproduced with permission from Shuching Ou, Sandeep Patel and Brad A. Bauer. "Free Energetics of Carbon Nanotube Association in Pure and Aqueous Ionic Solutions." *Journal of Physical Chemistry B.* **2012**, *116 (28)*, 8154-8168. Copyright 2012 American Chemical Society.

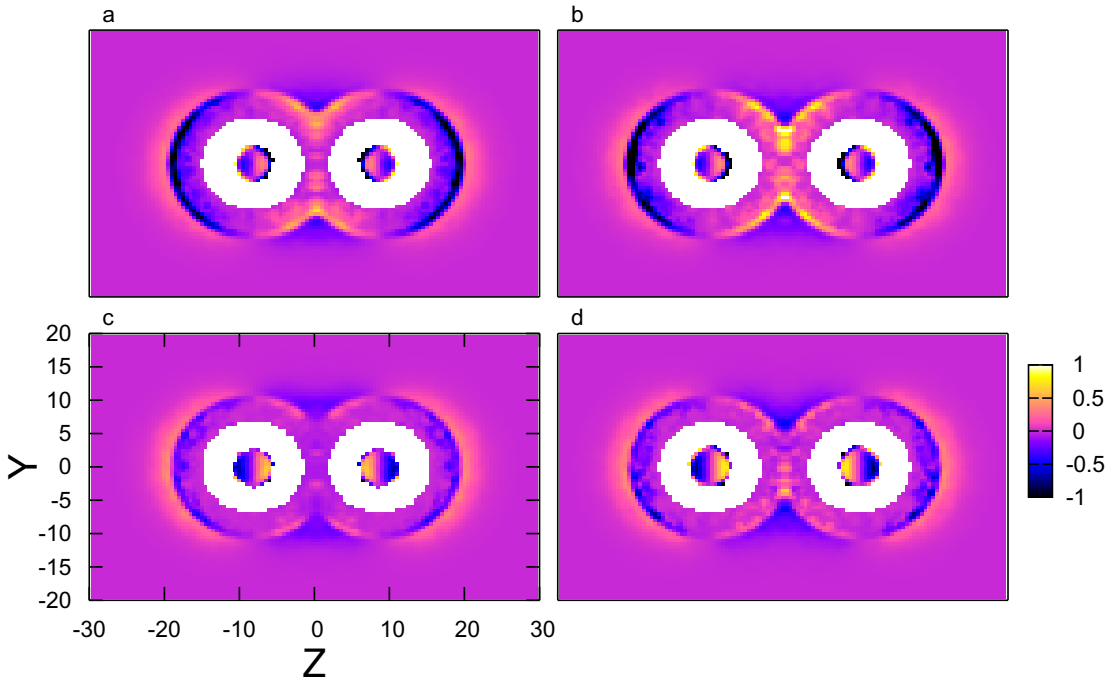

Figure 6.6: The z-component of total forces from anions applied on the carbon nanotubes at position (y, z), in (a) 3 m NaI solution with $d = 16.4$ Å, (b) 3 m NaI solution with $d = 19.4$ Å, (c) 3 m NaCl solution with $d = 16.4$ Å, (d) 3 m NaCl solution with $d = 19.4$ Å, respectively. Reproduced with permission from Shuching Ou, Sandeep Patel and Brad A. Bauer. "Free Energetics of Carbon Nanotube Association in Pure and Aqueous Ionic Solutions." *Journal of Physical Chemistry B.* **2012**, *116 (28)*, 8154-8168. Copyright 2012 American Chemical Society.

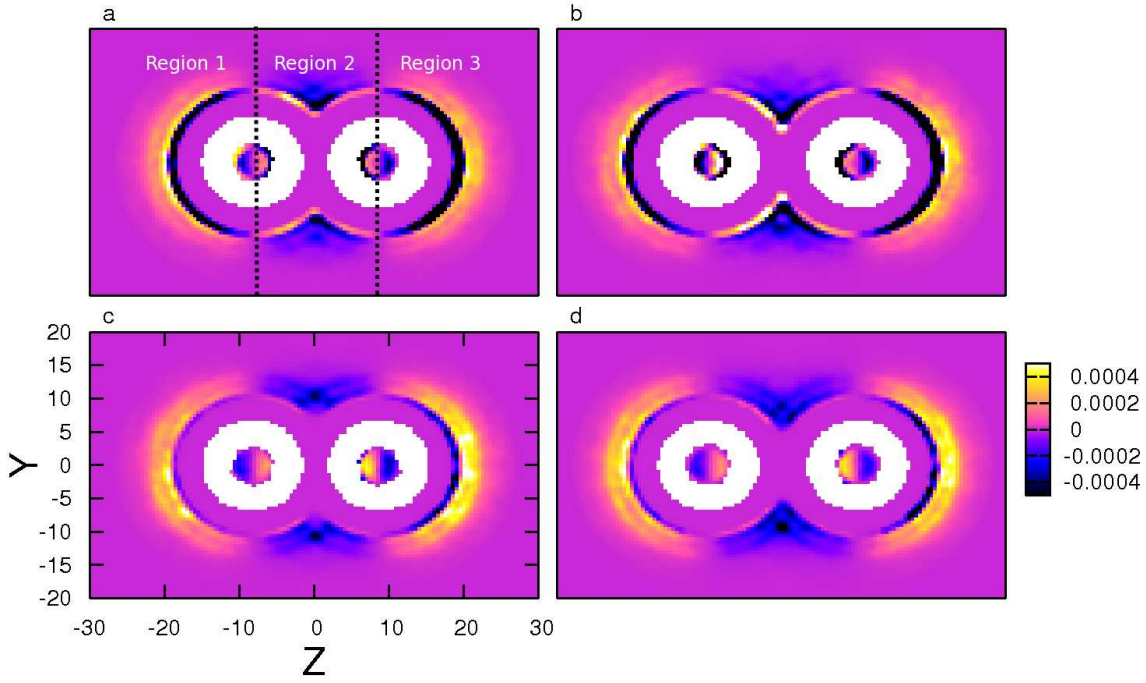

Figure 6.7: Product of the z-component of total forces ($\langle F_z \rangle$) from anions applied on the carbon nanotubes and the anion density (ρ_{anion}) at position (y, z), in (a) 3 m NaI solution with $d = 16.4$ Å, (b) 3 m NaI solution with $d = 19.4$ Å, (c) 3 m NaCl solution with $d = 16.4$ Å, (d) 3 m NaCl solution with $d = 19.4$ Å, respectively. The black dotted lines in panel a are used to separate the regions defined in the text. Reproduced with permission from Shuching Ou, Sandeep Patel and Brad A. Bauer. "Free Energetics of Carbon Nanotube Association in Pure and Aqueous Ionic Solutions." *Journal of Physical Chemistry B.* **2012**, *116 (28)*, 8154-8168. Copyright 2012 American Chemical Society.

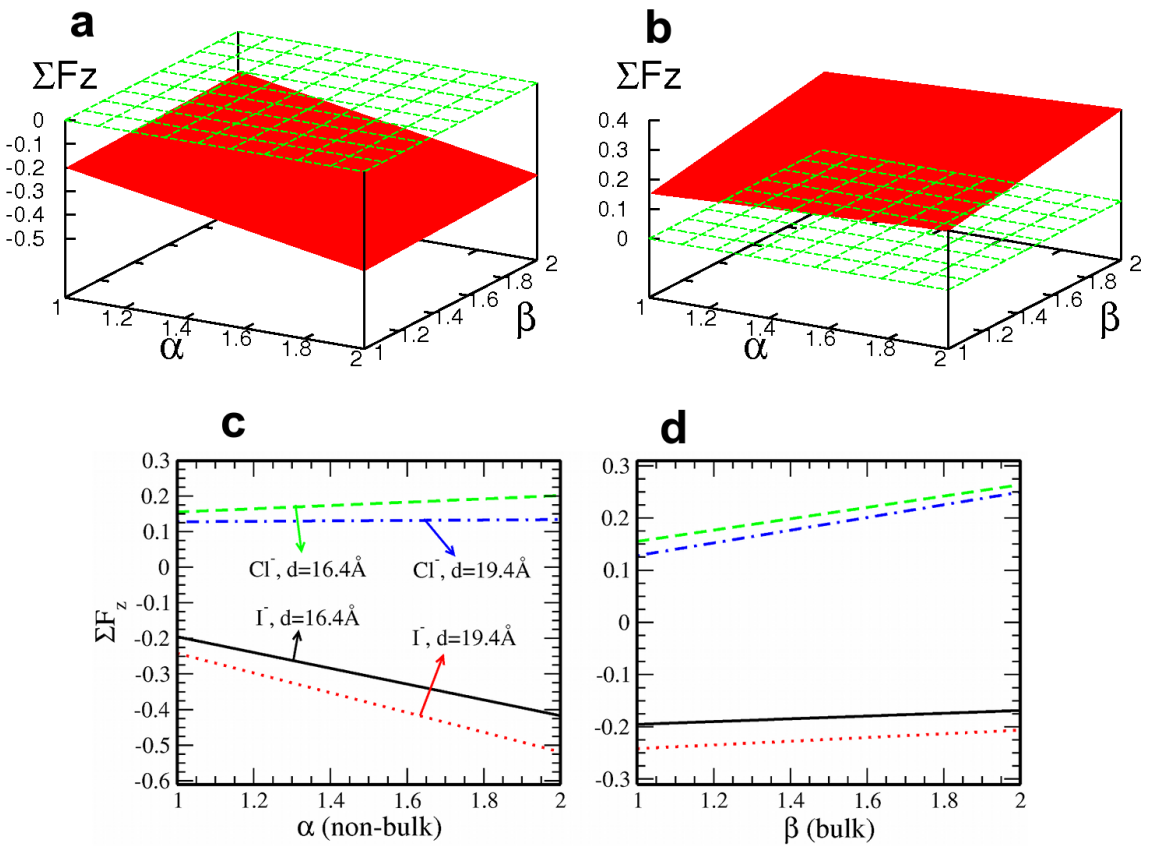

Figure 6.8: Scaling effect of bulk anions and non-bulk anions. α and β are scaling parameters for non-bulk and bulk anions, which are defined in the text. $\Sigma F_z(\alpha, \beta)$ is the sum of the forces from anions to the tube association. Panel (a) and (b) are the results of $\Sigma F_z(\alpha, \beta)$ for I^- and Cl^- at d = 16.4 Å. Panel (c) shows ΣF_z when $\beta = 1$ (no scaling for bulk anions) at d = 16.4 and 19.4 Å, while panel (d) shows the cases for $\alpha = 1$ (no scaling for non-bulk anions), respectively. Reproduced with permission from Shuching Ou, Sandeep Patel and Brad A. Bauer. "Free Energetics of Carbon Nanotube Association in Pure and Aqueous Ionic Solutions." *Journal of Physical Chemistry B.* **2012**, *116 (28)*, 8154-8168. Copyright 2012 American Chemical Society.

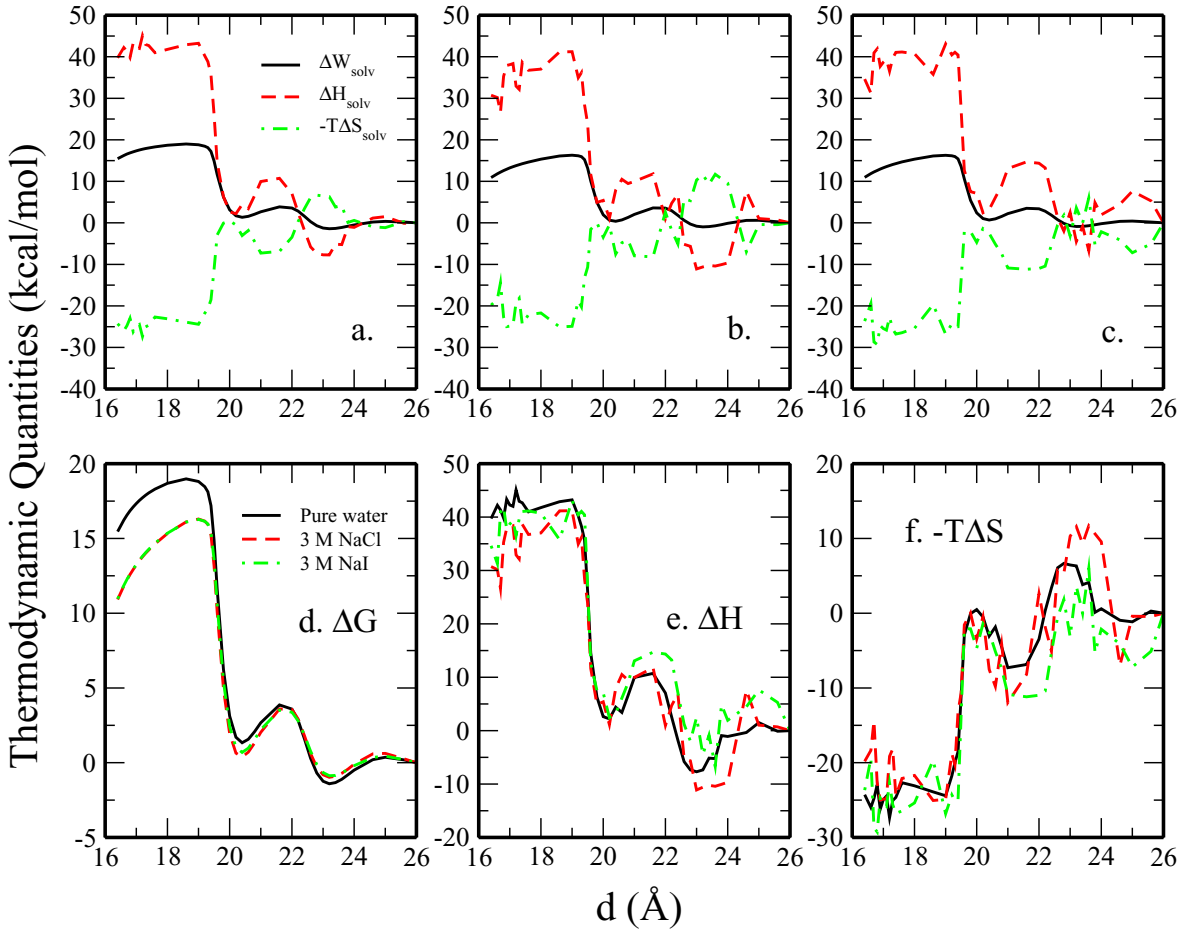

Figure 6.9: Solvent contribution, ΔW_{solv} to the PMF and its enthalpic contribution (ΔH_{solv}), and entropic contribution ($-T\Delta S_{\text{solv}}$) for (a) pure water (b) 3 m NaCl and (c) 3 m NaI systems. Panel d-f show the comparison of the different solvents for the same thermodynamic properties. Reproduced with permission from Shuching Ou, Sandeep Patel and Brad A. Bauer. "Free Energetics of Carbon Nanotube Association in Pure and Aqueous Ionic Solutions." *Journal of Physical Chemistry B.* **2012**, *116 (28)*, 8154-8168. Copyright 2012 American Chemical Society.

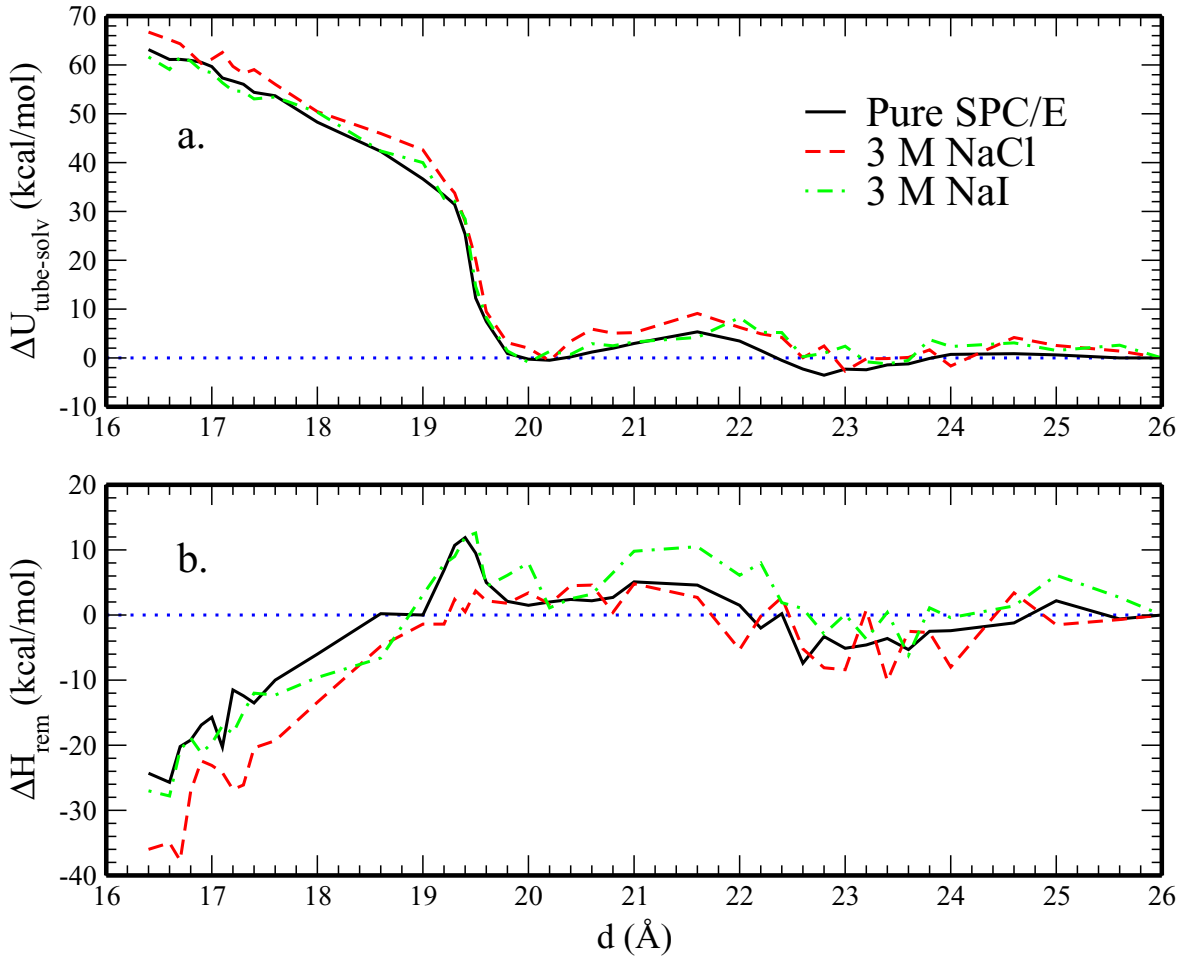

Figure 6.10: Solvent-induced contribution to enthalpy of tube association, ΔH_{solv} (from Figure 6.9 d) is split into (a) the change in tube-solvent interaction ($\Delta U_{\text{tube-solv}}$) and (b) the remaining contribution from the change in solvent-solvent interactions and other mechanic work (ΔH_{rem}). All the quantities are referenced to the values at the dissociated distance d = 26.0 Å. Reproduced with permission from Shuching Ou, Sandeep Patel and Brad A. Bauer. "Free Energetics of Carbon Nanotube Association in Pure and Aqueous Ionic Solutions." *Journal of Physical Chemistry B.* **2012**, *116 (28)*, 8154-8168. Copyright 2012 American Chemical Society.

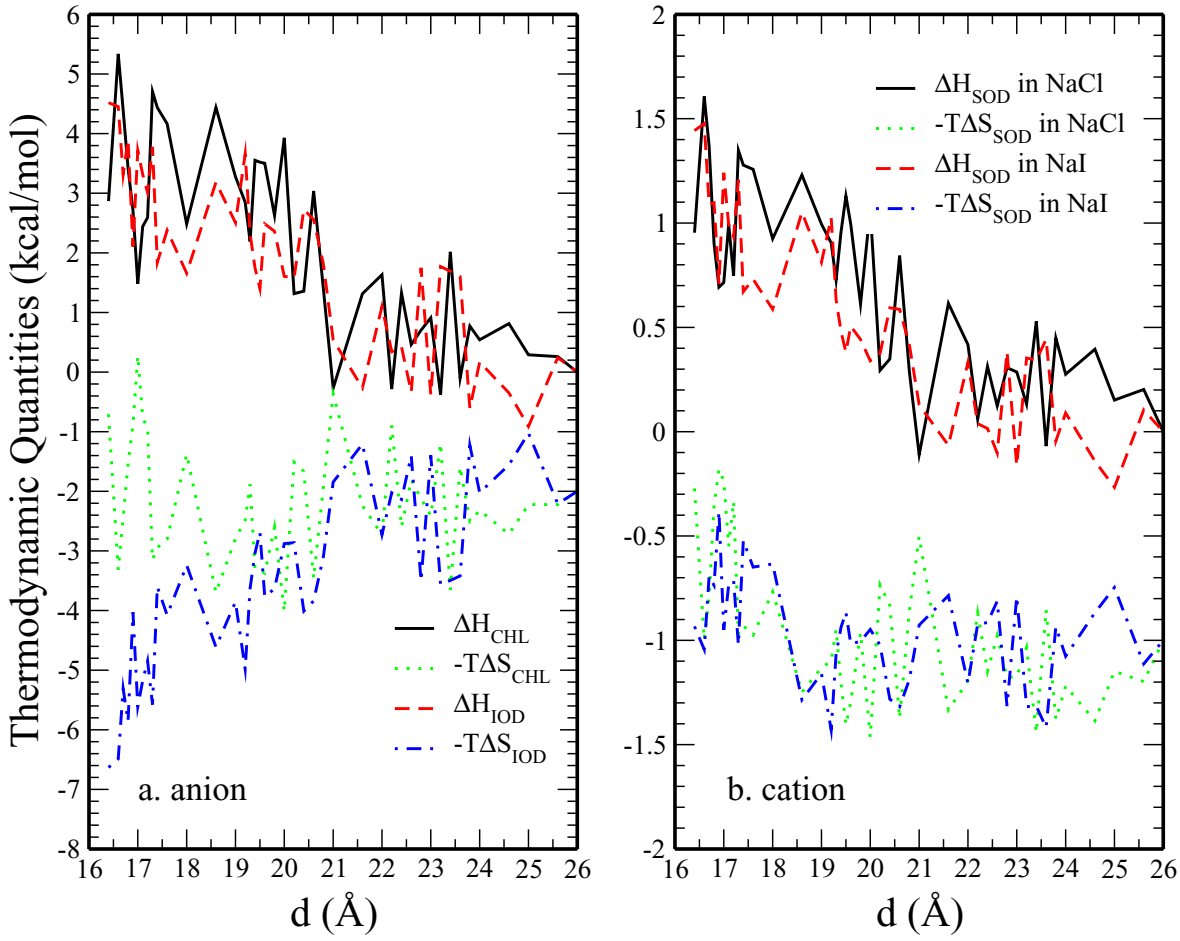

Figure 6.11: Ionic enthalpic contribution (ΔH_i, i = (Cl^-, I^-, Na^+)), and entropic contribution ($-T\Delta S_i$) in 3 m NaCl and NaI systems. Vertical offsets of -2 and -1 kcal/mol are applied for the entropic contribution in panel a and b, respectively. Reproduced with permission from Shuching Ou, Sandeep Patel and Brad A. Bauer. "Free Energetics of Carbon Nanotube Association in Pure and Aqueous Ionic Solutions." *Journal of Physical Chemistry B.* **2012**, *116 (28)*, 8154-8168. Copyright 2012 American Chemical Society.

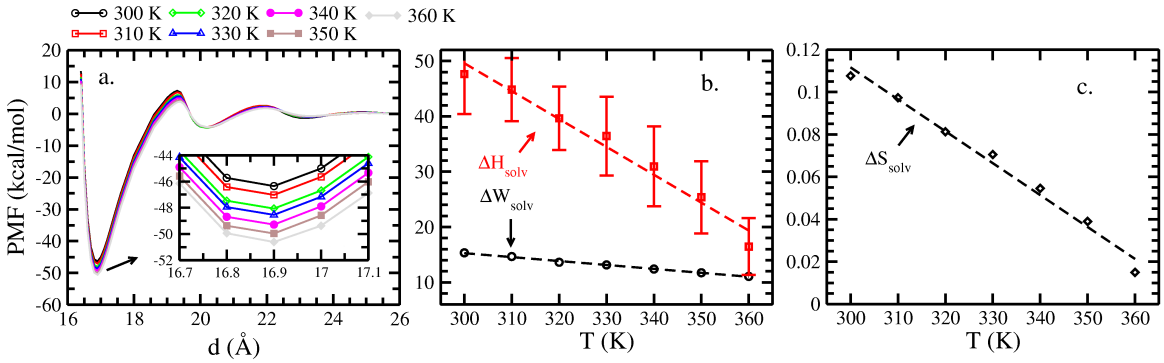

Figure 6.12: (a) Total potential of mean force for tube association in 3 m NaI solutions under different temperatures. The inset shows the minimum region of the profiles. (b)(c) The values of solvent-induced ΔW, ΔH and ΔS for association as functions of the temperature. The unit for y-axis in panel (a) and (b) is kcal/mol; for panel (c) it is kcal/mol/K.

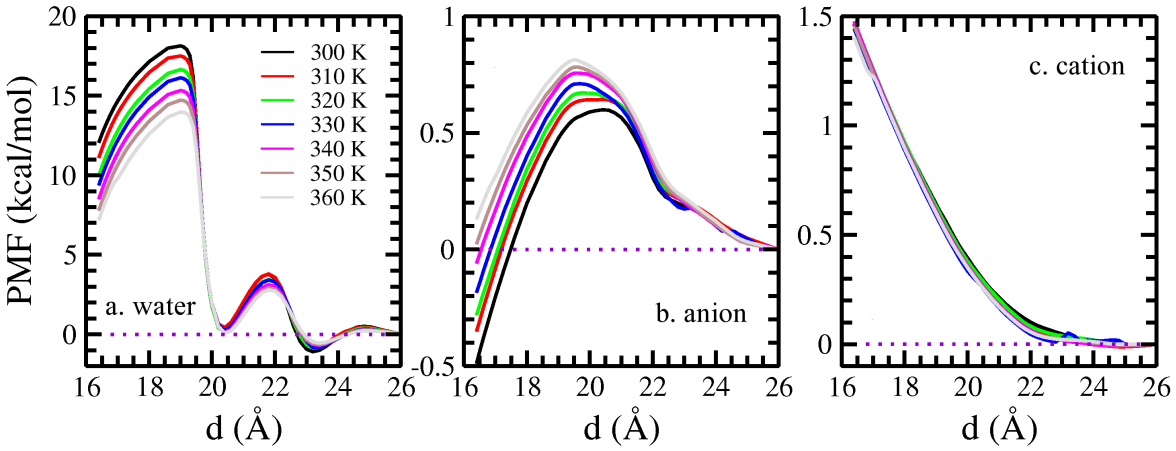

Figure 6.13: Decomposition of PMF into (a) water (b) anion (c) cation contributions.

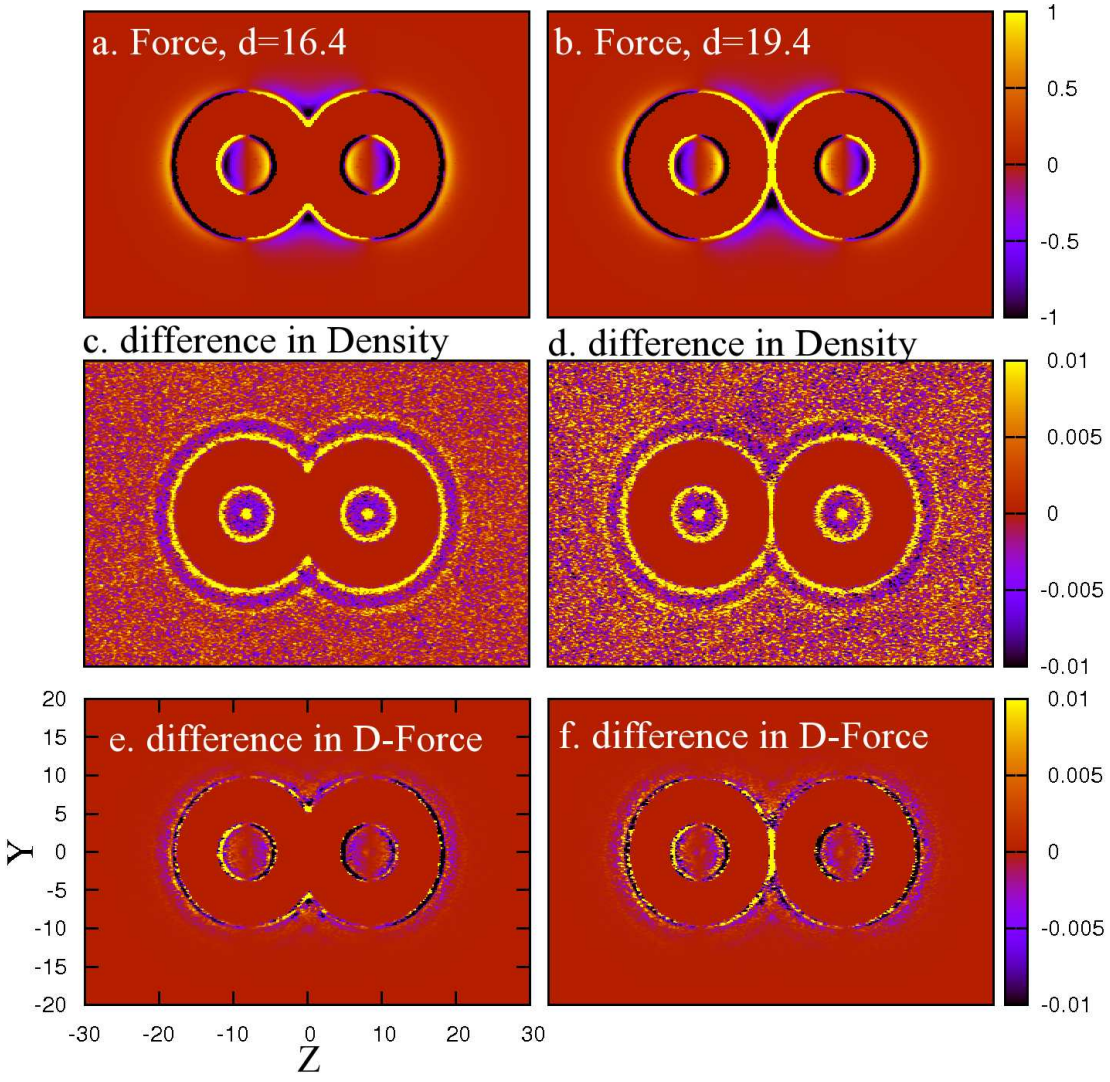

Figure 6.14: The z-component of total forces from water molecules applied on the carbon nanotubes at position (y, z) in NaI solution, for the intertube separation d = (a) 16.4 (b) 19.4 Å. Panel (c) and (d) show the difference of density of water oxygen at location (y, z) around the carbon nanotubes between 300 K and 360 K, at the corresponding intertube separations. (e) and (f) illustrates the difference of density-weighted force at location (y, z) between 300 K and 360 K.

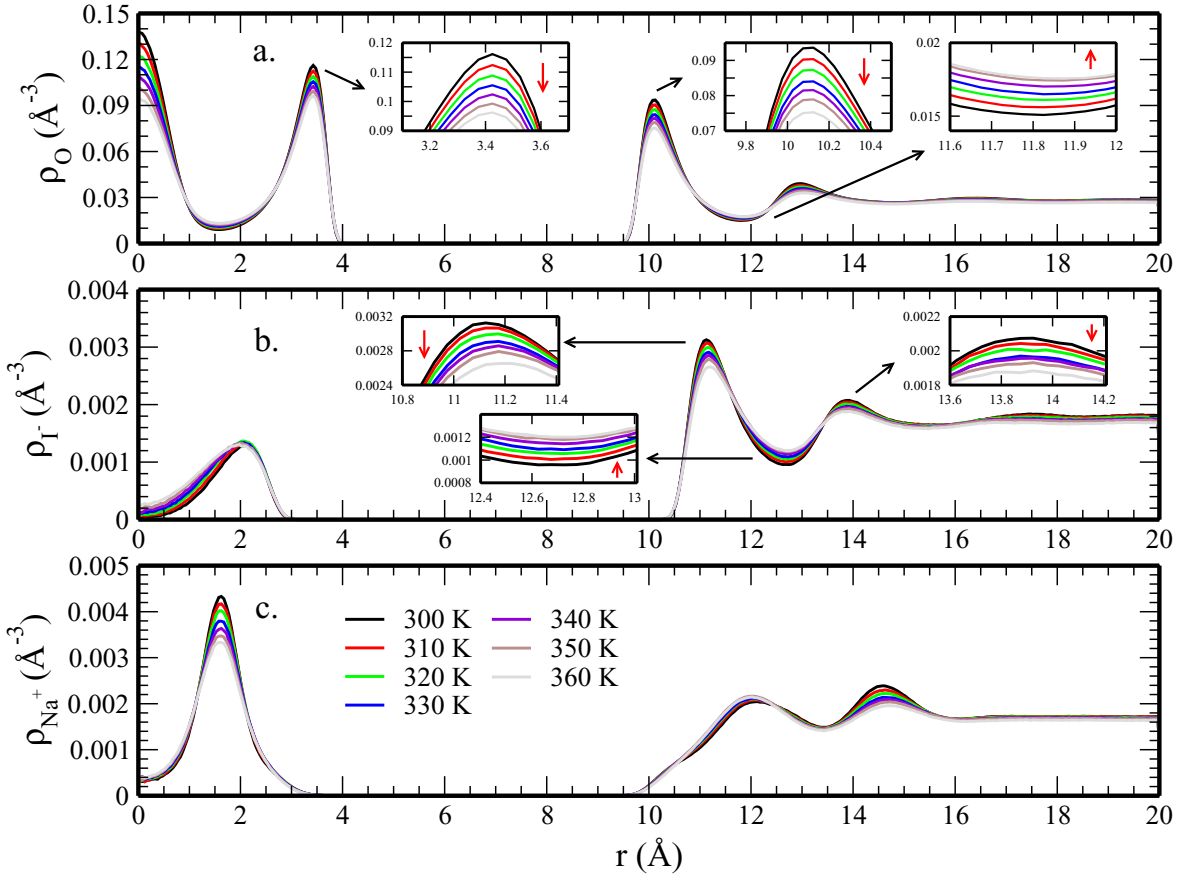

Figure 6.15: Radial number density profiles of (a) water molecules (b) anions (c) cations at $d = 16.4$ Å under different temperatures. Insets focus on the number density at the maximums/minima. Red arrows in the insets indicate from low temperature to high temperature.

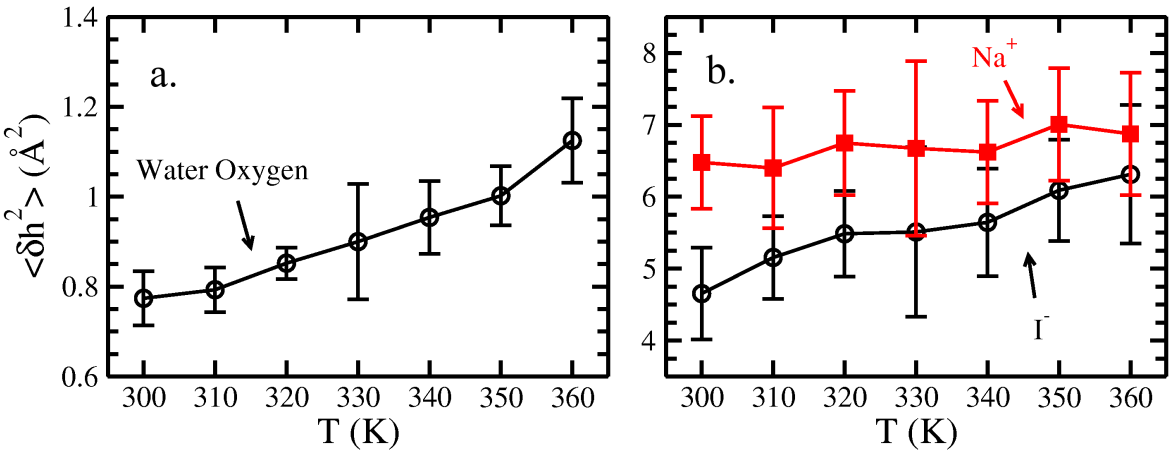

Figure 6.16: Surface fluctuations (side facing the bulk) for (a) tube-water (b) tube-ion surface in 3 m NaI solution at different temperature. Only $\langle \delta h^2(\theta, l) \rangle$ has -5 Å $\leq h \leq$ 5 Å and 85° $\leq \theta \leq$ 95° is used for the plotted value.

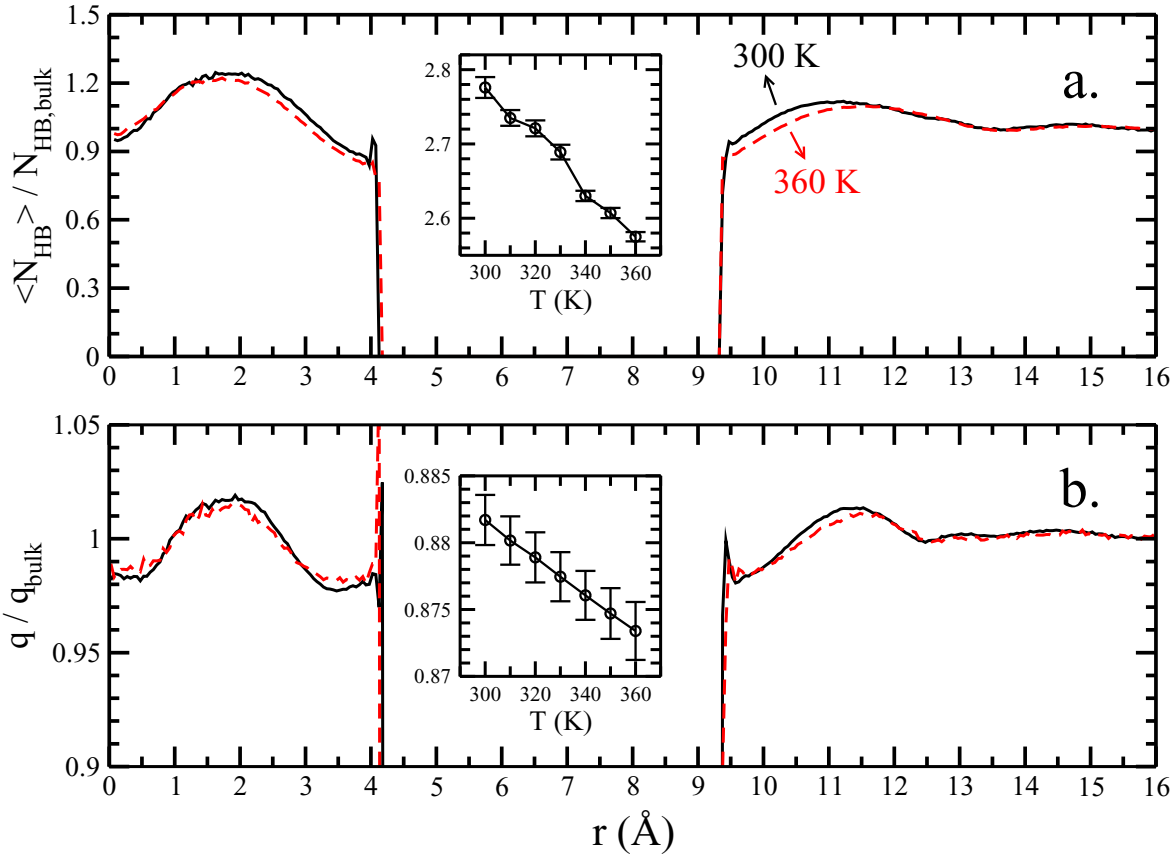

Figure 6.17: (a) Hydrogen bonds (N_{HB}) (b) tetrahedral configuration parameter (q) of water molecules as functions of r.

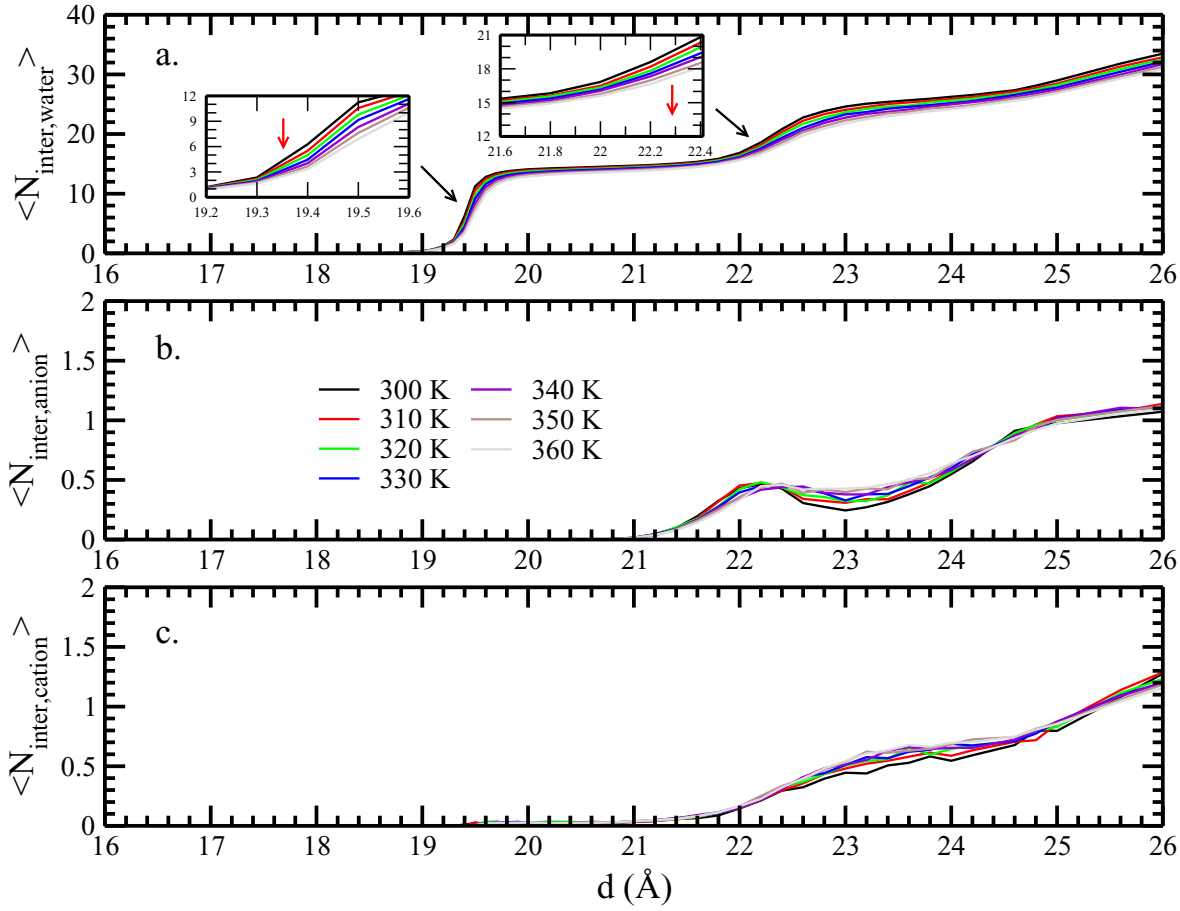

Figure 6.18: Average number of (a) water molecules, (b) anions, and (c) cations of the confined region in pure water and 3 m NaI solutions. Insets show focused view of the jump of quantities. Red arrows in the insets indicate from low temperature to high temperature.

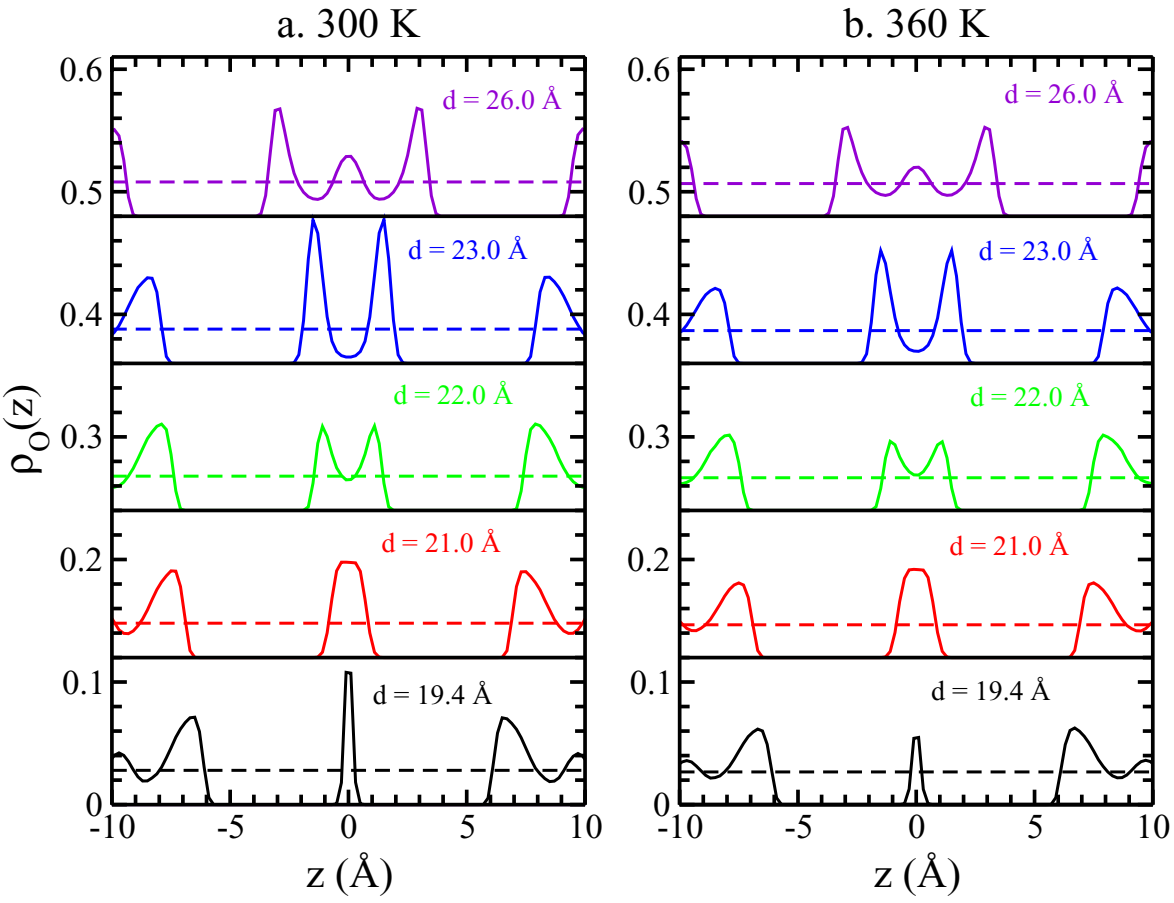

Figure 6.19: Intertube water oxygen density profile along z at several tube separations. The dashed lines indicate the corresponding water density from the outer bulk. A vertical offset of 0.12 Å^{-3} is added for clarity.

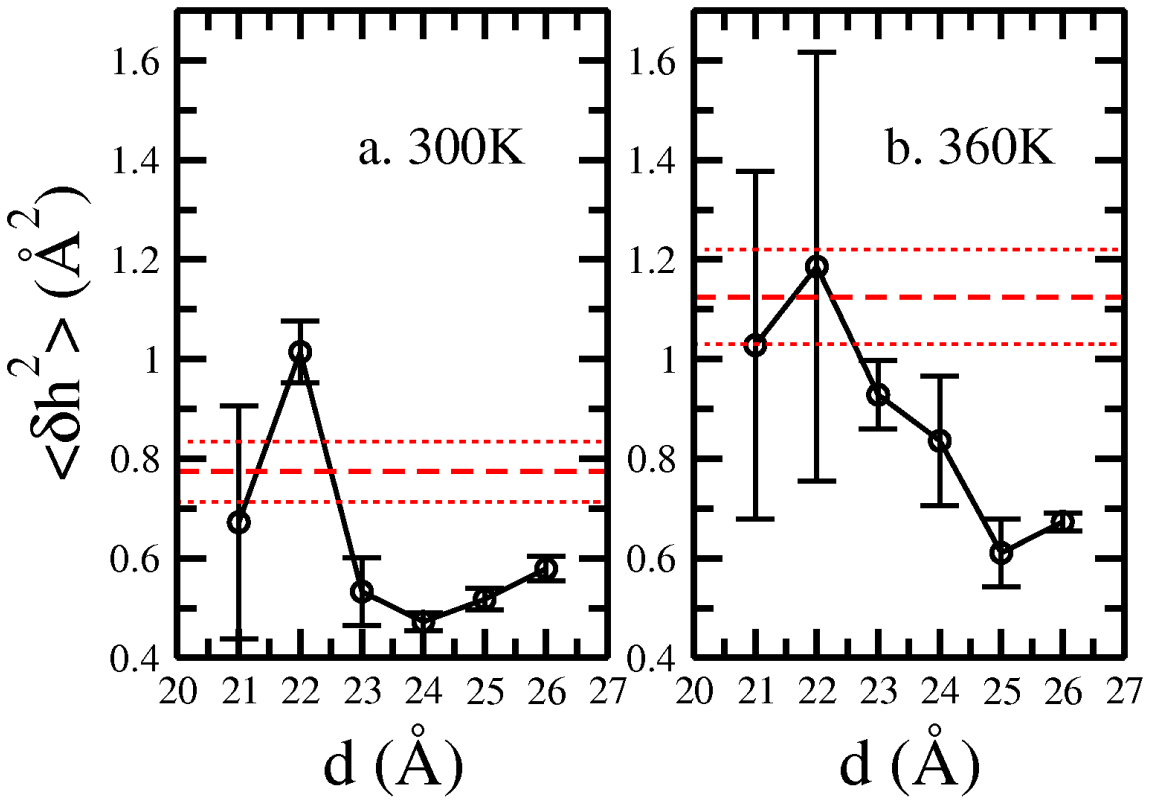

Figure 6.20: Intertube tube-water surface fluctuations. Only $\langle \delta h^2(\theta, l) \rangle$ has -5 Å $\leq h \leq$ 5 Å and -95° $\leq \theta \leq$ -85° is used for the plotted value. Red dashed lines indicate the fluctuation values for the sides facing the solvent bulk, along with the uncertainties (as plotted with the dotted lines).

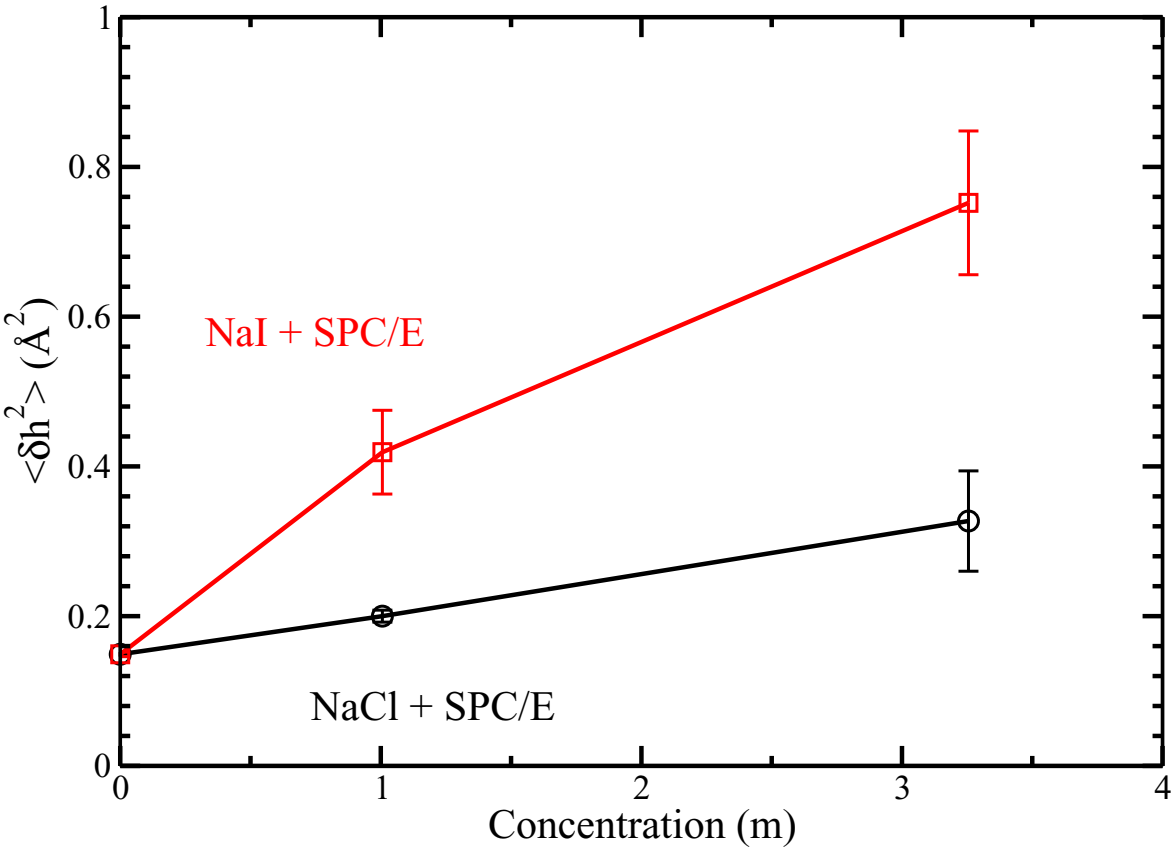

Figure 6.21: Tube-water surface fluctuation at the side facing the solvent bulk, for NaCl and NaI solutions at different concentration Only $\langle \delta h^2(\theta, l) \rangle$ has -5 Å $\leq h \leq$ 5 Å and -95° $\leq \theta \leq$ -85° is used for the plotted value.

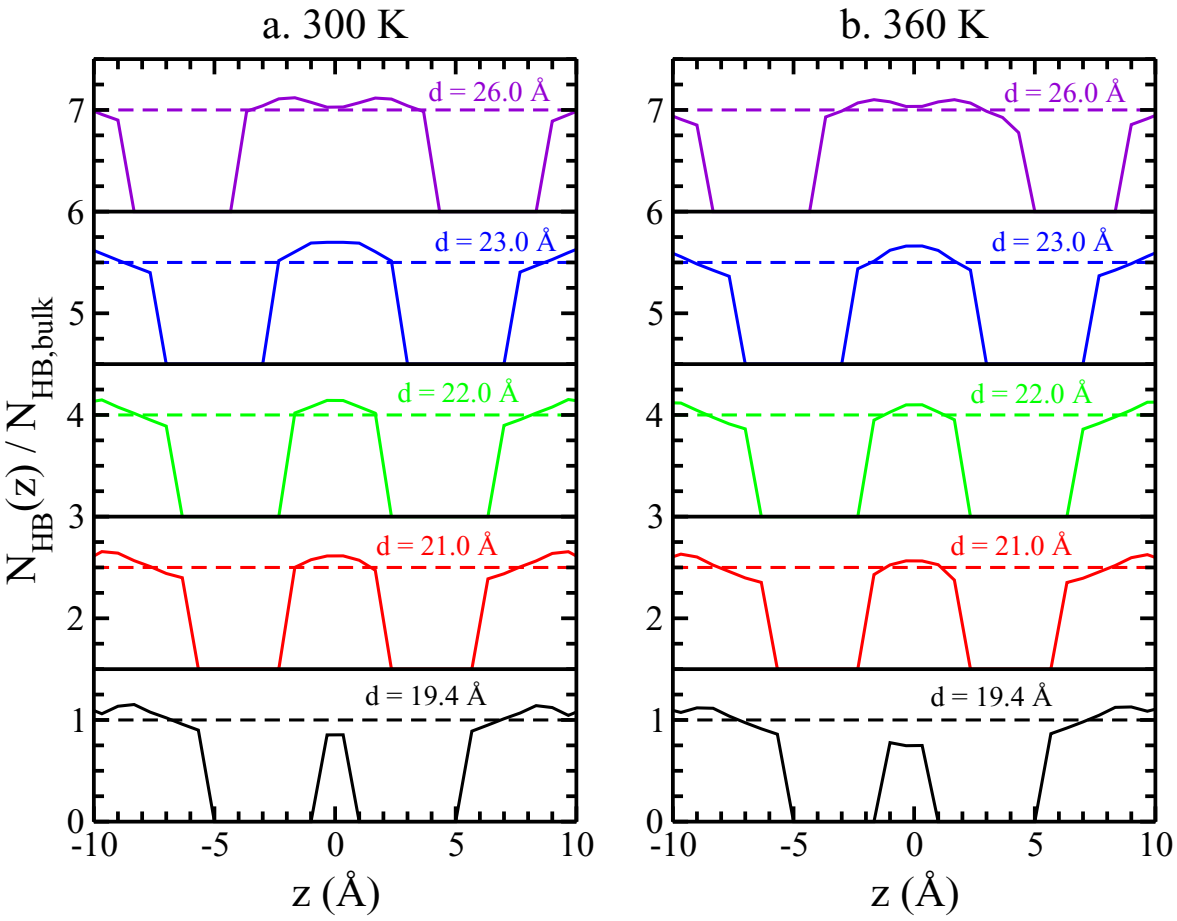

Figure 6.22: Normalized hydrogen bond profiles for (a) 300 K and (b) 360 K along z-axis at intertube region. A vertical offset of 1.5 is added for clarity.

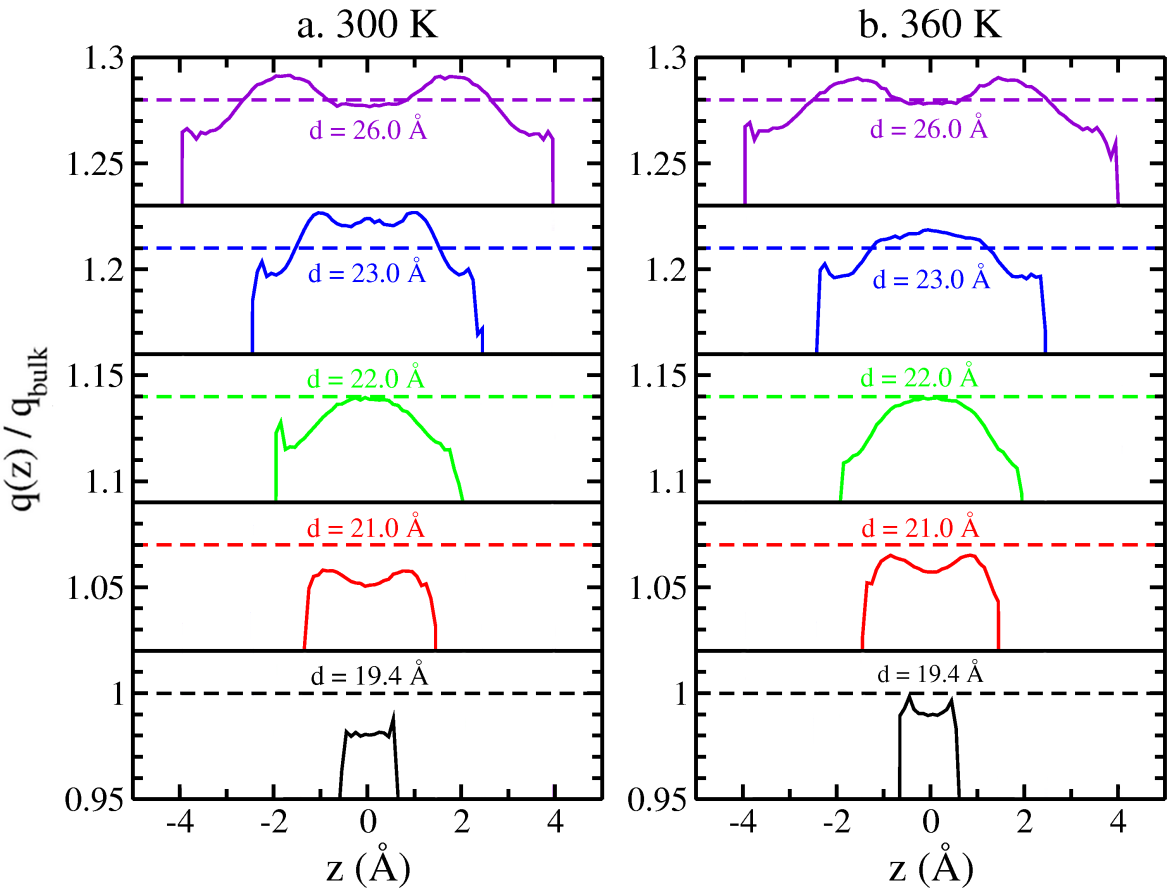

Figure 6.23: Tetrahedral configuration parameter (q) for (a) 300 K and (b) 360 K along z-axis at intertube region. A vertical offset of 0.07 is added for clarity.

Chapter 7

CONCLUSION

7.1 Summary of Key Results

This dissertation discussed several studies of ions and various aqueous interfaces, including liquid-vapor interfaces, protein-water interfaces, and hydrophobe-water interfaces, to examine the responses of aqueous interfaces to the addtives via molecular dynamics simulations. We began with single, spherical, monovalent anions/cations at aqueous liquid-vapor interfaces, using a set of different nonadditive and additive intermolecular potential functions to compute the reversible work (potential of mean force) of moving an ion from bulk to vapor through the interface. As all water-ion force field combinations were carefully parameterized and validated via extensive structural and thermodynamic analysis, our focus was to extract underlying behaviors among those force fields that helped to discern between surface stable and non-surface stable species. Specifically, we probed the interfacial fluctuations induced by the anion/cation at various positions relative to the liquid-vapor interface. Our findings indicated a connection between interface stability and induced interfacial fluctuations for a series of anions and cations: the species demonstrating an interfacial stability appeared to enhance liquid-vapor interfacial fluctuations significantly, while those that showed no interfacial stability induce no further fluctuations (or may even suppressed levels of fluctuations). The differences in induced fluctuations are traceable to the nature of the first few hydration shells of the ions. For ion species with surface stability, their hydration shells consist of water molecules that are more dynamic, less persistent (lower residence times), while the opposite is true for the species without surface stability. Approaching the liquid-vapor interface, coupling of local solvent with solvent further

away (up to 8 Å from our results) leads to differential contributions of surface entropy (arising from the different magnitudes of the interface fluctuations) to the stability of surface-adsorbed states. This behavior spanned a variety of force fields, and did not discriminate based on inclusion or exclusion of polarization in the force field.

A further thermodynamic study regarding the temperature dependcies between species with opposite surface affinity was also performed. We selected I^- (surface stable) and Cl^- (surface unstable) at liquid-vapor interfaces to investigate the free energetics and induced interfacial fluctuations at the temperature ranged from 280 K to 360 K. As temperature increased, the surface stability of I^- is reduced, as depicted by the trend of disappearance of the free energy minimum. This indicated an inherent negative entropy of adsoprtion, in agreement with the recent results reported by Otten et al. [19] and Netz et al. [128] On the other hand, the non-surface stable species Cl^- anion showed no temperature dependence. Detailed decomposition of thermodynamic free energies showed that, at all temperatures, water-water interactions provide the sole favorable enthalpic contribution to the free energy while the water-ion interactions contribute a balancing destabilizing contribution until beyond the Gibbs dividing surface (GDS), at which point the loss of water-ion interaction leads to the rapid increase in free energy. Approaching the interface, the long-ranged perturbations induced by both anions are more effectively damped by the local solvation shells of Cl^- compared to that of I^-; solvation structure perturbations are able to interact more easily with I^-'s solvation shell due to its malleability. In this picture, our interpretation is that the minimal perturbation of the interface by Cl^- is a non-effect; this interpretation is consistent with the different surface-stabilities of the two anions. An implication of the mechanism through which I^- effects its perturbations of the interface is that increasing temperature of the solvent, thus enhancing inherent thermally-excited fluctuations, should reduce the anions' effect on surface fluctuations; likewise, since there is no effect from Cl^-, its effect should show no temperature dependence. Our results demonstrated that the relative contributions to changes in interface fluctuations from I^- decrease with temperature, while no perceptible change is present for Cl^-. This

is again consistent with the decrease in surface-stability of I^- demonstrated by the disappearance of the free energy minimum before the GDS.

We also noted the similarity of hydration properties of the less charge-dense I^- to that of hydrophobic hydration [43]. Analogous to enhanced solvent density fluctuations seen for molecular hydrophobic solutes in water, I^- perturbs solvent structure and dynamics (to a greater degree than Cl^-) leading to more fluid, dynamic, and fluctuating solvent structure. Overall, our results indicated that ion-specific surface adsorption of ions may be discussed in the context of increasing ion hydrophobic character as recently suggested [128, 123, 394].

We extended our study with molecular ions at liquid-vapor interfaces. The molecular ions we chose were guandinium and methyl guandinium cations. On average, no liquid-vapor interfacial propensity (i.e., no free energy minimum) was found for either cation; however, as suggested by other studies [296, 295], we found a stark orientation-based dispersion of surface stabilities. The orientation of guanidinium face parallel to the interfacial plane is stable with an evidenced free energy minimum near the liquid-vapor interface. In agreement with the spherical ion case, this parallel orientation/configuration relative to the interface induced larger interfacial fluctuations. This is explained by the inherent hydration properties (or malleability of hydration shells) of the guandinium cation; the guandinium face presents a solvent environment that is less rigid, more malleable, and thus more amenable to inducing fluctuations of the interface as a consequence of a greater disruption of solvent structure on approach to the interface. In the biological context, when considering the denaturant properties of guandinium cation, and a direct contact mechanism, our result incates that association with sidechains groups that are not robustly hydrated is a plausible mechanism of action of this osmolyte.

Long-ranged perturbations are not only relevant to the bulk, but also to the nature of fluctuations at water-biomacromolecule and water-nanomaterial interfaces.

Building upon the insights gained from the specific ion behaviors at aqueous liquid-vapor interfaces, we have presented a discussion regarding the unique fluctuation inducing properties of two anions (I^- and Cl^-) as well as two orientations of the guanidinium cation (parallel and perpendicular) for which the degree of induced interfacial fluctuations correlates with stability at the protein-solvent interface. In considering the inherent chemical and topographical heterogeneities of the protein surface, we studied the stability of single ions in the vicinity of three different regions (hydrophobic patch, less hydrophobic, hydrophilic) of a protein, in this case HFBII. In the single anion case, I^- (as a less charge-dense species with more malleable solvation shell) has a stronger surface stability and larger induced fluctuations than Cl^- at the interface of the hydrophobic patch. This ion specific behavior was not found at the hydrophilic interfaces; instead, both anions displayed similar behaviors in terms of surface stability and induced interface fluctuations. We posit that where strong local interactions are not dominant, as in the case of hydrophobic surfaces that inherently holds higher fluctuations (i.e., higher solvent density fluctuations [341, 43]), the anions tend to differentiate themselves based on their "hydrophobicity"; the large, less charge-dense iodide thus has a higher propensity to associate with hydrophobic regions due to its inherent higher "hydrophobicity". In the case of hydrophilic interfaces presenting highly polar and charged species, the strong charge-dipole and charge-charge interactions dominate and equalize the stabilities and interface perturbing effects of both anions. Three specific orientations of a single guandinium cation (parallel, perpendicular-x and perpendicular-y, depending on the dimensionality of the guandinium normal vector) relative to the hydrophobic patch of HFBII were also examined with their surface stabilities and induced fluctuations. Results were qualitatively consistent with surface propensities revealed at the liquid-vapor interface. The parallel configuration induced more interface fluctuation along with a -2 kcal/mol surface stability as the cation approaches the hydrophobic patch; on the other hand, the perpendicular configurations induced less interface fluctuation and showed no surface affinity at the hydrophobic patch. This further solidifies the vision that hydrophobic effect/association, rather

than the electrostatic interactions, is a more plausible driving force for the surface stabilization of ions.

The specific identity of ions in solution significantly alters the behavior of hydrophobic molecules, in other words, reducing or amplifing their "effective hydrophobicity". We used two parallel single-walled carbon nanotubes in aqueous salt solutions to study how different salts (NaCl and NaI) and temperaturesaffected the hydrophobic association. Specifically, we calculated the reversible work (potentials of mean force, or free energies) of the nanotube association with the distance between tube axes as the order parameter. Addition of salts enhances stability of the contact state between two nanotubes on the order of 4 kcal/mol, however, the ion-specific spatial distribution of different halide anions gives rise to starkly different contributions to the free energy stability of nanotubes in the contact state. Iodide anion directly stabilizes the contact state to a much greater extent than chloride anion. In the case of I^- solutions, water is driven further away from the tube surface because of iodide anions segregating to the surface; the force contributed by water further away is to pull the tubes toward the water and away from one another, thus destabilizing the contact state. In the Cl^- solutions, much less water is expelled from the immediate vicinity of the tubes; water thus exerts a greater net destabilizing force in the iodide solutions compared to that in the chloride solutions. These different behaviors at the tube-solvent surface lead to the stabilization of the contact state in both NaCl and NaI relative to that in pure water.

We incorporated Graphical Processing Units (GPUs) as a new platform for molecular dynamics simulations to further study the temperature dependencies of tube association in NaI solution. Via the decomposition of free energy into individual components, we found that solvent contribution (including water, anion and cation contributions) is correlated with the spatial distribution of the corresponding species and is influenced distinctly by the temperature: water contributes to the tube association in a less destabilizing manner as the temperature increases, while I^- shows reversed trend, and Na^+ presents no dependence to temperature. Tube-solvent surface fluctuations were examined for the intertube region and the outer sides of nanotubes. The extent

of tube-water surface fluctuation in the intertube region is dependent on the tube-tube separation, i.e., the extent of hydrophobic confinement. At a critical separation, the intertube surface fluctuation coincides with the fluctuations at the outer sides of the tubes, indicating a comparative malleability of solvation shell or similar environment of "hydrophobicity".

7.2 Future Work

In this dissertation, we focused on the interfacial response to the addition of ions near the hydrophobic surface, particularly the connection between surface stabilities and ion-induced surface fluctuations. Other than air-water and protein-water interfaces, the presence of co-solutes in an aqueous solution adjacent to an organic liquid also lies at the heart of various environmental and biological processes, such as ion transport, environmental remediation, and the phase transfer catalysis. In general, oil-water interfaces are observed to be relatively sharp with considerable molecular orientation of interfacial water molecules [395]. Distinct surface stabilities and physical behaviors of ions at the oil-water were also studied via experiments [395] and simulations [396, 394]. For example, McFearin and Richmond studied the vibrational sum-frequency (VSF) spectra of Cl^-, Br^-, NO_3^- and SO_4^{2-} at the CCl_4-water interface, revealed that the monovalent anions cause a reduction of the orienting force on interfacial water molecules and a narrower interfacial region, while SO_4^{2-} behaves oppositely [395]. Wick et al. found the adsorption of halide anions at the n-alkane-water interface to be similar with their behaviors near liquid-vapor interfaces [394] using MD simulations. In principle, when we consider to place a charge at the oil-water interface, an electrostatic field is produced which reorients the water molecules from their initial neat configuration [26]. This field may also cause orienting of the nearby organic liquid, thus promote/expel the existence of ions within the region of the interface. In reality, depending on the organic liquid, its hydrophobicity may differ. Via VSFS, Richmond and co-workers found that the free OH peak frequencies from the alkane-water spectra were higher than that of the CCl_4-water spectra, indicating less interaction between

the OH oscillators in contact with the nonaqueous phase [397, 26]. These results implied hydrocarbons to be more hydrophobic than the nonpolar CCl_4. This difference in hydrophobicity of the organic liquid may result in varying behavior for the same ion at diversified interfaces. Wick and Dang examined molar solutions of halide ions at the CCl_4-water, DCE [1]-water interfaces via MD simulations [398, 399, 15]. Despite similar enhanced densities reported for Cl^- anion at the CCl_4-water and air-water interfaces, they suggested that Cl^- extends further into the CCl_4 phase, resulting in a larger overall presence of Cl^- at the CCl_4-water interface. Interestingly, no DCE-water interfacial stability for Cl^- was found. It is therefore intriguing to investigate how these distinct surface stabilities, ion-induced fluctuations and ionic solvation properties were associated with the choice of the organic liquid.

On the scales for an ion cavity, the hydrogen bonding network of water can accommodate the cavity without disruption, which indicates that hydrophobic solvation is an entropic effect, thus the solvation free energy of a small hydrophobic cavity increases with increasing temperature. On large scales, an energetic effect related to the formation of an interface disrupts the hydrogen bonding network, and the surface tension of an extended hydrophobic interface has a negative temperature dependence, which induces positive excess entropy [128]. When a small cavity merges with a large interface, it usually requires explicit simulations to determine if such process is entropic or enthalpic driven. In the scale of ions, Caleman et al. [9], Otten et al. [19], Netz et al. [128] and our results showed that the total entropic contribution disfavors the presence of the ion at the interface. In early studies, the adsorption entropies of alkanes (from pentane up to octane) on water were also shown to be negative [400]. These results serve as strong evidences that hydrophobic solvation of the solute is dominant in determining the stability near the hydropobic surface. Be that as it may, we admit that there remains differences between ions and hydrophobic solutes. For instance, in previous studies, methane was shown to be fully dissolvated in the vapor

[1] 1,2-Dichlorethane, commonly known as ethylene dichloride.

phase [401]; in our results, ions were never observed to be fully dissolvated, even when the ion was restrained 50 Å away from the Gibbs dividing surface (data not shown). A similar study with single hydrophobic solutes like alkanes transporting between water and vapor phases may therefore serve as a complement. Interestingly, in a recent study Biscay et al. investigated the thermodynamic stability of the adsorption layer formed by n-alkanes (from methane up to hexane) at the water surface via united-atom Monte Carlo simulations. The authors reported surface stabilities for the alkanes with less than four carbons, i.e., no free energy minimum was found for longer alkanes such as n-pentane or n-hexane near the interfacial region [402]. As the longer alkanes approach, the surface water-water hydrogen bonds reduce. They therefore explained the absence of the adsorption for longer alkanes as the associated entropy penalties in reorganizing water molecules not being compensated by the attractive interactions between water and methylene groups of the alkane chains. While the results of adsorption free energies may contradict other studies [403, 404, 405], the fact that their calculated n-alkane-water interfacial tensions are consistent with experiments [406, 402] still implies the effect of water-water hydrogen bonds reduction should be taken into account in the adsorption process; in other words, when a n-pentane already adsorbs at the water surface, its presence might reduce the ability of surrounding water molecules to accommodate another n-pentane. A detailed analysis regarding the hydrogen bonding and free energetics for this process might be enlightening.

It is well-known that urea is also an effective protein denaturant other than the guandinium cation. Despite the routine use of urea, our understanding of its molecular mechanism to denature proteins is still rather controversial. Basically it has been proposed that urea may produce its effect in two ways: the direct mechanism and the indirect mechanism [407, 408, 409, 345]. The former indicates that urea can "bind" to proteins through hydrogen bonding and/or other electrostatic interactions [409]. On the contrary, the latter mechanism posits that urea perturbs water structure and weakens hydrophobic interactions, such that hydrophobic residues on proteins become better solvated. Although experiments in urea solution suggest negligible effects on

bulk water structure from urea [68], VSF spectra indicate that urea near the protein surface may affect the hydrogen bonding of interfacial water molecules, thus affecting the solvation of the proteins [407]; hence, the indirect mechanism is more plausible. In spite of vast studies to compare guanidinium cation and urea [295, 410, 411], up to present it is still lacking an unified mechanism for both denaturants. With the spirit of this dissertation, we could construct similar systems to study single urea near liquid-vapor interfaces and the protein hydrophobic patch, as well as the orientation of urea relative to the surface. We could also analyze the solvent structure (such as the hydrogen bonds and associated tetrahedrality of water molecules) above the molecular plane, in order to examine the "hydrophobicity" of these two molecules, respectively. We also believe that the decomposition of potentials of mean force into van der Waals and electrostatic contributions will provide new physical insights.

Although not pursued in this work, there are evidences showing that polarizable force fields may provide more physical insight to the study of hydrophobic association. English and Macelroy [412] studied the structural and dynamical properties of methane clathrate hydrates using five different potential models at several temperatures and found that polarizable TIP4P-FQ model correlates significantly more closely with an experimental velocity spectrum for methane molecules in the hydrate. Jiang et al. also showed that the use of polarizable water models was able to reproduce more physically realistic molecular dipole along with its temperature dependence than the nonpolarizable water models [413]. In independent simulations, we have also observed that the hydrogen bond network of TIP4P-FQ may be more temperature sensitive than SPC/E (data not shown), which warrants further investigation on how the polarizability effects hydrophobic association. It is also important to incorporate polarizability into the ions to enrich our study. In order to develop such charge dependent polarizable ions, charge equilibration ions should be developed. Meanwhile, although the ion-water interactions are usually parameterized based on reproducing ab initio properties in vacuum and experimental hydration free energies, ion-ion interactions were treated via combining rules. A careful ionic force field optimization based on ion-pair solvation properties

is therefore required. Ultimately, the goal is to perform fully polarizable studies with protein-protein and/or protein-ligand associations.

BIBLIOGRAPHY

[1] M. G. Cacace, E. M. Landau, and J. J. Ramsden. The Hofmeister series: Salt and solvent effects on interfacial phenomena. *Quart. Rev. Biophys.*, 30:241–277, 1997.

[2] R. J. Piazza. Interactions in protein solutions near crystallisation: a colloid physics approach. *J. Cryst. Growth*, 196:415–423, 1999.

[3] L. Hua, R. Zhou, D. Thirumalai, and B. J. Berne. Urea denaturation by stronger dispersion interactions with proteins than water implies a 2-stage unfolding. *Proc. Nat. Aca. Sci.*, 105:16928–16933, 2008.

[4] K. A. Beauchamp, R. McGibbon, Y. S. Lin, and V. S. Pande. Simple few-state models reveal hidden complexity in protein folding. *Proc. Nat. Aca. Sci.*, 109:17807–17813, 2012.

[5] K. D. Collins. Ions from the Hofmeister series and osmolytes: Effects on proteins in solution and in the crystallization process. *Methods*, 34:300–311, 2004.

[6] R. Curtis and L. Lue. A molecular approach to bioseparations: Protein-protein and protein-salt interactions. *Chem. Eng. Sci.*, 61:907–923, 2006.

[7] J. H. Ha, M. W. Capp, M. D. Hohenwalter, M. Baskerville, and M. T. Record Jr. Thermodynamic stoichiometries of participation of water, cations and anions in specific and non-specific binding of lac repressor to dna: Possible thermodynamic origins of the 'glutamate effect' on protein-dna interactions. *J. Mol. Bio.*, 228:252–264, 1992.

[8] M. A. Brown, R. D'Auria, L. F. W. Kuo, M. J. Krisch, D. E. Starr, H. Bluhm, D. J. Tobias, and J. C. Hemminger. Ion spatial distributions at the liquid-vapor interface of aqueous potassium fluoride solutions. *Phys. Chem. Chem. Phys.*, 10:4778–4784, 2008.

[9] C. Caleman, J. S. Hub, P. J. van Maaren, and D. van der Spoel. Atomistic simulation of ion solvation in water explains surface preference of halides. *Proc. Nat. Aca. Sci.*, 108:6838–6842, 2011.

[10] L. X. Dang. Computational study of ion binding to the liquid interface of water. *J. Phys. Chem. B*, 106:10388–10394, 2002.

[11] D. Horinek, A. Herz, L. Vrbka, F. Sedlmeier, S. I. Mamatkulov, and R. R. Netz. Specific ion adsorption at the air-water interface: The role of hydrophobic solvation. *Chem. Phys. Lett.*, 479:173–183, 2009.

[12] P. Jungwirth and D. J. Tobias. Ions at the air/water interface. *J. Phys. Chem. B*, 106:6361–6373, 2002.

[13] M. N. Tamashiro and M. A. Constantino. Ions at the water-vapor interface. *J. Phys. Chem. B*, 114:3583–3591, 2010.

[14] L. Vrbka, M. Mucha, B. Minofar, P. Jungwirth, E. C. Brown, and D. J. Tobias. Propensity of soft ions for the air/water interface. *Curr. Opin. Colloid Inter. Sci.*, 9:67–73, 2004.

[15] C. D. Wick and L. X. Dang. Recent advances in understanding transfer ions across aqueous interfaces. *Chem. Phys. Lett.*, 458:1–5, 2008.

[16] S. Ghosal, J. C. Hemminger, H. Bluhm, B. S. Mun, E. L. D. Hebenstreit, G. Ketteler, D. F. Ogletree, F. G. Requejo, and M. Salmeron. Electron spectroscopy of aqueous solution interfaces reveals surface enhancement of halides. *Science*, 307:563–566, 2005.

[17] S. Ghosal, M. A. Brown, H. Bluhm, M. J. Krisch, M. Salmeron, P. Jungwirth, and J. C. Hemminger. Ion partitioning at the liquid/vapor interface of a multicomponent alkali halide solution: A model for aqueous sea salt aerosols. *J. Phys. Chem. A*, 112:12378–12384, 2008.

[18] D. Tobias and J. C. Hemminger. Getting specific about specific ion effects. *Science*, 319:1197–1198, 2008.

[19] D. E. Otten, P. R. Shaffer, P. L. Geissler, and R. J. Saykally. Elucidating the mechanism of selective ion adsorption to the liquid water surface. *Proc. Nat. Aca. Sci.*, 109:701–705, 2012.

[20] F. Hofmeister. Zur lehre von der wirkung der salze. *Arch. Exp. Pathol. Pharmakol.*, 24:247–260, 1888.

[21] R. L. Baldwin. How Hofmeister ion interactions affect protein stability. *Biophys. Jour.*, 71:2056–2063, 1996.

[22] L. M. Pegram, T. Wendorff, R. Erdmann, I. Shkel, D. Bellissimo, D. J. Felitsky, and M. T. Record. Why hofmeister effects of many salts favor protein folding but not dna helix formation. *Proc. Nat. Aca. Sci.*, 107:7716–7721, 2010.

[23] P. Jungwirth and D. J. Tobias. Specific ion effects at the air/water interface. *Chem. Rev.*, 106:1259–1281, 2006.

[24] P. Yi and K. L. Chen. Influence of surface oxidation on the aggregation and deposition kinetics of multiwalled carbon nanotubes in monovalent and divalent electrolytes. *Langmuir*, 27:3588–3599, 2012.

[25] N. Nelson and D. K. Schwartz. Specific ion (hofmeister) effects on adsorption, desorption, and diffusion at the solid-aqueous interface. *J. Phys. Chem. Lett.*, 4:4064–4068, 2013.

[26] C. L. McFearin, D. K. Beaman, F. G. Moore, and G. L. Richmond. From franklin to today: Toward a molecular level understanding of bonding and adsorption at the oil-water interface. *J. Phys. Chem. C*, 113:1171–1188, 2009.

[27] C. Tanford. How protein chemists learned about the hydrophobic factor. *Protein Sci.*, 6:1358–1366, 1997.

[28] M. A. Wilson, A. Pohorille, and L. R. Pratt. Surface potential of water liquid-vapor interface. *J. Chem. Phys.*, 88:3281–3285, 1988.

[29] M. J. P. Nijmeijer, A. F. Bakker, C. Bruin, and J. H. Sikkenk. A molecular dynamics simulation of the lennard-jones liquid-vapor interface. *J. Chem. Phys.*, 89:3789, 1988.

[30] M. Matsumoto and Y. Kataoka. Study on liquid vapor interface of water .1. simulational results of thermodynamic properties and orientational structure. *J. Chem. Phys.*, 88:3233–3245, 1988.

[31] R. S. Taylor, L. X. Dang, and B. C. Garrett. Molecular dynamics simulations of the liquid/vapor interface of spc/e water. *J. Phys. Chem.*, 100:11720–11725, 1996.

[32] M. Mecke, J. Winkelmann, and J. Fischer. Molecular dynamics simulation of the liquid-vapor interface: The lennard-jones fluid. *J. Chem. Phys.*, 107:9264, 1997.

[33] S. Jain and J. C. Ahluwalia. Differential scanning calorimetric studies on the effect of ammonium and tetraalkylammonium halides on the stability of lysozyme. *Biophy. Chem.*, 7:171–177, 1996.

[34] A. I. Frolov, A. G. Rozhin, and M. V. Fedorov. Ion interactions with the carbon nanotube surface in aqueous solutions: Understanding the molecular mechanisms. *Chem. Phys. Chem.*, 11:2612–2616, 2010.

[35] S. Lin and D. Blankschtein. Role of the bile salt surfactant sodium cholate in enhancing the aqueous dispersion stability of single-walled carbon nanotubes: A molecula dynamics simulation study. *J. Phys. Chem. B*, 2010:15616–15625, 2010.

[36] G. A. Zelada-Guillen, J. Riu, A. Duzgun, and F. X. Rius. Immediate detection of living bacteria at ultralow concentrations using a carbon nanotube based potentiometric aptasensor. *Angew. Chem. Int. Ed.*, 48:7334–7337, 2009.

[37] G. A. Zelada-Guillen, J. Riu, A. Duzgun, and F. X. Rius. Immediate detection of living bacteria at ultralow concentrations using a carbon nanotube based potentiometric aptasensor. *Angew. Chem.*, 121:7470–7473, 2009.

[38] R. J. Chen, S. Bangsaruntip, K. A. Drouvalakis, N. W. S. Kam, M. Shim, Y. Li, W. Kim, P. J. Utz, and H. Dai. Noncovalent functionalization of carbon nanotubes for highly specific electronic biosensors. *Proc. Nat. Aca. Sci.*, 100:4984–4989, 2003.

[39] L. Vaisman, H. D. Wagner, and G. Marom. The role of surfactants in dispersion of carbon nanotubes. *Adv. Coll. Int. Sci.*, 128:37–46, 2006.

[40] V. C. Moore, M. S. Strano, E. H. Haroz, R. H. Hauge, R. E. Smalley, J. Schimdt, and Y. Talmon. Individually suspended single-walled carbon nanotubes in various surfactants. *Nano Lett.*, 3:1379–1382, 2003.

[41] T. Ghosh, A. Kalra, and S. Garde. On the salt-induced stabilization of pair and many-body hydrophobic interactions. *J. Phys. Chem. B*, 109:642–651, 2005.

[42] K. A. Dill. Dominant forces in protein folding. *Biochem.*, 29:7133–7155, 1990.

[43] S. N. Jamadagni R. Godawat and S. Garde. Hydrophobicity of proteins and interfaces: Insights from density fluctuations. *Annu. Rev. Chem. Biomol. Eng.*, 2:147–171, 2011.

[44] A. S. Thomas and A. H. Elcock. Molecular dynamics simulations of hydrophobic association in aqueous salt solutions indicate a connection between water hydrogen bonding and the Hofmeister effect. *J. Am. Chem. Soc.*, 129:14887–14898, 2007.

[45] V. Yeh, J. M. Broering, A. Romanyuk, B. Chen, Y. O. Chernoff, and A. S. Bommarius. The Hofmeister effect on amyloid formation using yeast prion protein. *Prot. Sci*, 19:47–56, 2010.

[46] M. H. Suhre, S. Hess, A. V. Goiser, and T. Scheibel. Influence of divalent copper, manganese and zinc ions on fibril nucleation and elongation of the amyloid-like yeast prion determinant ^{35}P-NMR. *J. Inorg. Biochem.*, 103:1711–1720, 2009.

[47] O. V. Bocharova, l. Breydo, V. V. Sainikov, and I. V. Baskakov. Copper(II) inhibits in vitro conversion of prion protein into amyloid fibrils. *Biochemistry*, 44:6776–6787, 2005.

[48] M. Bostrom, D. R. Williams, and B. W. Ninham. Specific ion effects: Role of salt and buffer in protonation of cytochrome c. *Eur. Phys. J. E*, 13:239–245, 2004.

[49] Y. Zhang and P. S. Cremer. Interactions between macromolecules and ions: the Hofmeister series. *Curr. Opin. Chem. Bio.*, 10:658–663, 2006.

[50] M. Bostrom, D. R. Williams, and B. W. Ninham. Specific ion effects: Why the properties of lysozyme in salt solutions follow a Hofmeister series. *Prot. Sci*, 19:47–56, 2003.

[51] T. A. Beu. Molecular dynamics simulations of ion transport through carbon nanotubes. I. Influence of geometry, ion specificity, and many-body interactions. *J. Chem. Phys.*, 132:164513, 2010.

[52] T. A. Hilder, D. Gordon, and S.-H. Chung. Synthetic cation-selective nanotube: Permeant cations chaperoned by anions. *J. Chem. Phys.*, 134:045103, 2011.

[53] A. Berezhkovskii and G. Hummer. Single-file transport of water molecules through a carbon nanotube. *Phys. Rev. Lett.*, 89:064503, 2002.

[54] G. Hummer, J. C. Rassiah, and J. P. Noworyta. Water conduction through the hydrophobic channel of a carbon nanotube. *Nature*, 414:188–190, 2001.

[55] N. M. Uddin, F. M. Capaldi, and B. Farouk. Molecular dynamics simulations of the interactions and dispersion of carbon nanotubes in polyethylene oxide/water systems. *Polymer*, 52:288–296, 2011.

[56] P. Jungwirth and D. J. Tobias. Chloride anion on aqueous clusters, at the air-water interface, and in liquid water: Solvent effects on Cl^- polarizability. *J. Phys. Chem. A*, 106:379–383, 2002.

[57] H. D. B. Jenkins and Y. Marcus. Viscosity b-coefficients of ions in solution. *Chem. Rev.*, 95:2695–2724, 1995.

[58] Y. Marcus. Effect of ions on the structure of water: Structure making and breaking. *Chem. Rev.*, 109:1346–1370, 2009.

[59] A. P. dos Santos, A. Diehl, and Y. Levin. Surface tensions, surface potentials, and the Hofmeister series of electrolyte solutions. *Langmuir*, 13:10778–10783, 2010.

[60] K. D. Collins. Sticky ions in biological systems. *Proc. Nat. Aca. Sci.*, 92:5553–5557, 1995.

[61] M. Kondoha, Y. Ohshimab, and M. Tsubouchi. Ion effects on the structure of water studied by terahertz time-domain spectroscopy. *Chem. Phys. Lett.*, 591:317–322, 2014.

[62] Y. J. Zhang, S. Furyk, D. E. Bergbreiter, and P. S. Cremer. Specific ion effectis on the water solubility of macromolecules: Pnipam and the Hofmeister series. *J. Am. Chem. Soc.*, 127:14505–14510, 2005.

[63] R. Zangi, M. Hagen, and B. J. Berne. Effect of ions of the hydrophobic interaction between two plates. *J. Am. Chem. Soc.*, 129:4678–4686, 2007.

[64] D. F. C. Morris. Ionic radii and enthalpies of hydration of ions. *Struct. Bonding*, 6:157–159, 1969.

[65] K. D. Collins. Charge density-dependent strength of hydration and biological structure. *Biophy. J.*, 72:65–76, 1997.

[66] P. Lo Nostro and B. W. Ninham. Hofmeister phenomena: An update on ion specificity in biology. *Chem. Rev.*, 112:2286–2322, 2012.

[67] A. W. Omta, M. F. Kropman, S. Wouthersen, and H. J. Bakker. Negligible effect of ions on the hydrogen-bond structure in liquid water. *Science*, 301:347–349, 2003.

[68] J. D. Batchelor, A. Olteanu, A. Tripathy, and G. J. Pielak. Impact of protein denaturants and stabilizers on water structure. *J. Am. Chem. Soc.*, 126:1958–1961, 2004.

[69] P. B. Petersen and R. J. Saykally. Probing the interfacial structure of aqueous electrolytes with femtosecond second harmonic generation spectroscopy. *J. Phys. Chem. B*, 110:14060–14073, 2006.

[70] P. B. Petersen and R. J. Saykally. Confirmation of enhanced anion concentration at the liquid water surface. *Chem. Phys. Lett.*, 397:51–55, 2004.

[71] Y. R. Shen. Surface-properties probed by 2nd-harmonic and sum-frequency generation. *Nature*, 337:519–525, 1989.

[72] S. Baldelli, C. Schnitzer, and M. J. Shultz. The structure of water on hcl solutions studied with sum frequency generation. *Chem. Phys. Lett.*, 302:157–163, 1999.

[73] E. A. Raymond and G. L. Richmond. Probing the molecular structure and bonding of the surface of aqueous salt solutions. *J. Phys. Chem. B*, 108:5051–5059, 2004.

[74] D. Liu, G. Ma, L. M. Levering, and H. C. Allen. Vibrational spectroscopy of aqueous sodium halide solutions and air-liquid interfaces: Observation of increased interfacial depth. *J. Phys. Chem. B*, 108:2252–2260, 2004.

[75] M. J. Shultz, S. Baldelli, C. Schnitzer, and D. Simonelli. Aqueous solution/air interfaces probed with sum frequency generation spectroscopy. *J. Phys. Chem. B*, 106:5313–5324, 2002.

[76] R. Weber, B. Winter, P. M. Schmidt, W. Widdra, I. V. Hertel, M. Dittmar, and M. Faubel. Photoemission from aqueous alkali-metal-iodide salt solutions using euv synchrotron radiation. *J. Phys. Chem. B*, 108:4729–4736, 2004.

[77] B. Winter, R. Weber, P. M. Schmidt, I. V. Hertel, M. Faubel, L. Vrbka, and P. Jungwirth. Molecular structure of surface-active salt solutions: Photoelectron spectroscopy and molecular dynamics simulations of aqueous tetrabutylammonium iodide. *J. Phys. Chem. B*, 108:14558–14564, 2004.

[78] M. A. Brown, B. Winter, M. Faubel, and J. C. Hemminger. Spatial distribution of nitrate and nitrite anions at the liquid-vapor interface of aqueous solutions. *J. Am. Chem. Soc.*, 9:8354–8355, 2009.

[79] M. Salmeron and R. Schlögl. Ambient pressure photoelectron spectroscopy: A new tool for surface science and nanotechnology. *Surf. Sci. Rep.*, 63:169–199, 2008.

[80] B. W. Ninham and V. Yaminsky. Ion binding and ion specificity: The hofmeister effect and onsager and lifshitz theories. *Langmuir*, 13:2097–2108, 1997.

[81] J. T. O'Brien, J. S. Prell, M. F. Bush, and E. R. Williams. Sulfate ion patterns water at long distance. *J. Am. Chem. Soc.*, 132:8248–8249, 2010.

[82] K. J. Tielrooij. Cooperativity in ion hydration. *Science*, 328:1006–1009, 2010.

[83] R. Mancinelli, A. Botti, F. Bruni, M. A. Riccia, and A. K. Soper. Perturbation of water structure due to monovalent ions in solution. *Phys. Chem. Chem. Phys.*, 9:2959–2967, 2007.

[84] J. Horzmann, R. Ludwig, A. Geiger, and D. Paschek. Pressure and salt effects in simulated water: Two sides of the same coin. *Angew. Chemie Intl. Ed.*, 46:8907–8911, 2007.

[85] D. Paschek and R. Ludwig. Specific ion effects on water structure and dynamics beyond the first hydration shell. *Angew. Chemie Intl. Ed.*, 50:352–353, 2011.

[86] N. Galamba. Mapping structural perturbations of water in ionic solutions. *J. Phys. Chem. B*, 116:5242–5250, 2012.

[87] A. Botti, F. Bruni, S. Imberti, M. A. Ricci, and A. K. Soper. Solvation shell of H^+ ions in water. *J. Mol. Liq.*, 117:77–81, 2005.

[88] A. Botti, F. Bruni, S. Imberti, M. A. Ricci, and A. K. Soper. Solvation shell of OH^- ions in water. *J. Mol. Liq.*, 117:81–84, 2005.

[89] B .J. Alder and T. E. Wainwright. Studies in molecular dynamics. i. general method. *J. Chem. Phys.*, 31:459–466, 1959.

[90] B .J. Alder and T. E. Wainwright. Studies in molecular dynamics. ii. behavior of a small number of elastic spheres. *J. Chem. Phys.*, 33:1439–1451, 1959.

[91] P. Jungwirth and B. Winter. Ions at aqueous interfaces: From water surface to hydrated proteins. *Annu. Rev. Phys. Chem.*, 59:343–366, 2008.

[92] S. Ou, Y. Hu, S. Patel, and H. Wan. Spherical monovalent ions at aqueous liquid-vapor interfaces: Interfacial stability and induced interface fluctuations. *J. Phys. Chem. B*, 117:11732–11742, 2013.

[93] S. Ou and S. Patel. Temperature dependence and energetics of single ions at the aqueous liquid-vapor interface. *J. Phys. Chem. B*, 117:6512–6523, 2013.

[94] L. Perera and M. L. Berkowitz. Many-body effects in molecular dynamics simulations of Na^+ $(H_2O)_n$ and $Cl^-(H_2O)_n$ clusters. *J. Chem. Phys.*, 95:1954–1963, 1991.

[95] L. P. and M. L. Berkowitz. Ion solvation in water clusters. *Z. Phys. D*, 26:166–168, 1993.

[96] Raffaella D'Auria and Douglas J. Tobias. Relation between surface tension and ion absorption at the air-water interface: A molecular dynamics simulation study. *J. Phys. Chem. A*, 113:7286–7293, 2009.

[97] M. Vazdar, E. Pluhařová, P. E. Mason, R. Vácha, and P. Jungwirth. Ions at hydrophobic aqueous interfaces: Molecular dynamics with effective polarization. *J. Phys. Chem. Lett.*, 3:2087–2091, 2012.

[98] E. M. Knipping, M. J. Lakin, K. L. Foster, P. Jungwirth, D. J. Tobias, R. B. Gerber, D. Dabdub, and B. J. Finlayson-Pitts. Experiments and simulations of ion-enhancement interfacial chemistry on aqueous NaCl aerosols. *Science*, 288:301–306, 2000.

[99] E. C. Brown, M. Mucha, P. Jungwirth, and D. J. Tobias. Structure and vibrational spectroscopy of salt water/air interfaces: Predictions from molecular dynamics simulations. *J. Phys. Chem. B*, 109:7934–7940, 2005.

[100] M. Mucha, T. Frigato, L. M. Levering, H. C. Allen, D. J. Tobias, L. X. Dang, and P. Jungwirth. Unified molecular picture of the surfaces of aqueous acid, base, and salt solutions. *J. Phys. Chem. B*, 109:7617–7623, 2005.

[101] P. Jungwirth and D.J. Tobias. Surface effects on aqueous ionic solvation: A molecular dynamics simulation study of NaCl at the air/water interface from infinite dilution to saturation. *J. Phys. Chem. B*, 104:7702–7706, 2000.

[102] J. Heyda, J. C. Vincent, D. J. Tobias, J. Dzubiella, and P. Jungwirth. Ion specificity at the peptide bond: Molecular dynamics simulations of *n*-methylacetamide in aqueous salt solutions. *J. Phys. Chem. B*, 114:1213–1220, 2010.

[103] P. Jungwirth and D. J. Tobias. Molecular structure of salt solutions: A new view of the interface with implications for heterogeneous atmospheric chemistry. *J. Phys. Chem. B*, 105:10468–10472, 2001.

[104] X. Sun, C. D. Wick, and L. X. Dang. Computational study of ion distributions at the air/liquid methanol interface. *J. Phys. Chem. A*, 115:5767–5773, 2010.

[105] T. Chang and L. X. Dang. Recent advances in molecular simulations of ion solvation at liquid interfaces. *Chem. Rev.*, 106:1305, 2006.

[106] C. W. Wick and L. X. Dang. Distribution, structure, and dynamics of cesium and iodide ions at the H_2O-CCl_4 and H_2O-vapor interfaces. *J. Phys. Chem. B*, 110:6824, 2006.

[107] L. X. Dang and T. M. Chang. Molecular mechanism of ion binding to the liquid/vapor interface of water. *J. Phys. Chem. B*, 106:235–238, 2002.

[108] L. X. Dang. A mechanism for ion transport across the water/dichloromethane interface: A molecular dynamics study using polarizable potential models. *J. Phys. Chem. B*, 105:804–809, 2001.

[109] D. J. Tobias, A. C. Stern, M. D. Baer, Y. Levin, and C. J. Mundy. Simulation and theory of ions at atmospherically relevant aqueous liquid-air interfaces. *Annu. Rev. Phys. Chem.*, 64:339–359, 2013.

[110] S. Ou, B. A. Bauer, and S. Patel. Free energetics of carbon nanotube association in pure and aqueous ionic solutions. *J. Phys. Chem. B*, 116:8154–8168, 2012.

[111] B. A. Bauer, S. Ou, and S. Patel. Role of spatial ionic distribution on the energetics of hydrophobic assembly and properties of the water/hydrophobe interface. *Phys. Chem. Chem. Phys.*, 14:1892–1906, 2012.

[112] S. Enami, H. Mishra, M. R. Hoffmann, and A. J. Colussi. Hofmeister effects in micromolar electrolyte solutions. *J. Chem. Phys.*, 136:154707, 2012.

[113] P. B. Petersen, R. J. Saykally, M. Mucha, and P. Jungwirth. Enhanced concentration of polarizable anions at the liquid water surface: SHG spectroscopy and MD simulations of sodium thiocyanide. *J. Phys. Chem. B*, 109:10915–10921, 2005.

[114] W. H. Robertson and M. A. Johnson. Molecular aspects of halide ion hydration: The cluster approach. *Annu. Rev. Phys. Chem.*, 54:173–213, 2003.

[115] P. B. Petersen and R. J. Saykally. On the nature of ions at the liquid water surface. *Annu. Rev. Phys. Chem.*, 57:333–364, 2006.

[116] D. S. Walker and G. L. Richmond. Depth profiling of water molecules at the liquid-liquid interface using a combined surface vibrational spectroscopy and molecular dynamics approach. *J. Am. Chem. Soc.*, 129:9446–9451, 2007.

[117] D. S. Walker and G. L. Richmond. Understanding the effects of hydrogen bonding at the vapor-water interface: Vibrational sum frequency spectroscopy of h_2o/hod/d_2o mixtures studied using molecular dynamics simulations. *J. Phys. Chem. C*, 111:8321–8330, 2007.

[118] G. L. Richmond. Molecular bonding and interactions at aqueous surfaces as probed by vibrational sum frequency spectroscopy. *Chem. Rev.*, 102:2693–2724, 2002.

[119] W. T. Liu, L. Zhang, and Y. R. Shen. Interfacial structures of methanol : water mixtures at a hydrophobic interface probed by sum-frequency vibrational spectroscopy. *J. Chem. Phys.*, 125:144711, 2006.

[120] Z. Chen, R. Ward, Y. Tian, S. Baldelli, A. Opdahl, Y. R. Shen, and G. A. Somorjai. Detection of hydrophobic end groups on polymer surfaces by sum-frequeny generation vibration spectroscopy. *J. Am. Chem. Soc.*, 122:10615–10620, 2000.

[121] Y. Levin. Polarizable ions at interfaces. *Phys. Rev. Lett.*, 102:147803, 2009.

[122] Y. Levin, A. P. dos Santos, and A. Diehl. Ions at the air-water interface: An end to a hundred-year-old mystery? *Phys. Rev. Lett.*, 103:257802, 2009.

[123] A. Godec and F. Merzel. Physical origin underlying the entropy loss upon hydrophobic hydration. *J. Am. Chem. Soc.*, 134:17574–17581, 2012.

[124] N. Schelero and R. von Klitzing. Correlation between specific ion adsorption at the air/water interface and long-range interactions in colloidal systems. *Soft Matt.*, 7:2936–2942, 2011.

[125] D. F. Parsons, M. Boström, P. Lo Nostro, and B. W. Ninham. Hofmeister effects: interplay of hydration, nonelectrostatic potentials, and ion size. *Phys. Chem. Chem. Phys.*, 13:12352–12367, 2011.

[126] D. H. Herce, L. Perera, T. A. Darden, and C. Sagui. Surface solvation for an ion in a water cluster. *J. Chem. Phys.*, 122:024513, 2005.

[127] S. Pal and F. Müller-Plathe. Molecular dynamics simulation of aqueous naf and nai solutions near a hydrophobic surface. *J. Phys. Chem. B*, 109:6405–6415, 2005.

[128] R. R. Netz and D. Horinek. Progress in modeling of ion effects at the vapor-water interface. *Annu. Rev. Phys. Chem.*, 63:401–418, 2012.

[129] R. Zangi. Can salting-in/salting-out ions be classified as chaotropes/kosmotropes. *J. Phys. Chem. B*, 114:643–650, 2010.

[130] A. A. Deniz, S. Mukhopadhyay, and E. A. Lemke. Single-molecule biophysics: at the interface of biology, physics and chemistry. *J. Royal Soc. Interface*, 5:15–45, 2008.

[131] P. Hünenberger and M. Reif. *Single-Ion Solvation: Experimental and Theoretical Approaches to Elusive Thermodynamic Quantities*. Royal Society of Chemistry, London, United Kingdom, 2011.

[132] O. M. Cabarcos, C. J. Weinheimer, J. M. Lisy, and S. S. Xanthea. Microscopic hydration of the fluoride anion. *J. Chem. Phys.*, 110:5–8, 1999.

[133] J. E. Combariza and N. R. Kestner. Microscopic solvation of anions in water clusters. *Chem. Phys. Lett.*, 203:423–428, 1993.

[134] E. J. Bieske. Spectroscopic studies of anion complexes and clusters: A microscopic approach to understanding anion solvation. *Chem. Soc. Rev.*, 32:231–237, 2003.

[135] C. L. Brooks III, B. M. Pettitt, and M. Karplus. Structural and energetic effects of truncating long ranged interactions in ionic and polar fluids. *J. Chem. Phys.*, 83:5897–5908, 1985.

[136] J. A. Barker and R. O. Watts. Monte carlo studies of the dielectric properties of water-like models. *Mol. Phys.*, 26:789–792, 1973.

[137] T. Darden, D. York, and L. Pedersen. Particle mesh ewald: An $N\cdot\log(N)$ method for ewald sums in large systems. *J. Chem. Phys.*, 98:10089–10092, 1993.

[138] R. M. Venable, L. E. Chen, and R. W. Pastor. Comparison of the extended isotropic periodic sum and particle mesh ewald methods for simulations of lipid bilayers and monolayers. *J. Phys. Chem. B*, 113:5855–5862, 2009.

[139] U. Essmann, T. Darden, H. Lee, L. Perera, M. L. Berkowitz, and L. Pederson. A smooth particle mesh ewald method. *J. Chem. Phys.*, 103:8577–8593, 1995.

[140] E. Spohr. Effect of electrostatic boundary conditions and system size on the interfacial properties of water and aqueous solutions. *J. Chem. Phys.*, 107:6342–6348, 1997.

[141] L. Perera, U. Essmann, and M. L. Berkowitz. Effect of the treatment of longrange forces on the dynamics of ions in aqueous solutions. *J. Chem. Phys.*, 102:450–456, 1995.

[142] S. Ou, D. Cui, and S. Patel. Liquid-vapor interfacial properties of aqueous solutions of guanidinium and methyl guanidinium chloride: Influence of molecular orientation on interface fluctuations. *J. Phys. Chem. B*, 117:11719–11731, 2013.

[143] B. A. Bauer, S. Ou, and S. Patel. Solvation structure and energetics of single ions at the aqueous liquid-vapor interface. *Chem. Phys. Lett.*, 527:22–26, 2011.

[144] T. Yagasaki, S. Saito, and I. Ohmine. Effects of nonadditive interactions on ion solvation at the water/vapor interface: A molecular dynamics study. *J. Phys. Chem. A*, 114:12573–12584, 2010.

[145] A. Arslanargin and T. L. Beck. Free energy partitioning analysis of the driving forces that determine ion density profiles near the water liquid-vapor interface. *J. Chem. Phys.*, 136:104503, 2012.

[146] M. D. Baer, A. C. Stern, Y. Levin, D. J. Tobias, and C. J. Mundy. Electrochemical surface potential due to classical point charge models drives anion adsorption to the air-water interface. *J. Phys. Chem. Lett.*, 3:1565–1570, 2012.

[147] B. R. Brooks, R. E. Bruccoleri, B. D. Olafson, D. J. Stages, S. Swaminathan, and M. J. Karplus. CHARMM- a program for macromolecular energy, minimization, and dynamics calculations. *J. Comp. Chem.*, 4:187–217, 1983.

[148] B. R. Brooks, C. L. Brooks, III, A. D. MacKerell, Jr., L. Nilsson, R. J. Petrella, B. Roux, Y. Won, G. Archontis, C. Bartels, S. Boresch, A. Caflisch, L. Caves, Q. Cui, A. R. Dinner, M. Feig, S. Fisher, J. Gao, M. Hodoscek, W. IM, K. Kuczera, T. Lazaridis, J. Ma, V. Ovchinnikov, E. Paci, R. W. Pastor, C. B. Post, J. Z. Pu, M. Schaefer, B. Tidor, R. M. Venable, H. L. Woodcock, X. Wu, W. Yang, D. M. York, and M. Karplus. CHARMM: The biomolecular simulation program. *J. Comp. Chem.*, 30:1545–1614, 2009.

[149] A. R. Leach. *Molecular Modelling Principles and Applications (Second Edition)*. Pearson Education Limited, Essex, England, 2001.

[150] P. T. Sikora. Combining rules for spherically symmetric intermolecular potentials. *J. Phys. B: Atom. Molec. Phys.*, 3:1475–1482, 1970.

[151] B. E. F. Fender and G. D. Halsey Jr. Second virial coefficients of argon, krypton, and argonkrypton mixtures at low temperatures. *J. Chem. Phys.*, 36:1881–1888, 1962.

[152] C. L. Kong. Combining rules for intermolecular potential parameters. ii. rules for the lennardjones (12-6) potential and the morse potential. *J. Chem. Phys.*, 59:2464–2467, 1973.

[153] J. Delhommelle and P. Millie. Inadequancy of the Lorentz-Berthelot combining rules for accurate predictions of equilibrium properties by molecular simulation. *Mol. Phys.*, 99:619–625, 2001.

[154] A. K. Al-Matar and D. A. Rockstraw. A generating equation for mixing rules and two new mixing rules for interatomic potential energy parameters. *J. Comp. Chem.*, 2004:660–668, 2004.

[155] J. W. Ponder and D. A. Case. Force fields for protein simulations. *Adv. Prot. Chem.*, 66:27–85, 2003.

[156] A. Warshel, P. K. Sharma, M. Kato, and W. W. Parson. Modeling electrostatic effects in proteins. *Biochim. Biophys. Acta.*, 1764:1647–1676, 2006.

[157] L. Monticelli and D. P. Tieleman. Force fields for classical molecular dynamics. *Methods Mol. Bio.*, 924:197–213, 2013.

[158] A. K. Rappe and W. A. Goddard. Charge equilibration for molecular dynamics simulations. *J. Phys. Chem.*, 95:3358–3363, 1991.

[159] R. G. Parr and W. Yang. *Density-Functional Theory of Atoms and Molecules*. Oxford University Press, Oxford, 1989.

[160] R. T. Sanderson. *Chemical Bonds and Bond Energy*. Academic Press, New York, 1976.

[161] R. T. Sanderson. An interpretation of bond lengths and a classification of bonds. *Science*, 114:670–672, 1951.

[162] L. Pauling. *The Nature of the Chemical Bond*. Cornell University Press, Ithaca, NY, 1960.

[163] S. Patel and C. L. Brooks III. CHARMM fluctuating charge force fields for proteins: I parameterization and application to bulk organic liquid simulations. *J. Comp. Chem.*, 25:1–15, 2004.

[164] R. F. Nalewajski, J. Korchowiec, and Z. Zhou. Molecular hardness and softness parameters and their use in chemistry. *Int. J. Quantum Chem.: Quantum Chemistry Symposium 22*, 22:349–366, 1988.

[165] G. L. Warren, J. E. Davis, and S. Patel. Origin and control of superlinear polarizability scaling in chemical potential equilization methods. *J. Chem. Phys.*, 128:144110, 2008.

[166] R. Car and M. Parrinello. Unified approach for molecular dynamics and density functional theory. *Phys. Rev. Lett.*, 55:2471–2474, 1985.

[167] V. M. Anisimov, G. Lamoureux, I. V. Vorobyov, N. Huang, B. Roux, and A. D. MacKerell Jr. Determination of electrostatic parameters for a polarizable force field based on the classical Drude oscillator. *J. Chem. Theory Comput.*, 1:153–168, 2005.

[168] G. Lamoureux and B. Roux. Modeling induced polarization with classical Drude oscillators: Theory and molecular dynamics simulations algorithm. *J. Chem. Phys.*, 119:3025, 2003.

[169] G. Lamoureux, A. D. MacKerell Jr., and B. Roux. A simple polarizable model of water based on classical Drude oscillators. *J. Chem. Phys.*, 119:5185, 2003.

[170] G. Lamoureux, E. Harder, I. V. Vorobyov, B. Roux, and A. D. MacKerell Jr. Polarizable model of water for molecular dynamics simulations of biomolecules. *Chem. Phys. Lett.*, 418:245–249, 2006.

[171] P. Balbuena and J. M. Seminario. *Molecular Dynamics From Classical to Quantum Methods*. Elsevier Science, Amsterdam, 1999.

[172] J. W. Cahn and J. E. Hilliard. Free energy of a nonuniform system. i. interfacial free energy. *J. Chem. Phys.*, 28:258–267, 1958.

[173] J. S. Rowlinson and F. L. Swinton. *Liquids and Liquid Mixtures*. Butterworths, London, 1982.

[174] D. A. McQuarrie. *Statistical Mechanics*. University Science Books, Herndon, VA, 2000.

[175] J. P. Hansen and I. R. McDonald. *Theory of Simple Liquids*. Academic Press, San Diego, CA, 1986.

[176] T. Head-Gordon and G. Hura. Water structure from scattering experiments and simulation. *Chem. Rev.*, 102:2651–2670, 2002.

[177] B. J. Thijsse. The accuracy of experimental radial distribution functions for metallic glasses. *J. Appl. Cryst.*, 17:61–76, 1984.

[178] R. J. McQueeney. Dynamic radial distribution function from inelastic neutron scattering. *Phys. Rev. B*, 57:10560–10568, 1998.

[179] I. Benjamin. Chemical reactions and solvation at liquid interfaces: A microscopic perspective. *Chem. Rev.*, 96:1449–1475, 1996.

[180] P. Liu, E. Harder, and B. J. Berne. Hydrogen-bond dynamics in the air-water interface. *J. Phys. Chem. B*, 109:2949–2955, 2005.

[181] B. A. Bauer and S. Patel. Role of electrostatics in modulating hydrophobic interactions and barriers to hydrophobic assembly. *J. Phys. Chem. B*, 114:8107–8117, 2010.

[182] F. Starr, J. Nielsen, and H. Stanley. Hydrogen-bond dynamics for the extended simple point-charge model of water. *Phys. Rev. E*, 62:579–587, 2000.

[183] A. Godec, J. C. Smith, and F. Merzel. Increase of both order and disorder in the first hydration shell with increasing solute polarity. *Phys. Rev. Lett.*, 107:267801, 2011.

[184] A. E. Garcia and L. Stiller. Computation of the mean residence time of water in the hydration shells of biomolecules. *J. Comp. Chem.*, 14:1396–1406, 1993.

[185] R. H. Henchmen and J. A. McCammon. Structural and dynamic properties of water around acetylcholinesterase. *Protein Sci.*, 11:2080–2090, 2002.

[186] R. Kohlrausch. Theorie des elektrischen rückstandes in der leidner flasche. *Annalen der Physik und Chemie (Poggendorff)*, 91:179–213, 1854.

[187] M. N. Berberan-Santos, E. N. Bodunov, and B. Valeur. Mathematical functions for the analysis of luminescence decays with underlying distributions 1. kohlrausch decay function (stretched exponential). *Chem. Phys.*, 315:171–182, 2005.

[188] B. A. Bauer, S. Ou, S. Patel, and K. Siva. Dynamics and energetics of hydrophobically confined water. *Phys. Rev. E*, 85:051506, 2012.

[189] S. N. Taraskin and S. R. Elliott. Connection between the true vibrational density of states and that derived from inelastic neutron scattering. *Phys. Rev. B*, 55:117–123, 1997.

[190] V. Mazzacurati, M.A. Ricci, G. Ruocco, and M. Sampoli. Low-frequency raman spectra of liquid water: A molecular dynamics simulation. *Chem. Phys. Lett.*, 159:383–387, 1989.

[191] E. Henssge, , D. Dumont, D. Fischer, and D. Bougeard. Analysis of infrared and raman spectra calculated by molecular dynamics. *J. Mol. Structure*, 482-483:491–496, 1999.

[192] T. Hasegawa and Y. Tanimura. A polarizable water model for intramolecular and intermolecular vibrational spectroscopies. *J. Phys. Chem. B*, 115:5545–5553, 2011.

[193] Q. Wan, L. Spanu, G. A. Galli, and F. Gygi. Raman spectra of liquid water from ab initio molecular dynamics: Vibrational signatures of charge fluctuations in the hydrogen bond network. *J. Chem. Theory Comput.*, 9:4124–4130, 2013.

[194] M. Sharma, R. Resta, and R. Car. Intermolecular dynamical charge fluctuations in water: A signature of the h-bond network. *Phys. Rev. Lett.*, 95:187401, 2005.

[195] M. Thomas, M. Brehm, R. Fligg, P. Vlöhringer, and B. Kirchner. Computing vibrational spectra from ab initio molecular dynamics. *Phys. Chem. Chem. Phys.*, 15:6608–6622, 2013.

[196] B. Guillot. A molecular dynamics study of the infrared spectrum of water. *J. Chem. Phys.*, 95:1543–1551, 1991.

[197] A. Rahman. Correlations in the motion of atoms in liquid argon. *Phys. Rev.*, 136:A405–A411, 1964.

[198] N. Choudhury and B. M. Pettitt. Dynamics of water trapped between hydrophobic solutes. *J. Phys. Chem. B*, 109:6422–6429, 2005.

[199] J. Marti, G. Nagy, E. Guardia, and M. C. Gordillo. Molecular dynamics simulation of liquid water confined inside graphite channels: Dielectric and dynamical properties. *J. Phys. Chem. B*, 110:23897–23994, 2006.

[200] J. Martí, J. A. Padro, and E. Guàrdia. Molecular dynamics simulation of liquid water along the coexistence curve: Hydrogen bonds and vibrational spectra. *J. Chem. Phys.*, 105:639–649, 1996.

[201] G. D. Harp and B. J. Berne. Time-correlation functions, memory functions, and molecular dynamics. *Phys. Rev. A*, 2:975–996, 1970.

[202] M. Heyden, J. Sun, S. Funkner, G. Mathias, H. Forbert, M. Havenith, and D. Marx. Dissecting the thz spectrum of liquid water from first principles via correlations in time and space. *Proc. Nat. Aca. Sci.*, 107:12068–12073, 2010.

[203] M. P. Allen and D. J. Tildesley. *Computer Simulation of Liquids*. Clarendon Press, Oxford, United Kingdom, 1989.

[204] D. L. Beveridge and F. M. DiCapua. Free energy via molecular simulation: Applications to chemical and biomolecular systems. *Annu. Rev. Biophys. Biophys. Chem.*, 18:431–492, 1989.

[205] J. Kästner. Umbrella sampling. *WIREs: Comput. Mol. Sci.*, 1:932–942, 2011.

[206] R. W. Zwanzig. High-temperature equation of state by a perturbation method. i. nonpolar gases. *J. Chem. Phys.*, 22:1420–1426, 1954.

[207] P. Kollman. Free energy calculations: Applications to chemical and biochemical phenomena. *Chem. Rev.*, 93:2395–2417, 1993.

[208] J. A. Barker and D. Henderson. Perturbation theory and equation of state for fluids. ii. a successful theory of liquids. *J. Chem. Phys.*, 47:4714–4721, 1967.

[209] C. H. Bennett. Efficient estimation of free energy differences from monte carlo data. *J. Comp. Phys.*, 22:245–268, 1967.

[210] J. G. Kirkwood. Statistical mechanics of fluid mixtures. *J. Chem. Phys.*, 3:300–313, 1935.

[211] W. L. Jorgensen. Free energy calculations: A breakthrough for modeling organic chemistry in solution. *Acc. Chem. Res.*, 22:184–189, 1989.

[212] M. Orozco and F. J. Luque. Theoretical methods for the description of the solvent effect in biomolecular systems. *Chem. Rev.*, 199:4187–4225, 2000.

[213] P. A. Bash, U. C. Singh, R. Langridge, and P. Kollman. Free energy calculations by computer simulation. *Science*, 236:564–568, 1987.

[214] T. P. Straatsma and J. A. McCammon. Computational alchemy. *Annu. Rev. Phys. Chem.*, 43:407–435, 1992.

[215] M. Sprik and G. Ciccotti. Free energy from constrained molecular dynamics. *J. Chem. Phys.*, 109:7737–7744, 1998.

[216] E. A. Carter, G. Ciccotti, J. T. Hynes, and R. Kapral. Constrained reaction coordinate dynamics for the simulation of rare events. *Chem. Phys. Lett.*, 156:472–477, 1989.

[217] C. Chipot and A. Pohorille. *Free Energy Calculations: Theory and Applications in Chemistry and Biology*. Springer, Berlin, Germany, 2007.

[218] G. K. Schenter, B. C. Garrett, and D. G. Truhlar. Generalized transition state theory in terms of the potential of mean force. *J. Chem. Phys.*, 119:5828–5833, 2003.

[219] A. Fernández, J. A. Miller, S. J. Klippenstein, and D. G. Truhlar. Modeling the kinetics of bimolecular reactions. *Chem. Rev.*, 106:4518–4584, 2006.

[220] R. Elber. Calculation of the potential of mean force using molecular dynamics with linear constraints: An application to a conformational transition in a solvated dipeptide. *J. Chem. Phys.*, 93:4312–4321, 1990.

[221] K.-Y. Wong and D. M. York. Exact relation between potential of mean force and free-energy profile. *J. Chem. Theory Comput.*, 8:3998–4003, 2012.

[222] H. Flanders. Differentiation under the integral sign. *Am. Math. Monthly*, 80:615–627, 1973.

[223] G. M. Torrie GM and J. P. Valleau. Monte carlo free energy estimates using non-boltzmann sampling: Application to the sub-critical lennard-jones fluid. *Chem. Phys. Lett.*, 28:578–581, 1974.

[224] G. M. Torrie GM and J. P. Valleau. Non-physical sampling distributions in monte carlo free energy estimation: Umbrella sampling. *J. Comp. Chem.*, 23:187–199, 1977.

[225] S. Kumar, D. Bouzida, R. H. Swendsen, P. A. Kollman, and J. M. Rosenberg. The weighted histogram analysis method for free-energy calculations on biomolecules. I. The method. *J. Comp. Chem.*, 13:1011–1021, 1992.

[226] E. Darve and A. Pohorille. Calculating free energies using average force. *J. Chem. Phys.*, 115:9169–9183, 2001.

[227] E. Darve, M. A. Wilson, and A. Pohorille. Calculating free energies using a scaled-force molecular dynamics algorithm. *Mol. Simul.*, 28:113–144, 2002.

[228] D. Rodriguez-Gomez, E. Darve, and A. Pohorille. Assessing the efficiency of free energy calculation methods. *J. Chem. Phys.*, 120:3563–3578, 2004.

[229] E. Darve, D. Rodriguez-Gomez, and A. Pohorille. Adaptive biasing force method for scalar and vector free energy calculations. *J. Chem. Phys.*, 128:144120, 2008.

[230] J. G. Kirkwood and F. P. Buff. The statistical mechanical theory of surface tension. *J. Chem. Phys.*, 17:338–343, 1949.

[231] A. E. Ismail, G. S. Grest, and M. J. Stevens. Capilary waves at the liquid-vapor interface and the surface tension of water. *J. Chem. Phys.*, 125:014702, 2006.

[232] E. M. Blokhuis, D. Bedeaux, C. D. Holcomb, and J. A. Zollweg. Tail corrections to the surface-tension of a Lennard-Jones liquid-vapor interface. *Mol. Phys.*, 85:665–669, 1995.

[233] J. Alejandre, D. J. Tildesley, and G. A. Chapela. Molecular dyanmics simulation of the orthobaric densities and surface-tension of water. *J. Chem. Phys.*, 102:4574–4583, 1995.

[234] C. Vega and E. de Miguel. Surface tension of the most popular models of water by using the test-area simulation method. *J. Chem. Phys.*, 126:154707, 2007.

[235] S. W. Sides, G. S. Grest, and M.-D. Lacasse. Capillary waves at liquid-vapor interfaces: A molecular dynamics simulation. *Phys. Rev. E*, 60:6708–6713, 1999.

[236] F. P. Buff, R. A. Lovett, and Jr. F. H. Stillinger. Interfacial density profile for fluids in the critical region. *Phys. Rev. Lett.*, 15:621–623, 1965.

[237] J. S. Rowlinson and B. Widom. *Molecular Theory of Capillary*. Clarendon Press, Oxford, 1982.

[238] S. Senapati and M. L. Berkowitz. Computer simulation study of the interface width of the liquid/liquid interface. *Phys. Rev. Lett.*, 87:176101, 2001.

[239] P. S. Pershan and M. Schlossman. *Liquid Surfaces and Interfaces: Synchrotron X-ray Methods*. Cambridge University Press, Cambridge, 2012.

[240] D. B. Abraham. Capillary waves and surface tension: An exactly solvable model. *Phys. Rev. Lett.*, 47:545–548, 1981.

[241] A. Braslau, P. S. Pershan, G. Swislow, B. M. Ocko, and J. Als-Nielsen. Capillary waves on the surface of simple liquids measured by x-ray reflectivity. *Phys. Rev. A*, 38:2457–2470, 1988.

[242] M. K. Sanyal, S. K. Sinha, K. G. Huang, and B. M. Ocko. X-ray-scattering study of capillary-wave fluctuations at a liquid surface. *Phys. Rev. Lett.*, 66:628–631, 1991.

[243] B. M. Ocko, X. Z. Wu, E. B. Sirota, S. K. Sinha, and M. Deutsch. X-ray reflectivity study of thermal capillary waves on liquid surfaces. *Phys. Rev. Lett.*, 72:242–245, 1994.

[244] S. Mora, J. Daillant, K. Mecke, D. Luzet, A. Braslau, M. Alba, and B. Struth. X-ray synchrotron study of liquid-vapor interfaces at short length scales: Effect of long-range forces and bending energies. *Phys. Rev. Lett.*, 90:216101, 2003.

[245] P.S. Pershan. X-ray scattering studies of liquid surfaces. *Physica A: Stat. Mech. and its Applications*, 200:50–64, 1993.

[246] A. P. Willard and D. Chandler. Instantaneous liquid interfaces. *J. Phys. Chem. B*, 114:1954–1958, 2010.

[247] S. Ou, T. R. Lucas, Y. Zhong, B. A. Bauer, Y. Hu, and S. Patel. Free energetics and the role of water in the permeation of methyl guanidinium across the bilayer-water interface: Insights from molecular dynamics simulations using charge equilibration potentials. *J. Phys. Chem. B*, 117:3578–3592, 2013.

[248] N. A. Ahmed and D. V. Gokhale. Entropy expressions and their estimators for multivariated distributions. *IEEE Trans. Information Theory*, 35:688–692, 1989.

[249] X. Tadeo, B. López-Méndez, D. Castaño, and O. Millet. Protein stabilization and the Hofmeister effect: The role of hydrophobic solvation. *Biophy. J.*, 97:2595–2603, 2009.

[250] K. L. Foster, R. A. Plastridge, J. W. Bottenheim, P. B. Shepson, B. J. Finlayson-Pitts, and C. W. Spicer. The role of Br_2 and BrCl in surface ozone destruction at polar sunrise. *Science*, 291:471–474, 2001.

[251] K. L. Foster, M. A. Tolbert, and S. M. George. Interaction of hcl with ice: Investigation of the predicted trihydrate, hexahydrate, and monolayer regimes. *J. Phys. Chem. A*, 101:4979–4986, 1997.

[252] S. Gopalakrishnan, D. Liu, and H. C. Allen. Vibrational spectroscopic studies of aqueous interfaces: Salts, acids, bases, and nanodrops. *Chem. Rev.*, 106:1155–1175, 2006.

[253] Y. R. Shen and V. Ostroverkhov. Sum-frequency vibrational spectroscopy on water interfaces: Polar orientation of water molecules at interfaces. *Chem. Rev.*, 106:1140–1154, 2006.

[254] X. Chen, T. Yang, S. Kataoka, and P. S. Cremer. Specific ion effects on interfacial water structure near macromolecules. *J. Am. Chem. Soc.*, 129:12272–12279, 2007.

[255] X. Chen, S. C. Flores, S.-M. Lim, Y. Zhang, J. Kherb, and P. S. Cremer. Specific anion effects on water structure adjacent to protein monolayers. *Langmuir*, 26:16447–16454, 2010.

[256] B. M. Rankin, M. D. Hands, D. S. Wilcox, K. R. Fega, L. V. Slipchenko, and D. Ben-Amotz. Interactions between halid anions and a molecular hydrophobic interface. *Faraday Discuss.*, 160:255–270, 2013.

[257] D. E. Otten, P. B. Petersen, and R. J. Saykally. Observation of nitrate ions at the air/water interface by uv-second harmonic generation. *Chem. Phys. Lett.*, 449:261–265, 2007.

[258] J. Noah-Vanhoucke and P. L. Geissler. On the fluctuations that drive small ions towards and away from, interfaces between polar liquids and their vapors. *Proc. Nat. Aca. Sci.*, 106:15125–15130, 2009.

[259] J. C. Phillips, R. Braun, W. Wang, J. Gumbart, E. Tajkhorshid, E. Villa, C. Chipot, R. D. Skeel, L. Kale, and K. Schulten. Scalable molecular dynamics with namd. *J. Comp. Chem.*, 26:1781–1802, 2005.

[260] S. Nosé. A molecular dynamics methods for simulations in the canonical ensemble. *Mol. Phys.*, 52:255–268, 1984.

[261] H. J. C. Berendsen, J. R. Grigera, and T. P. Straatsma. The missing term in effective pair potentials. *J. Phys. Chem.*, 91:6269–6271, 1987.

[262] S. W. Rick, S. J. Stuart, and B. J. Berne. Dynamical fluctuating charge force fields: Application to liquid water. *J. Chem. Phys.*, 101:6141–6156, 1994.

[263] B. A. Bauer, G. L. Warren, and S. Patel. Incorporating phase-dependent polarizability in nonadditive electrostatic models for molecular dynamics simulations of the aqueous liquid-vapor interface. *J. Chem. Theory Comput.*, 5:359–373, 2009.

[264] B. A. Bauer and S. Patel. Properties of water along the liquid-vapor coexistence curve via molecular dynamics simulations using the polarizable TIP4P-QDP-LJ water model. *J. Chem. Phys.*, 131:084709, 2009.

[265] J. P. Ryckaert, G. Ciccotti, and H. J. C. Berendsen. Numerical integration of the cartesian equations of motion of a system with constraints: Molecular dynamics of *n*-alkanes. *J. Comp. Phys.*, 23:327–341, 1977.

[266] M. Fyta, I. Kalcher, J. Dzubiella, and R. R. Netz. Ionic force field optimization based on single-ion and ion-pair solvation properties. *J. Chem. Phys.*, 132:024911, 2010.

[267] M. Fyta and R. R. Netz. Ionic force field optimization based on single-ion and ion-pair solvation properties: Going beyond standard mixing rules. *J. Chem. Phys.*, 136:124103, 2012.

[268] B. A. Bauer and S. Patel. Molecular dynamics simulations of nonpolarizable salt solution interfaces: NaCl, NaBr, and NaI in transferable intermolecular potential 4-point with charge dependent polarizability TIP4P-QDP water. *J. Chem. Phys.*, 132:8107–8117, 2010.

[269] S. W. Rick, S. J. Stuart, J. S. Bader, and B. J. Berne. Fluctuating charge force fields for aqueous solutions. *J. Mol. Liq.*, 65/66:31, 1995.

[270] G. Lamoureux and B. Roux. Absolute hydration free energy scale for alkali and halide ions established from simulations with a polarizable force field. *J. Phys. Chem. B*, 110:3308–3322, 2006.

[271] G. L. Warren and S. Patel. Hydration free energies of monovalent ions in transferable intermolecular potential four point fluctuating charge water: An assessment of simulation methodology and force field performance and transferability. *J. Chem. Phys.*, 127:064509, 2007.

[272] G. L. Warren and S. Patel. Comparison of the solvation structure of polarizable and nonpolarizable ions in bulk water and near the aqueous liquid-vapor interface. *J. Phys. Chem. C*, 112:7455–7467, 2008.

[273] G. L. Warren and S. Patel. Electrostatic properties of aqueous salt solution interfaces: A comparsion of polarizable and nonpolarizable ion models. *J. Phys. Chem. B*, 112:11679–11693, 2008.

[274] C. D. Wick, A. J. Lee, and S. W. Rick. How intermolecular charge transfer influences the air-water interface. *J. Chem. Phys.*, 137:154701, 2012.

[275] A. J. Lee and S. W. Rick. The effects of charge transfer on the properties of liquid water. *J. Chem. Phys.*, 134:184507, 2011.

[276] H. Yu, T. W. Whitfield, E. Harder, G. Lamoureux, I. Vorobyov, V. M. Anisimov, A. D. MacKerell Jr., and B. Roux. Simulating monovalent and divalent ions in aqueous solution using a Drude polarizable force field. *J. Chem. Theory Comput.*, 6:774–786, 2010.

[277] S. Miyamoto and P. A. Kollman. Settle: An Analytical Version of the SHAKE and RATTLE Algorithm for Rigid Water Models. *J. Comp. Chem.*, 13(8):952–962, 1992.

[278] F. Zhu and G. Hummer. Convergence and error estimation in free energy calculations using the weighted histogram analysis method. *J. Comp. Chem.*, 33:453–465, 2012.

[279] H. Flyvbjerg and H. G. Petersen. Error estimates on averages of correlated data. *J. Chem. Phys.*, 91:461–466, 1989.

[280] G. Archontis, E. Leontidis, and G. Andreou. Attraction of iodide ions by free water surface, revealed by simulations with a polarizable force field based on Drude oscillators. *J. Phys. Chem. B*, 109:17957–17966, 2005.

[281] M. D. Baer and C. J. Mundy. Toward an understanding of the specific ion effect using density functional theory. *J. Phys. Chem. Lett.*, 2:1088–1093, 2011.

[282] G. Lamoureux and B. Roux. Modeling induced polarization with classical Drude oscillators: Theory and molecular dynamics simulation algorithm. *J. Chem. Phys.*, 119:3025–3039, 2003.

[283] A. C. Stern, M. D. Baer, C. J. Mundy, and D. J. Tobias. Thermodynamics of iodide adsorption at the instantaneous air-water interface. *J. Chem. Phys.*, 138:114709, 2013.

[284] R. Zangi and B. J. Berne. Temperature dependence of dimerization and dewetting of large-scale hydrophobes: A molecular dynamics study. *J. Phys. Chem. B*, 112:8634–8644, 2008.

[285] D. Rose and I. Benjamin. Free energy of transfer of hydrated ion clusters from water to an immiscible organic solvent. *J. Phys. Chem. B*, 113:9296–9303, 2009.

[286] J. L. England, V. S. Pande, and G. Haran. Chemical denaturants inhibit the onset of dewetting. *J. Am. Chem. Soc.*, 130:11854–11855, 2008.

[287] P. E. Mason, G. W. Neilson, J. E. Enderby, M. L. Saboungi, C. E. Dempsey, Jr. A. D. MacKerell, and J. W. Brady. The structure of aqueous guanidinum in chloride solutions. *J. Am. Chem. Soc.*, 126:11462–11470, 2004.

[288] P. E. Mason, G. W. Neilson, C. E. Dempsey, A. C. Barnes, and J. M. Cruickshank. The hydration structure of guanidinium and thiocyanate ions: Implications for protein stability in aqueous solution. *Proc. Nat. Aca. Sci.*, 100:4557–4561, 2003.

[289] J. Rösgen, B. M. Pettitt, and D. W. Bolen. An analysis of the molecular origin of osmolyte-dependent protein stability. *Protein Sci.*, 16(4):733–743, 2007.

[290] J. N. Scott, N. V. Nucci, and J. M. Vanderkooi. Changes in water stucture induced by the guanidinium cation and implications for protein denaturation. *J. Phys. Chem. A*, 112:10939–10948, 2008.

[291] G. I. Makhatadze and P. L. Privalovt. Protein interactions with urea and guanidinium chloride: A calorimetric study. *J. Mol. Bio.*, 226:491–505, 1992.

[292] F. Vanzi, B. Madan, and K. Sharp. Effect of the protein denaturants urea and guanidinium on water structure: A structural and thermodynamic study. *J. Am. Chem. Soc.*, 120:10748–10753, 1998.

[293] E. P. O'Brien, R. I. Dima, B. Brooks, and D. Thirumalai. Interactions between hydrophobic and ionic solutes in aqueous guanidinium chloride and urea solutions: Lessons for protein denaturation mechanism. *J. Am. Chem. Soc.*, 129:7346–7353, 2007.

[294] A. Kumar. Aqueous guanidinium salts part ii. isopiestic osmotic coefficients of guanidinium sulphate and viscosity and surface tension of guanidinium chloride, bromide, acetate, perchlorate and sulphate solutions at 298.15 K. *Fluid Phase Equil.*, 180:195–204, 2001.

[295] T. Koishi, K. Yasuoka, S. Y. Willow, S. Fujikawa, and X. C. Zeng. Molecular insight into different denaturing efficiency of urea, guanidinium, and methanol: A comparative simulation study. *J. Chem. Theory Comput.*, 9:2540–2551, 2013.

[296] E. Wernersson, J. Heyda, M. Vazdar, M. Lund, P. E. Mason, and P. Jungwirth. Orientational dependence of the affinity of guanidinium ions to the water surface. *J. Phys. Chem. B*, 115:12521–12526, 2011.

[297] M. C. Stumpe and H. Grubmüller. Aqueous urea solutions: Structure, energetics, and urea aggregation. *J. Phys. Chem. B*, 111:6220–6228, 2007.

[298] M. P. Allen and D. J. Tildesley. *Computer Simulations of Liquids*. Clarendon, 1987.

[299] S. Patel, A. D. MacKerell Jr., and C. L. Brooks III. CHARMM fluctuating charge force fields for proteins: II- protein/solvent properties from molecular dynamics simulations using a nonadditive electrostatic model. *J. Comp. Chem.*, 25:1504–1514, 2004.

[300] S. Nosé. A unified formulation of the constant temperature molecular dynamics methods. *J. Chem. Phys.*, 81:511–519, 1984.

[301] E. Y. Chi, S. Krishnan, T. W. Randolph, and J. F. Carpenter. Physical stability of proteins in aqueous solution: Mechanism and driving forces in nonnative protein aggregation. *Pharm. Res.*, 20:1325–1336, 2003.

[302] M. T. Record, C. F. Anderson, and T. M. Lohman. Thermodynamic analysis of ion effects on the binding and conformational equilibria of proteins and nucleic acids: the roles of ion association or release, screening, and ion effects on water activity. *Quart. Rev. Biophys.*, 11:103–178, 1978.

[303] S. N. Timasheff and T. Arakawa. Mechanism of protein precipitation and stabilization by co-solvents. *J. Cryst. Growth*, 90:1–3, 1988.

[304] P. H. Vonhippel and K. Y. Wong. Neutral salts: The generality of their effects on the stability of macromolecular conformations. *Science*, 7:577–580, 1964.

[305] X. Tadeo, M. Pons, and O. Millet. Influence of the hofmeister anions on protein stability as studied by thermal denaturation and chemical shift perturbation. *Biochem.*, 46:917–923, 2007.

[306] K. D. Collins and M. W. Washabaugh. The Hofmeister effect and the behavior of water at interfaces. *Q. Rev. Biophys.*, 18:323–422, 1985.

[307] S. N. Timasheff. Protein solvent preferential interactions, protein hydration, and the modulation of biochemical reactions by solvent components. *Proc. Nat. Aca. Sci.*, 99:9721–9726, 2002.

[308] P. Nandi and D. Robinson. Effects of salts on the free energy of the peptide group. *J. Am. Chem. Soc.*, 94:1299–1308, 1972.

[309] R. Schweiss, P. B. Welzel, C. Werner, and W. Knoll. Dissociation of surface functional groups and preferential adsorption of ions on self-assembled monolayers assessed by streaming potential and streaming current measurements. *Langmuir*, 17:4304–4311, 2001.

[310] D. Horinek and R. R. Netz. Specific ion adsorption at hydrophobic solid surfaces. *Phys. Rev. Lett.*, 99:226104, 2007.

[311] D. Horinek, A. Serr, D. J. Bonthuis, M. Bostrom, W. Kunz, and R. R. Netz. Molecular hydrophobic attraction and ion-specific effects studied by molecular dynamics. *Langmuir*, 24:1271–1283, 2008.

[312] M. Lund, R. Vacha, and P. Jungwirth. Specific ion binding to macromolecules: Effects of hydrophobicity and ion pairing. *Langmuir*, 24:3387–3391, 2008.

[313] M. Lund, L. Vrbka, and P. Jungwirth. Specific ion binding to nonpolar surface patches of proteins. *J. Am. Chem. Soc.*, 130:11582, 2008.

[314] R. Friedman, E. Nachliel, and M. Gutman. Molecular dynamics of a protein surface: Ion-residues interactions. *Biophy. J.*, 89:768–781, 2005.

[315] R. Friedman. Ions and the protein surface revisited: Extensive molecular dynamics simulations and analysis of protein structures in alkali-chloride solutions. *J. Phys. Chem. B*, 115:9213–9223, 2011.

[316] J. Wang, D. Bratko, and A. Luzar. Probing surface tension additivity on chemically heterogeneous surfaces by a molecular approach. *Proc. Nat. Aca. Sci.*, 108:6374–6379, 2011.

[317] A. J. Patel, P. Varilly, S. N. Jamadagni, M. F. Hagan, D. Chandler, and S. Garde. Sitting at the edge: How biomolecules use hydrophobicity to tune their interactions and function. *J. Phys. Chem. B*, 116:2498–2503, 2012.

[318] N. Giovambattista, P. Debenedetti, and P. Rossky. Hydration behavior under confinement by nanoscale surfaces with patterned hydrophobicity and hydrophilicity. *J. Phys. Chem. C*, 111:1323–1332, 2007.

[319] A. Willard and D. Chandler. Coarse-grained modeling of the interface between water and heterogeneous surfaces. *Faraday Discuss.*, 141:209–220, 2009.

[320] K. B. Rembert, J. Paterova, J. Heyda, C. Hilty, P. Jungwirth, and P. S. Cremer. Molecular mechanisms of ion-specific effects on proteins. *J. Am. Chem. Soc.*, 134:10039–10046, 2012.

[321] M. Lund, P. Jungwirth, and C. E. Woodward. Ion specific protein assembly and hydrophobic surface forces. *Phys. Rev. Lett.*, 100:258105, 2008.

[322] A. J. Patel, P. Varilly, S. N. Jamadagni, H. Acharya, S. Garde, and D. Chandler. Extended surfaces modulate hydrophobic interactions of neighboring solutes. *Proc. Nat. Aca. Sci.*, 108:17678–17683, 2011.

[323] H. Acharya, S. Vembanur, S. N. Jamadagni, and S. Garde. Mapping hydrophobicity at the nanoscale: Applications to heterogeneous surfaces and proteins. *Faraday Discuss.*, 146:353–365, 2010.

[324] A. J. Patel, P. Varilly, and D. Chandler. Fluctuations of water near extended hydrophobic and hydrophilic surfaces. *J. Phys. Chem. B*, 114:1632–1637, 2010.

[325] N. Giovambattista, C. F. Lopez, P. J. Rossky, and P. G. Debenedetti. Hydrophobicity of protein surfaces: Separating geometry from chemistry. *Proc. Nat. Aca. Sci.*, 105:2274–2279, 2008.

[326] D. Bratko, R. A. Curtis, H. W. Blanch, and J. M. Prausnitz. Interaction between hydrophobic surfaces with metastable intervening liquid. *J. Chem. Phys.*, 115:3873–3877, 2001.

[327] M. B. Linder. Hydrophobins: Proteins that self assemble at interfaces. *Curr. Opin. Colloid Inter. Sci.*, 14:356–363, 2009.

[328] N. A. Alexandrov, K. G. Marinova, T. D. Gurkov, K. D. Danov, P. A. Kralchevsky, S. D. Stoyanov, T. B. J. Blijdenstein, L. N. Arnaudov, E. G. Pelanb, and A. Lips. Interfacial layers from the protein HFBII hydrophobin: Dynamic surface tension, dilatational elasticity and relaxation times. *J. Colloid Inter. Sci.*, 376:296–306, 2012.

[329] J. Hakanpää, A. Paananen, S. Askolin, T. Nakari-Setala, T. Parkkinen, M. Penttila, M. B. Linder, and J. Rouvinen. Atomic resolution structure of the HFBII hydrophobin, a self-assembling amphiphile. *J. Bio. Chem.*, 279:534–539, 2004.

[330] A. D. MacKerell Jr., D. Bashford, M. Bellot, R. L. Dunbrack Jr., J. D. Evanseck, M. J. Field, S. Fischer, J. Gao, H. Gao, S. Ha, D. Joseph-McCarthy, L. Kuchnir, K. Kuczera, F. T. K. Lau, C. Mattos, S. Michnick, T. Ngo, D.T. Nguyen, B. Prodhom, W. E. Reiher III, B. Roux, M. Schlenkrich, J. C. Smith, R. Stote, J. Straub, M. Watanabe, J. Wiorkiewicz-Kuczera, D. Yin, and M. Karplus. All-atom empirical potential for molecular modeling and dynamics studies of proteins. *J. Phys. Chem. B*, 102:3586–3616, 1998.

[331] W. L. Jorgensen and C. Jenson. Temperature dependence of TIP3P, SPC, and TIP4P water from NPT Monte Carlo simulations: Seeking temperatures of maximum density. *J. Comp. Chem.*, 19:1179–1186, 1998.

[332] I. S. Joung and T. E. Cheatham III. Determination of alkali and halide monovalent ion parameters for use in explicitly solvated biomolecular simulations. *J. Phys. Chem. B*, 112:9020–9041, 2008.

[333] W. D. Cornell, P. Cieplak, C. I. Bayly, I. R. Gould, K. M. Merz Jr., D. M. Ferguson, D. C. Spellmeyer, T. Fox, J. W. Caldwell, and P. A. Kollman. A second generation force field for the simulation of proteins, nucleic acids, and organic molecules. *J. Am. Chem. Soc.*, 117:5179–5197, 1995.

[334] L. Kale, R. Skeel, M. Bhandarkar, R. Brunner, A. Gursoy, N. Krawetz, J. Phillips, A. Shinozaki, K. Varadarajan, and K. Schulten. Namd2: Greater scalability for parallel molecular dynamics. *J. Comp. Phys.*, 151:283–312, 1999.

[335] A. D. MacKerell, Jr. Empirical force fields for biological macromolecules: Overviews and issues. *J. Comp. Chem.*, 25:1584–1604, 2004.

[336] R. Kumar, V. Iyer, and W. Im. CHARMM-GUI: A graphical user interface for the CHARMM users. *J. Comp. Chem.*, 29:1859–1865, 2007.

[337] J. Hakanpää, M. B. Linder, A. Popov, A. Schmidt, and J. Rouvinen. Hydrophobin HFBII in detail: Ultrahigh-resolution structure at 0.75 Å. *Acta. Cryst.*, 62:356–367, 2006.

[338] M. B. Linder, G. R. Szilvay, T. Nakari-Setälä, and M. E. Penttilä. Hydrophobins: the protein-amphiphiles of filamentous fungi. *FEMS Microbio. Rev.*, 29:877–896, 2005.

[339] J. M. Kallio, M. B. Linder, and J. Rouvinen. Crystal structures of hydrophobin HFBII in the presence of detergent implicate the formation of fibrils and monolayer films. *J. Bio. Chem.*, 282:28733–28739, 2007.

[340] R. Godawat, S. N. Jamadagni, and S. Garde. Unfolding of hydrophobic polymers in guanidinium chloride solutions. *J. Phys. Chem. B*, 114:2246–2254, 2010.

[341] R. Godawat, S. N. Jamadagni, and S. Garde. Characterizing hydrophobicity of interfaces by using cavity formation, solute binding, and water correlations. *Proc. Nat. Aca. Sci.*, 106:15119–15124, 2009.

[342] M. Vazdar, F. Uhlig, and P. Jungwirth. Like-charge ion pairing in water: An Ab initio molecular dynamics study of aqueous guanidinium cations. *J. Phys. Chem. Lett.*, 3:2021–2024, 2012.

[343] J. L. England and G. Haran. Role of solvation effects in protein denaturation: From thermodynamics to single molecules and back. *Annu. Rev. Phys. Chem.*, 62:257–27, 2011.

[344] A. Kubickova, T. Krizek, P. Coufal, E. Wernersson, J. Heyda, and P. Jungwirth. Guanidinium cations pair with positively charged arginine side chains in water. *J. Phys. Chem. Lett.*, 2:1387–1389, 2011.

[345] D. Canchi, D. Paschek, and A. García. Equilibrium study of protein denaturation by urea. *J. Am. Chem. Soc.*, 132:2338–2344, 2010.

[346] R. Zangi. Driving force for hydrophobic interaction at different length scales. *J. Phys. Chem. B*, 115:2303–2311, 2011.

[347] Z. Xu, X. Yang, and Z. Yang. A molecular simulation probing of structure and interaction for supramolecular sodium dodecyl sulfate/single-wall carbon nanotube assemblies. *Nano Lett.*, 10:985–991, 2010.

[348] P. Angelikopoulos and H. Beck. The nanoscale cinderella problem: Design of surfactant coatings for carbon nanotubes. *J. Phys. Chem. Lett.*, 2:139–144, 2011.

[349] R. Zangi and B. J. Berne. Aggregation and dispersion of small hydrophobic particles in aqueous electrolyte solutions. *J. Phys. Chem. B*, 110:22736–22741, 2006.

[350] D. T. Bowron and J. L. Finney. Structure of a salt-amphiphile-water solution and the mechanism of salting out. *J. Chem. Phys.*, 118:8357–8372, 2003.

[351] F. Palombo, M. Paolantoni, P. Sassi, A. Morresi, and R. S. Cataliotti. Spectroscopic studies of the free oh stretching bands in liquid alcohols. *J. Mol. Liq.*, 125:139–146, 2006.

[352] D. Chandler. Interfaces and the driving forces of hydrophobic assembly. *Nature*, 437:640–647, 2005.

[353] F. H. Stillinger. Structure in aqueous solutions of nonpolar solutes from the standpoint of scaled-particle theory. *J. Solut. Chem.*, 2:141–158, 1973.

[354] K. Lum, D. Chandler, and J. D. Weeks. Hydrophobicity at small and large length scales. *J. Phys. Chem. B*, 103:4570–4577, 1999.

[355] D. M. Huang and D. Chandler. Temperature and length scale dependence of hydrophobic effects and their possible implications for protein folding. *Proc. Nat. Aca. Sci.*, 97:8324–8327, 2000.

[356] T. D. Nguyen, C. L. Phillips, J. A. Anderson, and S. C. Glotzer. Rigid body constraints realized in massively-parallel molecular dynamics on graphics processing units. *Comp. Phys. Commun.*, 182:2307, 2011.

[357] C. L. Phillips, J. A. Anderson, and S. C. Glotzer. Pseudo-random number generation for brownian dynamics and dissipative particle dynamics simulations on gpu devices. *J. Comp. Phys.*, 230:7191, 2011.

[358] J. A. Anderson, C. D. Lorenz, and A. Travesset. General purpose molecular dynamics simulations fully implemented on graphics processing units. *J. Comp. Phys.*, 227:5342–5359, 2008.

[359] C. L. Phillips, J. A. Anderson, G. Huber, and S. C. Glotzer. Optimal filling of shapes. *Phys. Rev. Lett.*, 108:198304, 2012.

[360] J. A. Anderson and S. C. Glotzer. The development and expansion of hoomd-blue through six years of gpu proliferation. *arXiv:1308.5587*, 2013.

[361] I. S. Haque and V. S. Pande. Paper-accelerating parallel evaluations of rocs. *J. Comp. Chem.*, 31:117–132, 2009.

[362] J. E. Stone, K. L. Vandivort, and K. Schulten. Gpu-accelerated molecular visualization on petascale supercomputing platforms. In *Proceedings of the 8th International Workshop on Ultrascale Visualization*, UltraVis '13, pages 6:1–6:8, New York, NY, USA, 2013. ACM.

[363] E. Roberts, J. E. Stone, and Z. Luthey-Schulten. Lattice microbes: High-performance stochastic simulation method for the reaction-diffusion master equation. *J. Comp. Chem.*, 34:245–255, 2013.

[364] JCrystalSoft. *http://jcrystal.com/products/wincnt/index.htm*, 2011.

[365] M. S. Dresselhaus, G. Dresselhaus, and P. C. Eklund. *Science of Fullerenes and Carbon Nanotubes*. Academic Press, San Diego, CA, 1995.

[366] C. Sendner, D. Horinek, L. Bocquet, and R. R. Netz. Interfacial water at hydrophobic and hydrophilic surfaces: Slip, viscosity, and diffusion. *Langmuir*, 25:10768–10781, 2009.

[367] C. Eun and M. L. Berkowitz. Origin of the hydration force: Water-mediated interaction between two hydrophilic plates. *J. Phys. Chem. B*, 113:13222–13228, 2009.

[368] B. A. Bauer, J. E. Davis, M. Taufer, and S. Patel. Molecular dynamics simulation of aqueous ions at the liquid-vapor interface accelerated using graphics processors. *J. Comp. Chem.*, 32:375–385, 2011.

[369] N. Ganesan, B. A. Bauer, T. R. Lucas, S. Patel, and M. Taufer. Structural, dynamic, and electrostatic properties of fully hydrated dmpc bilayers from molecular dynamics simulations accelerated with graphical processing units (gpus). *J. Comp. Chem.*, 32:2958–2973, 2011.

[370] N. Ottosson, J. Heyda, E. Wernersson, W. Pokapanich, S. Svensson, B. Winter, G. Öhrwall, P. Jungwirth, and O. Björneholm. The influence of concentration on the molecular surface structure of simple and mixed aquesou electrolytes. *Phys. Chem. Chem. Phys.*, 12:10693–10700, 2010.

[371] H.B. Saleh, L. D. Pfefferle, and M. Elimelech. Influcnece of bioacromolecules and humic acid on the aggregation kinetics of single-walled carbon nanobutes. *Environ. Sci. Technol.*, 44:2412–2418, 2010.

[372] B. Derjaguin and L. Landau. Theory of the stability of strongly charged lyophobic sols and of the adhesion of strongly charged particles in solutions of electrolytes. *Acta Physico Chemica URSS*, 14:633, 1941.

[373] E. J. W. Verwey and J. Th. G. Overbeek. *Theory of the Stability of Lyophobic Colloids*. Elsevier, Amsterdam, 1948.

[374] C. M. Baker, P. E. M. Lopes, X. Zhu, B. Roux, and A. D. MacKerell Jr. Accurate calculation of hydration free energies using pair-specific Lennard-Jones parameters in the CHARMM Drude polarizable force field. *J. Chem. Theory Comput.*, 6:1181–1198, 2010.

[375] SaltInstitute. *http://www.saltinstitute.org/*, 2011.

[376] L. Li, D. Bedrov, and G. D. Smith. Water-induced interactions between carbon nanoparticles. *J. Phys. Chem. B*, 110:10509–10513, 2006.

[377] L. Li, D. Bedrov, and G. D. Smith. A molecular-dynamics simulation study of solvent-induced repulsion between c60 fullerenes in water. *J. Chem. Phys.*, 123:204504, 2005.

[378] N. Choudhury and B. M. Pettitt. Enthalpy-entropy contributions to the potential of mean force of nanoscopic hydrophobic solutes. *J. Phys. Chem. B*, 110:8459–8463, 2006.

[379] M. V. Athawale, S. Sarupria, and S. Garde. Enthalpy-entropy contributions to salt and osmolyte effects on molecular-scale hydrophobic hydration and interactions. *J. Phys. Chem. B*, 112:5661–5670, 2008.

[380] R. L. Mancera and A. D. Buckingham. Further evidence for a temperature-dependent hydrophobic interaction: the aggregation of ethane in aqueous solutions. *Chem. Phys. Lett.*, 234:296–303, 1995.

[381] S. Shimizu and H. S. Chan. Configuration-dependent heat capacity of pairwise hydrophobic interactions. *J. Am. Chem. Soc.*, 123:2083–2084, 2001.

[382] N. V. Prabhu and K. A. Sharp. Heat capacity in proteins. *Annu. Rev. Phys. Chem.*, 56:521–48, 2005.

[383] A. D. Robertson and K. P. Murphy. Protein structure and the energetics of protein stability. *Chem. Rev.*, 97:1251–1267, 1997.

[384] S. Lüdemann, R. Abseher, H. Schreiber, and O. Steinhauser. The temperature-dependence of hydrophobic association in water. pair versus bulk hydrophobic interactions. *J. Chem. Phys.*, 119:4206–4213, 1997.

[385] A. Kuffel and J. Zielkiewicz. Why the solvation water around proteins is more dense than bulk water. *J. Phys. Chem. B*, 116:12113–12124, 2012.

[386] J. G. Davis, K. P. Gierszal, P. Wang, and D. Ben-Amotz. Water structural transformation at molecular hydrophobic interfaces. *Nature Lett.*, 491:582–585, 2012.

[387] J. L. Li, R. Car, C. Tang, and N. S. Wingreen. Hydrophobic interaction and hydrogen-bond network for a methane pair in liquid water. *Proc. Nat. Aca. Sci.*, 104:2626–2630, 2007.

[388] N. Giovambattista, P. J. Rossky, and P. G. Debenedetti. Effect of temperature on the structure and phase behavior of water confined by hydrophobic, hydrophilic, and heterogeneous surfaces. *J. Phys. Chem. B*, 113:13723–13734, 2009.

[389] M. S. Date and B. N. Dominy. Modeling the influence of salt on the hydrophobic effect and protein fold stability. *Commun. Comp. Phys.*, 13:90–106, 2013.

[390] P. Kumar, S. V. Buldyrev, F. W. Starr, N. Giovambattista, and H. E. Stanley. Thermodynamics, structure, and dynamics of water confined between hydrophobic plates. *Phys. Rev. E*, 72:051503, 2005.

[391] H. Mosaddeghi, S. Alavi, M. H. Kowsari, and B. Najafi. Simulations of structural and dynamic anisotropy in nano-confined water between parallel graphite plates. *J. Chem. Phys.*, 137:184703, 2012.

[392] D. Corradini, M. Rovere, and P. Gallo. Structural properties of high and low density water in a supercooled aqueous solution of salt. *J. Phys. Chem. B*, 115:1461–1468, 2011.

[393] N. Giovambattista, P. J. Rossky, and P. G. Debenedetti. Effect of pressure on the phase behavior and structure of water confined between nanoscale hydrophobic and hydrophilic plates. *Phys. Rev. E*, 73:041604, 2006.

[394] C. D. Wick, T. M. Chang, J. A. Slocum, and O. T. Cummings. Computational investigation of the n-alkane/water interface with many-body potentials: The effect of chain length and ion distributions. *J. Phys. Chem. C*, 116:783–790, 2012.

[395] C. L. McFearin and G. L. Richmond. The role of interfacial molecular structure in the adsorption of ions at the liquid-liquid interface. *J. Phys. Chem. C*, 113:21162–21168, 2009.

[396] F. Rodríguez-Ropero and M. Fioroni. Effect of na^{+}, mg^{2+}, and zn^{2+} chlorides on the structural and thermodynamic properties of water/n-heptane interfaces. *J. Comp. Chem.*, 32:1876–1886, 2011.

[397] M. Brown, D. S. Walker, E. A. Raymond, and G. L. Richmond. Vibrational sum-frequency spectroscopy of alkane/water interfaces: Experiment and theoretical simulation. *J. Phys. Chem. B*, 107:237–244, 2003.

[398] C. D. Wick and L. X. Dang. Molecular dynamics study of ion transfer and distribution at the interface of water and 1,2-dichlorethane. *J. Phys. Chem. C*, 112:647–649, 2008.

[399] C. D. Wick and L. X. Dang. Molecular mechanism of transporting a polarizable iodide anion across the water- ccl_4 liquid/liquid interface. *J. Chem. Phys.*, 126:134702, 2007.

[400] F. Hauxwell, N. R. Pallas, and B. A. Pethica. Adsorption of n-alkane vapors on water. *Langmuir*, 8:602–603, 1992.

[401] A. Ghoufi and P. Malfreyt. Numerical evidence of the formation of a thin microscopic film of methane at the water surface: a free energy calculation. *Phys. Chem. Chem. Phys.*, 12:5203–5205, 2010.

[402] F. Biscay, A. Ghoufi, and P. Malfreyt. Adsorption of n-alkane vapours at the water surface. *Phys. Chem. Chem. Phys.*, 13:11308–11316, 2011.

[403] C. P. Kelly, C. J. Cramer, and D. G. Truhlar. Predicting adsorption coefficients at air-water interfaces using universal solvation and surface area models. *J. Phys. Chem. B*, 108:12882–12897, 2004.

[404] F. Hauxwell R. H. Ottewill. A study of the surface of water by hydrocarbon adsorption. *J. Colloid Inter. Sci.*, 34:473–479, 1970.

[405] A. Javadi, N. Moradi, H. Möhwald, and R. Miller. Adsorption of alkanes from the vapour phase on water drops measured by drop profile analysis tensiometry. *Soft Matt.*, 6:4710–4714, 2010.

[406] S. Zeppieri, J. Rodróguez, and A. L. López de Ramos. Interfacial tension of alkane + water systems. *J. Chem. Eng. Data*, 46:1086–1088, 2001.

[407] X. Chen, L. B. Sagle, and P. S. Cremer. Urea orientation at protein surfaces. *J. Am. Chem. Soc.*, 129:4948–4949, 2007.

[408] M. E. Lee and N. F. A. van der Vegt. Does urea denature hydrophobic interactions? *J. Am. Chem. Soc.*, 128:4948–4949, 2006.

[409] J. Almarza, L. Rincon, A. Bahsas, and F. Brito. Molecular mechanism for the denaturation of proteins by urea. *Biochem.*, 48:7608–7613, 2009.

[410] N. Shukla, A. N. Bhatt, A. Aliverti, G. Zanetti, and V. Bhakuni. Guanidinium chloride- and urea-induced unfolding of fpra, a mycobacterium nadph-ferredoxin reductase: stabilization of an apo-protein by gdmcl. *FEBS J.*, 272:2216–2224, 2005.

[411] W. K. Lim, J. Rösgen, and S. W. Englander. Urea, but not guanidinium, destabilizes proteins by forming hydrogen bonds to the peptide group. *Proc. Nat. Aca. Sci.*, 106:2595–2600, 2009.

[412] N. J. English and J. M. D. Macelroy. Structural and dynamical properties of methane clathrate hydrates. *J. Comp. Chem.*, 24:1569–1581, 2003.

[413] H. Jiang, K. D. Jordan, and C. E. Taylor. Molecular dynamics simulations of methane hydrate using polarizable force fields. *J. Phys. Chem. B*, 111:6486–6492, 2007.

[414] A. Ben-Naim. Statistical thermodynamics for chemists and biochemists. *Plenum*, New York, 1992.

[415] P .G. Kusalik and G. N. Patey. The thermodynamic properties of electrolyte-solutions - some formal results. *J. Chem. Phys.*, 86:5110–5116, 1987.

[416] Y. Zhong and S. Patel. Non-additive empirical force fields for short-chain linear alcohols: Methanol to butanol. hydration free energetics and kirkwood-buff analysis using charge equilibration models. *J. Comp. Chem.*, 114:11076–11092, 2010.

Appendix A

FORCE FIELD VALIDATION FOR GUANIDINIUM CHLORIDE SOLUTION: KIRKWOOD-BUFF ANALYSIS

To test the force field in this study, bulk simulations were performed with a larger NPT system (no L-V interfaces). The simulation system contained 76 Gdm^+ or M-Gdm^+ ions and the same number of Cl^- ions along with 3954 water molecules per unit cell to generate 1.1 m environment. For 5.3 m concentration, the number of water molecules remained the same but the number of ion pairs changed to 380. Periodic boundary conditions were applied in all directions with isothermal - isobaric ensemble (NPT) simulations in a cubic box. The temperature was maintained at T = 300K by using a Nose-Hoover thermostat [260]. To probe the structure of the GdmCl and M-GdmCl solution, radial distribution functions (RDF) were obtained for the selected atoms shown in Figure A.1. In 1.1 m GdmCl solution, the first peaks for water oxygen, Cl^- and Gdm^+ center carbon are around 3.8 Å, 4.3 Å and 7.8 Å, respectively. These are in agreement with RDFs from the case of same concentration GdmCl solution simulated with the "Kirkwood-Buff force field" (KBFF) reported by Wernersson [296]. Compared the water oxygen RDFs for GdmCl solution obtained at lower concentration (a) and higher concentration (b), the locations of the first peak are the same but the magnitude is different. This may be due to the stronger hydrogen bonding environment with increasing concentration of GdmCl solutes. The slightly lower first peak of the water oxygen in M-GdmCl solution compared with that of the same concentration GdmCl solution is an indication of less interactions between the solute-solvent.

RDFs between water oxygen atoms and nitrogen atoms in the solute are also taken into consideration here. For a Gdm^+ ion, the three nitrogen atoms are identical,

so they have the same RDFs shown in Figure A.2 a and b. Notice that for clarity, each RDF is shifted with a vertical offset of 0.5. For the M-GdmCl, from the molecular structure, one nitrogen is quite different from the other two which corresponds to the blue lines of panel c and d. Interestingly, the two nitrogens that attached two hydrogens have slightly different RDFs as shown in red and green lines respectively in panel c and d, which may be due to the fact that the existence of the methyl group nearby will influence the environment of the two NH_2 nitrogen atoms. Further check of the distances of the two nitrogens with the carbon atom of the methyl group shows that one of them is closer to the carbon atom than another. Time profiles of the distances further show that the two nitrogen do not flip around the torsion, so the M-Gdm^+ ions are quite rigid during the simulation.

Kirkwood-Buff (K-B) theory has been widely used to analyze the macroscopic thermodynamic properties of solutions. Usually, it is expressed in terms of the K-B integrals between the different solution components as defined by Equation A.1 that was first developed in 1951 [230]. The K-B integrals is sensitive to small deviations from a bulk-like distribution due to the r^2 weighting factor arising from the volume element Jacobian. Here g_{ij} is the RDF between species i and j. To apply the K-B theory on simulation, we use the approximate Equation A.2. In a two-component system, which is made with water and solute, we are able to determine the solution properties including activity derivatives by using the computed K-B integrals shown in Equation A.3, Equation A.4 and Equation A.5 [414]. G_{ww}, G_{ss} and G_{sw} are the K-B integrals defined between water-water, solute-solute and solute-water respectively; ρ_{w} and ρ_{s} are the number densities; $\overline{V}_{\mathrm{w}}$ and $\overline{V}_{\mathrm{s}}$ are the partial molar volumes; a_{ss} is the solute activity. In a salt solution, as a consequence of the electro-neutrality condition, one can only treat the salt solutions as a binary system of indistinguishable ions and water [415]. So for the RDF g_{ss}, the cations and anions are treated equivalent; for the Gdm^+ cation, the position was based on the central carbon. The final K-B integrals are calculated by averaging values between 20 and 25 Å.

$$G_{ij} = 4\pi \int_0^\infty [{g_{ij}}^{\mu VT}(r) - 1] r^2 dr \tag{A.1}$$

$$G_{ij} = 4\pi \int_0^\infty [{g_{ij}}^{\mu VT}(r) - 1] r^2 dr \approx 4\pi \int_0^R [{g_{ij}}^{NPT}(r) - 1] r^2 dr \tag{A.2}$$

$$\begin{aligned} \overline{V}_{\mathrm{w}} &= \frac{1 + \rho_{\mathrm{s}}(G_{\mathrm{ss}} - G_{\mathrm{sw}})}{\eta} \\ \overline{V}_{\mathrm{s}} &= \frac{1 + \rho_{\mathrm{w}}(G_{\mathrm{ww}} - G_{\mathrm{sw}})}{\eta} \end{aligned} \tag{A.3}$$

$$\eta = \rho_{\mathrm{w}} + \rho_{\mathrm{s}} + \rho_{\mathrm{w}}\rho_{\mathrm{s}}(G_{\mathrm{ww}} + G_{\mathrm{ss}} - 2G_{\mathrm{sw}}) \tag{A.4}$$

$$a_{\mathrm{ss}} = \left(\frac{\partial \ln a_{\mathrm{s}}}{\partial \ln \rho_{\mathrm{s}}} \right)_{\mathrm{p,T}} = \frac{1}{1 + \rho_{\mathrm{s}}(G_{\mathrm{ss}} - G_{\mathrm{sw}})} \tag{A.5}$$

For the 1.1 m solution, we obtain 1.34 for the activity derivative, which is higher than for previously reported force fields and experiment (all falling in the range of 0.7 to 0.8). The 5.3m value is substantially larger than previously reported, though the trend of increasing activity derivative with concentration is captured. We emphasize that though previous force fields are able to recapitulate more closely the activity derivatives, there is no direct connection to the ability to accurately predict bulk thermodynamic solution properties such as hydration free energies of the salt when activity derivatives are accurately reproduced [416]. This represents work in progress and for further development. We note that the conclusions of interfacial stability and underlying fluctuations are robust with respect to different force fields.

Concentration	G_{ss} (cm^3/mol)	G_{sw} (cm^3/mol)	activity derivative
1.1 m GdmCl	-322	-99	1.344
5.3 m GdmCl	-344	-73	3.185

Table A.1: Coefficient activities at various concentrations. Reproduced with permission from Shuching Ou, Di Cui and Sandeep Patel. "Liquid-Vapor Interfacial Properties of Aqueous Solutions of Guanidinium and Methyl Guanidinium Chloride: Influence of Molecular Orientation on Interface Fluctuations." *Journal of Physical Chemistry B.* **2013**, *117 (39)*, 11719-11731. Copyright 2013 American Chemical Society.

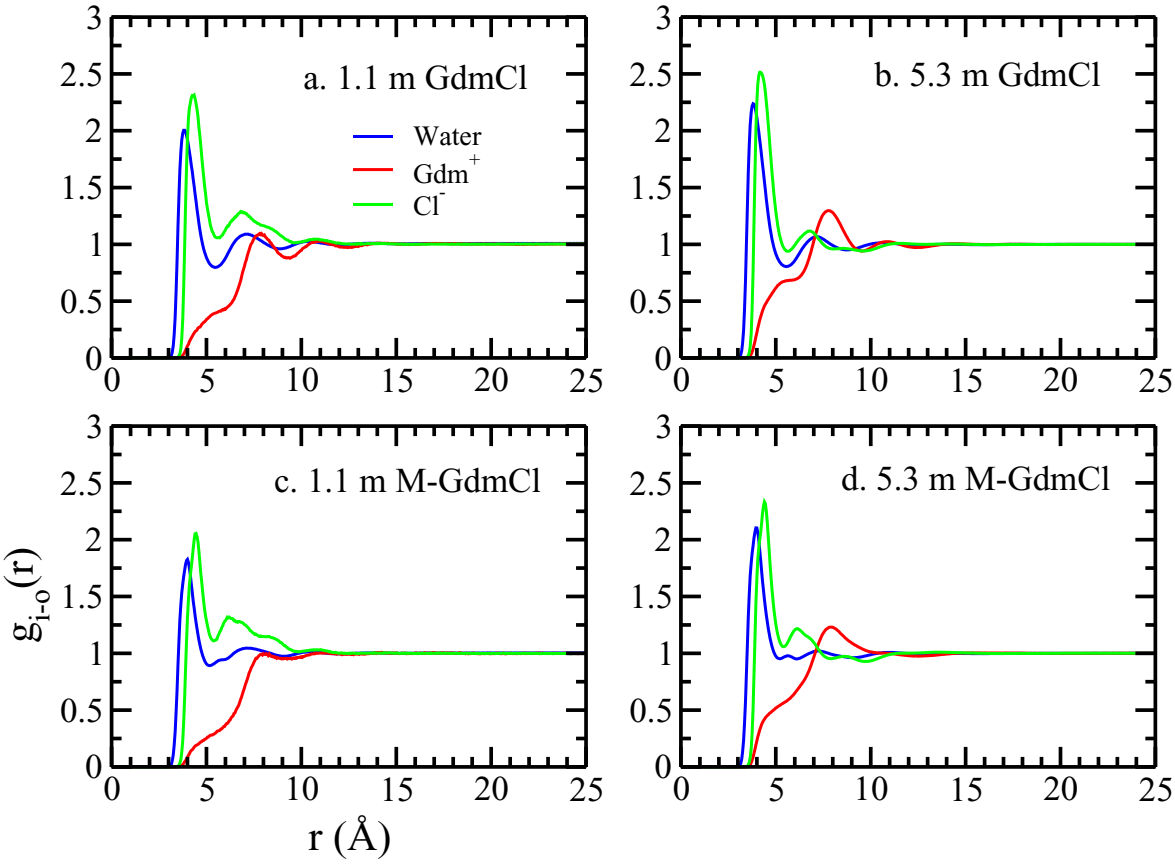

Figure A.1: RDF of the solute/solvent with water oxygen, for (a) 1.1 m GdmCl (b) 5.3 m GdmCl (c) 1.1 m M-GdmCl (d) 5.3 m M-GdmCl. For Gdm^+/M-Gdm^+, center carbon of the cation was chosen as the site for RDF calculation. Reproduced with permission from Shuching Ou, Di Cui and Sandeep Patel. "Liquid-Vapor Interfacial Properties of Aqueous Solutions of Guanidinium and Methyl Guanidinium Chloride: Influence of Molecular Orientation on Interface Fluctuations." *Journal of Physical Chemistry B.* **2013**, *117 (39)*, 11719-11731. Copyright 2013 American Chemical Society.

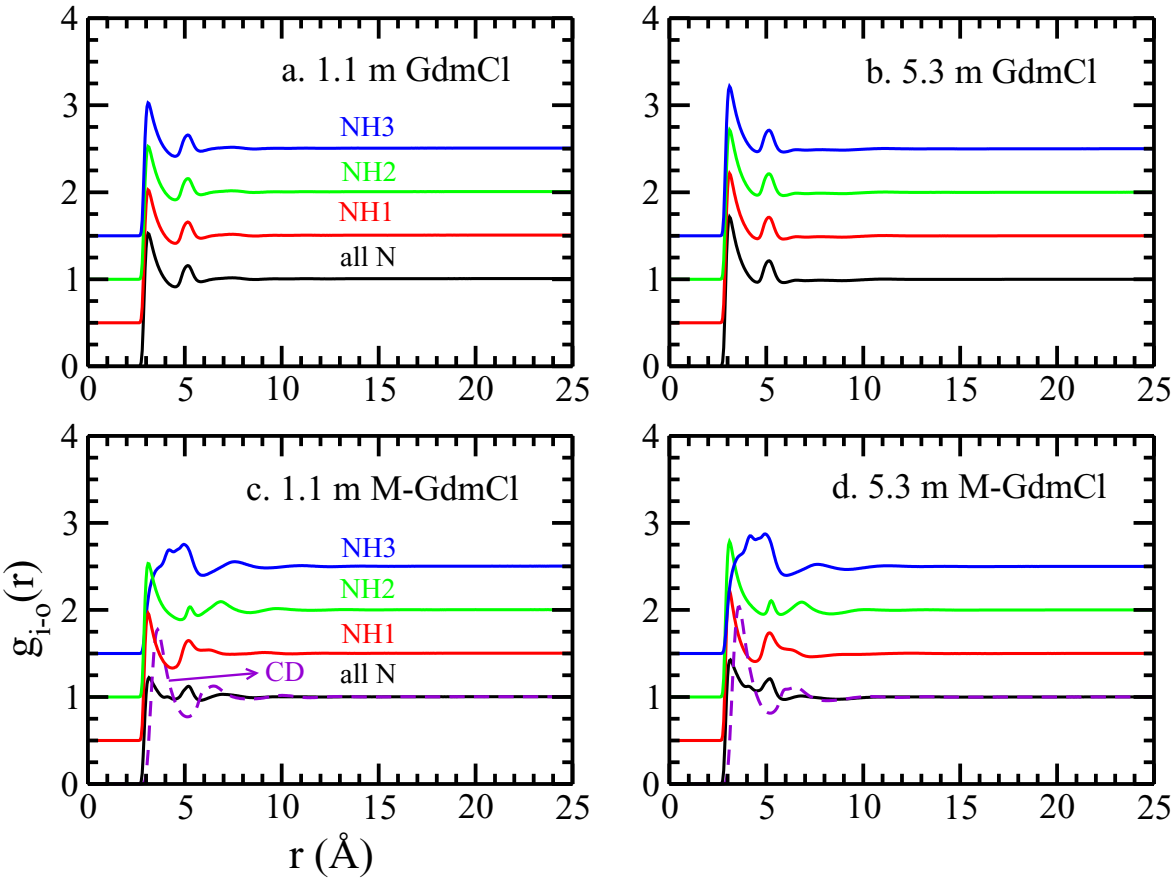

Figure A.2: RDFs between water oxygen atoms and solute nitrogen atoms in (a) 1.1 m GdmCl solution (b) 5.3 m GdmCl solution (c) 1.1 m M-GdmCl solution (d) 5.3 m M-GdmCl solution. In (c) and (d), the RDFs between water oxygen atoms and carbon atom from the methyl group are shown as purple dashed lines. Reproduced with permission from Shuching Ou, Di Cui and Sandeep Patel. "Liquid-Vapor Interfacial Properties of Aqueous Solutions of Guanidinium and Methyl Guanidinium Chloride: Influence of Molecular Orientation on Interface Fluctuations." *Journal of Physical Chemistry B.* **2013**, *117 (39)*, 11719-11731. Copyright 2013 American Chemical Society.

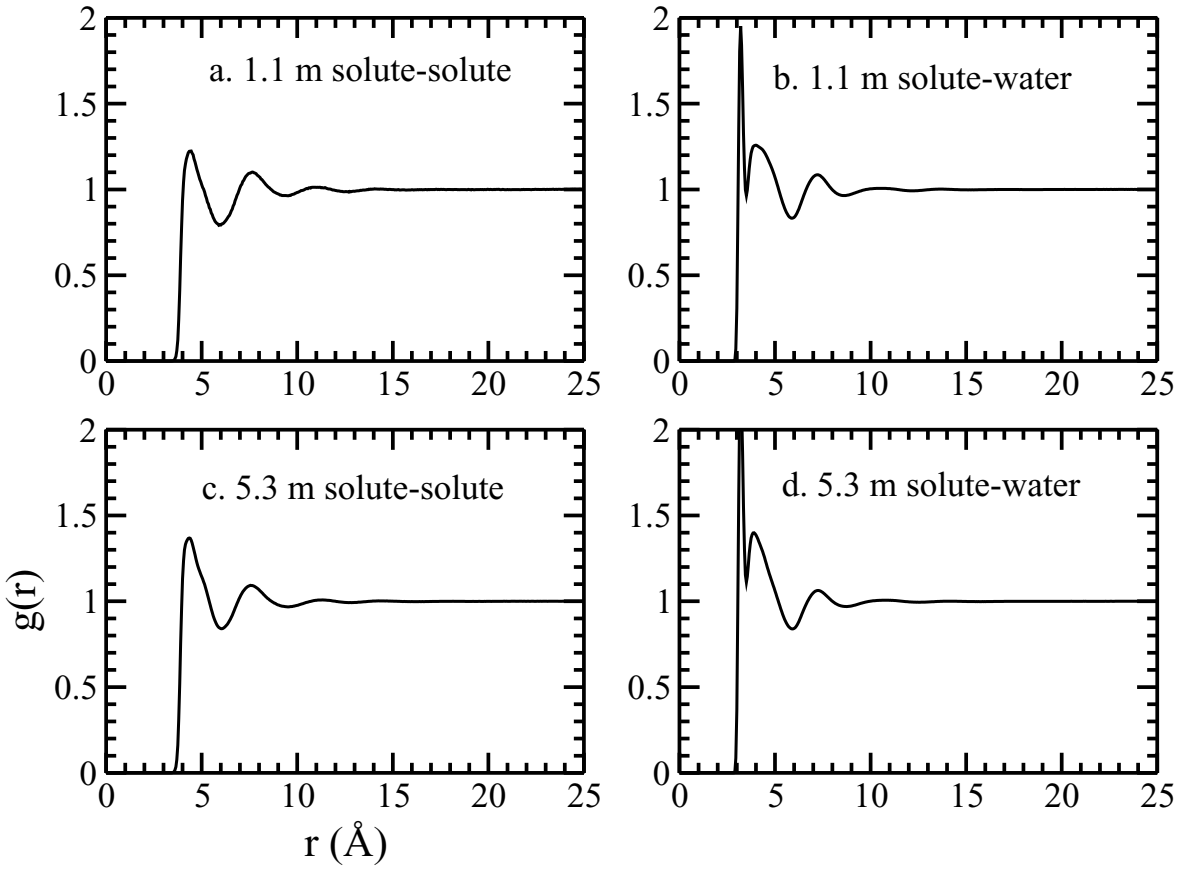

Figure A.3: RDFs for K-B analysis. Solute-solute RDF (a) in 1.1 m (c) 5.3 m GdmCl solution. Solute-water RDF in (b) 1.1 m (d) 5.3 m GdmCl. Reproduced with permission from Shuching Ou, Di Cui and Sandeep Patel. "Liquid-Vapor Interfacial Properties of Aqueous Solutions of Guanidinium and Methyl Guanidinium Chloride: Influence of Molecular Orientation on Interface Fluctuations." *Journal of Physical Chemistry B.* **2013**, *117 (39)*, 11719-11731. Copyright 2013 American Chemical Society.

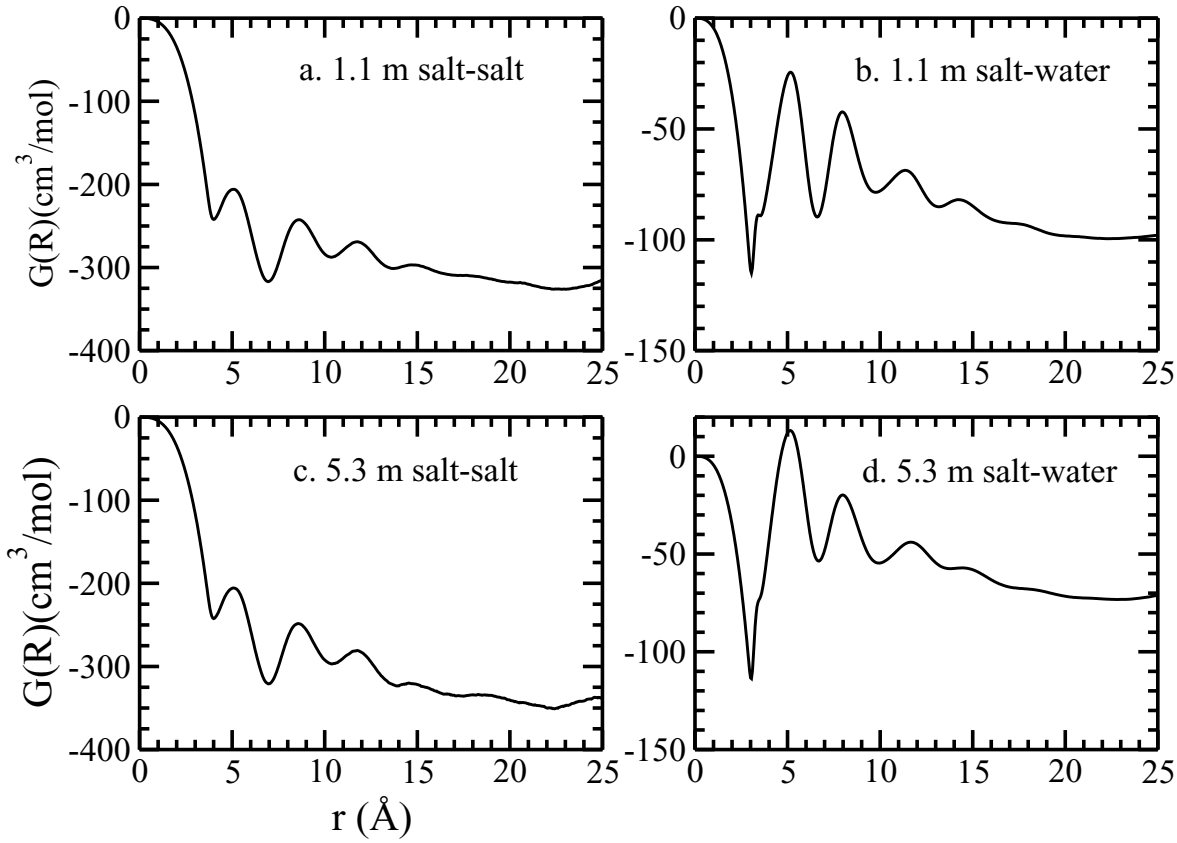

Figure A.4: Kirkwood-Buff integrals correspond to panels in Figure A.3. Reproduced with permission from Shuching Ou, Di Cui and Sandeep Patel. "Liquid-Vapor Interfacial Properties of Aqueous Solutions of Guanidinium and Methyl Guanidinium Chloride: Influence of Molecular Orientation on Interface Fluctuations." *Journal of Physical Chemistry B.* **2013**, *117 (39)*, 11719-11731. Copyright 2013 American Chemical Society.

Appendix B

CORRELATION LENGTH FOR TUBE-ION SURFACE

To define our tube-water surface, we used the correlation length (ξ) = 3 Å, which is roughly the size of a single water molecule in the bulk, to assign the Gaussian mass to each water oxygen. However, unlike the water, the total number of ions is less, as a result we need to consider a larger correlation length to render the coarse-grained surface. In Figure B.1 a we tested the mean tube-ion surface using ξ = 5, 6, 8, 10 Å, since the 0.75 bulk density of I^- lies in $r \approx 10.5$ Å (Figure B.1 b, from Reference [110]), we decided to use ξ = 6 Å as the correlation length in the further study of tube-ion surface.

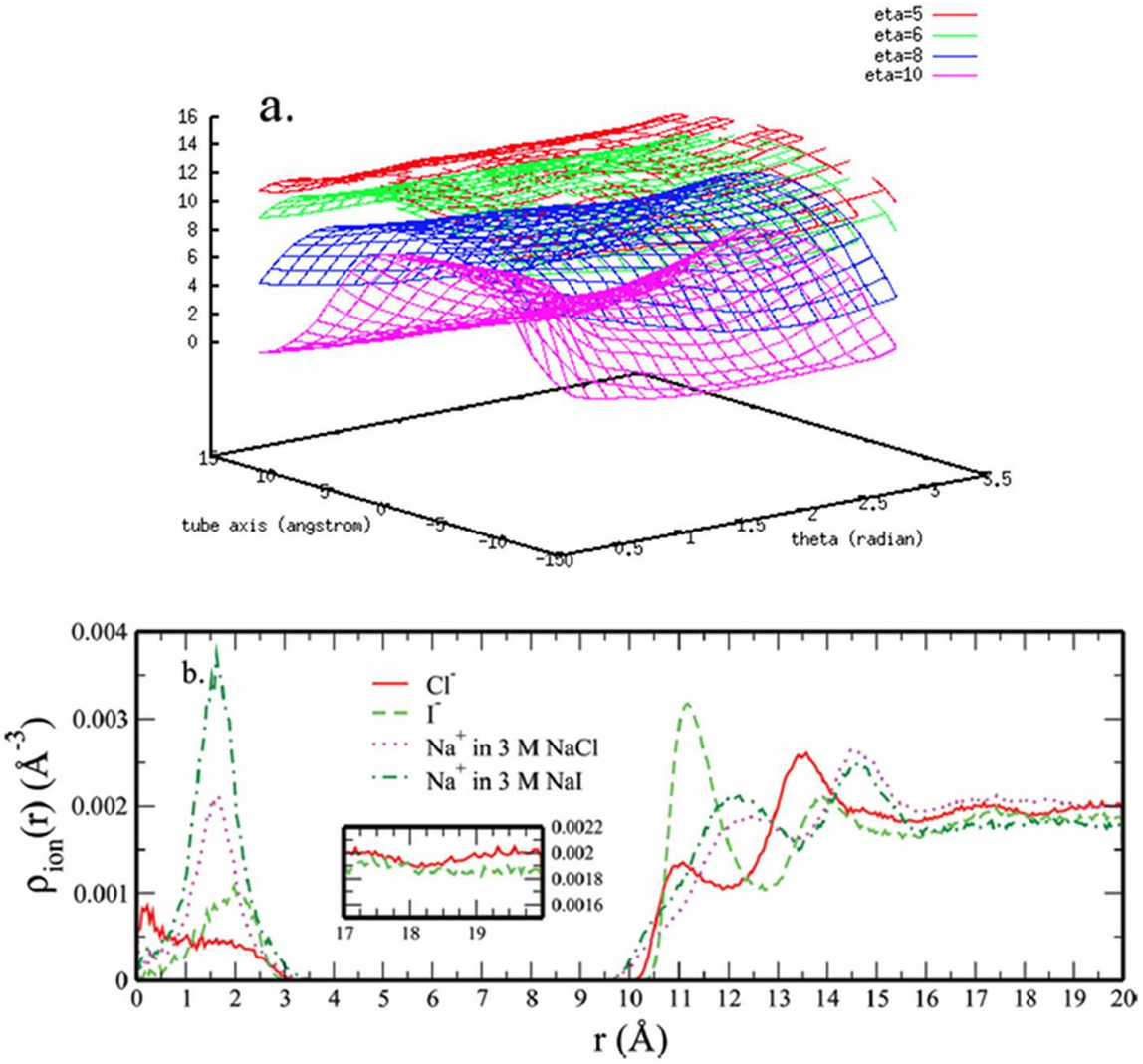

Figure B.1: (a) Mean surface of tube-ion using different correlation length (η). (b) Tube-ion radial number density.

Appendix C

INTERTUBE REGION: LARGER VOLUME

Here we use a large volume between the tubes to show the trends mentioned in the main paper still hold. The length (L) of the box is along the x-axis between $\pm$ 11.0 Å, which makes $L = 22.0$ Å; width (W) is along the z-axis and determined via subtracting the tube separation (d) with the tube diameter ($D = 13.56$ Å); the height (H) equals $D = 13.56$ Å and is along the y-axis. The results are shown in Figure C.1. We can see that the jump of $\langle N_{water} \rangle$ around $d = 19.4$ Å and the trends are consistent with the results in the paper. However, the second jump near the second barrier of PMF ($d = 21.8$ Å) becomes ambiguous. This is probably due to a lower fraction of the volume being "confined" and some washing out of the distinct jumps.

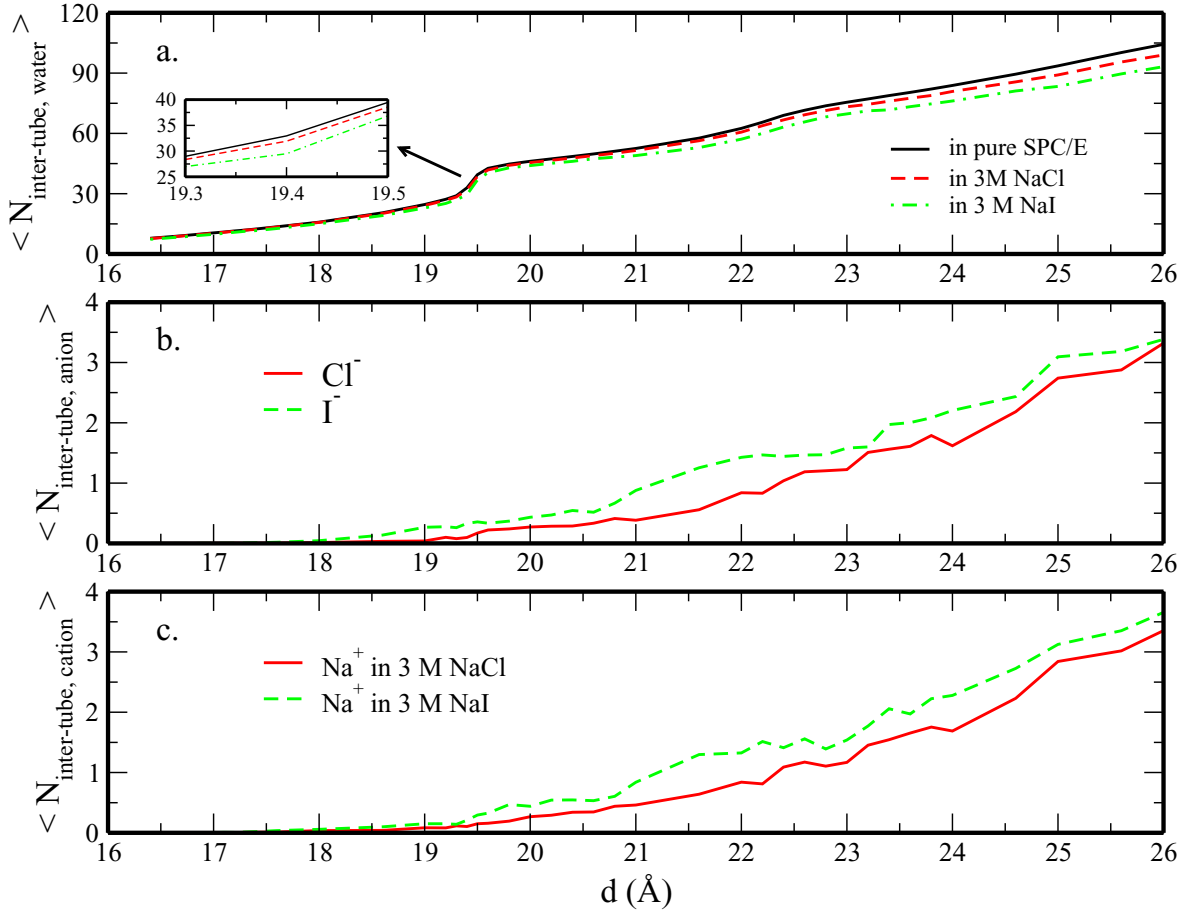

Figure C.1: Calculated average number of (a) water molecules, (b) anions, and (c) cations of the confined region in pure water and 3 M NaX (X = Cl, I) solutions. Insets in panel a show focused view of the density peaks. Reproduced with permission from Shuching Ou, Sandeep Patel and Brad A. Bauer. "Free Energetics of Carbon Nanotube Association in Pure and Aqueous Ionic Solutions." *Journal of Physical Chemistry B.* **2012**, *116 (28)*, 8154-8168. Copyright 2012 American Chemical Society.

Appendix D

LONG-RANGE CORRECTION OF LENNARD-JONES POTENTIAL FOR PMF CALCULATION OF NANOTUBE ASSOCIATION

In this section we test with the systems using longer cutoff which has been discussed in the manuscript. The long-range correction can be evaluated analytically via Equation D.1

$$\begin{aligned}\Delta E_{\mathrm{LJC}} &= \sum_i \sum_{j\neq i} 4\pi\rho_j\varepsilon_{ij}\{\int_{r_{\mathrm{on}}}^{r_{\mathrm{off}}} \left(\frac{R_{\mathrm{min},ij}^{12}}{r_{ij}^{12}} - 2\frac{R_{\mathrm{min},ij}^{6}}{r_{ij}^{6}}\right)[1-S(r_{ij})]r_{ij}^2 dr \\ &+ \int_{r_{\mathrm{off}}}^{r'_{\mathrm{on}}} \left(\frac{R_{\mathrm{min},ij}^{12}}{r_{ij}^{12}} - 2\frac{R_{\mathrm{min},ij}^{6}}{r_{ij}^{6}}\right) r_{ij}^2 dr \\ &+ \int_{r'_{\mathrm{on}}}^{r'_{\mathrm{off}}} \left(\frac{R_{\mathrm{min},ij}^{12}}{r_{ij}^{12}} - 2\frac{R_{\mathrm{min},ij}^{6}}{r_{ij}^{6}}\right) S(r_{ij}) r_{ij}^2 dr\} \end{aligned} \tag{D.1}$$

where i loops through all the tube atoms, j runs over all the atoms except for the corresponding atom i. r_{ij} is the distance between atom i and j, ρ_j is the number density of the species of atom j. ε_{ij} and $R_{\mathrm{min},ij}$ are the LJ parameters between atom i and j. $S(r)$ is the switching function, r_{on} and r_{off} are the original cutoff distances at which the switching function is turned on and off, which are 11.0 and 12.0 Å respectively. r'_{on} and r'_{off} are the longer cutoff distances which are used in this test.

With the long-range correction, we can rewrite the PMF into

$$\Delta W = \Delta W_{\mathrm{original}} + \Delta W^{\dagger} \tag{D.2}$$

where $\Delta W^{\dagger}$ is the long-range correction term. In practice, we can compute the force with the larger cutoff instead of the switching function between 11 Å (r_{on}) and 12 Å (r_{off}). Table D.1 list the results of the average force in z-dimension ($\langle F_{\mathrm{z}}\rangle$) with different cutoff using the last 1 ns of data at the tube separation d = 16.9 Å (contact state)

and 26.0 Å (dissociated state) as the representative windows. According to Table D.1, the results using 22 and 24 Å as the new cutoff show approximately -0.14 and -0.1 kcal/mol/Å for the separations of 16.9 and 26.0 Å regardless of the system being SWNT's in pure water or salt solutions. For a cutoff scheme larger than 22/24, the difference is trivial. The result indicates that the difference among the correction terms $\Delta W^{\dagger}_{\text{pure}}$, $\Delta W^{\dagger}_{\text{NaCl}}$ and $\Delta W^{\dagger}_{\text{NaI}}$ should be negligible.

System	r'_{on}/r'_{off}	11/12	22/24	24/26	26/28	28/30
$d = 26.0$ Å	Pure water	0.264	0.117	0.114	0.110	0.110
	3 m NaCl	0.411	0.281	0.278	0.274	0.273
	3 m NaI	0.960	0.818	0.815	0.811	0.818
$d = 16.9$ Å	Pure water	-4.911	-5.023	-5.023	-5.022	-5.023
	3 m NaCl	-5.661	-5.749	-5.749	-5.749	-5.749
	3 m NaI	-5.235	-5.342	-5.341	-5.341	-5.337

Table D.1: The average force in z-dimension ($\langle F_z \rangle$). Numbers in the head indicate r'_{on}/r'_{off} used in the switching function. Values in the table show the $\langle F_z \rangle$ between the corresponding cutoff listed and the cutoff used in the manuscript, which is 11/12. The units of the cutoff and $\langle F_z \rangle$ are Å and kcal/mol/Å, respectively. Reproduced with permission from Shuching Ou, Sandeep Patel and Brad A. Bauer. "Free Energetics of Carbon Nanotube Association in Pure and Aqueous Ionic Solutions." *Journal of Physical Chemistry B.* **2012**, *116 (28)*, 8154-8168. Copyright 2012 American Chemical Society.

Appendix E

PERMISSIONS

Portions of this thesis are reproduced with permission from the following original research articles:

Brad A. Bauer, Shuching Ou and Sandeep Patel. "Role of Spatial Ionic Distribution on the Energetics of Hydrophobic Assembly and Properties of the Water/Hydrophobe Interface." *Physical Chemistry Chemical Physics.* **2012**, *14*, 1892-1906. Copyright 2012 Royal Society of Chemistry.

Brad A. Bauer, Shuching Ou and Sandeep Patel. "Solvation Structure and Energetics of Single Ions at the Aqueous Liquid-Vapor Interface." *Chemical Physics Letters.* **2012**, *527*, 22-26. Copyright 2012 Elsevier.

Shuching Ou, Sandeep Patel and Brad A. Bauer. "Free Energetics of Carbon Nanotube Association in Pure and Aqueous Ionic Solutions." *Journal of Physical Chemistry B.* **2012**, *116 (28)*, 8154-8168. Copyright 2012 American Chemical Society.

Shuching Ou, Yuan Hu, Hongbin Wan and Sandeep Patel. "Spherical Monovalent Ions at Aqueous Liquid-Vapor Interfaces: Interfacial Stability and Induced Interface Fluctuations." *Journal of Physical Chemistry B.* **2013**, *117 (39)*, 11732-11742. Copyright 2013 American Chemical Society.

Shuching Ou and Sandeep Patel. "Temperature Dependence and Energetics of Single Ions at the Aqueous Liquid-Vapor Interface" *Journal of Physical Chemistry B.* **2013**, *117 (21)*, 6512-6523. Copyright 2013 American Chemical Society.

Shuching Ou, Di Cui and Sandeep Patel. "Liquid-Vapor Interfacial Properties of Aqueous Solutions of Guanidinium and Methyl Guanidinium Chloride: Influence of Molecular Orientation on Interface Fluctuations." *Journal of Physical Chemistry B.* **2013**, *117 (39)*, 11719-11731. Copyright 2013 American Chemical Society.

Shuching Ou, Timothy R. Lucas, Yang Zhong, Brad A. Bauer, Yuan Hu and Sandeep Patel. "Free Energetics and the Role of Water in the Permeation of Methyl Guanidinium across the Bilayer-Water Interface: Insights from Molecular Dynamics Simulations Using Charge Equilibration Potentials." *Journal of Physical Chemistry B.* **2013**, *117 (13)*, 3578-3592. Copyright 2013 American Chemical Society.

Samuel Schlachter, Stephen Herbein, Shuching Ou, Jeremy Logan, Sandeep Patel and Michela Taufer. "Pursuing Coordinated Trajectory Progression and Efficient Resource Utilization of GPU-enabled Molecular Dynamics Simulations." *Design & Test, IEEE.* **2014**, *31 (1)*, 40-50. Copyright 2014 IEEE.

Di Cui, Shuching Ou, Eric R. Peters and Sandeep Patel. "Ion-Specific Induced Fluctuations and Free Energetics of Aqueous Protein Hydrophobic Interfaces: Towards Connecting to Specific-Ion Behaviors at Aqueous Liquid-Vapor Interfaces." *Journal of Physical Chemistry B.* **2014**, *ASAP*, DOI: 10.1021/jp4105294. Copyright 2014 American Chemical Society.